College of Science
Department of Physics
Swansea University

Be^+-Assisted Antihydrogen Synthesis and Trapping

Maria Beatriz Gomes Gonçalves

Submitted to Swansea University in fulfilment
of the requirements for the Degree of Doctor of Philosophy

September 2025

To my parents for teaching me how to believe in myself and to always put everything I have into anything I do.
Nas palavras do Nandinho:

"Para ser grande sê inteiro: nada
Teu exagera ou exclui.
Sê todo em cada coisa. Põe quanto és
no mínimo que fazes.
Assim em cada lago a lua toda
Brilha, porque alta vive."

Ricardo Reis

Declarations

This work has not previously been accepted in substance for any degree and is not being concurrently submitted in candidature for any degree.

Signed.[redacted].....

Date.....

This thesis is the result of my own investigations, except where otherwise stated. Other sources are acknowledged by footnotes giving explicit references. A bibliography is appended.

Signed..[redacted].....

Date.....

I hereby give consent for my thesis, if accepted, to be available for electronic sharing

Signed...[redacted].....

Date.....

The University's ethical procedures have been followed and, where appropriate, that ethical approval has been granted.

Signed...[redacted].....

Date.....

Abstract

Antihydrogen, the bound state of a positron and an antiproton, is a uniquely well-suited system for testing fundamental symmetries between matter and antimatter. The Antihydrogen Laser Physics Apparatus (ALPHA collaboration) synthesises antihydrogen atoms by slowly merging cold non-neutral positron and antiproton plasmas and traps the antiatoms in a magnetic minimum trap. While trapping efficiency has improved since its first demonstration in 2010, it plateaued after 2017.

In ALPHA's experimental conditions, antihydrogen is predominantly formed via three-body recombination, which has been theoretically and experimentally shown to strongly depend on the temperature of the positron plasma: lower positron temperatures yield higher antihydrogen trapping rates. In the ALPHA-2 trap, positrons alone reach a lower temperature limit of $15 - 20$ K. The implementation of sympathetic cooling of positrons through collisions with laser-cooled Be^+ ions enabled stable lowering of these temperatures to below 10 K.

This thesis describes the work towards antihydrogen synthesis with positrons prepared using this cooling method. A novel ion plasma preparation technique was developed to improve reproducibility, and a sophisticated control system with automated beam steering was implemented to ensure long-term operational stability. Moreover, the first demonstration of sympathetic cooling of positrons to < 10 K in a radially asymmetric magnetic field was carried out. Culminating in the first Be^+-assisted antihydrogen synthesis and trapping. Careful optimisation of this technique resulted in a near eightfold increase in the antihydrogen trapping rate, and allowed for systematic studies of three-body recombination that were not possible before its implementation. Overall, this technique represents a paradigm shift for the ALPHA physics programme and provides a deeper understanding of antihydrogen synthesis, opening new avenues for precision studies of antimatter.

Acknowledgements

First of all, I would like to thank my supervisor, Prof. Niels Madsen, for his guidance and support during my time at ALPHA. Every interaction with you, Niels, is impossibly interesting.

I would like to thank Dr. Kurt Thompson for his patience and seemingly infinite knowledge. I truly could not have done any of this without you. Your work ethic and dedication are true inspirations to me. Nothing could have prepared me for the joy of seeing the number 36 on a screen while "Clean" very aptly played in the background, our sheer euphoria is one of the things I look back on the fondest. A big thank you also to the rest of the Be^+ team: to Asia for teaching me my way around a laser, to Tom for being the fastest learner and such fun data-taking company, and to Steve for his immense help in the early days.

An immeasurably large thank you to every person at ALPHA who helped me, taught me, and answered any of my many questions, you're too many to name. I would also like to thank the other students who inevitably became friends and drinking companions: Joos, Pooja, Jaspal, Ted, Lukas, Danielle...

Thank you, Abby, for being the best flatmate and friend, for all the ideas we came up with together, for the very needed chicken and Luigia trips that always made my soul feel a little less heavy. Thank you, Ginny, for the Taylor Swift listening parties and random Hamilton singing in the kitchen, for your endless help and kind words.

A thank you to Alyssa for being a breath of fresh non-ALPHA air during the many fries trips, for the fun conversations, and for those Thanksgiving sweet potatoes (yes I'm still thinking about them).

A big thank you to Sophie for always being there for me, for pulling me out of countless spirals, for the endless laughs, for everything.

Thank you to my friends from Portugal, who have grown with me. A special thank you to my oldest friends, to Raquel for the very long calls that keep us connected even when we're so far away, and to Alicia, who has always been the first person I tell when something happens.

A very special thank you to Craig for always, no matter what, making it his mission to make me laugh. Everything feels simpler when I'm next to you. Thank you for your support and for believing in me even when I didn't.

I couldn't have done this without my family: to my sister Rita and my brother Filipe, thank you for being my first and forever best companions; to my avó Maria and avó Dália, thank you for the endless laughs na ilha and for always worrying about me, I swear my brain is okay, you don't have to worry. To my avô Manel and avô Belinho, I know you're proud of me, I miss you. And to everyone else in my family, thank you for your support and encouragement.

The biggest thank you goes to my parents. Mãe, Pai... you made me the person I am today, you nourished my curiosity from the start, you tried to answer all my questions, and even when you were tired of them, you inspired me to ask more. I cannot even begin to explain how grateful I am to have won the parent lottery, so I'll just leave you with an *obrigada*.

These past four years have been filled with joy, stress, sleepless nights, unbridled celebrations in the control room, tears, laughter, some physics and many beers. Every person I crossed paths with helped make this experience the wonderful time it was, so thank you all. I wouldn't change a thing, and if you ask me now that it's over, it was 100% worth it.

Contents

1 Introduction

The Antihydrogen Laser PHysics Apparatus (ALPHA experiment) has been at the forefront of studying antimatter for many years, focusing on antihydrogen, the simplest pure antimatter bound state composed of an antiproton and a positron. Antimatter was first theoretically predicted by Paul Dirac in 1928 [1], and remained a theoretical concept until Carl Anderson's detection of the positron, the electron's antiparticle, in 1932 [2]. Over time, other antiparticles were discovered, most relevant to the work of this thesis, the antiproton in 1955 [3]. It is now widely accepted that for every particle, there exists an antimatter counterpart with equal mass and spin but opposite charge.

According to the Big Bang theory, matter-antimatter pairs produced in the early universe through pair production should have annihilated, producing photons. Yet, observations reveal a universe overwhelmingly dominated by matter, raising the fundamental question: *Where is the antimatter?* This discrepancy suggests that some process in the early universe must have favoured matter over antimatter, resulting in the significant asymmetry that we see today.

The Standard Model (SM) of particle physics formalises three fundamental symmetries:

- **Charge conjugation (C-symmetry):** Inverts the sign of fundamental charges, such as electromagnetic charge.
- **Parity inversion (P-symmetry):** Inverts the spatial coordinates used to describe a particle.

◇ **Time reversal (T-symmetry):** States that physical systems should behave identically when time is reversed.

Initially, it was theorised that all natural phenomena were invariant under these three symmetries separately. However, experimental discoveries have shown that P-symmetry [4] and CP-symmetry [5] are violated in nature. The only symmetry combination that remains unbroken is the combined *CPT-symmetry* (Charge Conjugation, Parity Inversion, and Time Reversal).

A violation of this symmetry may help explain the imbalance between matter and antimatter. CPT symmetry dictates that antiparticles should have equal mass and spin, and charge with the same magnitude but opposite sign when compared to their matter counterparts. The Baryon-Antibaryon Symmetry Experiment BASE at the European Organisation for Nuclear Research CERN investigates properties of antiprotons, such as their charge-to-mass ratio [6] and magnetic moment [7] to extreme precision, looking for asymmetries in these single-particle properties.

Another consequence of CPT invariance is that antimatter bound states must have exactly the same atomic energy spectrum as their matter counterparts [8]. Studying these systems provides comparisons with matter and enables precision tests, such as probing possible shifts in the fine-structure constant, comparing the hyperfine splitting in hydrogen and antihydrogen, and investigating how neutral antimatter interacts with gravity.

The simplest purely antimatter bound state is the antihydrogen atom, composed of one antiproton and one positron. Not only is this the easiest antimatter bound state to produce, but its matter counterpart, hydrogen, is a thoroughly studied system that plays a fundamental role in physics. Thus, studying antihydrogen is a very attractive endeavour to probe fundamental symmetries.

However, before we can study antihydrogen, we must first synthesise it. Unlike positrons, which are naturally occurring, antihydrogen must be produced through controlled experiments. The production of antiprotons requires significant energy, and once produced, they must be decelerated before they can be used in antihydrogen synthesis. Currently, the only facility in the world equipped to deliver low-energy antiprotons is the Antiproton Decelerator (AD) complex at CERN. Low-energy antihydrogen was first synthesised and observed by the ATHENA [9] and ATRAP [10] collaborations in 2002, and was first trapped by the ALPHA collaboration in 2010 [11]. Since then, ALPHA has performed several measurements on this antiatom.

1.1 Antihydrogen Experimentation at the ALPHA

The ALPHA experiment synthesises and traps antihydrogen to study its properties and compare them to those of its matter counterpart, hydrogen. There are two main research components: ALPHA-2, where precision spectroscopy of antihydrogen is performed, and ALPHA-g, where the interaction between antihydrogen and gravity is investigated.

In ALPHA, antihydrogen is trapped in a Ioffe-Pritchard magnetic trap, which consists of a radially inhomogeneous field providing radial confinement, together with two mirror coils that provide axial confinement. This was first demonstrated in 2010, with the detection of a total of 38 annihilation events consistent with the release of antihydrogen over 335 attempts, corresponding to about one antihydrogen atom every nine attempts. This was, of course, not enough for detailed experimentation, but, as shown in Fig. 1.1, the number of antihydrogen atoms trapped per hour

quickly increased due to various improvements. As of the beginning of my PhD, ALPHA could trap and accumulate around 300 antiatoms per hour.

This increased trapping rate enabled several groundbreaking measurements:

- ◇ Measurement of the 1s-2s transition to 2×10^{-12} precision [12, 13].
- ◇ First laser cooling of antihydrogen atoms [14].
- ◇ First measurement of the hyperfine splitting in antihydrogen [15].
- ◇ First observation of the effect of gravity on antimatter [16].

Further increases in the trapping rate would not only accelerate data collection and improve the precision of existing measurements, but also make possible entirely new experiments requiring larger numbers of antihydrogen atoms to achieve a statistically significant signal above background. In addition, a higher trapping rate would enable the selection of specific subsets of the trapped population, such as low kinetic energy antiatoms, opening the way to experimental approaches that have not yet been explored.

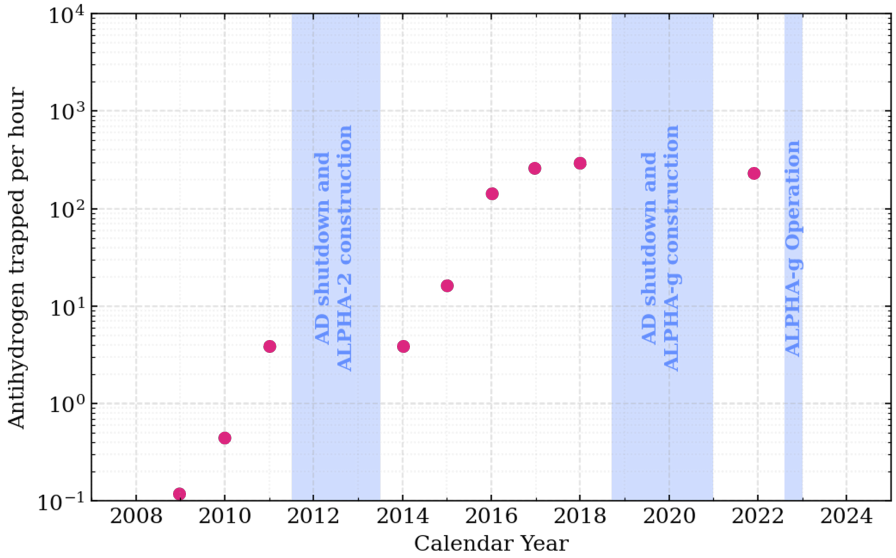

Figure 1.1: Antihydrogen trapped per hour over the years of operation of the ALPHA experiment. The blue shaded regions represent CERN and ALPHA hardware update periods, where antiproton production could not occur, or when antihydrogen physics was performed in the ALPHA-g apparatus and not in the ALPHA-2 device (2022 blue region). The trapping rate has significantly increased since the beginning of ALPHA, from less than an anti-atom per hour in 2010 to around 300 in 2022.

1.2 Enhancing Antihydrogen Synthesis and Trapping

Increasing the amount of antihydrogen atoms available for experimentation is crucial at ALPHA. Antiprotons are a precious resource, available only for a few months each year, determined by the CERN accelerator schedule. As a result, the window of time for synthesising and experimenting

with antihydrogen is also limited. Maximising the number of antihydrogen atoms per synthesis cycle is a continuous effort at ALPHA.

In the standard ALPHA antihydrogen synthesis procedure, a positron plasma and an antiproton cloud are confined in adjacent potential wells. The depths of these wells are slowly reduced, allowing the positrons to traverse the antiproton cloud, during which antihydrogen formation can occur. Some notable innovations that have led to significant increases in the number of trapped antihydrogen atoms per hour are:

- ◇ a novel synthesis scheme [17], which minimises potential differences between the positron and antiproton plasmas and introduces evaporative cooling during the synthesis process.
- ◇ a plasma stabilisation technique [18], allowing for reproducible production of lepton plasmas and full control of plasma parameters. This greatly reduced shot-to-shot variations in the trapping rate due to plasma instabilities.
- ◇ a major hardware upgrade [13], allowing synthesis cycles to be repeated without losing previously trapped antiatoms, this process is called *antihydrogen accumulation*.

After many years of steady improvement, ALPHA reached a plateau in the number of antihydrogen atoms trapped per hour around 2017, as shown in Fig. 1.1. After extensive optimisation, all known methods for improving the antihydrogen trapping rate had been exhausted. For inspiration on the next steps towards a higher antihydrogen trapping rate, we can investigate the fundamental properties of the antihydrogen formation process.

The main formation mechanism under the conditions of the ALPHA experiment is three-body recombination, where two positrons collide near an antiproton, one of the positrons loses energy and gets bound to the antiproton, and the second positron carries away excess energy [19,20]. The three-body recombination rate, Γ_{TBR}, has been hypothesised to strongly depend on the temperature of positrons during synthesis, T_{e^+}, and on the positron density n_{e^+}, [21]

$$\Gamma_{TBR} \propto n_{e^+}^2 T_{e^+}^{-3/2}. \tag{1.2.1}$$

This expression describes the behaviour of the system in a non-steady state, where the positrons quickly cross the antiprotons and several antihydrogen formation and ionisation cycles occur. At the start of the 2023 antiproton run, ALPHA used about 25 times more positrons than antiprotons during antihydrogen synthesis, which, along with simulations [22] and calculations [21], support the hypothesis that the positron parameters will more strongly dictate the temperature of the produced antihydrogen atoms.

Experimental evidence from the ATHENA collaboration also highlights the importance of the positron temperature on antihydrogen synthesis [23]. In general, lower positron temperatures have been shown to consistently enhance both synthesis and trapping efficiency. Given these findings, optimising positron temperature appears to be the next promising path for significantly improving the antihydrogen trapping rate at ALPHA.

We can then formulate a question which can guide us towards higher antihydrogen synthesis and trapping rates: **"How do we reduce the positron plasma temperature in a way that is compatible with the current antihydrogen synthesis procedure?"**. There are two main parts to this question:

- ◇ developing a method that further reduces the positron plasma temperature;
- ◇ making this new cooling technique compatible with the antihydrogen synthesis procedure at ALPHA.

1.2.1 Reducing the Positron Plasma Temperature

ALPHA uses a Penning-Malmberg trap to trap charged particles. These traps use a strong uniform magnetic field along the trap axis to provide radial confinement, combined with electrostatic potentials on cylindrical electrodes for axial confinement. When trapped, positrons move in circular orbits under the influence of the magnetic field. Their trajectory implies that they are constantly being accelerated and thus losing energy by emitting electromagnetic waves. This process is called *cyclotron cooling*. This cooling method is extremely efficient for particles with low mass, such as positrons. Through this cooling method, the positrons at ALPHA reach a minimum temperature of about 15 K. Reducing this temperature further without compromising other parameters, such as positron number, is not a viable option.

Fortunately, as we know from putting ice in our drinks, we can cool an already cold thing by mixing it with something even colder. And if there is something atomic physicists are good at doing, it is making ions really cold.

Laser cooling of trapped ions was first demonstrated in 1978 [24] and has since become a widely used method to obtain cold particles, often to sub-Kelvin temperatures. Laser cooling is based on the idea that radiation can exert pressure on particles. Photons carry momentum, thus when they scatter off an ion, the ion's momentum changes, preserving overall momentum. However, the interaction with the photon does not always reduce the ion's kinetic energy, it can also increase it. In a trap, ions oscillate within the confining potential, so their motion causes a Doppler shift: ions moving toward the laser see a lower light frequency than those moving against it. To cool the ions, the laser frequency should be slightly red-detuned from the ion's resonant transition. Due to the Doppler effect, ions moving toward the laser see the frequency shifted into resonance and preferentially absorb photons. Each absorption event slows the ion in the laser's direction, while spontaneous emission randomises its momentum, leading to an overall energy reduction and thus cooling. This is called **Doppler cooling**. The minimum temperature is limited by the fact that spontaneous emission slightly heats the ions; the equilibrium temperature is reached when the cooling balances this heating, as is often in the order of 1 mK or below.

If a cold positively charged ion plasma is mixed with a positron plasma and the ions are actively laser-cooled, the positrons can be cooled through energy exchange via Coulomb collisions with the laser-cooled ions. This technique is called **sympathetic cooling**, first demonstrated by cooling Hg^+ ions with laser-cooled Be^+ ions in a Penning trap [25]. Sympathetically cooling positrons using laser-cooled Be^+ ions was first shown in 2003 [26], where a few thousand positrons were cooled to less than 5 K.

This is then a promising technique for reducing the temperature of positron plasmas at ALPHA. These cryogenic positrons can then be used for synthesising antihydrogen, hopefully greatly increasing the trapping rate.

The project of sympathetically cooling positrons at ALPHA for enhancing antihydrogen synthesis was started many years ago, with the first step being to determine which ion is the best

candidate [27]. Be^+ was chosen as it is the lightest laser-coolable ion, minimising the mass ratio between the ion and the positron, maximising cooling efficiency. Moreover, Be^+ has a well-studied laser cooling transition at 313 nm and has a relatively simple electronic structure.

After selecting the appropriate ion, a Be^+ source was implemented in the main ALPHA apparatus and sympathetic cooling of a few million positrons to cryogenic temperatures was first demonstrated at ALPHA in 2019 [28–30]. This proof-of-principle measurement was a significant development towards Be^+-assisted antihydrogen production.

1.2.2 Compatibility with the Antihydrogen Synthesis Procedure

This aspect of the problem had not been fully addressed before the work in this thesis. The antihydrogen synthesis procedure has been finely tuned over many years, with incremental adjustments to parameters and timings leading to an optimal, albeit highly sensitive set of particle preparations and parameters. The first major challenge is ensuring the Be^+ plasma preparation and positron sympathetic cooling fit within the four-minute time window each synthesis cycle lasts. The procedure described in the proof-of-principle measurement [30] exceeded this limit by more than a factor of two.

In the original setup, laser cooling was restricted to a small region of the trap, spanning only a few electrodes near its centre. Extending laser cooling across the entire axial length of the trap would allow for more freedom in where to store the ions during other particle preparations and enable finer control of the Be^+ plasma parameters. An additional cooling beam with a trajectory through the electrode centres was added to allow for cooling at every trap electrode.

A radially asymmetric magnetic field is necessary for antihydrogen trapping. This field inhomogeneity causes heating and expansion of plasmas trapped in the Penning-Malmberg trap. Successful Be^+ laser cooling and positron sympathetic cooling had never been demonstrated before under these conditions, and it was unclear whether it was possible to overcome the heating induced by the asymmetric magnetic field.

From a more technical standpoint, this procedure had to be robust and reproducible daily over many weeks, ideally requiring minimal expert interventions. This required major hardware upgrades and the development of an active beam stabilisation system to maintain the beam pointing of the cooling beams through the trap.

Additionally, there are the interesting unforeseen problems that experimental physics inevitably throws at unsuspecting PhD students.

So very succinctly answering the main question of this thesis, **"How do we reduce the positron temperature in a way that is compatible with the current antihydrogen synthesis procedure?"** Sympathetically cooling the positrons using laser-cooled Be^+ ions through a carefully and methodically developed procedure. And perhaps most importantly, by having a lot of fun with laser beams and plasmas.

All the challenges outlined here were successfully addressed, leading to the first-ever attempt at Be^+-assisted antihydrogen synthesis. This technique proved highly successful, resulting in a near 8-fold increase in the number of trapped antihydrogen atoms per synthesis cycle. Be^+-assisted antihydrogen synthesis and trapping is now the standard method for antihydrogen production at ALPHA.

1.3 Thesis Outline

This thesis discusses the work conducted by me and other members of the Be^+ team to develop Be^+-assisted antihydrogen synthesis, its implementation as the main antihydrogen production mechanism at ALPHA, and the study of different parameters and features of the antihydrogen synthesis process.

Chapter 2 outlines important theoretical concepts such as the dynamics of charged particles in a Penning-Malmberg trap and the theory of laser cooling, along with a description of some experimental techniques used at ALPHA for particle preparation.

Chapter 3 describes the various components of the ALPHA apparatus and discusses the plasma diagnostic techniques employed at ALPHA.

Chapter 4 explains how the Be^+ plasma is produced and prepared before merging it with the positron plasma. Many hardware and software upgrades were necessary, such as an active beam stabilisation system and an overall control system compatible with the general ALPHA control system. Moreover, a plasma parameter control technique, previously developed by the ALPHA collaboration for leptons, was coupled with laser cooling and implemented for the first time on an ion plasma, mitigating fluctuations in the ion number and plasma radius: a major step towards stable and reproducible Be^+ plasma preparation.

Chapter 5 describes how the positron and Be^+ plasmas are merged and prepared, fulfilling the criteria for compatibility with the overall antihydrogen production scheme, while minimising the positron plasma temperature through sympathetic cooling with the laser-cooled Be^+ ions.

Chapter 6 begins with a discussion of theoretical and simulation work on antihydrogen synthesis, followed by a description of how these antiatoms are produced and trapped at ALPHA. It then details the implementation of Be^+-assisted antihydrogen synthesis, the tuning of experimental parameters to optimise this process, and how this new technique allows us to detect and eliminate losses during antihydrogen accumulation, mitigating its saturation.

Chapter 7 outlines potential applications of Be^+ ions beyond their role in antihydrogen production. Spectroscopy of Be^+ offers several possibilities, such as measuring the on-axis magnetic field in ALPHA-2 and characterising the microwave standing wave pattern in this trap. Be^+ spectroscopy can also provide a complementary temperature diagnostic method, offering a way to benchmark ALPHA's existing method and set a lower limit for the positron plasmas used for antihydrogen synthesis. This chapter proposes experimental procedures for these future studies and concludes with a potential different approach to antihydrogen synthesis, aimed at increasing trapping efficiency by maintaining a constant positron density throughout synthesis.

Finally, Chapter 8 summarises the work presented in the previous chapters and provides a discussion of possible future developments to further improve antihydrogen synthesis and trapping. It also explores other areas where Be^+ can be useful in the context of the ALPHA experiment and concludes with final remarks.

1.4 Author Contributions

I joined ALPHA as a PhD student in 2021, becoming a part of a subgroup of the ALPHA experiment called the *Be$^+$ team*. Led by my supervisor, Prof. Niels Madsen, the team included a Postdoc, Dr. Kurt Thompson, with whom I worked closely throughout my PhD. When I first joined, Dr. Joanna Pezska was in the end stages of her PhD, and at the end of 2023, a new PhD student, Tom Robertson-Brown, also joined the team. We are responsible for maintaining all the hardware related to Be^+ production and preparation at ALPHA, ensuring its smooth operation throughout the antiproton runs.

Within the Be^+ team, I was primarily responsible for laser optics and alignment, including their setup and maintenance. I also designed and installed an active beam path stabilisation system for both of our cooling beams, over the long beam paths. Additionally, I played a key role in developing all the techniques used for Be^+- assisted antihydrogen synthesis.

Following the implementation of Be^+- assisted antihydrogen synthesis, I significantly contributed to diagnosing the performance and stability of the antihydrogen synthesis efficiency, ensuring the trapped antihydrogen population was sufficient for the various experiments performed at ALPHA. I also designed and performed multiple studies of antihydrogen synthesis and trapping, investigating aspects of these processes that had not previously been explored experimentally.

Beyond my direct PhD research, I took part in shift work from 2021 to 2024. This involved troubleshooting hardware issues, monitoring the experiment's performance, optimising particle preparation for antihydrogen synthesis, and data-taking. I also participated in general ALPHA interventions, including reassembling or repairing diagnostic stations and preparing the experiment for each antiproton run. During the summer of 2023, I supervised a CERN summer student, Sarah Price. I guided her investigations of the performance of UV fibre optic cables for 313 nm laser beam delivery.

1.5 Publications

As a co-author:

- [16] Anderson, E.K., Baker, C.J., Bertsche, W. *et al.*, Observation of the effect of gravity on the motion of antimatter. *Nature* **621**, 716–722 (2023). https://doi.org/10.1038/s41586-023-06527-1.
- Submitted to *Nature* on 08/09/2025: ALPHA Collaboration, Four ppm measurement of the antihydrogen ground state hyperfine splitting: a hundred-fold improvement.

As a main author:

- [31] Akbari, R., de Araujo Azevedo, L.O., Baker, C.J. *et al.*, Be^+-assisted, simultaneous confinement of more than 15000 antihydrogen atoms. *Nat Commun* **16**, 10106 (2025). doi.org/10.1038/s41467-025-65085-4

2 Theoretical Concepts and Experimental Techniques

ALPHA is a very complex experiment that requires expertise from a wide range of fields of physics to produce, trap and study antihydrogen. From plasma physics, related to the initial high-energy bunch of antiprotons and positron preparation, to low-energy atomic physics, when we perform high precision spectroscopy on an < 0.5 K antihydrogen volume, many different techniques have been applied and developed over the years to study fundamental physics at ALPHA. This chapter outlines some of the main theoretical concepts needed for the functioning of the experiment. I will focus on notions and techniques relevant to the work on this thesis. In addition, certain experimental methods that are fundamental to ALPHA's operation will be discussed, highlighting how they are motivated and guided by the underlying theoretical concepts.

2.1 Trapping Charged Particles

Trapping charged particles using electromagnetic fields allows the localisation and observation of such particles for long periods. Thus, creating prime conditions for detailed research of their properties as well as providing a stable environment to manipulate and control them. At ALPHA, trapping antiprotons, positrons, and other charged particles is imperative for producing antihydrogen.

Three-dimensional confinement is achieved using a combination of static electric fields and a magnetic field; these electromagnetic fields in the trap govern the motion of a trapped particle. At ALPHA, multiple particles are trapped within the same well simultaneously, often in a strongly coupled plasma regime. This introduces collective effects as the particles interact through the Coulomb force, changing their dynamics within the trap.

Understanding the motion and properties of the plasmas trapped at ALPHA is important for optimising antihydrogen synthesis, as plasma properties directly influence the efficiency and stability of the synthesis and trapping processes.

2.1.1 The Penning Trap

A Penning trap confines charged particles using a combination of magnetic and static electric fields. It was developed by Hans Dehmelt in the 1960s [32]. The original Penning trap design consists of three electrodes shaped as a hyperboloid of revolution: two endcaps and a ring electrode, as shown in Fig. 2.1. These electrodes have such a shape to produce a quadratic electrostatic potential, ϕ,

$$\phi(r,z) = \frac{V_0}{r_0^2 + 2z_0^2}(2z^2 - r^2), \tag{2.1.1}$$

where V_0 is the applied trap potential and r_0 and z_0 are the distances between the trap centre and the ring electrode and the trap centre and the endcaps, respectively, as defined in Fig. 2.1. This potential provides axial confinement of the particles in the trap.

The radial confinement is provided by a homogeneous axial magnetic field $\mathbf{B}$,

$$\mathbf{B} = B_0\hat{z}, \tag{2.1.2}$$

where B_0 is the magnitude of the field.

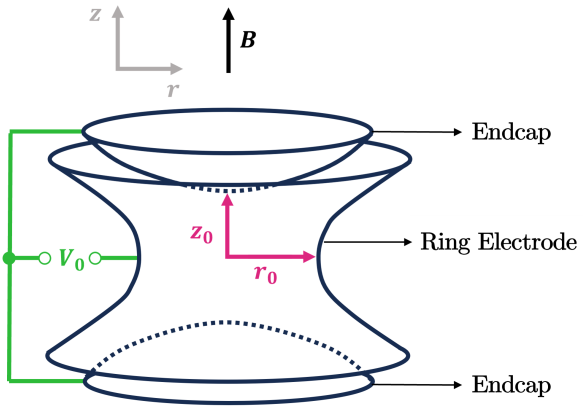

Figure 2.1: Penning trap diagram with two endcap and one ring electrodes. The uniform magnetic field $\mathbf{B}$ along the z direction provides radial confinement and a voltage V_0 applied to the endcaps provides axial confinement.

The Lorentz force allows us to define the equation of motion for a particle of mass m and charge

q in an electromagnetic field,

$$m\ddot{\mathbf{r}} = q(-\nabla\phi + \dot{\mathbf{r}} \times \mathbf{B}). \tag{2.1.3}$$

Substituting with the electrostatic potential form in Eq. 2.1.1 and with the axial magnetic field in Eq. 2.1.2, the motion can be split into the x, y and z components, given that $\mathbf{r} = (x, y, z)$,

$$\ddot{x} = \frac{\omega_z^2}{2}x - \omega_c\dot{y}, \tag{2.1.4}$$

$$\ddot{y} = \frac{\omega_z^2}{2}y + \omega_c\dot{x}, \tag{2.1.5}$$

$$\ddot{z} = -\omega_z^2 z. \tag{2.1.6}$$

The motion along the z component (axial motion) Eq. 2.1.6, is just a simple harmonic motion, since the electric force is the only restoring force in this direction. We can then define the **axial frequency,** w_z:

$$\omega_z = \sqrt{\frac{4qV_0}{m(r_0^2 + 2z_0^2)}}. \tag{2.1.7}$$

The motion in the x and y components (radial motion) is determined by the magnetic field $\boldsymbol{B}$, which introduces a cyclotron motion. The frequency of this motion is called *cyclotron frequency*, ω_c, and is proportional to the magnetic field strength, B_0 and the charge-to-mass ratio of the particle in the trap,

$$\omega_c = \frac{qB_0}{m}. \tag{2.1.8}$$

To solve Eq. 2.1.4 and Eq. 2.1.5 we can be clever and make the substitution $u = x + iy$, combining them into a single equation,

$$\ddot{u} - i\omega_c\dot{u} - \frac{\omega_z^2}{2}u = 0. \tag{2.1.9}$$

This equation has two solutions corresponding to two frequencies which describe the radial motion,

$$\omega_\pm = \frac{1}{2}\left(\omega_c \pm \sqrt{\omega_c^2 - 2\omega_z^2}\right). \tag{2.1.10}$$

The lower frequency solution, ω_- is called the **magnetron frequency**, also denoted as ω_m, represents a slow, large rotation around the trap axis, as shown in Fig. 2.2. The higher frequency solution, ω_+, is the **modified cyclotron frequency**, usually denoted as $\omega_c^{'}$, and is characterised by small, fast rotations along magnetic field lines, as depicted in Fig. 2.2.

The resulting motion is a combination of three different oscillatory motions: a simple harmonic motion along the trap axis, and two superimposed motions in the radial direction.

The motion described here is for a single particle trapped in an ideal Penning trap. At ALPHA, we work with hundreds of thousands, or even millions of particles, often in a strongly coupled plasma regime, which changes the dynamics of the particles within the trap.

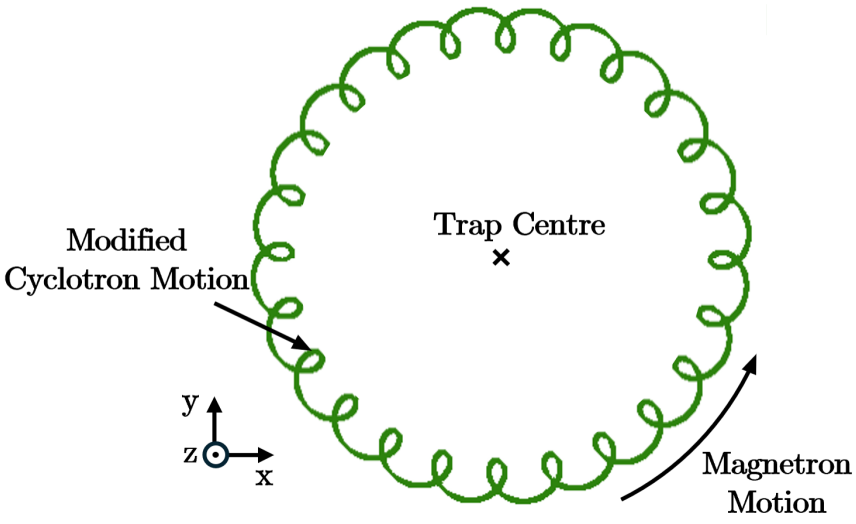

Figure 2.2: Radial $x - y$ plane motion of a single particle in a Penning trap. The particle follows a slow, large magnetron rotation and fast, small rotations at the modified cyclotron frequency. Axially, the particle also undergoes simple harmonic motion, which is not depicted in this plane.

The Penning-Malmberg Trap

Penning traps are widely used for trapping single particles in a well-defined volume. However, the classical Penning trap configuration, shown in Fig. 2.1, is not well-suited for ALPHA's requirements. This configuration does not allow the simultaneous confinement of oppositely charged particles in the same trap (an essential capability for antihydrogen synthesis, as positrons and antiprotons have opposite charges). Additionally, the closed endcap design presents practical challenges: loading particles into the trap is difficult, and laser access is severely limited. In ALPHA's case, where the trap is housed inside a cryostat, directing laser beams through gaps between electrodes becomes especially complex.

Luckily, a solution to these limitations was provided by J. Malmberg, who developed a variant of the Penning trap to study pure electron plasmas [33], the *Penning-Malmberg trap*. This design consists of stacked hollow cylindrical electrodes with open endcaps, allowing for extended particle confinement along the trap axis. If many electrodes are stacked, there can be several trapping regions, and by simply changing the polarity of the applied voltage, the sign of the trappable particles is inverted. The open endcap design also facilitates straightforward particle loading and provides direct laser access along the trap axis. Fig. 2.3 shows a sketch of a four-electrode Penning-Malmberg trap. The blue cloud illustrates a plasma trapped within the central two electrodes. This confinement is achieved by creating a potential well, making this region energetically favourable for the particles. For instance, if the plasma consists of negatively charged particles, a positive voltage can be applied to the central electrodes while keeping the endcaps at ground potential.

All of the charged particle traps at ALPHA are Penning-Malmberg traps.

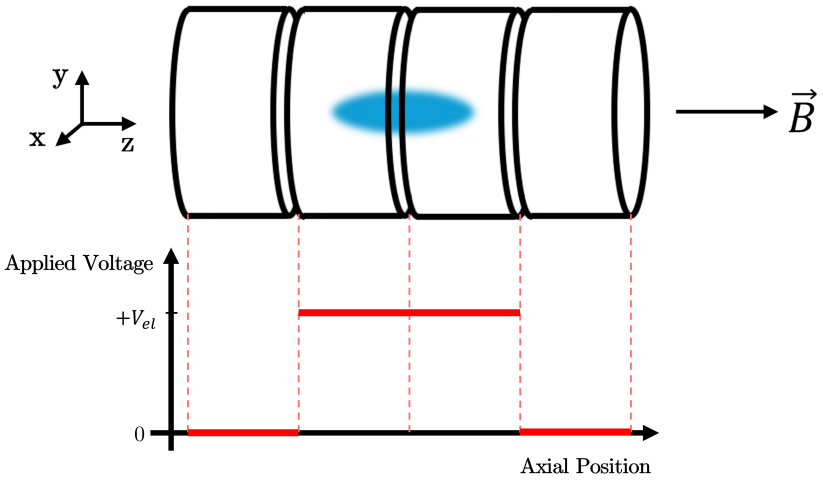

Figure 2.3: Sketch of a Penning-Malmberg trap. Example of a four-electrode Penning-Malmberg trap. The blue cloud represents a plasma confined in the middle two electrodes, and the red solid lines show the voltages applied to each electrode. In this example, a positive voltage, $+V_{el}$, is applied to two central electrodes, while the endcap electrodes remain at $V = 0$, creating a positive potential well. This configuration traps a negatively charged plasma (blue). To trap positively charged particles, negative voltages must instead be applied to the electrodes.

2.2 Plasmas in a Penning-Malmberg Trap

The single particle dynamics described in subsection 2.1.1 do not describe inter-particle interactions. When many particles are simultaneously trapped in a potential well, these interactions become relevant to the particle dynamics in the trap. At ALPHA, we often trap and manipulate particles in the plasma regime.

Since the particles trapped in the Penning-Malmberg traps at ALPHA are charged, we will focus on non-neutral plasmas.

A plasma is an ensemble of many particles where the electric and/or magnetic fields generated by the particles are non-negligible and affect single-particle dynamics. These fields are strong enough to shield the particles inside the plasma from externally applied electromagnetic fields, this phenomenon is called *Debye shielding*. The Debye length, λ_D, is a parameter related to plasmas which depends on the plasma density n and its temperature T,

$$\lambda_D = \sqrt{\frac{\varepsilon_0 k_B T}{nq^2}}, \tag{2.2.1}$$

where q is the charge of the particles that make up the plasma, ε_0 is the vacuum permittivity, and k_B is the Boltzmann constant. Debye shielding occurs when, within a few Debye lengths from the surface, the plasma effectively neutralises and cancels out external electric fields, preventing them from penetrating deeper into the plasma. To display plasma properties, the particle ensemble

must have a length, L, significantly larger than the Debye length,

$$\lambda_D \ll L. \tag{2.2.2}$$

A common rule of thumb is $L/\lambda_D > 10$ to ensure strong collective behaviour. In addition, the density of the plasma must vary slowly on the scale of the mean inter-particle spacing $a = n^{-1/3}$. On the scale of the Debye length, however, the density varies, and we can apply one additional constraint to the plasma state,

$$n\lambda_D^3 \gg 1. \tag{2.2.3}$$

This dimensionless quantity $n\lambda_D^3$ is called the plasma parameter, and can be defined from Eq. 2.2.1 as,

$$n\lambda_D^3 = \left[\frac{k_B T}{q^2/\varepsilon_0 a}\right]^{3/2}. \tag{2.2.4}$$

The plasma parameter is essentially the ratio of a particle's mean kinetic energy $(k_B T)$ and the mean interaction potential energy between nearest neighbours $(q^2/\varepsilon_0 a)$.

The timescale over which plasma behaviour is observed is the inverse of the plasma frequency, ω_p,

$$\omega_p = \sqrt{\frac{nq^2}{\varepsilon_0 m}}. \tag{2.2.5}$$

In general, the time it takes for a particle to travel one Debye length is $1/w_p$.

In the plasma regime, the charged particles experience not only the imposed fields from the trap, which generate the trap potential $\Phi_{trap}(r,z)$, but also the electric field produced by the other particles in the plasma. This modifies the electric field both within and around the plasma. The plasma must satisfy Poisson's equation,

$$\nabla^2 \Phi_{plasma}(r,z) = -\frac{qn(r,z)}{\epsilon_0}, \tag{2.2.6}$$

where $\Phi_{plasma}(r,z)$ is the potential due to the plasma itself. Since the plasma has a temperature T, its particle distribution must also follow the Maxwell-Boltzmann distribution,

$$n(r,z) = n_0 \exp\left[-\frac{q\Phi_{plasma}(r,z)}{k_B T}\right]. \tag{2.2.7}$$

Let us consider only the direction parallel to the magnetic field in a Penning-Malmberg trap, z. If the plasma is not in thermal equilibrium, then $\partial\Phi_{plasma}/\partial z \neq 0$, indicating the presence of an electric field (and hence a force) acting along the z direction. This force will redistribute the particles in the plasma until there is no electric field along the plasma, at which point $\partial\Phi_{plasma}/\partial z = 0$, causing the potential to flatten across the plasma column.

In addition to $\Phi_{trap}(r,z)$ and $\Phi_{plasma}(r,z)$, the presence of charged particles in the trap induces image charges on the walls of the electrodes, producing $\Phi_{image}(r,z)$. However, this contribution is negligible when the radius of the electrodes is significantly larger than the plasma radius. At ALPHA, typical plasma radii are in the order of 1 mm or less, while the electrode radii are in the

order of centimetres. Therefore, this assumption holds, and the potential from the image charges can be neglected. The total effective electric potential inside the plasma is then the sum of the trap potential and the potential from the charges in the plasma itself,

$$\Phi_{eff}(r,z) = \Phi_{trap}(r,z) + \Phi_{plasma}(r,z). \tag{2.2.8}$$

The potential from the trap electrodes (often called the vacuum potential) is then modified in the presence of a plasma, flattening the region where the plasma is held, as illustrated in Fig. 2.4. The level at which the potential flattens is called the plasma's *space charge* or its *self-potential*. In

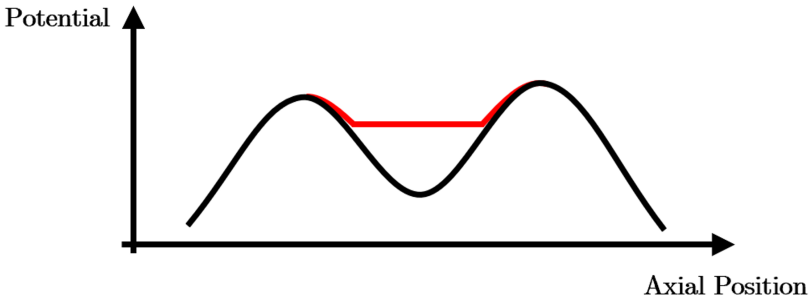

Figure 2.4: Flattening of the trapping potential due to a plasma. This diagram shows the potential on axis of a Penning-Malmberg trap caused solely by applying voltages to the electrodes (black), and the flattening that occurs due to the presence of a trapped plasma. The level at which the potential flattens is denoted as the plasma self-potential (or space charge).

a Penning-Malmberg trap, the shape of a confined plasma can be approximated to a cylinder (in reality, it resembles a 'cigar' shape). In the presence of a magnetic field along z, this cylinder rotates around the axis of the trap at the $\mathbf{E} \times \mathbf{B}$ frequency. The dominant electric field will be the plasma's radial self-field [34],

$$E_r = \frac{qrn}{2\epsilon_0}. \tag{2.2.9}$$

The rotation frequency of the plasma, f, can then be defined as,

$$f = \frac{qn}{4\pi\epsilon_0 B}. \tag{2.2.10}$$

This expression assumes uniform density across the plasma column. For non-zero temperature plasmas, the density varies across a few Debye lengths according to Eq. 2.2.7, producing a pressure gradient across the plasma that peaks at $r = 0$, where density is highest. This gradient gives rise to differential angular velocities across the plasma's radial profile. However, for cold non-neutral plasmas, the zero-temperature limit is a good approximation. The implications of this density gradient effect will be discussed further in subsection 2.2.3.

Plasma coupling regimes

An important parameter characterising plasmas is called the *Coulomb coupling constant*, Γ. It is defined as the ratio of the average Coulomb potential energy, E_C, to the thermal kinetic energy, $k_B T$:

$$\Gamma = \frac{E_C}{k_B T}. \tag{2.2.11}$$

We can define the average inter-particle spacing by the Wigner-Seitz radius, a_S,

$$a_S = \sqrt[3]{\frac{3}{4\pi n}}, \tag{2.2.12}$$

and then define the Coulomb energy between neighbouring particles as,

$$E_C = \frac{q^2}{4\pi\epsilon_0 a_S}. \tag{2.2.13}$$

Using the definitions in Eq. 2.2.12 and Eq. 2.2.13, the coupling constant can be rewritten as,

$$\Gamma = \frac{q^2}{4\pi\epsilon_0 a_S k_B T}. \tag{2.2.14}$$

If $\Gamma \ll 1$, the plasma is *weakly coupled*. In this regime, the thermal energy dominates over the Coulomb interactions, and the particles in the plasma move largely independently, only weakly interacting with other particles. Weakly coupled plasmas tend to be hot and diffuse.

If $\Gamma \gg 1$, the plasma is *strongly coupled*, where the Coulomb interactions are comparable to the thermal energy. The particles in these plasmas are strongly correlated and exhibit collective behaviour. These plasmas can arrange into structures, for example, if $\Gamma \gtrsim 175$, the plasma can undergo a phase transition into a Coulomb crystal [35,36], in which the particles form a rigid and ordered structure. Strongly coupled plasmas are often cold and dense and arise in contexts such as ion traps and ultracold plasmas.

Collision rate

In a trapped plasma, energy can be exchanged between the axial and radial motions through collisions. The collision rate depends on the magnetisation parameter $\bar{\kappa}$,

$$\bar{\kappa} = \frac{\bar{b}}{r_c\sqrt{2}}, \tag{2.2.15}$$

where $r_c = \sqrt{k_B T/m}/\omega_c$ is the cyclotron radius and $\bar{b} = 2q^2/(4\pi\varepsilon_0 k_B T)$ is twice the distance of closest approach. This phenomenon was studied for pure electron plasmas by Glinsky et al. [37] Glinsky defined the collision rate, $\nu_{\perp\|}$, as,

$$\nu_{\perp\|} = n\bar{\nu}\bar{b}^2 I(\bar{\kappa}), \tag{2.2.16}$$

where n is the density of the plasma and the thermal velocity is given by $\bar{\nu} = \sqrt{2k_BT/m}$.

The magnetisation parameter is directly proportional to the magnetic field strength and inversely proportional to $T^{3/2}$. For $\bar{\kappa} \ll 1$, the plasma is weakly magnetised (low magnetic field and/or high plasma temperature). An expression for $I(\bar{\kappa})$ was found in [37], $I(\bar{\kappa}) = -(\sqrt{2\pi})/15 \cdot \ln(\bar{\kappa}C)$, where $C = 0.333(65)$. In this regime, energy exchange between axial and radial motions is relatively efficient.

For $\bar{\kappa} \gg 1$, the plasma is strongly magnetised (high magnetic field and/or low plasma temperature) and $I(\bar{\kappa}) \propto \exp[-5(3\pi\bar{\kappa})^{2/5}/6]$. The exchange of energy between the radial and axial motions is small for strongly magnetised plasmas.

2.2.1 Multispecies Plasmas

Multispecies plasmas are plasmas with distinct species of the same charge trapped within the same potential well. The species interact with one another through Coulomb collisions if they spatially overlap. In this regime, changing the parameters of one species affects the other. Multispecies plasmas are critical for antiproton plasma preparation at ALPHA: the antiprotons are cooled by merging them with electron plasmas in high magnetic field regions. As the topic of this thesis indicates, Be^+/e^+ plasmas have also become integral to the antihydrogen synthesis process.

Centrifugal Separation

Non-neutral plasmas in a Penning-Malmberg trap rotate around the axis of the trap due to the crossed magnetic field and the electric field from their self-potential. In a multispecies plasma, this rotation gives rise to centrifugal forces that drive species separation: lighter particles tend to accumulate near the trap centre, while heavier species form a surrounding shell at larger radii [38].

The components of a multispecies plasma exchange energy through Coulomb collisions, resulting in momentum transfer. Centrifugal separation is driven by momentum exchanges in the ϕ-direction (using cylindrical coordinates (r, ϕ, z)). Initially, the species in the plasma rotate at different frequencies; momentum transfer in the ϕ-direction occurs until the whole plasma rotates as a rigid body and thermal equilibrium is reached.

Take a multispecies plasma made of two distinct particles with masses m_a and m_b. The separation length l_{sep} between the two species is defined as [34],

$$l_{\text{sep}} = \frac{k_BT}{|m_a - m_b|\,\omega_R^2 R_P}, \tag{2.2.17}$$

where ω_R is the rotation frequency of the plasma and R_P is the plasma radius.

Centrifugal separation is observed at ALPHA in antiproton/electron ($\bar{p}/e^-$) plasmas [39]. The antiprotons are trapped in the same well as the electrons to allow for the sympathetic cooling of the heavier species. If the multispecies plasma is imaged, the separation between the two species becomes apparent, as shown in Fig. 2.5. Another case of multispecies plasma where centrifugal separation plays an important role at ALPHA is Be^+/positron (Be^+/e^+) plasma. Imaging these two species simultaneously becomes challenging: the MCP gain needed to image Be^+ ions causes the positron plasma to saturate the image, making it difficult to discern between the two. However,

utilising a lepton removal technique makes it possible to image each species separately without collapsing the Be^+ ring. The separation between the two species can be used to estimate the plasma temperature, as l_{sep} depends on this parameter Eq. 2.2.17 [30] [26].

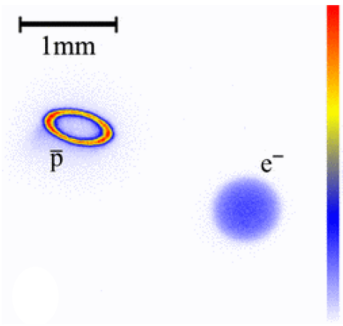

Figure 2.5: Radial profile of an antiproton/electron ($\bar{p}/e^-$) multispecies plasma at ALPHA, in a 1 T magnetic field. Inside the trap, the antiproton ring and electron cloud are concentric, though the imaging process results in different apparent centres. The heavy species (antiprotons) migrated to the edge of the plasma, while the light species (electrons) remained at the centre of plasma. The color scale is linear where red represents high intensity and blue low intensity. Image adapted from [39].

Centrifugal separation can be partial where the density in the gap between the two species is non-zero, meaning there is still significant overlap between them. This occurs when $l_{sep} < R_P$. On the other hand, if the density in the gap between the two species becomes exponentially small, this is called complete separation and occurs when $l_{sep} \ll \lambda_D$ [38]. In this regime, energy exchange through Coulomb collisions is minimal.

Lepton Removal (*e-kick*)

The axial bounce frequency, ω_z, of charged particles in a Penning trap scales with $m^{1/2}$, where m is the particle's mass (as per Eq. 2.1.7). This dependency can be exploited to separate dual-species plasmas where the particles have significantly different masses. Relevant examples for ALPHA are $\bar{p}/e^-$ and Be^+/e^+ plasmas. If trapped in the same well, the electrons in a $\bar{p}/e^-$ plasma will have a bounce frequency ~ 43 times higher than the antiprotons; similarly, positrons in a Be^+/e^+ plasma will have a bounce frequency ~ 129 times greater than the ions.

As a result, if one side of the potential barrier in the confining electrostatic well is lowered and raised back quickly enough, only the particles with higher ω_z will experience this momentary low potential region and exit the well. The time scale of these manipulations depends on the well shape, but it is typically in the order of 100 ns or less. This technique must be very carefully tuned, as this potential change can cause heating or induce off-axis motion to part or all remaining particles. Both of these side effects are highly undesirable for any plasma preparations at ALPHA, and must be minimised by maintaining the magnitude and duration of the manipulations as short as possible while effectively removing the leptons from the well.

2.2.2 The Rotating Wall Technique

Non-neutral plasmas confined in a Penning-Malmberg trap can be affected by imperfections in the electrodes, slight misalignments with the Penning-Malmberg trap magnetic field or interactions

with background gas, which can all exert drag on the plasma, resulting in its expansion. Maintaining and even changing the plasma radius are essential requirements for the reproducibility and stability of confined non-neutral plasmas. The Rotating Wall (RW) technique was developed in 1997 by Huang et al. [40] for manipulating the plasma radius and increasing confinement times of Mg^+ ions trapped in a Penning trap. A rotating electric field acting on a plasma applies a torque which can change its rotation frequency and, consequently, its radius. If the rotating wall drive frequency, f_{RW}, is higher than the plasma rotation, f_{plasma}, the interaction will cause an increase in f_{plasma} and reduce the plasma's radial size. If $f_{RW} < f_{plasma}$, the plasma will slow down and expand.

The rotating wall technique requires an azimuthally segmented electrode, divided into N segments such that voltage can be independently provided to each segment. The rotating electric field is generated by applying a sinusoidal voltage, Φ_{RWj}, to the segments. The signal must be phase-shifted by $\theta_j = 2\pi j/N$, where j is an integer labelling each segment. The electric field is defined as,

$$\Phi_{RWj} = A_{RW}\cos[m(\theta_j - 2\pi f_{RW}t)]. \tag{2.2.18}$$

where A_{RW} is the amplitude of the voltage applied and m is the number of the plasma mode: $m = 1$ corresponds to the dipole mode and $m = 2$ to the quadrupole. At ALPHA, the rotating wall electrodes are divided into 6 segments (the phase shift is then $\theta_j = 2\pi j/6$), and typically $m = 1$ when the rotating wall technique is applied.

To successfully interact with the plasma, the rotating field and the plasma must, of course, spatially overlap. Theoretically, if a dipole drive ($m = 1$) is applied to the whole plasma, the resulting applied torque can be zero [41]. This has been experimentally corroborated [42], concluding that the plasma length must be larger than that of the RW electrode for successful radius changes. At ALPHA, we usually spread the plasma over two or three electrodes and apply the rotating electric field to one of the ends of the plasma.

The amplitude of the RW influences how the field couples to the plasma. Low amplitudes only allow discrete f_{RW} to interact with the plasma rotation frequency. The interactions occur only when f_{RW} is resonant with Trivelpiece-Gould modes and have been demonstrated for electrons and ions [43]. This is called the *weak drive regime*.

If A_{RW} is high enough, the interaction between the RW and the plasma can be in the *strong drive regime*. Here, the rotation of the plasma matches the rotating electric drive rotation frequency across a wide range of frequencies, without coupling to any specific plasma modes. This allows for control of the plasma density as there is a linear relation between the drive and the plasma's rotation frequencies. The strong drive regime has only been thoroughly studied in lepton plasmas, [42]. At ALPHA, the rotating wall technique is applied in the strong drive regimes with amplitudes between $1 - 10$ V, often with the intent of compressing plasmas.

The rotating wall does work on the plasma due to the drag from frequency differences between f_{RW} and f_{plasma}. This results in the heating of the plasma, which reduces collisions between the particles and dampens plasma modes. Thus, a significant increase in temperature can reduce the coupling between the RW and the plasma. To counteract this heating, a cooling mechanism is necessary; for leptons, cyclotron cooling is sufficient to maintain the plasma temperatures around a few tens of Kelvin. For ions, laser cooling is often the chosen cooling mechanism, as the timescales

of ion cyclotron cooling are much larger than the experiment's duration (see Section 2.3).

2.2.3 Control and reproducibility of non-neutral plasmas

In the zero-temperature limit the plasma rotation frequency, f , and self-potential, ϕ_c, of an infinitely long cylindrical plasma column are given by,

$$f = \frac{q}{4\pi\varepsilon_0 B} n, \tag{2.2.19}$$

and

$$\phi_c = \frac{nqr_p^2}{a4\varepsilon_0}\left[1 + 2\ln\left(\frac{R_W}{r_p}\right)\right], \tag{2.2.20}$$

where ε_0 is the permittivity of free space, n is the density of the plasma, B is the strength of the magnetic field, q is the charge of the particles in the plasma, and r_p and R_W are the plasma and electrode radii, respectively.

The rotation frequency of the plasma can be set by applying the rotating wall technique in the strong drive regime, which will consequently set its density. If the plasma is confined in a shallow electrostatic well, and the density is defined by the experimentally imposed rotation frequency, the self-potential equation admits only one solution for the radius of the plasma. Moreover, the number of particles in the plasma depends on both its density and radius,

$$N = \int_0^V ndV = n\pi r_p^2 L. \tag{2.2.21}$$

In our Penning-Malmberg traps, the segmented electrodes can apply a rotating electric field to the plasma, with frequencies in the Strong Drive Regime [42], (SDR), while the evaporative cooling technique (EVC) reduces the well depth. When applied simultaneously, the plasma radius and number are set independently of the initial plasma parameters. This technique, called Strong Drive Regime EVaporative Cooling (SDREVC), was initially developed at ALPHA [18] for controlling the positron and electron plasmas for antihydrogen production. Fig. 2.6 displays the final number of particles, N_e, and density, n_e, with and without the SDREVC technique for a wide range of initial electron numbers: $6 - 20$ million particles. This figure was taken from Figure 4 of [18]. The final plasma parameters are completely independent of the initial parameters when SDREVC is applied. This technique is extremely powerful, with applications outside of the ALPHA experiment. It was implemented within our antihydrogen production protocol during the 2018 antiproton run: the increased stability in electron number and plasma size allowed for the final antiproton numbers and temperatures to be consistent shot-to-shot, coupled with an increase in positron plasma reproducibility, the shot-to-shot variation in trapped antihydrogen was greatly decreased. Allowing for higher trapped antihydrogen numbers over many repetitions of the synthesis process. Perhaps more importantly, the SDREVC technique opened the door for reproducibly scanning parameters such as positron plasma number and radius. Altogether, this yielded a tenfold increase in antihydrogen production rate, making SDREVC a staple of lepton plasma preparations at ALPHA.

However, it is important to note that Eq. 2.2.19 and Eq. 2.2.20 are only formally valid in the

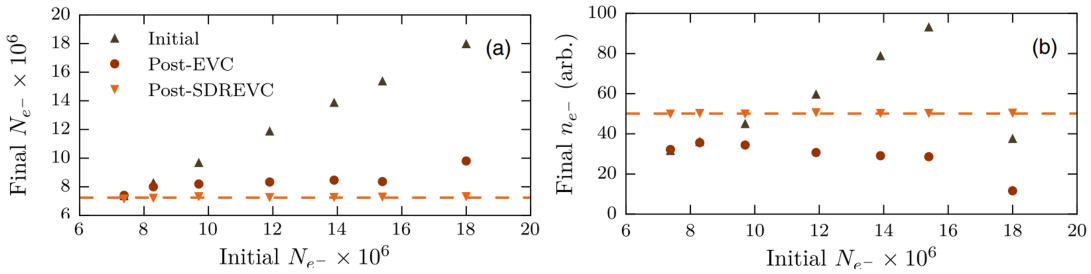

Figure 2.6: Initial (filled triangle), post-EVC (filled circle), and post-SDREVC (filled invert triangle) measurements for a variety of plasma parameters. Figure is taken from Figure 4 of [18]. (a) The final number of electrons as a function of the initial number of electrons; (b) the final plasma density as a function of the initial number of electrons. The orange lines mark the average post-SDREVC values.

zero-temperature regime. In [18], the temperature of the electron plasmas was measured to be up to 300 K after SDREVC. In this regime, two of the assumptions underlying the zero-temperature model fail:

- ◇ The plasma density is no longer constant across the radial profile. Eq. 2.2.20, assumes the plasma is a rigid rotor of uniform density, but at non-zero temperatures, the plasma density falls over a few Debye lengths.

- ◇ Evaporative cooling depends on the axial escape of the highest energy particles in the plasma distribution. At non-zero temperature, the effective well depth ϕ_c is lower than the vacuum potential by several $k_B T$.

The density variation was investigated in [18] by solving the equilibrium equations developed by Prasad and O'Neil [44]. For the temperature range of $30 - 300$ K, this computational analysis found only a 1% change between the calculated central density and the experimental values. This indicates that the radial density fall has a negligible impact on the final plasma parameters after the application of this technique.

In the same temperature range $(30 - 300\ \text{K})$, the change in well depth can result in $5\,\% - 10\,\%$ variations between the predicted number from the model and the actual particle number left in the plasma [18]. This will not necessarily influence the stability of the method, only its agreement with the zero-temperature prediction, given that the temperature profile of the plasma is likely to be the same shot-to-shot if the initial plasma preparation steps are identical.

The principles of this technique were applied to ion plasmas for the first time as part of the work presented in this thesis, further details can be found in Section 4.5.

2.3 Particle Cooling Techniques

2.3.1 Cyclotron cooling

Charged particles in a Penning-Malmberg trap have a combined motion, which can be separated into three motions with different frequencies: cyclotron, axial bounce, and magnetron motions.

According to Maxwell's equations, an accelerating charged particle will emit energy in the form of electromagnetic waves. Such is the case for particles in a Penning-Malmberg, where typically, this emission is dominated by cyclotron radiation, given that this motion has a much higher frequency than the other two mentioned above. The rate at which the particles lose energy is given by the Larmor formula. Moreover, assuming a thermal Maxwell-Boltzmann distribution for the trapped charged particles, one can derive the characteristic cooling time, τ, [45],

$$\tau = \frac{9\pi\epsilon_0 m^3 c^3}{2q^4 B^2}. \tag{2.3.1}$$

For light particles, such as electrons and positrons, the cooling time is a few seconds in a 1 T field, and less than a second in the highest field regions at ALPHA, 3 T. This form of cooling is thus extremely efficient for lepton plasmas, even when there are external sources of heating like an external rotating electric field. Unfortunately, the cooling time increases with m^3, so for heavier particles, it quickly becomes an irrelevant cooling source. In a 3 T field, the characteristic cooling time for an antiproton is 84 years, and for the heaviest species trapped in ALPHA, Be^+, it is tens of thousands of years. Both of these timescales are of course, effectively infinite when compared to the particle trapping duration of a few minutes.

The cooling time was studied for electron plasmas in cryogenic traps in [45], where it was found that the plasma does not thermalise with the 4 K environment, rather the temperature stabilises at around 20 K, and for temperatures below 50 K, the cooling time is slower than the one predicted in Eq. 2.3.1. This experiment was performed for magnetic field strengths in the range $0.2 - 0.6$ T, so the actual temperatures may be different for the $1 - 3$ T range in the ALPHA trap, but the conclusion remains the same: there are heating sources in the trap which, at low temperatures, overcome the cyclotron cooling power.

Regardless, cyclotron cooling plays a key role in the long-term confinement of leptons and the production of antihydrogen in the ALPHA experiment.

2.3.2 Sympathetic Cooling

Some cooling techniques are only efficient at cooling certain types of particles. For example, cyclotron cooling is extremely effective at cooling low-mass particles such as electrons and positrons. On the other hand, laser cooling is very effective at cooling species with the appropriate electronic structure, such as Be^+ ions.

However, not all species can be directly cooled. Some particles are too heavy for cyclotron cooling to sufficiently reduce their temperature within experimental timescales, or they lack the appropriate electronic structure for laser cooling. A prime example in the context of the ALPHA experiment is the antiproton. In such cases, *sympathetic cooling* can often be employed.

Sympathetic cooling is an indirect cooling method in which a species that can be readily cooled (through laser cooling, for example), called the *coolant species*, is mixed with another species called the *target species*, which we aim to cool. Through Coulomb collisions, the two species exchange energy, resulting in a gradual reduction in the temperature of the target species.

This cooling technique has been successfully applied since the 1980s. Sympathetic cooling of a two-species non-neutral plasma in a Penning trap was first demonstrated in 1986 [25] by cooling

$^{198}Hg^+$ through Coulomb collisions with laser-cooled $^9Be^+$. In this case, the $^9Be^+$ was the coolant species and the $^{198}Hg^+$ was the target.

An important observation from this experiment was that the two species did not reach thermal equilibrium: the $^{198}Hg^+$ temperatures ranged from 0.4 to 1.8 K, whereas the $^9Be^+$ temperatures were between 0.05 K and 2 K. This difference was attributed to centrifugal separation between the two species: as the overlap between the two decreases, so do the Coulomb collisions. This was also the first observation of this phenomenon in multispecies non-neutral plasmas.

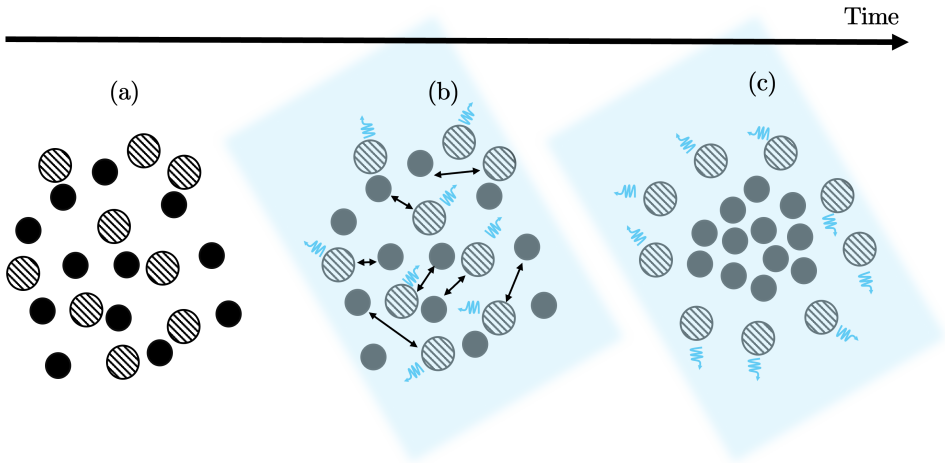

Figure 2.7: Sketch of the sympathetic cooling of a lighter target species (black circles) via a laser-cooled heavier coolant species (striped circles). (a) Initial stage where the two species are mixed and no active laser cooling is applied. The temperature or radial profile of the mixed plasma does not dramatically change at this stage. (b) A cooling beam (light blue rectangle) is sent towards the plasma and starts laser cooling the coolant species, as evidenced by the blue curly arrows. The temperature of the coolant species decreases. Significant energy exchange starts occurring between the coolant and target species through Coulomb collisions (black arrows). The temperature of both species decreases, and the heavier species starts migrating to the outskirts of the plasma. (c) The centrifugal separation between the coolant and the target species is such that the coolant species creates a shell around the target species; there is no physical overlap between both populations, and sympathetic cooling stops, even though laser cooling is still active.

As the plasma cools, the heavier species tend to migrate towards larger radii, forming a shell-like structure around the lighter species. This physical separation between the two species increases the average distance between particles, simultaneously reducing the number of Coulomb collisions that occur and diminishing the energy exchanged per collision. Eventually, the separation is such that sympathetic cooling no longer occurs, leading to a lower limit on the achievable target species temperature. However, cooling of the coolant species is not limited by centrifugal separation, and often is colder than the target species.

This process is illustrated in Fig. 2.7, which shows a schematic of sympathetic cooling in a two-species plasma, where the heavier coolant species is represented by the striped circles and the lighter target species by the black circles. Initially, the two species are mixed uniformly. As laser cooling is applied to the coolant species, their temperature decreases and, through Coulomb collisions, so does the temperature of the target species. After some time, the heavier coolant particles have migrated to a high radius region, where Coulomb collisions are suppressed, and thus, sympathetic cooling no longer significantly impacts the temperature of the target species.

Sympathetic cooling has become a standard technique in non-neutral plasma physics. A notable example is the cooling of antiprotons using cold electron plasmas, first demonstrated in 1989 [46], where about $60\,000$ antiprotons were cooled to less than 1 eV. This method remains essential in antihydrogen physics; ALPHA traps antiprotons with energies up to 4 keV, far too hot for antihydrogen production. Sympathetic cooling allows for the cooling of antiprotons down to a few hundred K, which greatly facilitates particle manipulation and enables antihydrogen production. Another advantage of sympathetic cooling is that its timescale is compatible with the experiment's, the sympathetic cooling of antiprotons through collisions with electrons takes $20 - 40$ s, depending on their initial temperature.

Another important application is sympathetic cooling of positrons using laser-cooled Be^+ ions. This was first demonstrated in [26], where a few thousand positrons were sympathetically cooled to less than 5 K through Coulomb collisions with laser-cooled Be^+ ions. This technique was later extended in the ALPHA experiment, where millions of positrons were cooled to cryogenic temperatures in a Penning-Malmberg trap [30].

2.3.3 Evaporative Cooling

EVaporative Cooling (EVC) is a technique used to reduce plasma temperature by allowing the higher energy particles to escape the potential well confining the plasma. This selective loss causes an overall reduction in kinetic energy, resulting in a lower temperature plasma. In a Penning-Malmberg trap, EVC is easily implemented by lowering the confining potential well barrier to the level of the plasma space charge or lower. Particles with energy higher than the potential barrier will exit the well, effectively truncating the Maxwell-Boltzmann distribution at this energy level. Subsequent collisions between the remaining particles lead to re-thermalisation at a lower temperature. The degree of cooling depends on how much the potential barrier is lowered: the greater the reduction, the lower the final plasma temperature. An illustration of this process is shown in Fig. 2.8.

However, this technique has two main shortcomings. First, it inherently results in particle loss, which is undesirable when dealing with scarce resources such as antiprotons. Perhaps more significantly, EVC induces radial expansion of the plasma. The centre of the plasma lies near the centre of the trap electrodes, where the confining potential is lowest. While lowering the potential barrier, particles near the centre will preferentially exit the well, leaving a density hole at the centre of the plasma. Collisions will subsequently result in the refilling of this hole. To ensure conservation of the total canonical angular momentum, this refilling causes some particles to migrate outwards, leading to radial expansion of the plasma,

$$\frac{N_{in}}{N_{final}} = \frac{< r_{final}^2 >}{< r_{in}^2 >}, \tag{2.3.2}$$

where N_{in} and N_{final} are the initial and final particle numbers, and r_{in}^2 and r_{final}^2 are the initial and final radii. This expansion, coupled with the field inhomogeneity from the neutral trap (see subsection 2.4.1), can cause plasma instabilities as well as further particle loss.

At ALPHA, this technique was used to cool antiprotons to cryogenic temperatures (about 9 K) in an effort to increase the antihydrogen trapping rate [47]. However, the associated antipro-

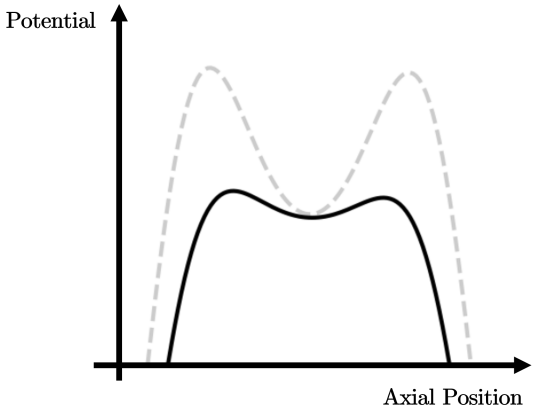

Figure 2.8: Well depth manipulations during evaporative cooling (EVC). Particles begin in a deep potential well (dashed line), often deeper than the plasma self-potential. Over the course of the EVC, the well depth is gradually reduced until it becomes shallower than the initial self-potential, allowing higher-energy particles to escape. In this example, the particles exit to the right. The particles that remain in the well will be colder than the initial sample.

ton loss during EVC proved more detrimental to the trapping rate than the benefits gained from the lower antiproton temperatures. Nevertheless, evaporative cooling remains a powerful tool in plasma physics and is still widely used at ALPHA in other contexts. In subsection 2.2.3, a description of a technique for controlling plasma parameters will make clear how to mitigate the expansion issue and reliably apply EVC, thereby enhancing its utility for experimental applications.

2.3.4 Adiabatic cooling

An adiabatic invariant is a physical quantity that remains constant when conditions change slowly compared to the system's natural timescale. For particles trapped in a Penning-Malmberg trap, one such invariant is the axial bounce action, J, defined as,

$$J = \int_a^b v_{\parallel} dl, \tag{2.3.3}$$

where a and b are the turning points of the axial motion, and $v_{\parallel}$ is the velocity component parallel to the magnetic field. This motion is a one-dimensional harmonic motion as derived in Eq. 2.1.7, with the potential $U_z = \frac{1}{2} m\omega_z^2 z^2$. In this case, the adiabatic invariant can be expressed as,

$$J = \frac{E}{\omega_z}, \tag{2.3.4}$$

where ω_z is the axial bounce frequency and E is the energy of the particle.

Adiabatic cooling exploits this invariance. By increasing the length of the well where the particles are trapped, the axial bounce frequency will decrease. If this change is done slowly, to preserve J, the particle's energy E must decrease accordingly during this manipulation, as shown

in Eq. 2.3.4. At ALPHA, typical bounce frequencies are in the scale of MHz to GHz. Therefore, a manipulation performed over a few seconds satisfies the adiabatic condition.

This technique was first applied to antiprotons by the ATRAP collaboration in 2011 [48], achieving temperatures of (3.5 ± 0.7) K. It has since been developed for cooling antihydrogen atoms in a magnetic minimum trap by the ALPHA collaboration [49], where adiabatically expanding the volume of the trap in which they are confined enables antihydrogen temperatures below the fundamental limits of laser cooling.

2.4 Trapping Neutral Particles

2.4.1 The Magnetic Minimum Trap

Antihydrogen, $\bar{H}$, is a neutral system and, therefore, cannot be trapped within an ion trap. However, due to its magnetic moment, $\boldsymbol{\mu}$, it can be trapped using magnetic fields. The potential energy, $\boldsymbol{U}$, of a particle within a magnetic field, $\boldsymbol{B}$ is given by,

$$\boldsymbol{U} = -\boldsymbol{\mu} \cdot \boldsymbol{B}. \tag{2.4.1}$$

Antihydrogen's magnetic moment is largely dominated by the positron's magnetic moment, as it is about 2000 times lighter than the antiproton's, thus $\mu_{\bar{H}} \approx \mu_{e^+}$. Whether the antihydrogen's magnetic moment is parallel or anti-parallel to the magnetic field is then determined by the spin of the positron. Fig. 2.9 shows the ground state antihydrogen energy levels. These were calculated assuming the energy levels are identical to those of hydrogen. The energy of the anti-atoms formed with positron spin anti-parallel to the magnetic field lines increases with the magnitude of the magnetic field. These are called *low-field seeking states*, and since they tend towards the magnetic field minimum, they are trappable.

The shape of a magnetic minimum trap is akin to a bathtub, in which the magnetic field strength increases in all directions away from the minimum magnetic field. If the sum of the kinetic and magnetic potential energies of a low-field seeking antihydrogen atom is lower than the depth of the magnetic minimum trap, the anti-atom will remain confined within the trap volume.

The anti-atoms with a positron spin parallel to the magnetic field lines have decreasing energy with increasing magnetic field magnitude; therefore, they tend to move towards high-field regions, hence the name *high-field seeking states*. At ALPHA, these anti-atoms are directed towards the electrode wall where they annihilate. These are thus untrappable.

At ALPHA, the antihydrogen atoms are axially trapped by two mirror fields, peaking towards the trap ends. Radial confinement is achieved using an octupole field, which increases radially. This type of trap is called an Ioffe-Pritchard trap, at ALPHA we refer to it as the Neutral Trap. The depth of the magnetic minimum trap used at ALPHA is about 0.5 K [50].

2.4.2 Perturbations to the Penning-Malmberg Trap

The radial confinement requires a radially inhomogeneous magnetic field, which can be generated by quadrupole or higher-order fields. Penning-Malmberg traps rely on the azimuthal symmetry

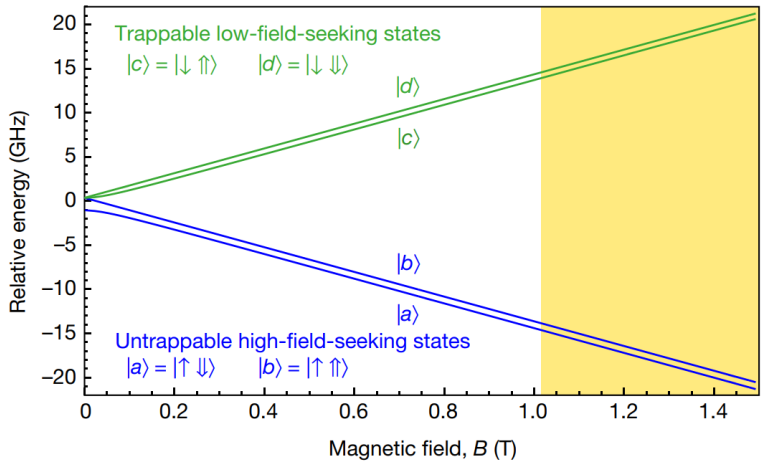

Figure 2.9: Antihydrogen ground-state hyperfine energy levels. The calculation of the energy levels assumes they are identical to those of hydrogen. The positron spin is indicated with ↑ and ↓, the antiproton spin with ⇑ and ⇓. The yellow shaded region corresponds to the magnetic field magnitudes available in the ALPHA-2 antihydrogen trap. Figure taken from page 2 of [15].

of their solenoid field to stably trap charged particles. However, the multipole field necessary for antihydrogen trapping perturbs the solenoid field lines, bending them toward the electrode walls [51]. This distortion can lead to particle loss from the Penning-Malmberg trap. Extensive studies were conducted regarding this problem in the early stages of the ALPHA experiment [51–53], concluding that using an octupole field is the best compromise between minimising the distortions felt by the trapped plasmas and maintaining the trap depth for the neutral particles.

Even though an octupole minimises the distortions to the field lines compared to lower-order fields, they still affect the plasmas trapped in the Penning-Malmberg trap. Particles above a certain radius will inevitably be lost from the trap as the bend in the solenoid field lines intersects with the electrode walls. Moreover, plasma heating and expansion have been widely observed at ALPHA within the octupole field region, even for plasmas with radii significantly smaller than the electrode radius. The loss of cylindrical symmetry causes the plasma to experience effective torques which drive cross-field transport and radial expansion. As particles follow the distorted field lines, the first adiabatic invariant $\mu = \frac{mv_\perp^2}{2B}$ must be conserved, where $v_\perp$ is the perpendicular velocity, and B is the magnetic field strength. As the particles move to a higher radius, the magnetic field strength increases, causing the perpendicular velocity to also increase, leading to adiabatic heating of the plasma. In addition, the octupole's azimuthally varying field perturbs the $E \times B$ rotation and converts a fraction of the plasma's coherent rotational kinetic energy into random thermal motion, generating Joule heating of the plasma [54]. Fig. 2.10 shows the positron temperature as a function of wait time with (orange circles) and without (blue circles) the octupole field. The heating rate of the positron plasma is twice as large with the octupole energised than without.

The heating rate can be exacerbated by other factors, such as vacuum quality within the trap, but the octupole field is one of the most prominent heating and expansion causes for trapped charged plasmas at ALPHA. Maintaining small radii and reducing the time the particles spend within the octupole field are techniques that can help minimise these perturbations; however,

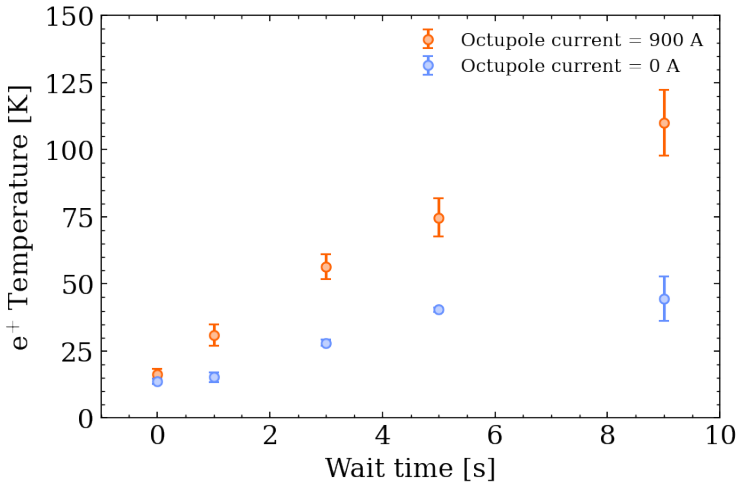

Figure 2.10: Effect of the octupole field of positron plasma heating rate. Positron temperature as a function of wait time with (orange circles) and without (blue circles) the octupole field. The nominal current for the octupole at ALPHA is 900 A.

since antihydrogen must be produced within the Neutral Trap, some heating and expansion from the octupole field interference are inevitable.

2.4.3 Magnetic Field Measurements

Precisely measuring magnetic fields at ALPHA is critical for its operation and for the interpretation of experimental results. The current method, known as Electron Cyclotron Resonance (ECR) magnetometry [55] [56], is the primary diagnostic used for this purpose.

The cyclotron frequency of an electron in a magnetic field of $B = 1$ T lies in the microwave regime and is given by

$$f_{ECR} = \frac{eB}{2\pi m_e} \approx 28 \text{ GHz}, \tag{2.4.2}$$

where m_e is the mass of the electron and e is the elementary charge. This frequency depends directly on the local magnetic field experienced by the electrons. By measuring the cyclotron frequency of electrons trapped in a Penning-Malmberg trap, the magnetic field at their location can be calculated from Eq. 2.4.2. This principle forms the basis of the magnetic field measurement technique employed at ALPHA.

In practice, an electron plasma is confined at the desired axial location in the trap, and microwaves are injected at a given frequency. When the applied microwave frequency is resonant with the cyclotron motion, this motion is excited and the electron plasma's temperature increases. Their temperature is destructively measured using the temperature diagnostic described in Section 3.2, after the microwave injection. By scanning the microwave frequency across a range, a resonance curve can be obtained, and a centre frequency can be extracted, from which the magnetic field can be calculated.

By repeating the measurement with electron plasmas at different axial locations, the on-axis magnetic field can be mapped throughout the full extent of the Penning-Malmberg trap. These measurements are critical for designing Neutral Trap fields for various experiments, and for de-

termining the correct laser detuning during laser spectroscopy measurements.

Knowledge of the magnetic field is crucial for the implementation of Be^+-assisted antihydrogen synthesis, as the laser cooling frequencies depend directly on this parameter.

ECR magnetometry is inherently a destructive measurement, requiring a fresh electron plasma to be loaded for each measurement, and it is limited to probing the on-axis field. Development of techniques for measuring the magnetic field at larger radii is ongoing, but beyond the scope of this thesis [57].

2.5 Laser Cooling

Laser cooling is the process of reducing the kinetic energy of atoms or ions through interactions with coherent light radiation. Efficient laser cooling requires a *closed transition* (or *cycling transition*), where the particle repeatedly absorbs a photon from a laser, exciting an electron from the ground state $|1\rangle$ to an excited state $|2\rangle$, which then spontaneously decays back to $|1\rangle$. Each absorption/emission cycle imparts a small momentum change to the particle, reducing its temperature under the right conditions. If the excited state can decay to a different state $|3\rangle$, the particle will leave the cooling cycle, halting the cooling process. A closed transition effectively puts the atom in a two-level loop $|1\rangle \rightarrow |2\rangle \rightarrow |1\rangle$..., enabling continuous photon scattering and thus, continuous laser cooling.

In practice, the probability of decaying to another state $|3\rangle$ is never exactly zero. In high-precision or long-duration experiments, a repumping laser is often used to drive transitions such as $|3\rangle \rightarrow |2\rangle$, returning particles to the closed cycle. Alternatively, other repumping methods can be employed, for example, off-resonant repumping to redistribute the population back into the cooling cycle without requiring an extra cooling beam.

This section will focus on laser cooling of ions since that is what's relevant for the work on this thesis.

2.5.1 Doppler laser cooling

When a trapped ion is illuminated by laser light resonant with the energy difference between an excited and the ground state, the ion will scatter photons. The photon absorption will be in the direction of the incident light. The subsequent photon emission can occur via two processes:

i *stimulated emission*, the atom emits a photon in the same direction as the absorbed photon, cancelling the recoil kick from the photon absorption, which results in no net change in the atom's velocity;

ii *spontaneous emission*, in contrast, is isotropic: over many cycles, its average momentum results in zero contribution to the change in the ion's momentum from the photon emission, but importantly, does not cancel the effect of the recoil from each photon absorption.

The total velocity change over N scattering events is then $N \times v_{rec}$, where $v_{rec} = p_{photon}/m_{ion}$ is the recoil velocity after an absorption event, p_{photon} is the photon momentum, and m_{ion} is the mass of the ion. However, this alone does not guarantee cooling: whether the particle slows depends on its motion relative to the laser beam.

An ion in a trap moves both towards and away from the laser. To describe this precisely, let us define the ion velocity along this direction such that $v > 0$ corresponds to motion away from the laser. Then, ions moving toward the laser have $v < 0$. The effective detuning of the laser, δ, in the ion's rest frame is given by,

$$\delta = \omega - \omega_0 - kv \tag{2.5.1}$$

where ω is the laser frequency, ω_0 is the resonance frequency, and kv is the shift in frequency due to the Doppler effect.

For $v < 0$ (ions moving towards the laser), $-kv > 0$, thus the ion "sees" a higher frequency, bringing the laser closer to resonance. For $v > 0$ (ions moving away from the laser), the ions experience a lower frequency laser, making scattering less probable.

To enable cooling, the laser must be red-detuned in the lab frame ($\delta = \omega - \omega_0 < 0$). In this configuration, ions moving toward the laser see the light Doppler-shifted closer to resonance, so they scatter photons more efficiently, while ions moving away see the light further from resonance and are less likely to interact with the photons. Each absorption provides a momentum kick opposite the ion's motion, gradually reducing its velocity. Over many absorption/emission cycles, this results in a net reduction of kinetic energy, thus cooling the ions.

Doppler cooling limit

Spontaneous emission is isotropic, thus, the average momentum change from this process is zero. However, these emissions will slightly increase the kinetic energy because the mean square velocity will not equal zero. This heating is negligible compared to the cooling achieved through Doppler cooling at high temperatures; however, as the atoms cool, the magnitude of this heating can become relevant. At equilibrium, the recoil heating is balanced by the Doppler cooling, thus creating a minimum temperature achievable through this technique, T_D.

$$T_D = \frac{\hbar\Gamma}{2k_B}. \tag{2.5.2}$$

This is the Doppler cooling limit, and does not represent a fundamental lower temperature limit since other techniques besides Doppler cooling can be used to cool the ions further, but they are beyond the scope of this thesis. [58] For $^9Be^+$, the natural linewidth of the cooling transition is $\Gamma = 2\pi \times 19.6$ MHz [59], resulting in a minimum temperature of $T_D = 0.47$ mK.

The scattering rate and force

Doppler cooling relies on the fact that the photons exert a force on the ions. The magnitude of this force depends on the momentum of the photon ($p_{photon} = \hbar k$) and on the photon scattering rate R_{scatt},

$$R_{\text{scatt}} = \frac{\Gamma}{2}\frac{\Omega^2/2}{\delta^2 + \Omega^2/2 + \Gamma^2/4}, \tag{2.5.3}$$

where Ω is the Rabi frequency, Γ is the natural linewidth of the transition, and δ is the laser detuning defined in Eq. 2.5.1. [58]. The Rabi frequency can be defined through the saturation intensity,

$2\Omega^2/\Gamma^2 = I/I_{sat}$, where I is the laser intensity and

$$I_{sat} = \frac{\pi}{3}\frac{hc\Gamma}{\lambda^3} \tag{2.5.4}$$

is the saturation intensity. We can also define the saturation parameter as $s = I/I_{sat}$. The scattering force can then be written as

$$F_{\text{scatt}} = \hbar k R_{\text{scatt}} = \hbar k \frac{\Gamma}{2}\frac{I/I_{sat}}{1 + I/I_{sat} + 4\delta^2/\Gamma^2} = \hbar k \frac{\Gamma}{2}\frac{s}{1 + s + 4\delta^2/\Gamma^2}. \tag{2.5.5}$$

The maximum scattering force is then $F_{\text{scatt, max}} = \hbar k R_{\text{scatt, max}} = \hbar k\Gamma/2$. The scattering rate saturates at high s. The saturation intensity for the cooling transition on $^9\text{Be}^+$ is $I_{sat} \approx 0.0835$ W.cm^{-2}. The laser power used for cooling this ion at ALPHA is in the range $100 - 180$ mW, and the cooling beam has a waist of 1.90 mm, which corresponds to a saturation parameter of $10 - 19$ in these conditions. The beam intensity in this power range is then $0.8817 - 1.5871$ W.cm^{-2}.

Power broadening

Increasing the beam power of the cooling beam increases the scattering rate until it saturates at $\Gamma/2$. Another effect of increasing this parameter is the broadening of the full width half maximum (FWHM), [58]

$$\Delta\omega_{\text{FWHM}} = \Gamma\left(1 + \frac{I}{I_{sat}}\right)^{1/2} = \Gamma\big(1 + s\big)^{1/2}. \tag{2.5.6}$$

Fig. 2.11 shows the scattering rate as a function of the laser detuning in the lab frame $(\omega - \omega_0)$ for a $^9\text{Be}^+$ ion. As the saturation parameter increases, so does the scattering rate and the FWHM of the transition. For a stationary ion, the transition is centred at $\omega - \omega_0 = 0$, however, for an ion velocity of $v = 100$ m/s, the laser detuning in the lab frame must be about -320 MHz detuned to be resonant with the cooling transition.

Another consequence of power broadening is that it modifies the minimum temperature achievable via Doppler cooling. It effectively increases the natural linewidth of the transition,

$$\Gamma_{\text{eff}} = \Gamma\sqrt{1 + \frac{I}{I_{sat}}}, \tag{2.5.7}$$

where Γ_{eff} is the linewidth broadened by the laser intensity. Substituting Γ_{eff} from Eq. 2.5.7 into Eq. 2.5.2, the minimum possible temperature using Doppler cooling in the intensity range $0.8817 - 1.5871$ W.cm^{-2} becomes $1.54 - 2.08$ mK. This represents a fourfold increase over T_D when this effect is not taken into account.

2.5.2 Laser cooling plasmas in a Penning-Malmberg trap

In our setup, we are not cooling a single stationary ion; at ALPHA, the goal is to cool hundreds of thousands to millions of ions trapped in a Penning-Malmberg trap. As discussed in subsection 2.1.1, a particle trapped in a Penning-Malmberg trap exhibits a motion with three superimposed frequencies. The axial motion is approximately harmonic in the z-axis, and a cooling beam

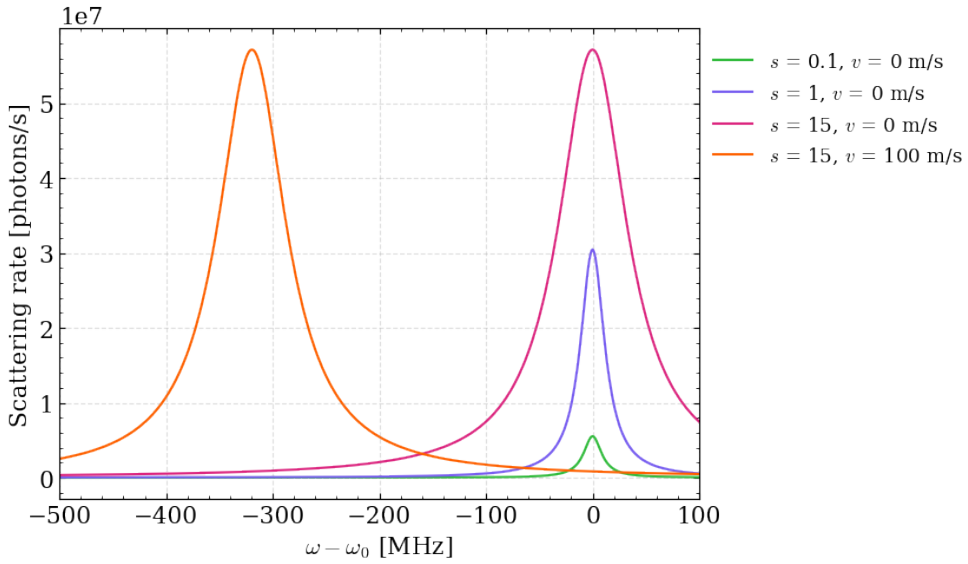

Figure 2.11: Scattering rate for a Be^+ ion as a function of laser detuning for different saturation parameters, s and ion velocities, v. The green curve shows the scattering rate of a stationary ion, $v = 0$ m/s and for low laser intensity, $s = 0.1$. Increasing the saturation parameter increases the maximum scattering rate, as is evidenced by the blue ($s = 1$) and magenta curves ($s = 15$). The ion's velocity shifts the detuning that maximises the scattering rate: the faster the ion, the more red-detuned the laser must be to remain resonant, as shown by the orange ($v = 100$ m/s) curve.

along this axis primarily cools this motion. Cooling the cyclotron and magnetron motions requires introducing an angle between the cooling beam and the trap axis.

In a Penning-Malmberg trap, the time a trapped ion spends in resonance with the cooling laser is limited by its oscillatory motion and the Doppler shift associated with its velocity. The natural linewidth of the transition defines a narrow velocity window over which the ion absorbs photons, so each trapped ion is only resonant for a small fraction of its oscillation period. Power broadening, which occurs when the laser intensity approaches or exceeds the saturation intensity, effectively increases the linewidth of the transition, increasing the velocity range over which the ions are Doppler-shifted into resonance. Consequently, ions spend a larger fraction of their oscillatory period in resonance. In our experiment, we use laser powers that would saturate the transition for a stationary ion. However, because moving ions experience a reduced effective saturation due to their brief time in resonance, these higher powers are necessary to achieve efficient cooling.

Plasma rotation and three-dimensional cooling

In the context of laser cooling, the main difference between the single particle and plasma regimes in a Penning-Malmberg trap is that the plasma rotates around the trap axis at a frequency ω_R. This rotation shifts the velocity distribution of the ions by $\omega_R r$, where r is the radial distance from the trap centre. Moreover, collisions between ions redistribute kinetic energy between the axial and radial motions, allowing a single beam to contribute to three-dimensional cooling. In the single particle regime, several cooling beams in different geometries are necessary to achieve similar cooling conditions. [29]

Laser beams can also induce torque on the plasma if an intensity gradient is present across it. Such a torque can modify the plasma rotation frequency and, consequently, the plasma radius. In our setup, the cooling beam waist is 1.90 mm, and the plasma radius is typically ~ 0.5 mm. When the plasma and the beam are aligned with the trap centre, this corresponds to a $\sim 13\,\%$ intensity drop across the plasma, assuming a Gaussian beam profile. If the beam is displaced from the trap centre, the differential torque can alter the plasma radius. For details on this phenomenon, see [60].

Energy exchange and dependence on collisions

As discussed in Section 2.1, particles in a plasma can exchange energy between the radial and axial motions. This exchange is dictated by the collision rate, which depends on parameters such as the magnetic field, plasma density, and, more importantly in this context, the plasma temperature. As the temperature decreases, the collision rate decreases and energy exchange slows. Laser cooling in the ALPHA-2 Penning-Malmberg trap heavily depends on this exchange of energy to cool all degrees of freedom: for cooling Be^+ ion plasmas, we have employed two cooling beams, one parallel to the axis of the trap and one displaced in z by 2.4°, both of which will primarily cool the axial motion.

Using the relations found by Glinsky et al. in [37], a Be^+ plasma of density $n_{Be^+} = 10^{14}$ m^{-3}, temperature $T_{Be^+} = 20$ K in a 1 T field has a magnetisation parameter of 0.85, corresponding to a weakly magnetised plasma with a collision rate of 61 kHz. For the same plasma but at 5 K, the magnetisation increases and the collision rate decreases to 45 kHz. In either case, energy exchange between axial and radial motion is still very fast, in the order of a few hundred microseconds.

2.5.3 Laser cooling Be^+ ions

The $^9Be^+$ ion has a lithium-like electronic structure, with two electrons forming a closed $1s$ shell and a single valence electron occupying the $2s^2S_{1/2}$ orbital in the ground state. The ground-state valence electron occupies an S-orbital ($L = 0$), so the total electronic angular momentum is determined by its spin, giving $J = S = 1/2$. The first excited electronic state is $2s^2P$, which has a total angular momentum of $J = 3/2$. Spin-orbit coupling splits this $2P$ state into the fine structure levels $2P_{1/2}$ and $2P_{3/2}$. [61]

The nucleus, consisting of four protons and five neutrons, has a nuclear spin of $I = 3/2$. The nuclear spin couples with the electronic angular momentum, splitting each electronic state into multiple hyperfine levels, in both the ground and excited states. When a magnetic field is applied, the degeneracy of the hyperfine levels is lifted via the Zeeman effect. A diagram of the $^9Be^+$ electronic level structure is shown in Fig. 2.12 with the cooling and repumping transitions highlighted in green and orange, respectively.

Calculating the transition frequencies, the energy levels of Be^+ in a magnetic field must be evaluated. This can be achieved by solving the effective Hamiltonian,

$$H = hA\mathbf{J}\cdot\mathbf{I} + \mu_B g_J \mathbf{J}\cdot\mathbf{B} + \mu_B g_I' \mathbf{I}\cdot\mathbf{B}, \tag{2.5.8}$$

where h is the Planck constant, μ_B is the Bohr magneton, and g_J is the g-factor, the values of

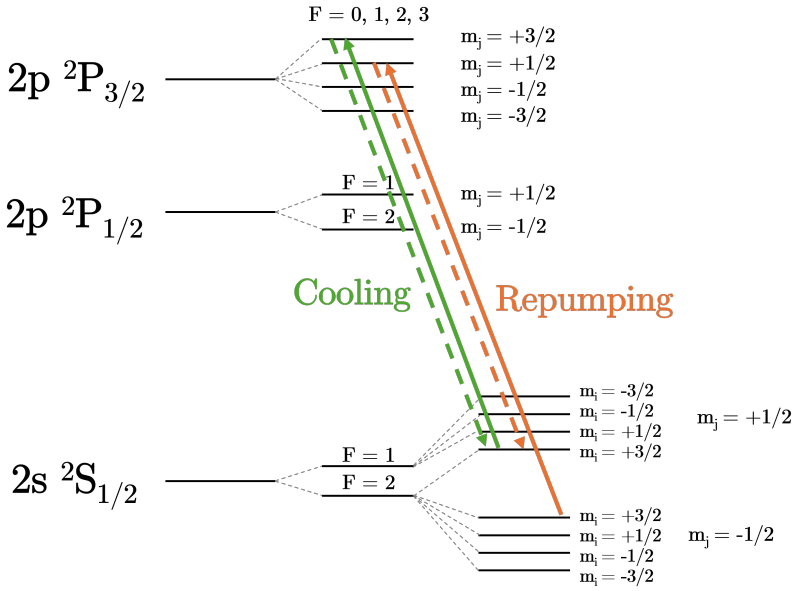

Figure 2.12: $^9\mathrm{Be}^+$ **energy level structure.** The level split represents the electronic structure in a high magnetic field. The $2p\,m_i$ states have a splitting significantly smaller than the natural linewidth of the cooling transition, and thus are not illustrated. The cooling transition is highlighted in green, and the repump transition in orange.

which can be obtained from the CODATA [62]. The magnetic hyperfine constant is given by $A(B) = A_0(1 + k \cdot B^2)$, the constants A_0 and k were evaluated in [63]. Finally, $g_I' = -\mu_I/I_{\mu_B}$, and the ratio g_I'/g_J was also investigated in [63]. The first term of Eq. 2.5.8 is the magnetic dipole hyperfine interaction, the second the nuclear Zeeman interaction, and the third the electronic Zeeman interaction. The eigenvalues of this equation give the relative energies of the hyperfine states within the ground $2S_{1/2}$ and excited state $2P_{3/2}$ states, [61, 63], which can then be used to determine the transition frequencies for the cooling and repump transitions.

Cooling transition for $^9\mathbf{Be}^+$

The relevant energy levels are $2S_{1/2}$ and $2P_{3/2}$ since the cooling transition is,

$$^2S_{1/2}\,(m_J = +1/2, m_I = +3/2) \rightarrow {}^2P_{3/2}\,(m_J = +3/2, m_I = +3/2)\,, \tag{2.5.9}$$

driven by a laser of polarisation σ^+, this transition has a linewidth of 19.6 MHz, or a lifetime of 8.1 ns [59]. The frequency of this transition depends on the magnetic field, Fig. 2.13. At zero magnetic field, the cooling transition frequency is $957\,397$ GHz or a wavelength around 313 nm.

Repump transition for $^9\mathbf{Be}^+$

The transition defined in Eq. 2.5.9 is a cycling transition, therefore, most of the ions decay to the original ground state. However, there is a non-zero probability of the ions decaying to the ground state with opposite spin orientation, $^2S_{1/2}\,(m_J = -1/2, m_I = +3/2)$. An ion in this state will no longer strongly interact with the laser beam tuned to the cooling transition. An additional laser

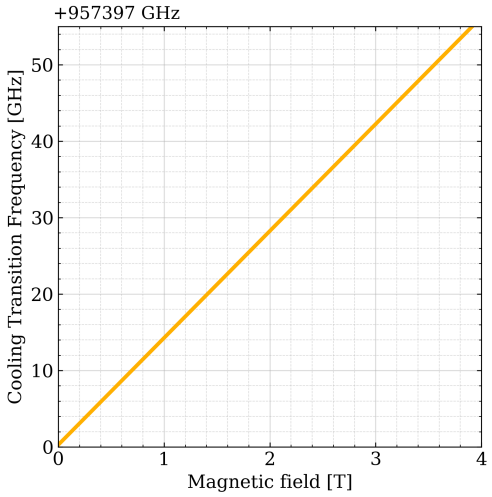

Figure 2.13: $^{9}\mathrm{Be}^{+}$ **Cooling transition frequency as a function of magnetic field.** The plotted transition corresponds to the cooling transition defined in Eq. 2.5.9. There are two magnetic field operational regions at ALPHA: $B \sim 1\ T$, and $B \sim 3\ T$. The difference in the cooling transition frequency between these two magnetic field regions is about 28 GHz.

beam tuned to the repump transition,

$$^{2}S_{1/2}\,(m_J = -1/2, m_I = +3/2) \rightarrow {}^{2}P_{3/2}\,(m_J = +1/2, m_I = +3/2)\,, \tag{2.5.10}$$

would provide fast optical repumping of the ions into the cooling transition. However, there is another option for repopulating the cycling transition: *off-resonant repumping*. This process occurs when an ion is excited by light whose frequency is not exactly matched to the repump transition but is close enough that absorption can still occur. Although inefficient when compared to resonant excitation, off-resonant repumping can still transfer population between states.

The difference between the cooling and repump frequencies is shown in Fig. 2.14. At 1 T, the difference between the two transitions is ~ 8 GHz, whereas at 3 T, it is ~ 27 GHz. At ALPHA, we rely on off-resonant repumping. At 3 T, the cooling requirement is less stringent (we need an ion plasma temperature of a few hundred Kelvin), so off-resonant repumping is sufficient even with 27 GHz between the transition frequencies.

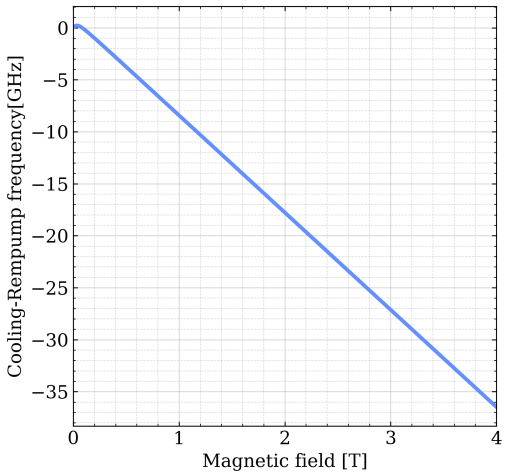

Figure 2.14: Difference between $^9Be^+$ cooling and repump transitions as a function of magnetic field. The plotted frequency corresponds to the difference between cooling transition defined in Eq. 2.5.9 and the repump transition defined in Eq. 2.5.10. There are two operational regions at ALPHA: $B = 1\,T$, where the difference is about 8 GHz; and $B = 3\,T$, where the difference is about 27 GHz.

3 ALPHA Experimental Apparatus

The Antihydrogen Laser PHysics Apparatus, more fondly referred to as the ALPHA experiment, is one of the many experiments located in the Antiproton Decelerator (AD) complex at CERN. As the name suggests, ALPHA studies the properties of antihydrogen. Antiprotons, one of the key components required to produce antihydrogen, are not readily available. In fact, producing these particles involves a series of complex processes which can only be performed in a select number of facilities worldwide. Not only do the experiments in the AD need antiprotons, they also require them to be very low energy, as most experiments aim to trap these particles. These stringent requirements make CERN and its AD complex the only facility in the world where low-energy antihydrogen experiments can be conducted.

The antiproton production process begins with an accelerated proton beam provided by the Proton Synchrotron (PS). The protons are accelerated to about 26 GeV, and directed towards an iridium target [64]. Upon collision with the target, proton-antiproton pairs are produced, and the antiprotons are magnetically selected from the collision products and sent into the AD [65].

Antiprotons enter the AD with a kinetic energy of 2.69 GeV and are decelerated to about 5.31 MeV within the AD ring [66]. Due to a new addition to the AD complex in 2018, the Extra Low ENergy Antiproton ring (ELENA), the particles are further decelerated to 100 keV [67]. ELENA provides antiproton bunches every $110-130$ s, depending on the cycle duration of the other accelerators at CERN. During the development of the work on this thesis, improvements to ELENA's

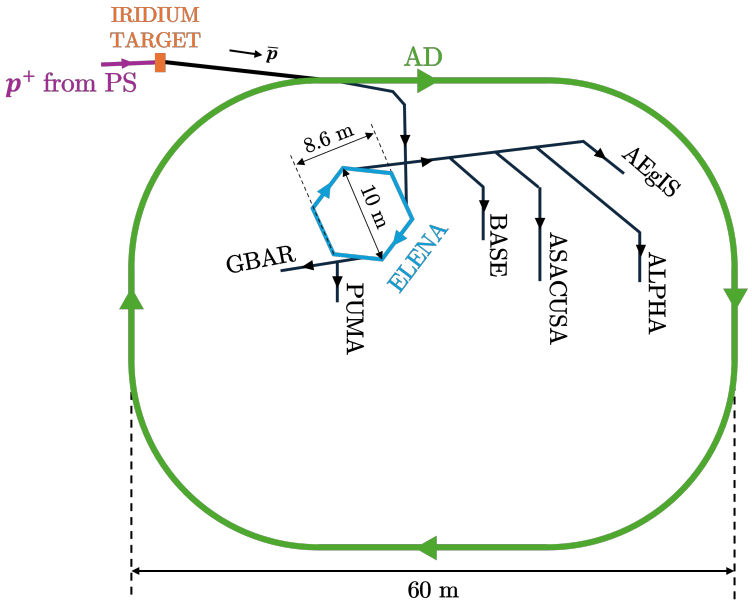

Figure 3.1: Diagram of the Antiproton Decelerator (AD) complex as of 2024. The antiprotons ($\bar{p}$) are formed as a result of the collision between accelerated protons (p^+) from the Proton Synchrotron (PS) and an iridium target. The antiprotons are guided into the Antiproton Decelerator (AD), depicted in green. For further deceleration, they are then loaded into ELENA, depicted in blue. Finally, the antiproton bunches are distributed to the various experiments in the AD. All the elements in the figure besides the iridium target are to scale. This image was adapted from [68].

efficiency increased the beam intensity, and the number of antiprotons per bunch delivered to ALPHA varied between $8-10$ million. Fig. 3.1 shows a diagram of the AD complex and its experiments as of 2024. All the elements, with the exception of the iridium target, are to scale.

This chapter provides a detailed overview of the experimental apparatus used in the ALPHA experiment, including its key components. It also outlines the specific paths and preparation processes of antiprotons and positrons leading to antihydrogen synthesis, as well as the tools and techniques employed at ALPHA for diagnosing plasma parameters.

3.1 ALPHA Experiment Overview

ALPHA comprises four Penning-Malmberg traps where the various particles are trapped and prepared for antihydrogen production, along with two Ioffe-Pritchard traps where the antihydrogen can be stored for experimentation. The theory for how to trap particles in each of these traps can be found in Chapter 2.

Fig. 3.2 shows a schematic of the ALPHA's experimental apparatus. As discussed in Chapter 1, ALPHA pursues two main research paths: high precision antihydrogen spectroscopy and tests of the interaction between antimatter and gravity. Since the mechanical requirements differ, two different experimental setups are necessary:

- **ALPHA-2:** a horizontal system with four laser access ports providing direct laser illumination into the trap. This apparatus is used for precision spectroscopy measurements.

◇ **ALPHA-g:** a vertical system with a complex magnet configuration which allows for precise control of the magnetic field in the trap. This setup enables the study of the interaction between gravity and antihydrogen.

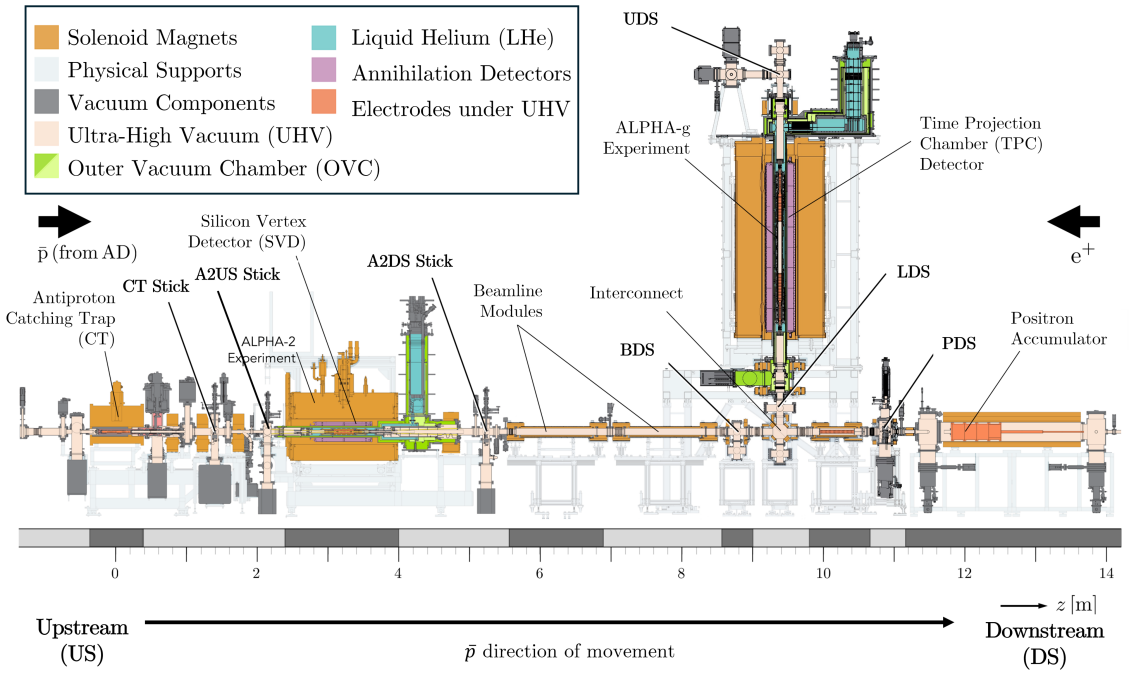

Figure 3.2: Cross-sectional diagram of the ALPHA experiment. The antiprotons ($\bar{p}$) move from upstream (US) to downstream (DS). Figure adapted from [69].

Even though the final experimental goals differ between the two experimental setups, the process of synthesising antihydrogen and the particle preparations beforehand are very similar. In short, the antiprotons are caught and cooled in the Antiproton Catching Trap (CT), then they are transported to either experiment through magnetic beamlines. The positrons are produced and accumulated in the positron source and positron accumulator, respectively, and magnetically transported to the relevant experiment. The particles are then caught in a Penning-Malmberg trap and, after some preparations, are brought together for antihydrogen synthesis. The antihydrogen atoms with low enough energy will become trapped, and the remainder will annihilate with the trap walls. The beamlines between the CT and ALPHA-2, and between ALPHA-2 and the positron accumulator do not allow for on-demand polarity switching. Therefore, simultaneous operation of ALPHA-2 and ALPHA-g is not currently possible. More details about each component can be found later in this chapter. This thesis will focus solely on work done in ALPHA-2.

3.1.1 Translational Diagnostic Stations

ALPHA has several diagnostic stations, familiarly referred to as "sticks". These are translational stages with several instruments in an array located inside the vacuum volume. The devices can move to different positions, allowing the various instruments to be utilised for their intended purpose. Fig. 3.2 shows the locations and naming conventions of each translational stage in bold.

An important naming convention to keep in mind for the remainder of this thesis is the use of terms **upstream (US)** and **downstream (DS)**, which refer to the direction of antiproton motion through the experiment. Antiprotons travel from US to DS. These terms are frequently used to label hardware, for example, the two diagnostic stations around A2 are differentiated as the *A2US Stick* on the antiproton arrival side, and as the *A2DS Stick* on the opposite side. Some instruments are common to almost every diagnostic station:

- **Micro Channel Plates (MCPs):** used for particle imaging, more details in Section 3.2. When a diagnostic station has multiple MCPs, they are distinguished by the orientation of the active area. For example, the A2US stick has two MCPs: one to image antiprotons from the Catching Trap, called the A2US US-facing MCP, and another used to image particles from inside the ALPHA-2 trap, called the A2US DS-facing MCP.
- **Electron guns (e-guns):** sources of electrons.
- **Pass-throughs:** metal tubes allowing particles to move through the stick. It is also possible to apply a voltage to these instruments for important measurements such as bunch length or energy distribution determinations.

Other instruments are only necessary in certain diagnostic stations, as their purpose is less generalised:

- **Beryllium target:** solid Beryllium metal target used as a source of Be^+ ions, situated in the A2US stick.
- **Laser mirrors:** UV-coated mirrors used to reflect laser beams into the Penning-Malmberg traps along the electrode centres. There are laser mirrors in both the A2US and A2DS sticks.
- **Faraday Cups, (FCs):** used for determining the absolute number of charges in a plasma. These are not common instruments in the sticks since using an MCP to measure the same quantity is preferable. More details in Section 3.2.

3.1.2 Antiproton Catching Trap (CT)

The antiproton Catching Trap (CT) is a cryogenic Penning-Malmberg trap with a solenoidal field of 3 T, provided by a magnet called the Swansea magnet. This trap is located at the end of the ELENA distribution beam for ALPHA, which can be seen in Fig. 3.2. The antiproton beam is delivered to ALPHA at an energy of about 100 keV, passing through a thin degrader foil, which slows the bunch [70]. The first and thirteenth electrodes in the catching trap are high-voltage electrodes, allowing the electrostatic potentials to be raised to about 4 kV in these trap regions. Therefore, only the antiprotons decelerated to below 4 keV can be trapped in the CT. This trap is the only Penning-Malmberg trap at ALPHA with such voltage ranges available; in general, the electrodes have a range within ± 140 V. The catching trap acts as a first stage for antiproton bunch cooling and stabilisation. This apparatus is not used for antihydrogen production or experimentation.

Due to their high mass, cyclotron cooling is not an effective cooling mechanism, as discussed in Section 2.3. Cooling is achieved by pre-loading an electron plasma into the catching region. These leptons will cool down in a few seconds before catching antiprotons. When the antiproton bunch

is trapped, some particles will be lost if they have not been slowed below 4 keV by the interaction with the foil, or if they travel at a high radius and annihilate with the trap walls. The remaining antiprotons will be trapped in a well with the pre-loaded electrons and cool down by collisions with the cold leptons (sympathetic cooling, details in Section 2.3). The multispecies plasma undergoes a compression step, reducing the final antiproton radius to minimise losses during the transfer to the antihydrogen production traps. Before transfer, the electrons are ejected from the antiproton plasma using the e-kick technique described in Section 2.1. The bunch provided by ELENA contains about 10 million antiprotons. After capture and preparation, about 500 thousand particles remain in the CT ready for transfer.

3.1.3 Positron Accumulator

At ALPHA, positrons are obtained by the decay of a radioactive sodium source, $^{22}\mathrm{Na}$ into $^{22}\mathrm{Ne}$, a reaction that happens around 90 % of the time [71],

$$^{22}_{11}\mathrm{Na} \rightarrow ^{22}_{10}\mathrm{Ne} + \mathrm{e}^{+} + \nu_{\mathrm{e}}. \tag{3.1.1}$$

This isotope has a half-life of 2.6 years, enabling day-to-day reproducibility in positron yield. However, the emitted positrons are at energy ranges of several keV, making them unsuitable for antihydrogen production directly after the source. The source is at about 7 K, frozen directly onto the source, a solid Neon moderator slows the positrons down to < 100 eV. This moderator has an efficiency of less than 1% [72], greatly reducing the positron flux out of the source. Still, it is a necessary step in the accumulation process, as it not only reduces the positron's energy by over an order of magnitude, it also causes a reduction in the energy spread of the outgoing positrons.

The moderated positrons are then magnetically guided to a three-stage accumulator with N_2 as the buffer gas. This positron accumulator was based on the design developed by C. Surko and his colleagues at UCSD, San Diego [73, 74]. Fig. 3.3 shows the on-axis electrostatic potentials during the current ALPHA positron accumulation procedure. The grey and white shaded areas represent the electrodes of the Penning-Malmberg trap. The field providing radial confinement is about 300 Gauss. The N_2 is introduced through a gas inlet in stage 1 and gradually diffuses to stages 2 and 3. The first two electrodes have a much smaller radius than the rest of the trap; coupled with differential pumping, the pressure varies between each accumulation stage. As the positrons travel through the trap, they lose energy through collisions with the nitrogen molecules. The stepped potential applied to the electrodes ensures the positrons stay confined in stage 3. One of the electrodes in stage 3 is a segmented electrode, which allows for control of the positron cloud radius through the application of a rotating electric field. This maintains the radius of the trapped positrons at the ideal size for transfer.

During normal operation, the accumulation time is 100 s, which typically yields ~ 20 million positrons. The Neon moderator degrades over time, gradually reducing the number of accumulated positrons. After a few weeks of operation, it is necessary to sublimate the moderator and freeze a new Neon layer onto the source.

After accumulation, the buffer gas is pumped out to minimise vacuum contamination of the rest of the experiment. Once the N_2 has been properly pumped out of the system, the potential

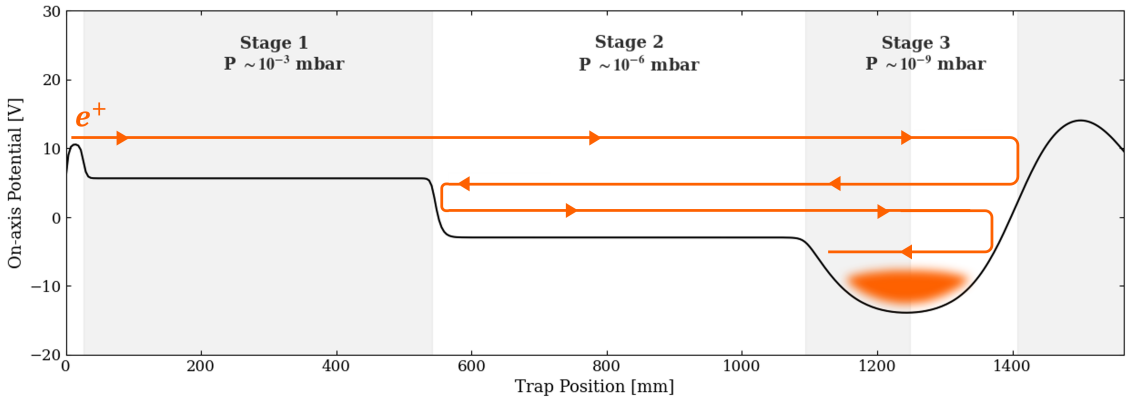

Figure 3.3: Three-stage accumulation potentials in a Penning-Malmberg trap. The solid black line represents the electrostatic potentials at $r = 0$, in the positron accumulator at ALPHA. The pressure P progressively decreases from 10^{-3} mbar on stage 1 to 10^{-9} mbar on stage 3. This decrease in pressure is achieved through differential pumping and different electrode radii. The orange cloud and arrows illustrate the positron's behaviour in this setup.

barrier on stage 3 is lowered. The positrons are ejected from the accumulator and guided to the desired experimental apparatus by a magnetic beamline.

3.1.4 Particle transfers between traps

As mentioned beforehand, both antiprotons and positrons need to be transferred from the CT or positron accumulator, respectively, into one of the antihydrogen experimentation traps. There are two main travel regions.

Transfer between CT and ALPHA-2

The beamline between the CT and ALPHA-2 comprises two water-cooled solenoid magnets, which are always ramped to the target current during both the antihydrogen production and experimentation stages. During ALPHA-2 operation, the currents applied to these magnets and their positions are tuned to optimise the transfer efficiency between the catching trap and the ALPHA-2 Penning-Malmberg trap. In the 2023 antiproton run, about $130\,000$ antiprotons were successfully transferred and caught into ALPHA-2, giving a 26 % transfer efficiency. The antiproton transfer was improved during the 2024 antiproton run, increasing the number of antiprotons available for antihydrogen synthesis to $\sim 350\,000$ in ALPHA-2.

ALPHA-g beamline

During the 2018 ALPHA-g installation, a magnetic beamline was installed between ALPHA-2 and the positron accumulator. This beamline includes a section featuring curved magnetic field lines that direct particles "upward" toward the ALPHA-g trap, in Fig. 3.2, this turning region is shown and labelled *interconnect*. Unlike the magnets described above, this beamline ramps the magnets up to the target current and down to zero as needed. It also allows for different types of mag-

net ramp configurations, streamlining particle transfers and extractions [1]. Unfortunately, these magnets do not currently allow for automatic switching of their polarity, which prohibits simultaneous operation of ALPHA-2 and ALPHA-g. Further details on this topic can be found in Dr. M. Johnson's thesis [69].

Particles are transferred through this beamline with energies of approximately 100 eV, a range compatible with the electrode setup and favourable for recapture. The positron accumulator yields ~ 20 million positrons per accumulation cycle $(100\ \mathrm{s})$, and about 6 million particles are caught in ALPHA-2, corresponding to a transfer and trapping efficiency of 30 %. The positron losses are mostly due to the defocusing of the positron beam over the long distance travelled. At the DS entrance of the ALPHA-2 trap, the positron bunch is 1.4 m long, which is more than double the trapping region in ALPHA-2. With this current transfer method, achieving 100 % transfer and trapping efficiency is not possible, regardless of the beamline configuration.

3.1.5 ALPHA-2 Apparatus

ALPHA-2 is one of the two antihydrogen synthesis and experimentation apparatuses at ALPHA. It consists of a Penning-Malmberg trap, where charged particles are trapped and manipulated, overlaid with a magnetic minimum trap, where antihydrogen is stored. The dynamics of both of these traps are discussed in subsection 2.1.1 and subsection 2.4.1.

Fig. 3.4 shows a diagram of the ALPHA-2 Penning-Malmberg trap along with the magnets providing the field for the Neutral Trap. The Penning-Malmberg trap electrodes are shown in yellow. It is very important to note the difference between the normal and thin electrodes: normal electrodes have an inner diameter of 29.60 mm and a thickness of 3.00 mm, which allows for the manufacturing and assembly of segmented electrodes; thin electrodes have an inner diameter of 44.55 mm and a thickness of only 1.50 mm, these dimensions allow us to exploit as much as possible of the Neutral Trap depth. Details about the manufacturing and features of this trap can be found in [50]. The ALPHA-2 Penning-Malmberg trap is made of 27 electrodes placed symmetrically: seven normal electrodes (left normal trap), followed by thirteen thin electrodes (antihydrogen synthesis trap) and finally seven other normal trap electrodes (right normal trap). There are two 6-way segmented electrodes, one in each normal trap, which are vital for preparing both the antiproton and positron plasmas. The antihydrogen is synthesised near the centre of the antihydrogen trap.

Lasers can be sent into the trap through the off-axis laser ports or through the vacuum windows by reflecting the beam on mirrors placed on both diagnostic stations.

Throughout the remainder of this thesis, the electrodes will be referred to with the letter E followed by the electrode number. The first electrode, or E01, is defined to be the first electrode in the direction US $\rightarrow$ DS.

ALPHA-2 Neutral Trap

Antihydrogen atoms cannot be trapped in a Penning-Malmberg trap, instead they are trapped in a magnetic minimum trap, called the Neutral Trap. The magnetic field shapes resembles a bathtub,

[1] In ALPHA-g, many diagnostics rely on the ramping up of this beamline for particle extraction

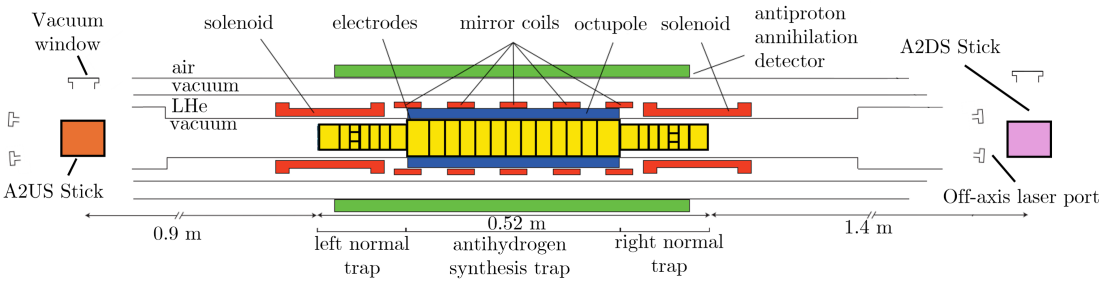

Figure 3.4: ALPHA-2 trap diagram. The Penning-Malmberg trap electrodes are shown in yellow. The solenoid providing the 1 T field for the charged particle trap is not depicted. The mirror coils and solenoid magnets (red) and the octupole (blue) provide the magnetic field for the magnetic minimum trap (the Neutral Trap). The ALPHA-2 diagnostic stations are shown in orange and purple. The Neutral Trap magnets are superconductive and are within a liquid helium (LHe) volume. The trap electrodes are then kept at around 4.2 K.

with the field minimum near the centre of the Penning-Malmberg trap where the antiatoms are synthesised. The field in this region is in the range 1 - 1.1 T. The magnetic field increases towards the left and right normal traps, where it reaches a maximum of around 3.3 T near the segmented electrodes. Fig. 3.5 plot (a) shows a 3-D model of the magnetic field in the ALPHA-2 trap.

Producing a 3-D magnetic minimum requires a particular magnet configuration. Fig. 3.5 (b) shows the magnet configuration in the ALPHA-2 experiment. Solenoids A and B increase the field towards the ends of the Neutral Trap, creating 'walls' and axially trapping the anti-atoms. A multipole magnet is used to radially trap antihydrogen. A multipole magnet consists of n wires cylindrically placed, with current flowing in opposite directions to each neighbouring wire. In ALPHA-2, an octupole is used. Mirrors A through E are used to subtly change the shape of the magnetic field allowing for adaption to a wide range of experiments. During antihydrogen synthesis, the field is designed to be as axially flat as possible across the synthesis trap. This increases the region where an antiatom can be trapped, Fig. 3.5 (b) shows the flat-field configuration on-axis ($r = 0$), the dashed lines illustrate the start and end of the Penning-Malmberg trap.

High currents are necessary for obtaining these fields, (for example during antihydrogen synthesis the octupole is energised with 900 A), therefore all of the magnets in Fig. 3.5 are superconducting.

ALPHA-2 Detector: Silicon Vertex Detector (SVD)

Antihydrogen atoms are lost from the trap in two main ways: they either migrate towards the electrode walls and annihilate with the protons or neutrons in the material, or they are lost inside the trap by annihilations with the background gas or ionisations through interactions with other particles used for antihydrogen production. When an antiproton annihilates with nuclear matter, the result is mostly the release of pions (π^+, π^- or π^0). The number of pions created depends on the energy of the antiproton. Charged pions can be detected using a charged particle detector. The annihilation between a positron and an electron almost exclusively yields a back-to-back pair of gamma rays with the distinguishable energy of ~ 511 keV. The ATHENA experiment determined that antiproton annihilations are sufficient for successfully identifying antihydrogen

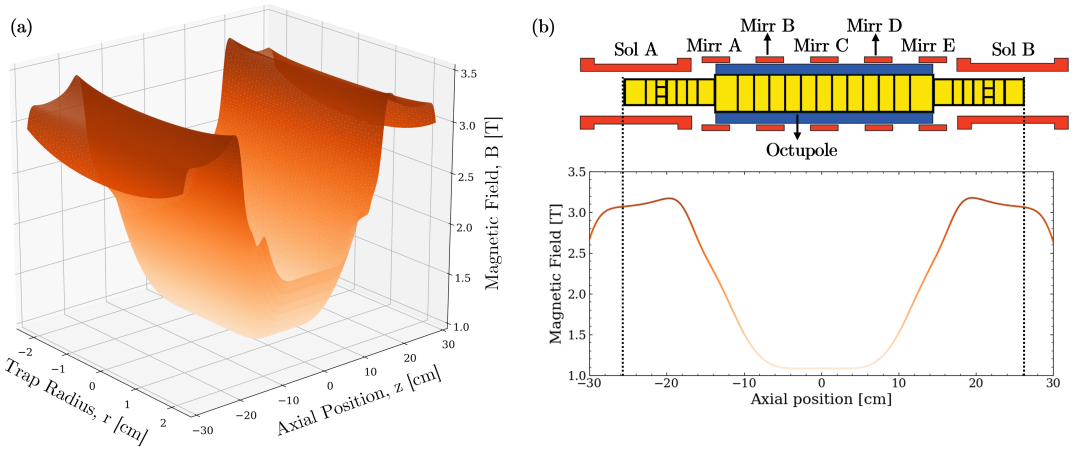

Figure 3.5: (a) Neutral trap magnetic field as a function of axial and radial position in ALPHA-2. (b) ALPHA-2 Neutral Trap magnet configuration and magnetic flat-field at $r = 0$ as a function of axial position. The various magnets are labelled, "Sol" stands for solenoid and "Mirr" stands for mirror. The dashed lines illustrate the start and en of the Penning-Malmberg trap in the 2-D magnetic field plot.

annihilations [75], therefore, the annihilation detector designed for ALPHA aims to detect only antiproton annihilations.

The Silicon Vertex Detector (SVD) is the main tool used to perform antihydrogen detection in ALPHA-2. It consists of three concentric layers of 60 silicon microstrip modules around the Neutral Trap magnets. A detailed description of this detector can be found in [76]. When a pion traverses a silicon module, energy is deposited directly into the device. The positions of the deposited energy through each layer allow for the reconstruction of the location of the antiproton annihilation, referred to as the *annihilation vertex*. This detector gives both spatial and temporal information about each annihilation event.

This detector's main background source is cosmic rays passing through it at a rate of 6 Hz before applying any selection criteria to the recorded events. However, the trajectory of a cosmic ray is inherently different from the trajectory of the pions resulting from antiproton annihilation. Fig. 3.6 shows two reconstructed events in the SVD annihilation detector. The event on the right shows a typical cosmic ray reconstruction. Cosmic rays will travel through the detector in a mostly straight line, which the analysis algorithm interprets as two tracks back-to-back with an annihilation vertex in an unphysical location. As in the example in Fig. 3.6, the vertex is estimated to be outside the trap walls, into the SVD structure. In the case of an antiproton annihilation, the SVD will detect several near-simultaneous events which, after track reconstruction, coincide at a point either at the electrode wall position or inside the trap electrodes. The resolution along the axis of the trap, z resolution, is (0.521 ± 0.005) cm, and the radial resolution, r resolution, is (0.893 ± 0.008) cm. The antihydrogen detection efficiency is $(78.6 \pm 0.2\ )$ % [77].

3.1.6 ALPHA-g Apparatus

ALPHA-g is the second antihydrogen synthesis and experimentation area in the ALPHA experiment. Similarly to ALPHA-2, it consists of Penning-Malmberg trap overlaid with a magnetic min-

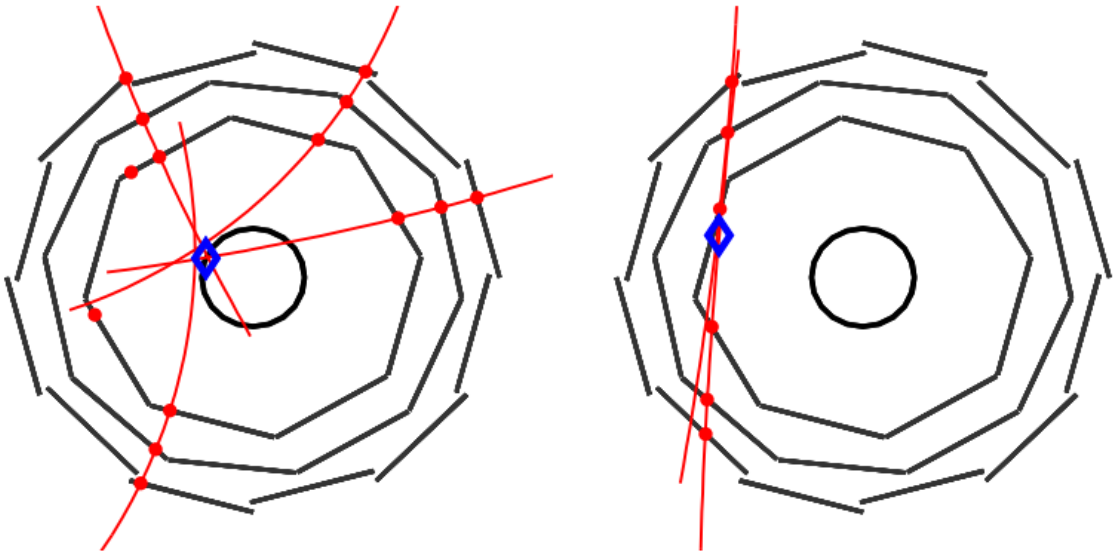

Figure 3.6: Reconstructed events in the ALPHA-2 annihilation detector. The three silicon layers are depicted as three concentric polygon-like shapes, with the inner surface of the Penning-Malmberg trap electrodes as the inner circle. The blue diamond represents the position of the reconstructed vertex, while the red dots represent the locations where charge has been deposited in the detector. The red tracks identify the fitted particle tracks. Left: reconstructed event from an antiproton annihilation with four tracks. Right: reconstructed comic ray event. The algorithm has interpreted this signal as two near colinear tracks with an unphysical vertex. This diagram has been taken from page two of [78].

imum trap with an octupole field. These traps are vertical to ground (more importantly, parallel with gravity). The internal layout of each trap differs from ALPHA-2, as the Penning-Malmberg trap needs to be longer and the positrons and antiprotons must enter the trap from the same end, which complicates the particle preparation protocols. The magnetic minimum trap comprises more short solenoid magnets which allow for finer tuning of magnetic field shape. The antihydrogen synthesis process is akin to the one developed in ALPHA-2, but the experiments performed in ALPHA-g are mostly related to studying the interactions between gravity and antihydrogen. In 2023, the first observation of the effect of gravity on the motion of antimatter was observed in ALPHA-g [16]. The final analysis yielded a value of $(0.75 \pm 0.13$ (statistical + systematic) ± 0.16 (simulation)) g for the local acceleration of antimatter towards the Earth. More efforts are being taken to increase the precision of this measurement. ALPHA-g is mostly irrelevant to the work in this thesis, however, implementing Be^+-assisted antihydrogen synthesis in ALPHA-g is of great interest as the antihydrogen production rate was only about 50 antihydrogen atoms an hour.

3.2 Plasma Diagnostic Tools

Measuring plasma parameters is essential for optimising particle preparations at ALPHA. Different tools are used depending on which parameter one would like to probe; usual interesting parameters are the number of particles, plasma radius, and plasma temperature.

Most of the methods applied at ALPHA are destructive and entail scans during which a new plasma must be created for each data point. Thus, reproducible control of plasmas is also pivotal

for the operations at ALPHA, subsection 2.2.3 provides further details on this topic.

3.2.1 MicroChannel Plate (MCP) and Phosphor Screens

Microchannel plates/phosphor screens are a widely used method for plasma diagnostics in plasma physics. MCPs consist of a phosphor screen placed between two plates (the front and back plates), which are charged such that the incoming particles are accelerated upon approach. When an incoming charged particle collides with the MCP, a cascade of electrons is created, effectively amplifying the signal. This amplification makes it much easier to detect the incoming particle. The collision results in photons created from phosphorescence, which are then collected by a CCD camera. These devices allow us to measure the $x-y$ plane of the plasma, their *radial profile*. The use of MCPs for imaging antimatter was first reported in [79].

Upon imaging, one can fit a Gaussian power law to the signal S,

$$S = Ae^{-\frac{|r-r_0|}{b}^n}, \tag{3.2.1}$$

and extract several parameters: A is the peak signal intensity, r_0 are the coordinates of the plasma centre, n is the order of the Gaussian function (typically $n \approx 2$), and b is the plasma radius. Additionally, we extract another quantity, the Net Norm Intensity (NNI), which is a measure used to estimate the number of particles in the imaged plasma. It is obtained by integrating the intensity of the image across the plasma area. This number must be calibrated to represent real plasma parameters. More details of this calibration can be found in the next section.

Due to spatial and thermal limitations, the MCPs have to be placed within the fringe field of the Penning-Malmberg trap solenoid field, which can introduce some distortion of the radial profile. [80].

For strongly magnetised plasmas (such as leptons), the fringe field will radially expand the plasma such that the radius of the plasma in the trap, r_{trap}, can be inferred by the following relation,

$$r_{\mathrm{trap}} = r_{\mathrm{MCP}}\sqrt{\frac{B_{\mathrm{MCP}}}{B_{\mathrm{trap}}}}, \tag{3.2.2}$$

where r_{MCP} is the radius observed at the MCP, and $\mathrm{B_{MCP}}$ and B_{trap} are the magnetic field strengths at the MCP and trap locations, respectively. Fig. 3.7 shows the calculated magnetic field across ALPHA-2. The left plot shows the field near the A2US Stick, whose position is marked in orange. The centre plot shows the field in the ALPHA-2 trap region. The three locations are: in yellow, the segmented electrode in the left normal trap, in blue, the location where antihydrogen is formed, and in green, the segmented electrode in the right normal trap. These are the most common and relevant locations from where plasmas are diagnosed. Finally, on the right plot, the magnetic field in the A2DS Stick location is marked in pink. When imaging plasmas from inside the trap, these fields must be taken into account to extract the actual plasma radius inside the trap. The plasma length cannot be directly measured and must be calculated using the plasma profile measured by the MCP, the trap geometry and the on-axis electric field.

The MCP detection efficiency was shown to heavily depend on the particle mass [80]. Heavier particles are detected less efficiently. In the setup described in [80], for typical particle ejection

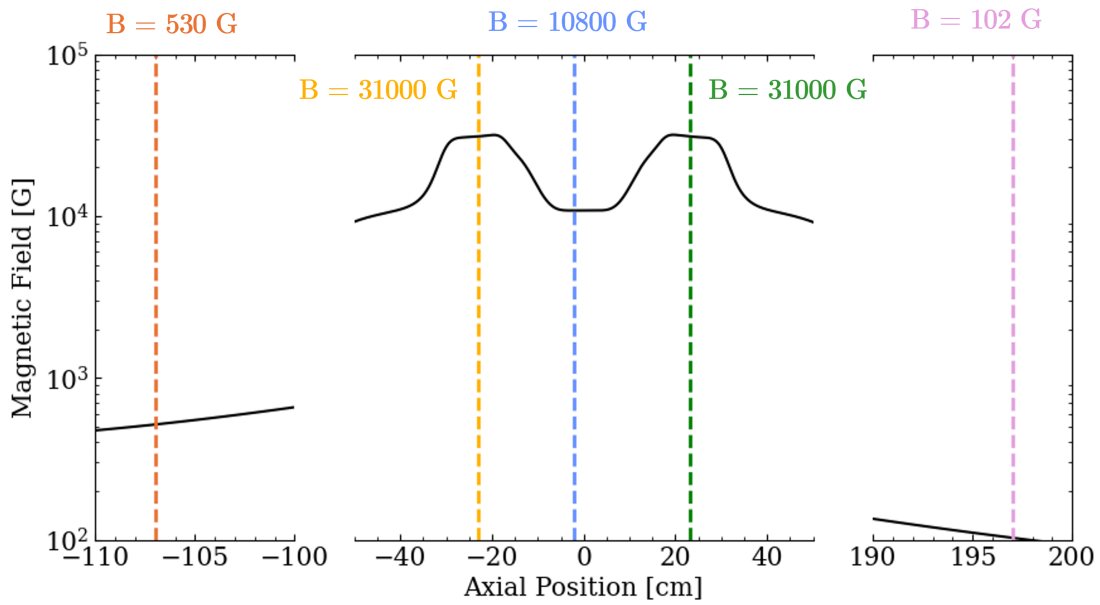

Figure 3.7: Calculated magnetic field as a function of axial position in ALPHA-2. The solid black line represents the calculated field. Highlighted in dashed lines, are some relevant positions and their magnetic fields: in orange, the A2US Stick; in yellow, the segmented electrode in the left normal trap; in blue, the antihydrogen synthesis location; in green, the right normal trap segmented electrode; and in pink, the A2DS Stick.

energies at ALPHA (between 50-150 V), the efficiency for Be^+ would be $\sim 10\%$, and $\sim 30\%$ for antiprotons. This efficiency will differ for the ALPHA apparatus since the MCP models and applied voltages are different from the ones used in this paper, but this effect should nevertheless be accounted for. To correct for it, the absolute number of charges must be calibrated (see next subsection). This mass-dependent efficiency should not affect the radius measurements because the extraction is fast and the detection efficiency does not depend on the MCP region probed (unless the active region is damaged).

Plasma solver for density determinations

The Poisson-Boltzmann equation describes a plasma in axial thermal equilibrium,

$$\begin{cases} \nabla^2\phi(r,z) = -\dfrac{qn(r,z)}{\epsilon_0} \\ n(r,z) = \mathcal{N}(r)\exp\left(-\dfrac{q\phi(r,z)}{k_B T}\right), \end{cases} \tag{3.2.3}$$

where $n(r,z)$is the number density of the particles, $\phi(r,z)$is the net electric potential, and $\mathcal{N}(r)$ is the normalisation factor setting the amount of particles at each radius. [81] Here, the Poisson equation determines the potential generated by the charge distribution, while the Boltzmann factor describes how a thermalised plasma is distributed in that potential. In a Penning-Malmberg trap, both the plasma's self-potential and applied electrode fields are taken into account.

If the total number of charges, the plasma radius and the trap's vacuum potential are known, this equation can be used to estimate the density profile of the plasma. At ALPHA, a dedicated solver was developed to compute solutions to the Poisson-Boltzmann equation from plasma radii and numbers obtained from MCP radial profiles and electrode potentials in our specific traps. The details of this algorithm can be found in [81], and are beyond the scope of this thesis. Here, it was used as a tool to extract plasma densities. This solver assumes a stationary, zero-temperature plasma and employs the water bag model to compute its density and electric potential as a function of the radius of the plasma.

3.2.2 Absolute Charge Measurements

Faraday Cup (FC)

A Faraday Cup (FC) is a tool used to measure the absolute charge of a plasma. The cup consists of a metal device connected to an RC circuit. When a number N of particles of charge q are deposited on the conductive surface, a voltage spike will be induced in the system. The peak voltage, V_{peak} measured is proportional to the total charge deposited like so,

$$V_{peak} = qN/C. \tag{3.2.4}$$

The circuit will then exponentially discharge following the usual RC circuit behaviour,

$$V(t) = V_{peak}e^{-t/RC}. \tag{3.2.5}$$

An important consideration to have when applying this method is that the time it takes for the particles to be deposited on the surface must be much smaller than the time it takes for the circuit to discharge, otherwise, the peak voltage will no longer be linear to the total charge.

Faraday Cups are not commonly used at ALPHA due to several limitations: errors can arise from secondary electrons generated during particle impact or from backscattering caused by the geometry of the device. Moreover, the small active surface area of typical Faraday Cups can cause part of the plasma to miss the device altogether and induce errors in the charge measurement.

However, the working principle of the Faraday Cup remains significant. For instance, it is possible to utilize the front plate of a MCP detector to measure the absolute charge of a plasma based on similar assumptions. MCPs offer advantages over traditional Faraday Cups due to their larger active surface area and higher sensitivity, making them better suited for plasma diagnostics at ALPHA.

MCP charge number calibration

The analysis of an MCP image gives a normalised net intensity for the plasma imaged. This number is proportional to the real number of charges in the plasma, therefore, to get a good estimate of actual plasma parameters, one must calibrate this number against a measurement of the charge number, as was discussed above. This calibration changes depending on several parameters:

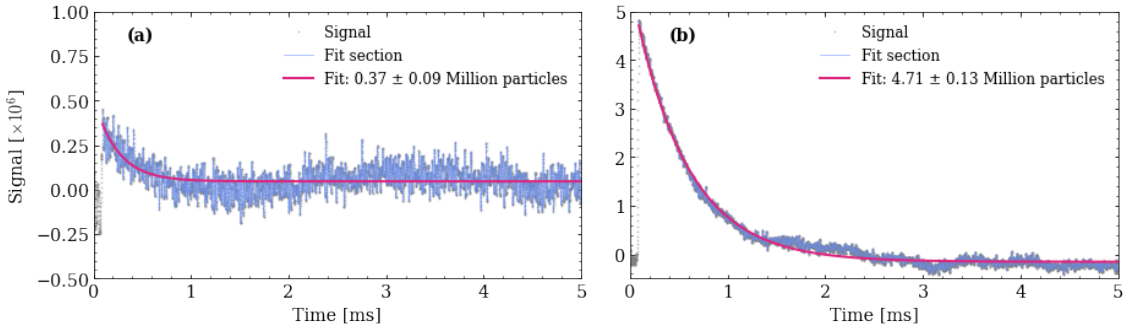

Figure 3.8: Be^+ absolute charge measurements for low and high plasma numbers. (a) Plasma with low particle number. The signal is barely above the noise. (b) Plasma with a high particle number, the signal is clear and above the background noise. The grey dots represent the raw data captured using the MCP front plate as an FC. The blue section showcases the decay region where the fit was applied, and the magenta line shows the fit for each case.

- ◇ **Imaged Particle**: as discussed in the previous subsection, the imaging efficiency depends on the mass of the particle;
- ◇ **MCP Location**: the magnetic fields are different at each of the imaging locations at ALPHA, as well as the path followed by the particles;
- ◇ **Front Plate Voltage:** the voltage of the front plate influences the acceleration of the particles upon approaching the MCP, which can change the bunch energy and thus affect the signal.
- ◇ **Back-to-Front Gain**: different back-to-front gains provide different amplification factors, which influence the signal amplitude.

In the current experimental setup, there are no Faraday Cups for each MCP location and orientation. Fortunately, the front plate of an MCP can be used as a Faraday Cup to measure the charge number. This method is also preferred because it eliminates factors such as active surface area disparities from the calibration. If one connects the MCP front through a capacitance, C, to ground then the voltage measured at this plate, V, is proportional to the charge, Q, like so: $V = Q/C$.

The calibration process consists of imaging N identical plasmas using the MCP in its normal state, followed by measuring the charge number of N identical plasmas using the MCP front as an absolute charge counter. Q remains constant during both measurement procedures and C is measured and constant during the charge number measurement, typical capacitances are between $400 - 500$ pF, depending on the hardware used. Thus, one can calibrate the norm net intensity of the MCP analysis. This procedure was followed for both relevant MCPs in ALPHA-2 and for both Be^+ ion and e^+ plasmas. The MCP front was connected to an SRS SR560 preamplifier, and the capacitance of the whole circuit was determined before taking the charge measurements.

To estimate V_{peak}, the decay region is selected from the signal as well as the particle arrival time t_0. A function of the form,

$$V(t) = Ae^{-tb}. \tag{3.2.6}$$

is fitted to the decay region, and the value at t_0 is calculated, which will give V_{peak}. Note that in these measurements, the signal has already been divided by the measured capacitance by our data

Particle	MCP	Front Voltage [V]	Back to Front Gain [V]	Calibration Factor
Be^+	A2DS US-facing	-300	900	0.362
Be^+	A2DS US-facing	-300	1000	0.797
Be^+	A2US DS-facing	-300	1000	0.017
e^+	A2DS US-facing	-100	800	1.200

Table 3.1: Particle number calibration factors for Be+ in DSAT US-facing and USAT DS-facing MCPs for various gains, as well as for e+ for DSAT US-Facing MCP.

collection software. Otherwise, that needs to be considered when fitting the decay region. Fig. 3.8 shows two signals obtained while calibrating the A2DS US-facing MCP for Be^+ ions. The decay region is highlighted in blue, and in magenta we have the exponential decay fit and the V_{peak} estimates for both cases. Signal (b) is an example of an attempt where the signal is significantly above background and not affected by background fluctuations. When performing these calibrations, we should aim for such strong signals. Signal (a), on the other hand, is too low to be significantly distinguished from background noise and can induce error into the calibration. During calibrations measurements, it was imposed that the plasmas should have more than 1 million particles to avoid inducing errors due to background fluctuations. Tab. 3.1 shows the relevant calibration factors for the work in this thesis: Be^+ calibration factors for different gains and in different MCP locations in ALPHA-2 and e^+ calibration factor in ALPHA-2 downstream MCP for the nominal operational gain.

3.2.3 Silicon Photomultipliers (SiPM) for Temperature Diagnostic

In general, plasma temperature is a relevant parameter to measure, and in particular, the Be^+/e^+ plasma temperature is one of the most interesting parameters to investigate when studying antihydrogen formation. Fluorescence-based temperature diagnostics are not possible for lepton species and are not currently routinely available for diagnosing Be^+ at ALPHA. A method employing a silicon photomultiplier as a temperature diagnostic was developed at Berkeley for electron plasmas in a Penning trap [82–84]. Using this approach, cold electron plasmas (about 10 K) were measured with $\sim 20\,\%$ uncertainty, while hot electron plasmas (about 10,500 K) were measured with $\sim 10\,\%$ uncertainty. This method has since been applied at ALPHA as a temperature diagnostic and is now used routinely.

The rate at which particles escape electrostatic axial confinement as a function of barrier height can be used to infer the plasma temperature. By slowly lowering one side of the trap potential, we can obtain a time history of the extraction by detecting the photons created when the particles hit a charged MCP. The photons are detected by a Silicon Photomultiplier (SiPM) located near the CCD camera used for plasma imaging. The barrier height $E_B(t,r)$ can be defined as,

$$E_{\mathrm{B}}(t,r) = -q[V(t,r) - \Phi(t,r)], \tag{3.2.7}$$

where r is the radial distance from the trap axis, q is the unit charge, $V(t,r)$ is the depth of the vacuum electrostatic well created by the Penning-Malmberg trap electrodes and $\Phi(t,r)$ is the plasma's

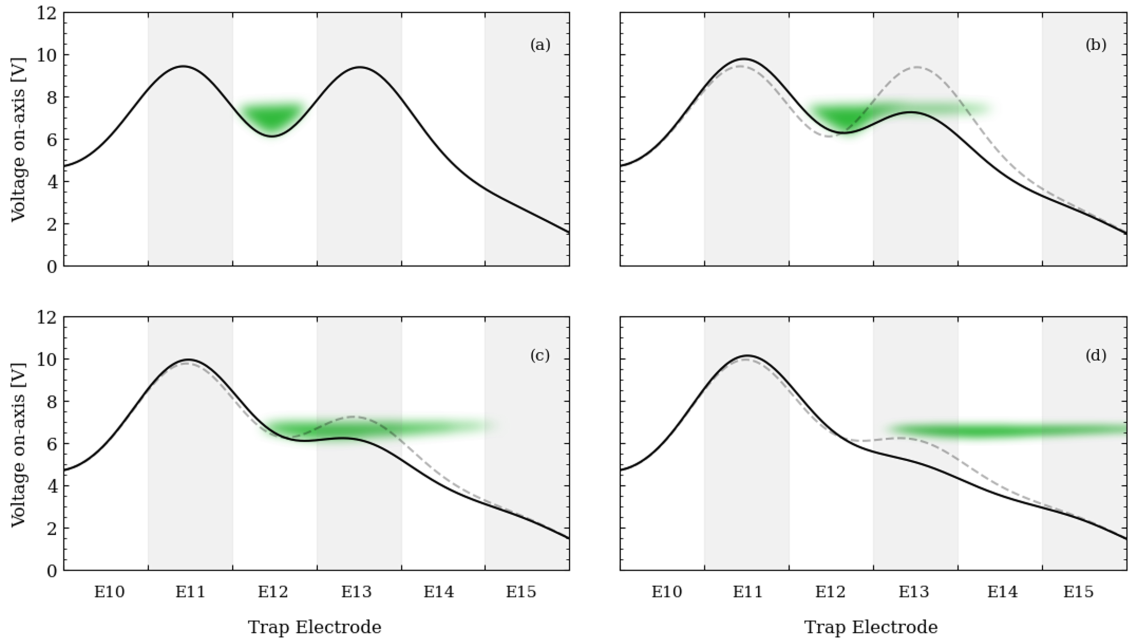

Figure 3.9: Electrostatic potential well manipulations during a positron temperature diagnostic. The well depth is lowered at a constant rate for 10 ms. The particles exit towards the right, eventually colliding with a charged MCP. The photons created during the collision are reflected off a mirror and collected by a SiPM. The green clouds illustrate the particle behaviour when exiting the well.

self-potential. One can then extract the temperature T by fitting the rising edge of the signal, $N(E_B)$ on the SiPM, to an exponential of the form,

$$N\left(E_{\mathrm{B}}\right) \propto \exp\left[-E_{\mathrm{B}}(t,r)/k_{\mathrm{B}}T\right], \tag{3.2.8}$$

where k_B is the Boltzmann's constant. For a more detailed explanation of this method, refer to [84].

Only particles that escape from the central radial core of the plasma contain useful temperature information, as these will be the first particles to escape the trap. As the voltage drops, the plasma is essentially being evaporatively cooled and rethermalised to a lower temperature. Therefore, only about 10% of the signal carries information about the initial plasma temperature [82]. Moreover, the self-consistent plasma potential changes as more particles escape, and the signal becomes increasingly independent of initial temperature as the dump progresses.

Unlike the potential manipulations used for MCP imaging, the particles must be slowly released for a temperature diagnostic, since we need to record the time history of the extraction. Typically, extraction times of around 10 ms are ideal for this type of diagnostic. As the potential barrier is lowered, the centre of the plasma is extracted, which can lead to diocotron or Helmholtz instabilities, perturbing the extraction of the plasma in the later stages of the diagnostic. These instabilities complicate the interpretation of the later signal, reinforcing why only the initial extraction data is reliable for temperature measurement. Fig. 3.9 shows the time evolution of a typical temperature diagnostic dump for positrons; the total dump time in this example is 10 ms, and the particles will exit to the right. For negatively charged particles, the well direction needs to be reversed, but the process is the same.

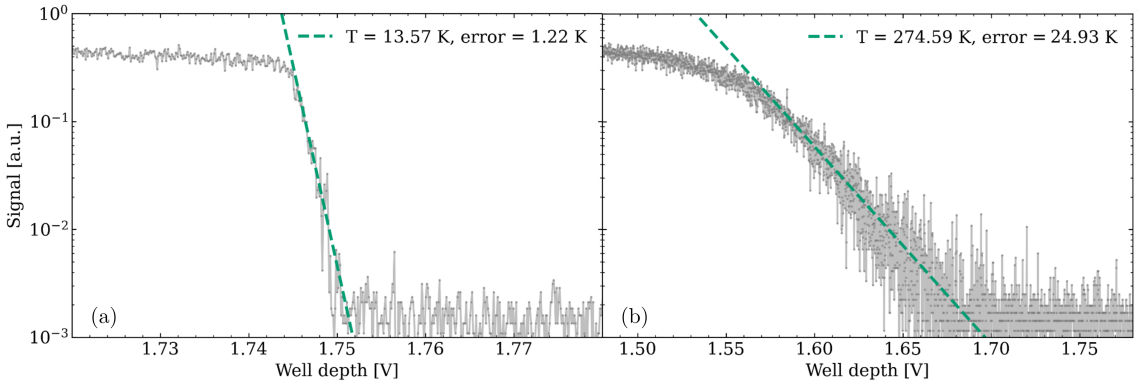

Figure 3.10: Temperature diagnostic signal for cold (a) and hot (b) plasmas. The fit was performed using the method described above and developed by E.D. Hunter et al in [84]

Suppose we wish to measure temperatures to a precision of α. Neglecting background noise and detector sensitivity, L. T. Evans [83] quantified the absolute limit on the usable range of this temperature diagnostic,

$$T_{\text{min}} = 8\,\text{K}\left(\frac{1\,\text{cm}}{L_p}\right)\left(\frac{0.1}{\alpha}\right)^2, \tag{3.2.9}$$

where L_p is the plasma length in cm. For example, positrons for antihydrogen synthesis in ALPHA-2 have a length of approximately 1.1 cm. If we wanted to measure their temperature for $\alpha = 0.1$, the minimum absolute temperature which can be extracted with this diagnostic is $T_{\text{min}} = 7.3\,\text{K}$. Below this limit, the uncertainty increases, making it difficult to distinguish between temperatures. In addition, the potential manipulations during extraction inherently slowly increase the length of the well, adiabatically cooling the plasma in the parallel direction. This effect was investigated in [83] and [82], and was shown to result in an error of up to a factor of two in the absolute temperature. However, while this effect can change the measured absolute temperature, it affects all samples similarly if they are held in the same well and have comparable parameters (particle number and radius). Therefore, meaningful comparisons between their relative temperatures remain valid.

Fig. 3.10 shows two SiPM signals used for temperature measurements of positron plasmas. The right panel shows the signal for a hot positron plasma, and the left panel shows a cold positron plasma. The initial wells and potential barrier ramps are equal for both of these plasmas. The signal for the cold positron plasma is nearing the limitations of this method, as discussed above.

Another interesting parameter that can be extracted from this method for cold plasmas is their self-potential. For dense, cold plasmas, the self-potential is large compared to the kinetic energy of the particles. Thus, the initial detection of particles corresponds to the point where the confinement potential well depth equals the plasma self-potential [84]. For example, in Fig. 3.10, from the cold positron plasma signal (a), we can extrapolate the self-potential to be 1.7505 V, where the signal rise begins. For the hot positron plasma signal (b), the kinetic energy of the particles is such that they can exit the well before it matches the self-potential, and extracting this parameter is no longer reliable. This diagnostic is useful when searching for instabilities in the positron plasma preparation for antihydrogen synthesis, as the temperatures in this regime should be < 20 K.

Finally, this temperature diagnostic method is less suitable for measuring the temperature of heavier particles, such as Be^+. Because the detection efficiency depends on the particle mass, [80], only a small fraction of the Be^+ ions are detected, resulting in a significant loss of temperature information. Nevertheless, qualitative measurements between Be^+ plasma temperatures are still possible if the extraction parameters remain consistent.

4

Be^+ Experimental Setup and Plasma Preparation

In 2019, sympathetic cooling of positrons with laser-cooled Be^+ plasmas was demonstrated in the ALPHA-2 trap [30]. The positrons were estimated to be cooled to cryogenic temperatures of about 7 K. This was a very exciting result which laid the foundation for deeper investigation into this topic. However, the procedure was incompatible with antihydrogen synthesis and trapping in many ways.

From a hardware perspective, the long optical paths (about 12 m) were inherently unstable: slow drifts required frequent expert interventions, while short-term vibrations often misaligned the beams altogether. Since antihydrogen is accumulated in the trap for many hours, often overnight, such interventions would be impractical if this technique were to be applied to standard ALPHA operations.

Moreover, only one cooling beam was sent through the ALPHA-2 trap: an *off-axis* cooling beam, displaced from the centre of the trap by $2.4°$. This geometry restricted cooling to a narrow section of the trap (near the centre of the antihydrogen synthesis trap), making it impossible to apply laser cooling simultaneously with more complex plasma manipulations, such as rotating-wall (RW) compression. As a result, the manipulation and control of the Be^+ plasma parameters was cumbersome: five Be^+ ablation shots had to be accumulated to average over laser energy fluctuations, and plasma radii were adjusted by alternating sequences of laser cooling and rotating wall compression. This preparation procedure took several minutes, whereas compatibility with the

nominal antihydrogen production cycle requires that Be+ preparation be completed in a fraction of the antihydrogen cycle time (approximately 100 s from antiproton capture to antiatom trapping). Without the introduction of a cooling beam overlapping with the axis of the trap, reducing the duration and stability of the ion plasma preparation was not feasible. Details of the original preparation and experimental setup can be found in Dr. J. Jones' thesis [28].

Finally, all the Be^+ studies before the work of this thesis were performed without the Neutral Trap magnets energised; only the 1 T Penning-Malmberg trap solenoid was used. This greatly reduces plasma instabilities, as the octupole field used to trap antihydrogen causes expansion and heating of plasmas. It was not immediately apparent that reproducible and stable cryogenic positron temperatures could be achieved through sympathetic cooling in a radially asymmetric magnetic field, as this had never been attempted before.

This chapter details the upgrades and new techniques necessary to implement reproducible preparation of Be^+ plasmas compatible with antihydrogen synthesis: automated beam steering and stabilisation, the addition of an on-axis cooling beam enabling reproducible plasma control, and a preparation protocol reduced to ~ 30 s demonstrated with the Neutral Trap magnets energised.

4.1 Laser setup and performance

To produce and laser-cool Be^+, at least two laser beams are needed:

- **Pulse ablation beam:** the chosen method for ion production was pulsed laser ablation. More details about this process can be found in Section 4.2. A pulsed laser beam must be directed towards a metal beryllium source. The source needs to be located in the vacuum volume near the Penning-Malmberg trap to allow for Be^+ loading into the electrodes. The chosen laser was a 355 nm pulsed flashlamp laser.

- **Cooling beam:** a laser beam is necessary to perform laser cooling. The targeted cooling transition requires a laser wavelength of 313 nm.

The trap and cryostat were originally designed with off-axis laser ports, with the intent of illuminating only the centre of the trap for antihydrogen experimentation. Given that the antihydrogen atoms are confined only in the antihydrogen synthesis trap region, laser illumination elsewhere was not originally relevant in the context of the ALPHA experiment.

However, to enable Be^+ laser cooling throughout the whole axial extension of the trap, a beam overlapping with the trap axis was necessary. When the proof-of-principle e^+ sympathetic cooling using Be^+ ions measurement was first performed at ALPHA [30], the only available laser path for the cooling laser was one of the off-axis laser port, as shown in Fig. 4.1 (depicted in blue). This beam will be referred to as the *off-axis cooling beam*. The beam is tilted from the z axis of the trap by 2.4°, and coincides with $r = 0$ at the axial centre of the trap (electrode 14 or E14). While the small tilt allows limited laser cooling outside E14, it does not overlap with the ions trapped in any normal trap electrodes. This constraint significantly limited the preparation procedure described in [30], as the lack of cooling under segmented electrodes restricted the ability to effectively control plasma size since particles were lost due to heating from the rotating electric field.

There are a total of four off-axis ports, one is used for the internal enhancement cavity of the 243 nm laser used in for $1S \rightarrow 2S$ transition spectroscopy [12], another is used for the Ly-α laser for antihydrogen laser cooling [14] and the last free port is used for fluorescence detection using a Photomultiplier Tube PMT (more details in Section 2.5).

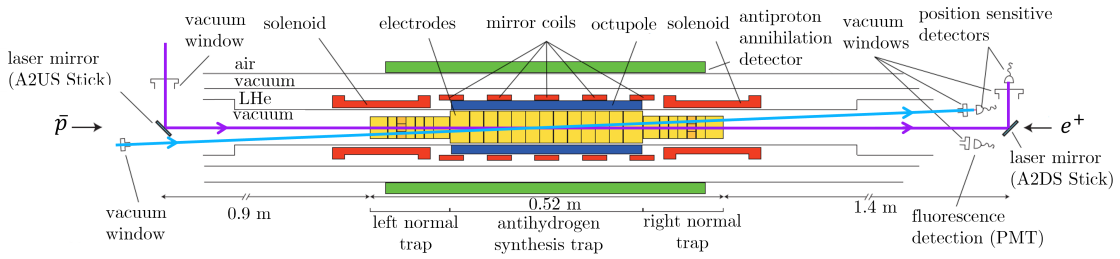

Figure 4.1: Cooling laser beam paths through ALPHA-2. The blue and purple lines represent the off and on-axis cooling beam trajectories, respectively.

The vacuum tubes where the diagnostic stations (A2US and A2DS sticks) are installed are crosses with vacuum windows on the arms perpendicular to the z direction of the trap, as shown in Fig. 4.1. This was originally done to allow visual inspection of the stick position and tilt. These windows also allow for the injection of a laser beam, which can be reflected from the A2US stick into the trap, and reflected out of the vacuum volume from the A2DS stick. This laser path is shown in purple in Fig. 4.1, corresponding to the *on-axis cooling beam*. These vacuum laser mirrors were manufactured by LASEROPTIK GmbH and are coated for 313 nm (Be^+ cooling beam), 243 nm (in case this laser path is ever necessary for $1S \rightarrow 2S$ spectroscopy), and 532 nm (pointing laser to aid in alignment through the trap centres). Fig. 4.2 is a photograph of the A2US stick with the laser mirror highlighted in blue. We aimed to have the largest possible mirror so that its dimensions would not be a limitation to the alignment. The geometry of the stick allowed for the dimensions to be 2.5 cm by 3.5 cm.

The lasers are located in the laser laboratory and travel to the experimental zone (where the traps and cryostats are located) through free-space periscope delivery. The details of the ablation laser setup are discussed in Section 4.2. The 313 nm light is generated using a frequency-quadrupled diode laser from TOPTICA. It is a two-stage resonant frequency-doubling TA-FHG Pro system, which converts 1252 nm into 626 nm and finally 313 nm. Under ideal conditions, the laser outputs about 700 mW out of the fourth harmonic generation (FHG) cavity.

Fig. 4.3a shows the beam path of all three laser beams in the laser laboratory. The beam out of the 313 nm TOPTICA laser is elliptical, hence the need for a cylindrical telescope to correct the beam shape. To divide the main beam into the on-axis and off-axis cooling beams, we have a Polarisation Beam Splitter PBS (instrument ③ in Fig. 4.3a). To control the power in each arm, a zero-order $1/2$ waveplate (instrument ②) is used to adjust the polarisation of the beam before the PBS. This waveplate is mounted on a motorised high-precision rotation stage, which can be remotely controlled, allowing for automated polarisation control. The two beams are then sent into periscope A, which directs them towards the experimental zone. The distance between the beginning of periscope A in the laser laboratory and the end of periscope A in the experimental zone is about 5 m.

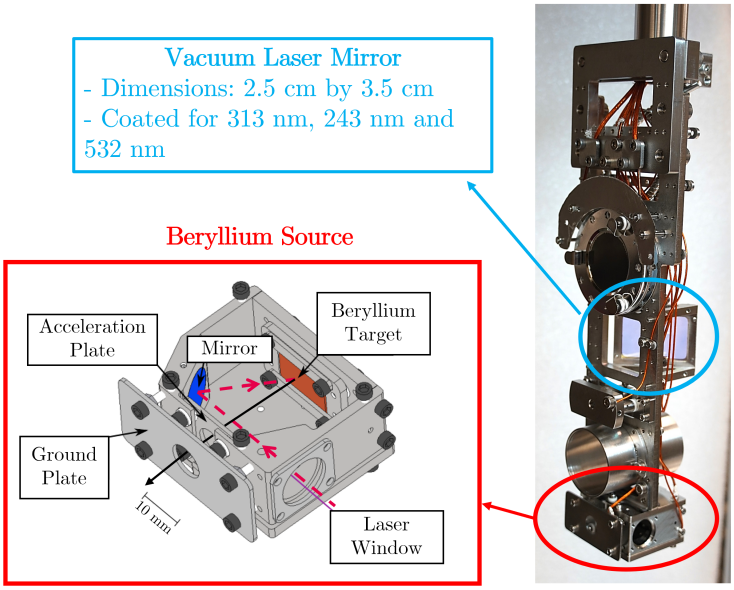

Figure 4.2: Photograph of A2US stick and its components. Highlighted in red is the Beryllium source along with a diagram of the device. The ablation pulse enters through the laser window, reflects off of a mirror and hits the target producing a cloud of Be^+ which are directed out of the source by the magnetic field lines. Highlighted in blue is the vacuum laser mirror used to reflect the on-axis cooling beam through the centre of the trap electrodes.

In the experimental zone, Fig. 4.3b, the off-axis cooling beam is sent into the vacuum volume towards the trap electrodes through an off-axis laser port. The on-axis cooling beam and ablation pulse are directed towards different instruments on the A2US stick through a vacuum window. Since the cooling transition requires circular polarisation, both cooling beams traverse a zero-order $1/4$ waveplate (instrument (18) in Fig. 4.3b).

The total distance travelled by the ablation pulse is $\sim$ 8 m, and by the cooling beams is $\sim$ 12 m. One of the main limitations of the system when utilising free-space periscope delivery in past iterations of the setup was position instabilities due to the long path and outside sources of vibrations and drifts. To address this issue, we developed an automated position stabilisation system, nearly eliminating position instabilities. In Fig. 4.3, the hardware used for this system is shown, instruments (4) and (8) are 2-axis piezo mirrors and instruments (17) and (19) are power and position detectors. The details of this system are laid out further down this section.

The divergence of the cooling beams was measured to be 0.14 ± 0.04 mrad, which results in a radius increase across the length of the trap of 0.07 ± 0.03 mm. This is not a significant increase in the beam size as the beam radius into the trap is around 1.90 mm, representing only a $3\,\%$ in the beam size over the length of the trap.

Be^+ Control System

Our experimental setup requires a complex control system comprising a CompactRIO system and three control computers. Together, these control several motorised devices, shutters, the cooling and ablation lasers and the cooling pump for the 313 nm laser system, as well as monitor several

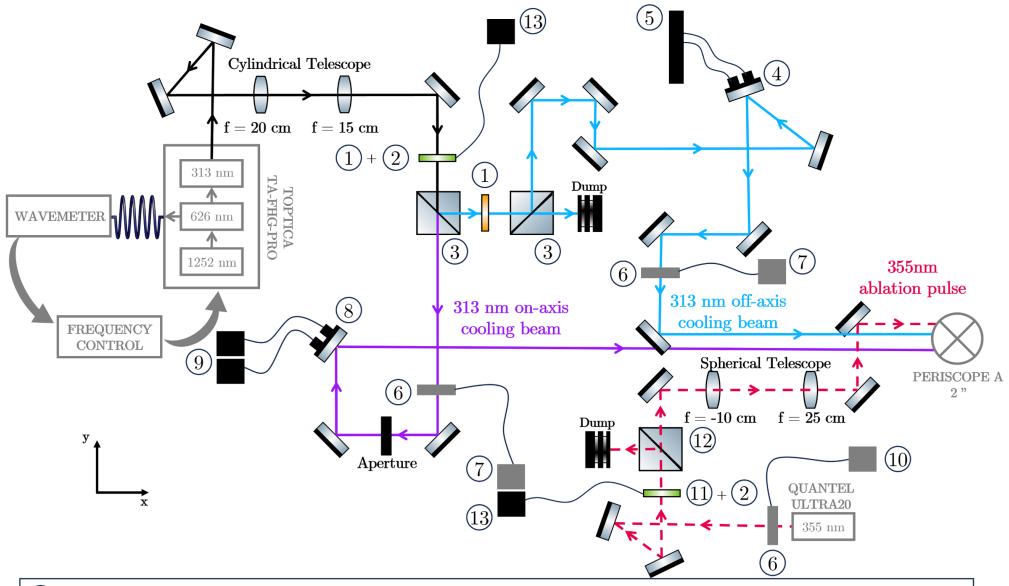

(1) Thorlabs PRM1/MZ8 Motorised High Precision Rotation stage
(2) Thorlabs WP10M-308 Zero Order 1/2 Waveplate - 1”
(3) Bernard Halle Nachff 2016.0132.0001 Polarisation Beamsplitter Cube
(4) Physics Instruments 2-axis Piezo Mirror
(5) FP1099A Dual Piezo Driver (Aarhus)
(6) Thorlabs Shutter SH05/M
(7) Thorlabs KSC101 Controller
(8) Thorlabs POLARIS-K1S2P 2-axis Piezo Mirror
(9) Thorlabs KPZ101 Controller
(10) Thorlabs TSC001 Controller
(11) Thorlabs WP05M-355 Zero Order 1/2 Waveplate - 0.5”
(12) Thorlabs GLB10-UV Polarisation Beamsplitter Cube
(13) Thorlabs KDC101 Controller

(**a**) Optical setup in the laser laboratory.

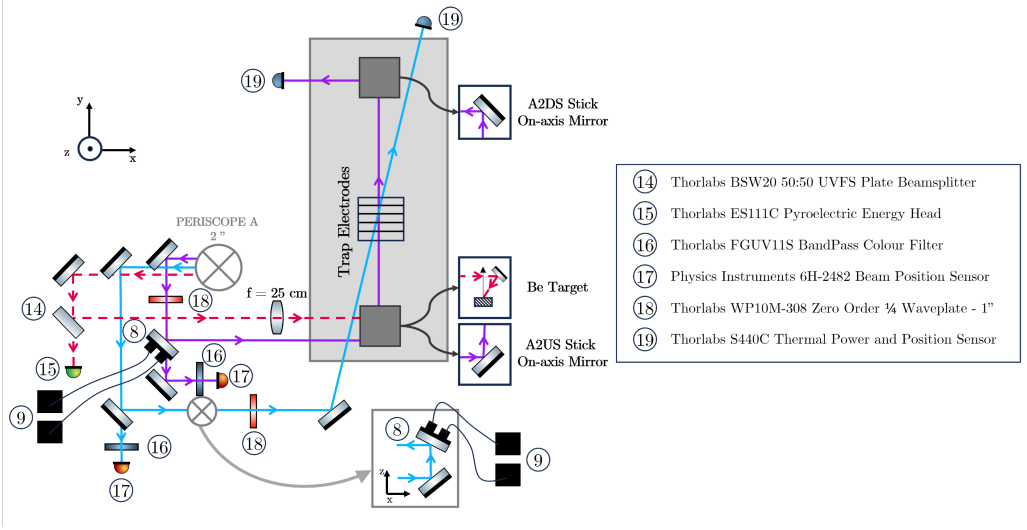

(14) Thorlabs BSW20 50:50 UVFS Plate Beamsplitter
(15) Thorlabs ES111C Pyroelectric Energy Head
(16) Thorlabs FGUV11S BandPass Colour Filter
(17) Physics Instruments 6H-2482 Beam Position Sensor
(18) Thorlabs WP10M-308 Zero Order ¼ Waveplate - 1”
(19) Thorlabs S440C Thermal Power and Position Sensor

(**b**) Optical setup in the experimental zone.

Figure 4.3: Laser beam path diagram for both cooling laser beams and the ablation pulse. The distance travelled between both ends of "PERISCOPE A" is about 5 m. The total distance travelled by the ablation pulse is $\sim$ 8 m, and by the cooling beams $\sim$ 12 m. Figure not to scale.

quantities such as the power and position of the cooling beams, the energy of the ablation pulses and the temperatures in several locations of the laser laboratory:

- ◇ ***alphabe01* computer:** where the main control system software is located. This software was written in LabVIEW 2020. This is the main interface, and every other part of the system can communicate with it. This computer is also responsible for controlling some hardware: the TOPTICA TA-FHG Pro laser (cooling laser) and the Quantel Ultra20 laser (ablation laser). It communicates with the cooling laser through Ethernet communication, and with the ablation through an RS232 connection.

- ◇ ***alphabe02* computer:** contains the software responsible for position stabilisation of the cooling beams. The Thorlabs piezo mirrors and detectors communicate with the computer via USB connections. The Physics Instruments devices communicate with the CompactRIO system through coaxial cables, and their variables are communicated to *alphabe02*.

- ◇ ***alphabe03* computer:** most of the hardware located in the laser laboratory is connected to this computer through USB connections. This computer allows for control of the motorised rotation stages, cooling pump for the cooling laser and temperature monitoring.

- ◇ **CompactRIO:** the shutters and other devices are connected to this system through coaxial cables. It allows for communication with the main ALPHA control system as well as live monitoring of several variables, such as the A2DS and A2US stick positions. It communicates with *alphabe01* through Ethernet communication, which then distributes the information received by the compact RIO to the other computers through state machines.

Fig. 4.4 shows a block diagram of the control system's main components. The arrows represent the communication between devices.

There are safety features incorporated into the main control system, which are referred to as *interlocks*. These are put in place to protect hardware from user error or system failures, such as power cuts on certain devices. For example, one of these interlocks prevents the on-axis cooling beam shutter from opening if the A2DS and A2US sticks are not in the "Laser mirror" positions, avoiding the UV beam from being sent towards fragile instruments such as MCPs.

Long-term power evolution of TA-FHG-Pro laser

The output FHG power was observed to decrease over time, primarily due to poor temperature control in our laser laboratory. Large fluctuations of up to 10 °C a day were regularly recorded, affecting the stability of the laser system. These large fluctuations occur due to the power cycling of equipment in the laser laboratory which produces a lot of heat. Both the internal laser cavity crystals and alignment mirrors are sensitive to temperature fluctuations, leading to a steady decrease in output FHG power over time. Fig. 4.5 shows the power evolution of the internally measured FHG output power over three months of operation. The blue data points are the average power measured over a 24-hour period. Gradual declines in power are apparent in periods without cavity interventions.

The laser control system allows for automatic realignment of the internal laser cavities using mirrors with servo motors which can be remotely controlled. Often, this alignment can increase

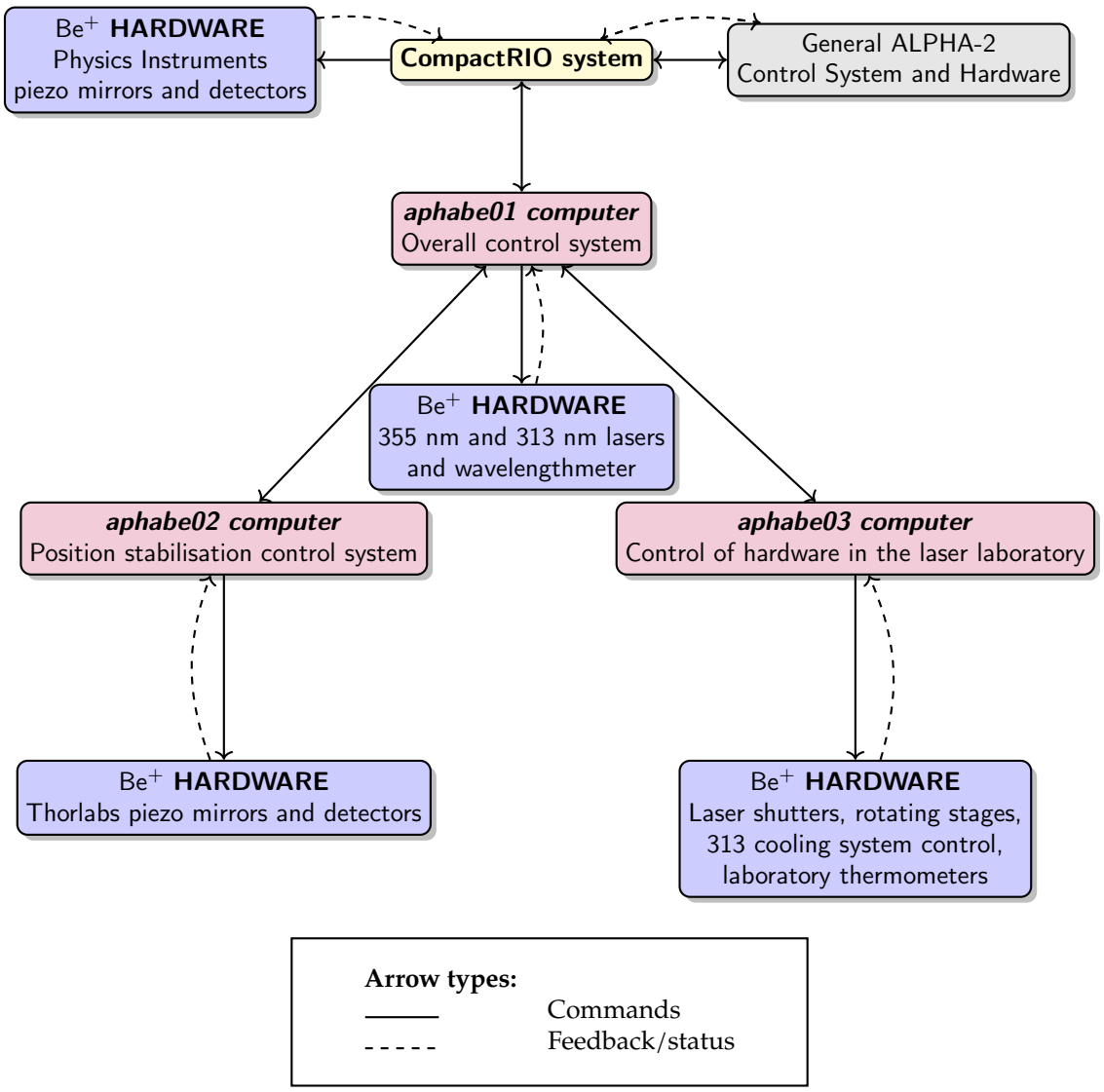

Figure 4.4: Block diagram of the Be^+ system control devices with ALPHA-2 colours. Solid arrows represent commands from computers to other computers or hardware, while dashed arrows indicate feedback/status signals from hardware back to computers. The Compact RIO communicates directly with the general ALPHA-2 hardware and control system, it also communicates with aphabe01, which distributes commands to the other control computers (aphabe02 and aphabe03). Each computer controls its assigned hardware, which in turn reports voltages, positions, or status back to the controlling computer.

the output power, but the permitted range of motion of the servo motors is too small to correct for large shifts.

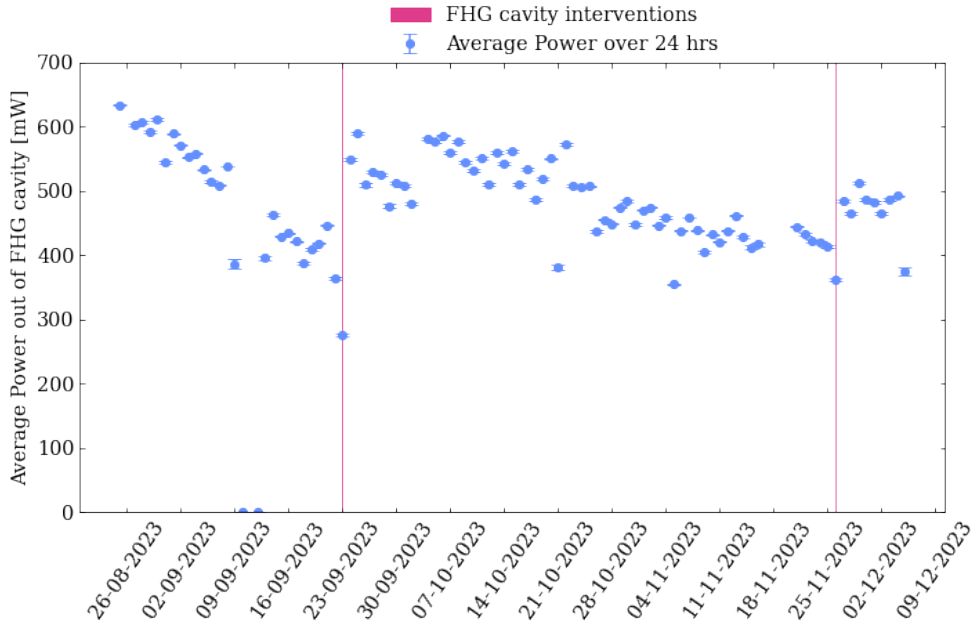

Figure 4.5: Long-term power evolution of 313 nm TA-FHG-Pro laser. The blue dots are the average power over 24-hr periods, the magenta lines correspond to days when FHG interventions occurred.

To address large power decreases, periodic manual cavity interventions are needed. During these interventions, an expert operator has to manually perform the alignment into the FHG cavity to optimise the cavity mode structure and output power. Fig. 4.5 marks the intervention dates in magenta lines, two interventions were necessary over three months of operation. In some cases, slight alignments to the second harmonic generation (SHG) cavity may also be needed. An FHG output power of over 400 mW is required to ensure that at least 100 mW reaches the Penning-Malmberg trap after accounting for optical system transmission losses. With 100 mW available for laser cooling, the corresponding intensity is 880 mW/cm^{-2}. Maintaining this power level is crucial for consistent experimental results.

Finally, these cavities have a limited operational lifetime. Eventually, the internal cavity will have to be replaced with a new cavity provided by TOPTICA. During the work presented in this thesis, this did not occur.

Automated Beam Steering and Stabilisation

The laser laboratory and the experimental area are in different rooms in the AD complex. Consequently, the total beam path length for the cooling lasers directed into ALPHA-2 is substantial, as discussed before. Not only is this laser path long, but it is also affected by numerous vibration sources that are beyond our control. These include vacuum pumps located near the laser box in the experimental area, stairs connected to the frame supporting this box, and general activity by experiment operators. These factors contribute to both fast misalignment of the laser beams and slow long-term drifts, which affect our ability to reproducibly prepare and cool Be^+ ions. Thus,

minimising the effect of the misalignment sources was imperative for the successful implementation of Be^+-assisted antihydrogen synthesis and trapping.

The initial iteration of the system during this project included 10 m fibre optic cables, which transported the 313 nm beams from the laser laboratory to the vacuum window outside the vacuum chamber. This set-up was not sustainable as small changes in the fibre position (sub-mm changes) could reduce the 313 nm transmission to 0 %, making this setup unsustainable. The transmission through these UV fibres was investigated at NIST [85] for short fibre lengths. In the ALPHA setup, a summer student I supervised, Sarah Price, studied the effect of temperature fluctuations and bend radius on the UV fibres [86], concluding that prolonged usage of these fibres in our current setup is not sustainable. Thus, the setup had to be reverted to free-space periscope laser delivery instead. All of the data in this thesis was collected with free-space delivered cooling beams. The ablation beam was always delivered through this method.

Fig. 4.6 demonstrates how the steering of both cooling beams evolved over seven hours of operation without any manual or automated beam steering. During this particular time period, the on-axis beam was not severely impacted by external vibrations or drifts. However, the off-axis beam drifted by about a millimetre in both the x and y axes. Typical sizes for the trapped Be^+ plasmas are about $200 - 500$ μm, thus the drift shown in Fig. 4.6 will change the interaction between the cooling beam and the ions.

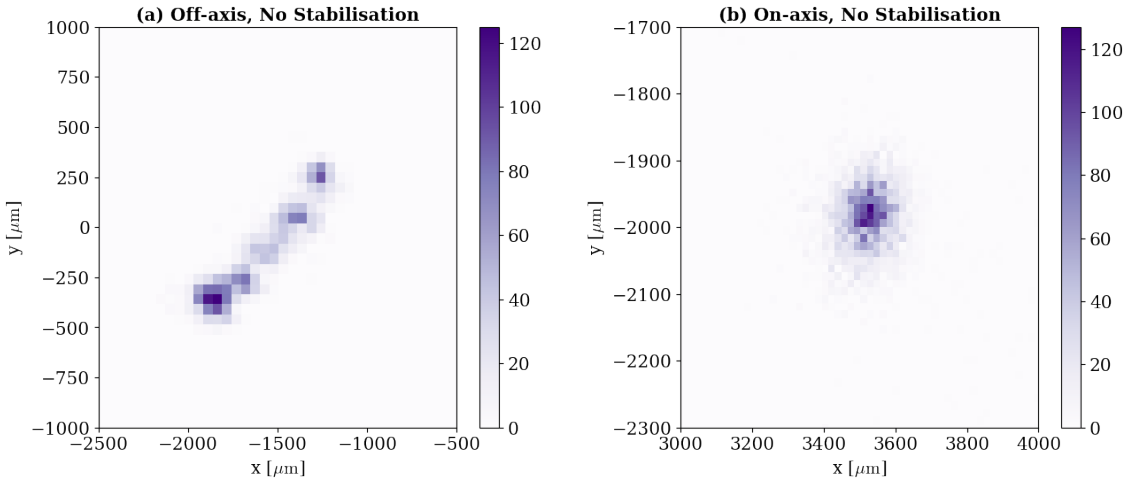

Figure 4.6: Beam steering through the trap with no automated beam stabilisation for both cooling beams. The x and y positions were measured after the ALPHA-2 trap during seven consecutive hours of operation for the off-axis (a) and on-axis (b) cooling beams. No manual or automated alignment was performed during the operational period.

Fig. 4.7 shows the x and y position distributions for both cooling beams without any beam stabilisation or steering, let's refer to this dataset and the *non-stabilised* set. The data was normalised to the highest value of each dataset, and a horizontal shift was applied to centre the peaks at $x = 0$ and $y = 0$, for easier comparison. A Gaussian function was fit to the data,

$$f(x) = Ae^{-\frac{(x-\mu)^2}{2\sigma^2}}, \tag{4.1.1}$$

where A is the amplitude of the data, in this case the magnitude of the number of counts per bin, μ is the average position of the distribution, and σ is the standard deviation of the data. The off-axis position distributions are not Gaussian due to the large drift. These locations were detected downstream of the trap, after the beams traversed it. These detectors are called on-axis D2 and off-axis Da and their physical location is shown in Fig. 4.8.

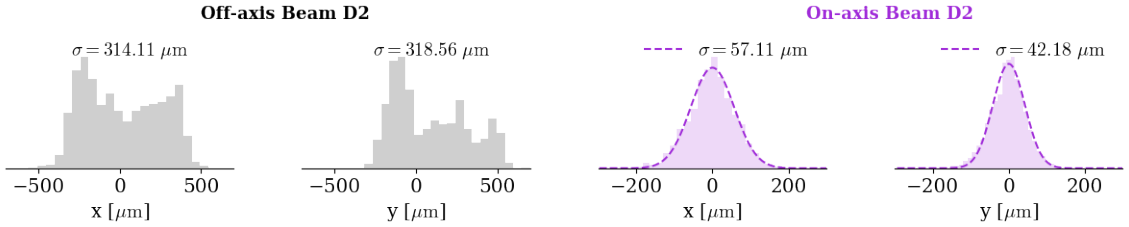

Figure 4.7: x and y position distributions for off-axis and on-axis cooling beams without beam stabilisation. A Gaussian function was fit to the data (dashed lines), and a standard deviation was extracted, σ for the on-axis data (purple). The off-axis data distribution is clearly not Gaussian, and the standard deviation represents the statistical spread of the positions.

The first implementation of the periscope system relied entirely on manual alignment to maintain beam steering through the trap. Daily realignments by an expert were required to maintain the target positions on the detectors, and sudden misalignments demanded immediate intervention. This high level of manual involvement was incompatible with a stable, reproducible system designed for extended operation. Thus, we aimed to develop a system that minimised the need for expert intervention and maximised beam stability through the whole beam path.

To achieve this, we replaced some of the "static" mirrors throughout the on and off-axis beam paths with piezo mirrors, which can be remotely controlled. Each piezo mirror needed a dedicated detector as a reference point. Fig. 4.8 is a simplified diagram of both cooling beam paths, where all the piezo/detector pairs have been highlighted for easier reading. M stands for mirror and D for detector, the steering of on-axis M1 will target a position in on-axis D1, and so on for the remaining piezo/detector pairs.

The beam stabilisation control system was written in LabVIEW 2020 and relies on the use of Proportional-Integral-Derivative (PID) controllers, also known as PID loops. This is a widely used feedback control mechanism wherein an input process variable is manipulated based on an error signal. The error signal is the difference between the measured process variable and a setpoint for the value of said variable. The PID loop looks to minimise this difference over time by adjusting a control variable. In the case of this beam stabilisation system, the process variables are the x and y positions measured by a detector, the setpoints are the target x and y positions and the control variables are the voltages applied to both axes of the corresponding piezo mirror. By continuously monitoring the detector's measurements and adjusting the voltages, the system self-regulates to maintain the beam at the target positions.

Fig. 4.9 shows a block diagram of the specific PID loop implemented in the beam stabilisation control system. Some things have to be taken into account during active beam stabilisation to ensure smooth operation. The detectors read some background and can detect a beam reflection rather than the main beam, thus by adding a condition that the power detected must be above a Power Threshold (PT), we ensure the loop feedbacks only on the main beam. Moreover, the piezo

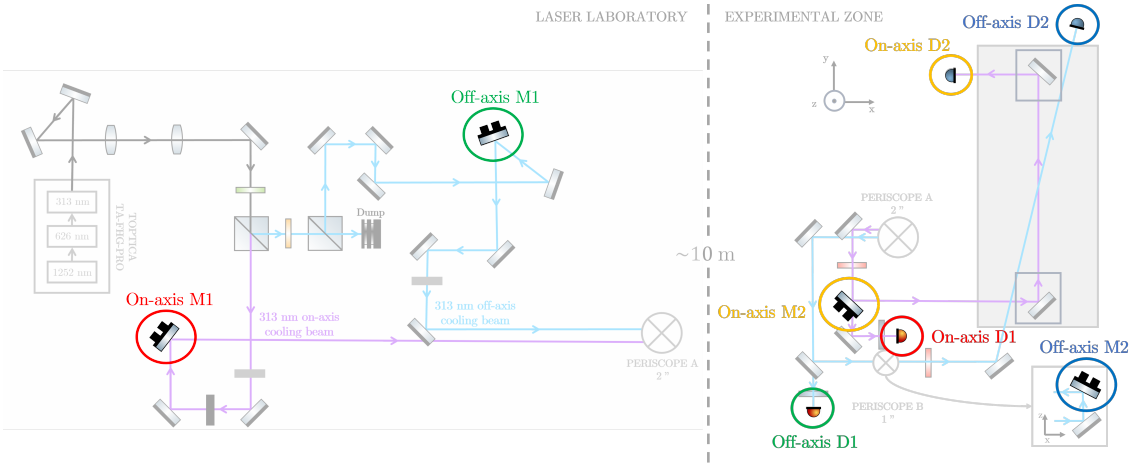

Figure 4.8: Simplified cooling beam paths highlighting beam steering hardware. The mirror highlighted in red (on-axis M1) is a Physics Instruments 2-axis Piezo Mirror controlled by a FP1099A Dual Piezo driver; all of the other highlighted mirrors are Thorlabs POLARIS-K1S2P 2-axis Piezo Mirror controlled by KPZ101 Thorlabs Controllers. Both D1 detectors are Physics Instruments 6H-2482 Beam Position Sensors and both D2 detectors are Thorlabs S440C Thermal Power and Position Sensors read by PM102. The mirrors and detectors are colour-coded such that the mirror highlighted in red stabilises the position in the detector highlighted in the same colour and so on for the remaining piezo/detector pairs.

mirrors have an operational range, the Thorlabs POLARIS-K1S2P 2-axis Piezo Mirror operates between 0 V and 150 V, and the Physics Instruments 2-axis Piezo Mirror allow voltage inputs between -10 V and 10 V. These limits must be a condition for the PID loop output to protect the hardware.

The Thorlabs hardware can be directly read and controlled through LabVIEW virtual instruments provided by the company. The mirror axis voltages and the detector variables are sent to *alphabe02* where the control system runs, simply through USB connections. The Physics Instruments hardware requires an intermediary step, the x and y positions, and power read by the detectors are amplified and sent to a CompactRIO system, which then shares these variables with the control system (written in LabVIEW). As for the Physics Instruments Piezo Mirrors, the voltages applied to each mirror axis are read and controlled by an FP1099A Dual Piezo driver, which communicates with the CompactRIO system. The signals are analogically sent to and from the CompactRIO through coaxial cables.

The performance of the real-time beam stabilisation system was notable. Whereas the beams previously required daily steering, after this upgrade, manual steering was only necessary due to exceptional circumstances, such as swapping broken optics. Fig. 4.10 shows the x and y position distributions for the off and on-axis beams with active beam stabilisation enable, the *stabilised set*, now for two different detectors each: D1 (upstream of the trap) and D2 (downstream of the trap). This data was taken over eight hours of operation. As in Fig. 4.7, the data was normalised to the highest value and shifted to peak at 0. There is no longer a relevant difference between the stability of the off-axis and on-axis beams. The D2 y position of the off-axis beam shows a secondary distribution centred about $+200\,\mu\mathrm{m}$ from the overall average position. This is likely because the inherent cause of the drift observed in Fig. 4.6 was not addressed, the laser beam still tends to drift, but the PID loop corrects this effect and quickly brings the beam back to the target position.

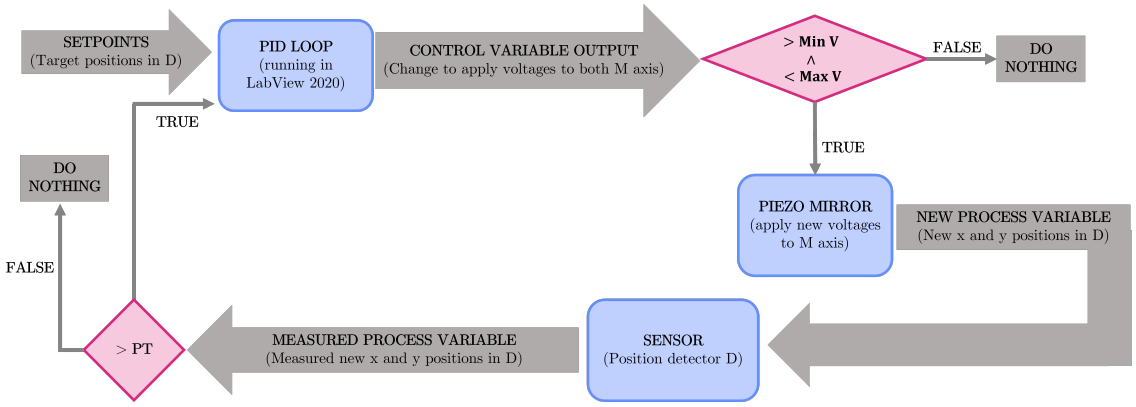

Figure 4.9: Block diagram of automated beam steering control system. The process variables (measured x and y positions) and the beam power are read by detector D. If the power of the beam is above a Power Threshold, PT, the process variables are sent to the PID loop, along with the setpoints (target x and y positions). The PID loop calculates the difference between the process variables and the setpoints and chooses a change of the control variables such that this difference is minimised. In this case, the control variables are the voltages applied to each axis of the piezo mirror M. Before requesting the voltages calculated by the PID loop, we must ensure they are within the piezo's operational range, that is, between the minimum (Min V) and maximum (Max V) voltages handled by the hardware. If the requested voltages are within this range, the changes are applied to M and the beam position is changed, thus creating new process variables, and the whole process begins again.

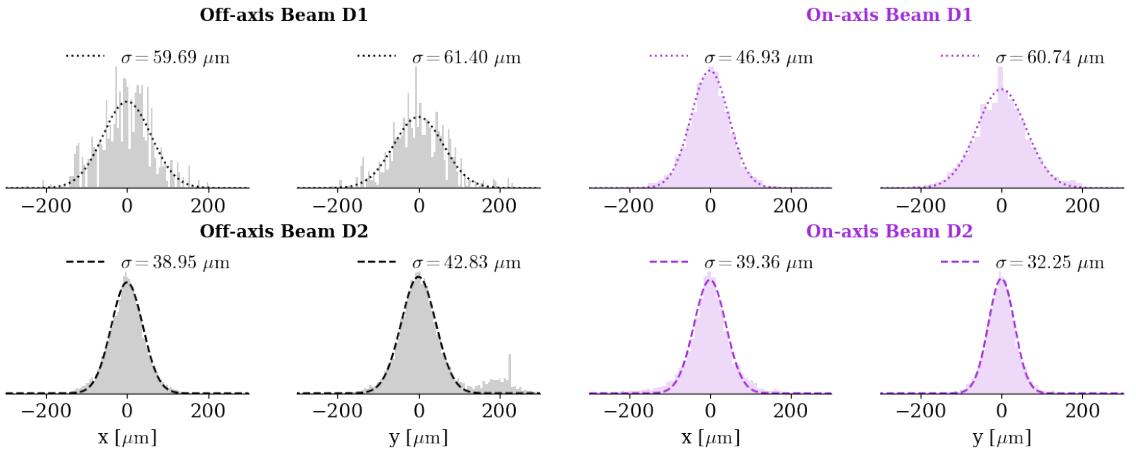

Figure 4.10: x and y position distributions for off-axis and on-axis cooling beams with beam stabilisation. A Gaussian function was fit to the data for detector 1 (dotted lines) and for detector 2 (dashed lines), and a standard deviation was extracted, σ.

Comparing the *non-stabilised* and *stabilised* sets, the stability of the off-axis beam has improved by almost a factor of 8 in both axes, and the on-axis stability has improved by a factor of about 1.5 for both axes. However, the benefits of this active control system are immeasurable and its implementation was one of the key upgrades which allowed Be^+-assisted antihydrogen synthesis and trapping to be as stable and reproducible as it showed to be.

313 nm Frequency Control and Chirping

A small pickoff beam out of the 626 nm cavity from the SHG cavity in the TA-FHG-Pro laser is coupled into an optical fibre and sent to a HighFinesse Wavelengthmeter WS Ultimate 2, a device referred to as the *wavemeter*. The wavemeter determines the wavelength of an incoming beam using an interferometer to measure the laser frequency against a stable frequency reference. We use a He-Ne laser as the reference for the wavemeter, which is often calibrated to the ULE cavity used to determine the frequency of the 243 nm system. This wavemeter has a precision of about $\pm$ 1 MHz.

To chirp the laser frequency, we can request a laser detuning and a chirp time in *alphabe01*. The control software will calculate a frequency ramp profile between the current measured laser detuning and the requested laser detuning setpoint. The laser frequency is changed by altering the piezo voltage in the grating of the diode laser. The calibration factor between the frequency out of the diode and the voltage applied to this piezo is the feed-forward factor (FFF). The software in *alphabe01* can then transform the list of frequency steps into a list of voltage steps, where each step is V_{FFF}. However, this calibration does not account for frequency drifts. To correct for this, another term is added to the voltage step list. After each step, the control software requests a wavelength reading from the wavemeter and calculates the difference between the requested frequency and the measured one. This information is then fed through a PID loop, which gives a correction to the voltage step applied, V_{PID}. The total voltage change is then $V_{total} = V_{\text{FFF}} + V_{\text{PID}}$. It is important to note that the only communication between the 313 nm laser and the wavemeter is the optical fibre cable used to measure the frequency. All the voltage step requests are performed by the control system software in *alphabe01*.

4.2 Laser Ablation of a Metal Beryllium Target

Pulsed Laser Ablation (PLA) can be defined as the ejection of ions, atoms or material clusters from a target by depositing energy on its surface via a laser pulse. For simplicity, I will refer to this process as laser ablation for the remainder of this thesis. The exact mechanism that dominates laser ablation is not entirely known: heating due to the deposited energy could cause the evaporation of the surface material, the energy of the pulse could cause breaking in structural bonds of the atoms in the target, or even mechanical defects and stress. Regardless, laser ablation is a widely used method for creating ion sources. While nanosecond laser ablation is sufficient for the needs of the ALPHA experiment, applications such as surface patterning benefit from pico- or femtosecond laser ablation, which allows for higher precision and resolution. An extensive study of laser ablation can be found in [87]

Other methods for creating ions are widely used, such as electron-beam bombardment of a

neutral atomic beam or, more recently, two-photon ionisation of an atomic Beryllium beam [88]. However, all known alternative methods require an atomic oven to produce the atomic Beryllium beam. Due to the geometry of the ALPHA apparatus, the ion source would need to be positioned within the vacuum volume near the trap, which is geometrically impossible. Moreover, it would lead to vacuum contamination, reducing the lifetime of particles in the trap and increasing heating rates. Therefore, these methods are incompatible with the experiments conducted at ALPHA. Furthermore, the ion plasma density for successful positron sympathetic cooling must be on the same order of magnitude as the positron density [26], at ALPHA, typical positron densities are within the range $10^7 - 10^8$ particles/cm^2, thus the ion yield required from the source must be in the order of a few hundred thousand to millions of ions per Be^+ bunch, which can be very easily achieved through laser ablation.

Over the last few decades, multiple facets of laser ablation have been thoroughly studied, including comparisons of various metal sources [89], studies of the energy distribution and dynamics of the ablated ion plume [89–92], investigations into the effects of different wavelengths [93] and the feasibility and development of various ion sources for ion trapping experiments using this laser ablation [94–99].

From the extensive body of literature on laser ablation, certain key conclusions can be drawn regarding this process. The ablation effectiveness and ion bunch parameters are closely related to the fluence of the pulse, which can be defined as the energy deposited in the target per surface area. Ions will only be ablated above a minimum fluence, often called the *fluence threshold*. The fluence threshold increases with the charge of the desired ion, the smallest threshold is for Be^+ followed by Be^{2+}, and so on. Since the only ion of interest for this work is Be^+, it is important to maintain the fluence of the pulse between the thresholds for ablating Be^+ and Be^{2+}. The kinetic energy of the ions is also dependent on the energy deposited, the higher the fluence, the higher the kinetic energy. In general, we want to keep the forward kinetic energy below 140 V, given that is the highest potential barrier in the current trap configuration. In addition, if we keep the fluence near the threshold, a Maxwell-Boltzmann distribution explains the energy distribution of the Be^+ bunch. Finally, the ion production is not isotropic and has a clear peak in the direction normal to the surface of the target, thus, this is the most efficient direction for ion extraction. To summarise the most important points,

- ◇ Production of ions only begins above a certain fluence, this is called the *fluence threshold*;
- ◇ The fluence threshold increases for more highly charged ions;
- ◇ The kinetic energy distribution of ions produced close to the fluence threshold is well explained by a Maxwell-Boltzmann distribution,
- ◇ Higher fluence leads to higher kinetic energy,
- ◇ The ion yield is higher in the direction normal to the source surface.

In his thesis, Dr. M. Sameed thoroughly investigated the feasibility of utilising laser-ablated Be^+ as an ion source in the ALPHA cryogenic traps for antihydrogen formation [27]. During his study, he measured the fluence thresholds for Be^+ and Be^{2+}, which can be found in Tab. 4.1. The ALPHA-2 operational range is then between 15 - 26 μJ to avoid the presence of Be^{2+} in the trap.

Ion	Fluence Threshold [Jcm^{-2}]	Minimum Pulse Energy [μJ]
Be^+	2.0	15.0
Be^{2+}	3.5	26.1

Table 4.1: Be^+ and Be^{2+} ablation fluence thresholds and minimum pulse energies for 15.4 μm pulse waist and 6 ns pulse duration. Fluence threshold values obtained from [27].

In summary, laser ablation has been widely used as a source for ions and is experimentally and spatially compatible with Be^+ production at ALPHA. It minimises vacuum contamination, provides high ion yields and densities, and strict time control of Be^+ bunch generation.

ALPHA-2 Be^+ set up and ion generation

The laser used to generate the ablation pulse is a Quantel Ultra 20, a 1064 nm pulsed Nd:YAG with a frequency-tripling stage to obtain $\lambda = 355$ nm laser pulses. This frequency photoionises a large amount Be atoms during the ablation process, thus voiding the need for an extra laser beam to create the Be^+ bunch. The laser outputs 6 ns pulses of up to 4 mJ, the beam directly after the laser aperture has a diameter of 1 mm and 1 mrad divergence.

The laser is located in a laser laboratory, the ablation pulse reaches the experimental zone through periscope delivery. Fig. 4.3 shows the ablation pulse's beam path in red and its optical and mechanical components. Periscope A has a length of about 5 m. In general, 4 mJ is an extreme amount of energy to send towards the Beryllium target. To control the energy of the pulses we use a half-waveplate ($\lambda/2$-waveplate) (instrument (11)) followed by a Polarisation Beam Splitter (PBS), (instrument (12)). The angle of the half-waveplate can be remotely controlled using a high-precision rotation stage (instrument (2), which is controlled and powered by instrument (13)). This angle influences the polarisation of the light and changes the transmitted vs reflected ratio in the PBS, thus setting the energy sent to the experimental zone. The final mirror before the vacuum chamber is a $50:50$ beam splitter (instrument (14)), which directs part of the beam to an energy detector (instrument (17)) to monitor pulse energy, with the remainder of the beam reflected toward the target.

To achieve fluences above the Be^+ fluence threshold (2 J/cm^2) the optical setup was designed to yield a 20 μm pulse diameter at the source. Measuring the beam size at the source is severely complicated by the location of the Beryllium target inside the vacuum chamber. To estimate the spot size, the energy of the pulse was lowered until no Be^+ ions were ablated. The minimum pulse energy yielding ions for the current ALPHA-2 setup was measured to be 15 μJ, thus, the pulse diameter can be inferred to be 15.4 μm at the Beryllium target. Note that the pulse energy was measured before the vacuum window, therefore, this measurement estimates the maximum pulse diameter. The window is coated for 355 nm light, which should minimise the energy loss through it.

Plot (a) in Fig. 4.11 shows the energy reflected as a function of the energy transmitted by the beam splitter mirror, which was used to calibrate the measured beam energy and estimate the pulse energy deposited at the source. The calibration factor is 0.61. Energy monitoring provides a useful diagnostic tool for interpreting failed attempts at plasma preparation. For example, plot

(b) shows 2329 consecutive ablation shots over nine days of operation. If the system is functioning as expected, the energy at the source will depend only on the half-waveplate angle; therefore, when there are sudden drops in beam energy, as in the $20 - 20.5$ degree region of plot (b), this indicates there is a problem with the beam path alignment or with the ablation laser itself. In this instance, the drop in energy was caused by a misalignment of one of the periscope mirrors. Plot (b) also shows that the beam energy fluctuates significantly even when the half-waveplate angle is unchanged, with an average variance of approximately $11\,\%$. Flashlamp-pumped lasers often have instabilities in both energy output and beam quality due to factors such as thermal lensing effects, electrical instabilities or degradation of the flashlamp over time. This contributes to large shot-to-shot variations, which, along with the unpredictable nature of the ablation process, causes an extremely large variation in the number of Be^+ ions produced, even if the experimental conditions are seemingly unchanged. Plot (c) in Fig. 4.11 illustrates 100 consecutive Be^+ ablation attempts for two energy ranges, $18 - 22$ μJ (just above the Be^+ fluence threshold), and $27 - 31$ μJ. The number of ablated ions is varies by up to an order of magnitude for both energy ranges.

In conclusion, while many factors can be controlled, such as beam size, pulse length and pulse energy, due to the unknown interactions during the ablation process and instabilities in the light generation and beam path, it remains extremely challenging, if not impossible, to ablate reproducible amounts of ions with each ablation pulse.

4.3 Be^+ trapping

After producing the ions, the next step is to trap them in our Penning-Malmberg trap. The source is located on the upstream side of the trap, thus, when ablated, the ions will travel in the same direction as the antiprotons. An electric potential wall is raised on E07, to stop the ions from being lost downstream, followed quickly by raising a potential on a gate electrode, E01 [1]. The catching process is depicted in Fig. 4.12, the time between the ablation pulse and the raising of the potential in E01 is called the *gate time*. This is a crucial parameter to tune to ensure high Be^+ catching efficiency.

A scan of the gate time was performed for two different energy ranges: 18 - 22 μJ (just above Be^+ fluence threshold) and 27 - 31 μJ (just above Be^{2+} fluence threshold). The ideal gate time should differ for the two ranges, since higher fluence results in higher forward kinetic energy. If the particles have a higher speed, the gate must be raised sooner after the ablation pulse. This is exactly the result found in Fig. 4.13: the magenta data points, corresponding to the lower energy range, maximise ion capture at 70 μs gate time; and the blue data points, corresponding to the higher energy range, maximise ion capture at around 50 μs. This scan was performed with all the Neutral Trap magnets energised to mimic antihydrogen synthesis conditions as closely as possible.

An interesting feature of the data displayed in Fig. 4.13, is that the blue data points show an extended tail, with a much higher gate time range where particles are caught. This is indicative of more than one species in the plasma, likely Be^{2+}. The two species will have two different energy distributions and thus require different gate times for each population. Finer scans are needed to

[1] Gate electrodes allow for extremely potential changes, the gate is charged before the ablation pulse is requested, when trapping is wanted, this is connected to the electrode and the potential raised.

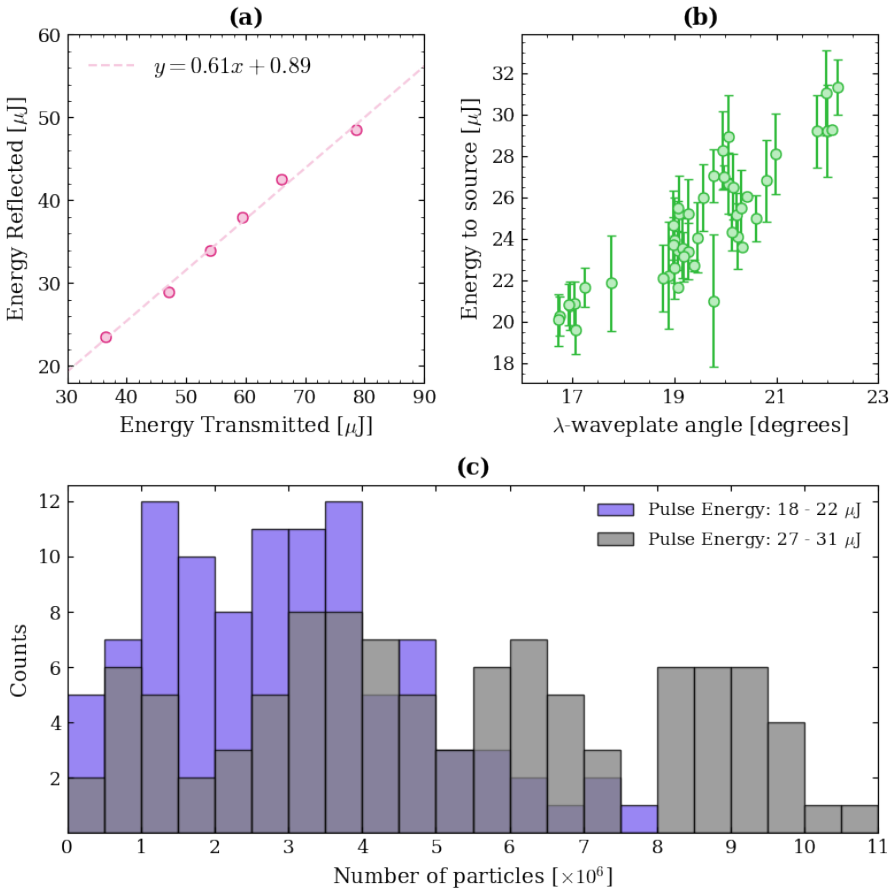

Figure 4.11: Ablation pulse energy characterisation and performance. (**a**) 50:50 beam splitter calibration, 61% of the beam is transmitted into the energy meter for energy monitoring, and 39% is reflected towards the Be^+ target for ablation. (**b**) Energy towards the source as a function of the $\lambda/2$-waveplate angle. This data comprises 2329 consecutive shots over nine days of operation. The energy dip around 20°-20.5 ° was due to a misalignment of the beam. The variance in beam energy is 11%. (**c**) Distribution of the number of ablated Be^+ ions for two different energy ranges. The number of particles can vary within an order of magnitude for pulses within the same range.

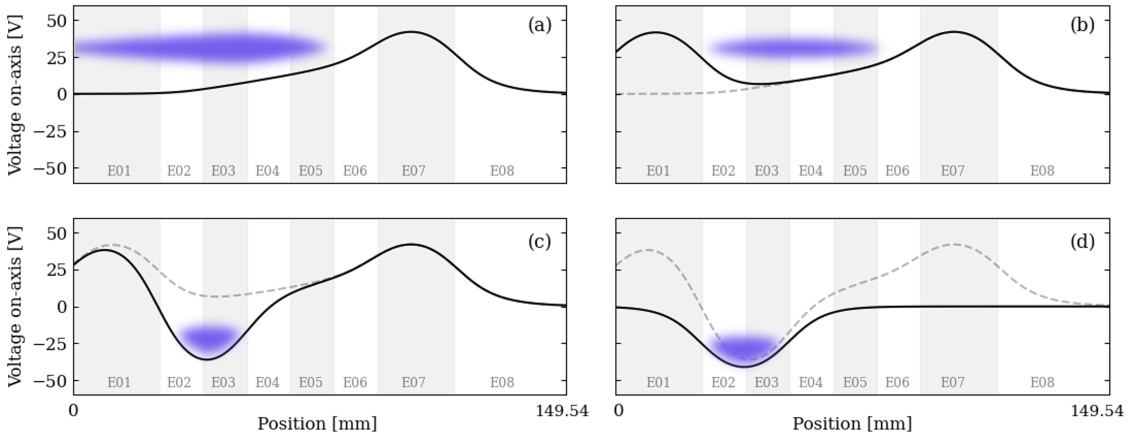

Figure 4.12: Be^+ trapping potentials. (a) Raised wall to trap the ion bunch on the right side. (b) E01 gate electrode is quickly raised to trap the ions on the left side. (c) The potential well in E02 and E03 is made deeper to direct the plasma towards that region. (d) The ions are stably trapped. The full and dashed lines are the calculated on-axis potentials, and the purple clouds are illustrations of the ion behaviour during this process.

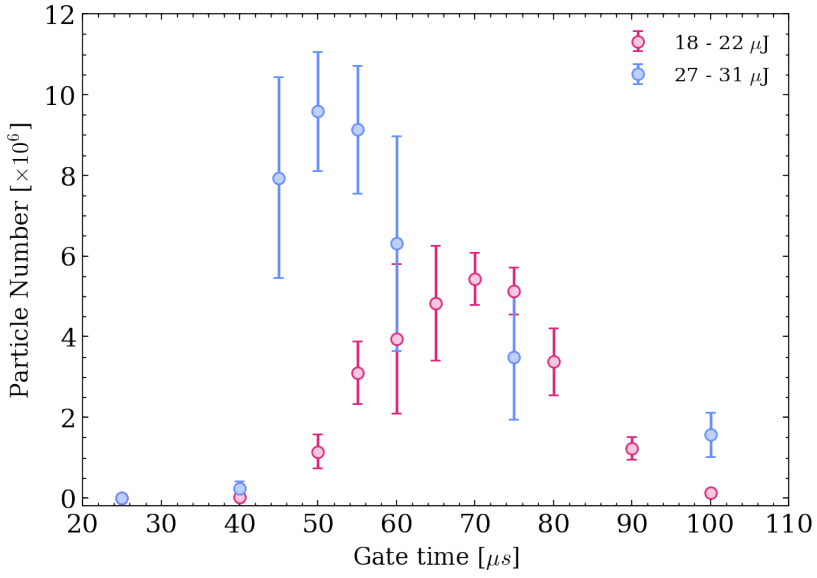

Figure 4.13: Be^+ trapping gate timing scan. Two different energy ranges are displayed: in magenta, 18 to 22 μJ and in blue, 27 to 31 μJ.

truly understand how capture differs between higher charge Be ions. However, this is beyond the scope of this work, as we are only interested in the capture and manipulation of Be^+ ions. To avoid trapping other species, it is important to remain in the energy range $18 - 22$ μJ, where the ideal gate time was found to be 70 μs. These values will change if the beam alignment is significantly changed, as a difference in the angle of the beam can result in a difference in spot size at the source.

Additionally, the Gaussian-like profile of the signal for this energy range indicates the trapping efficiency is not $100\,\%$ since this was the case, the signal would show a flat top profile, where a range of gate times allows for the capture of all the ablated particles. To resolve this, we would need to increase the length of the trapping region. Since we can already trap millions of ions, and previous experimental tests have indicated we only need less than a million ions to cool our available range of positron numbers [30], we continued developing the Be^+ plasma preparation with the blocking potential in E07 as described above.

Directly after ablation and trapping, the plasmas are measured to be at thousands of Kelvin. Before any further preparations can occur, this temperature needs to be significantly reduced.

4.3.1 Particle number monitoring: the Half-Dump technique

To diagnose whether the stabilisation technique was successful, it is necessary to image the plasma, a destructive process as discussed in Section 3.2. The cooling of positrons is extremely sensitive to ion number, [30] for a Be^+/e^+ mixture in a Penning-Malmberg trap; the sensitivity to ion number is even more pronounced in the presence of an octupole field as discussed in detail in Chapter 5. To check the performance of the number stabilisation technique (described in detail later in this chapter) and monitor the number of ions used for sympathetic cooling, we developed a technique that divides the plasma in half, only imaging one of the halves, leaving the remainder of the plasma to be used for sympathetic cooling of positrons. This technique was aptly named the Half-Dump, HD.

The Half-Dump is a relatively simple process: spread the plasma across an odd number of electrodes, and lift the middle electrode. Fig. 4.14 shows a 3-electrode HD, the plasma is spread over E04-E06 by applying -140 V to these electrodes, followed by a rise of E05 to $+50$ V, leaving half of the initial plasma in each side well (E04 and E06) between the HD inner wall (E05).

When developing this technique, two criteria must be fulfilled:

1. Stable $x - y$ position from shot-to-shot, ensuring the HD does not induce any off-axis plasma motion;

2. The number of ions left in each side well is equal. Ideally, we aim for a 50/50 cut for a true HD.

Fig. 4.15 shows the three HD parameters that were most relevant to achieve the criteria above. When performing this study, the plasma was trapped, the SDREVC-like technique was applied to set a constant number of particles (see Section 4.5 for details), the HD was performed, and the plasmas were sequentially imaged on the A2DS MCP. The first half we call the Half-Dump image, and the second half we call the Final-Dump image. The data displayed in this figure consisted of $10 - 20$ repetitions of each parameter combination; the HD must be reproducible since we will use it for diagnosing Be^+ number stability.

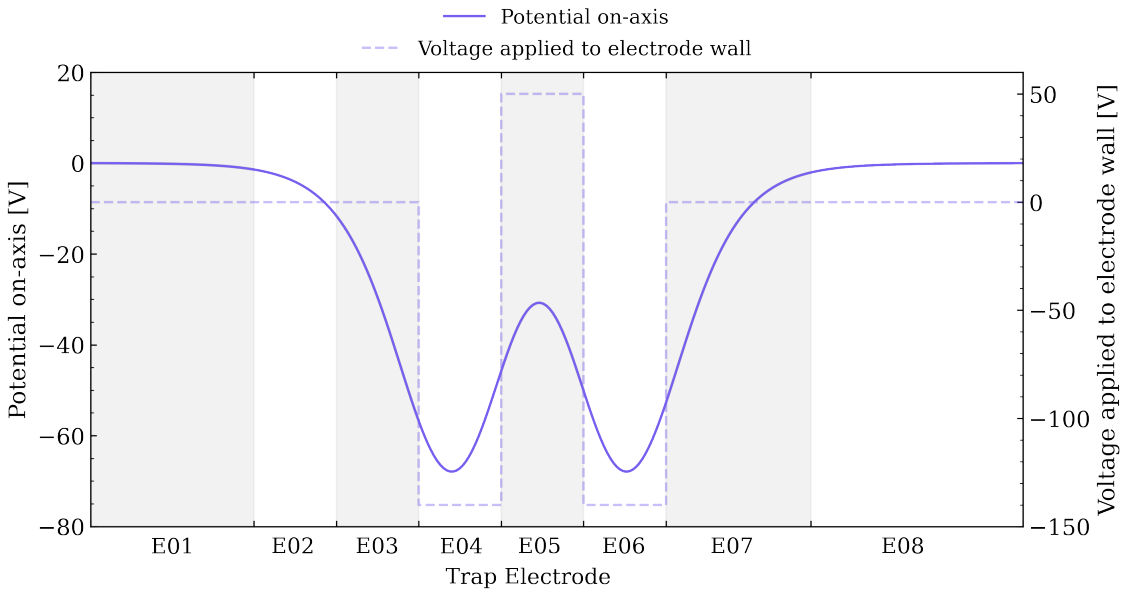

Figure 4.14: Be^+ half dump potential in the left normal trap. 3-electrode half dump: the dashed line shows the voltage applied to the electrode wall; the solid line is the on-axis potential that the ions will experience.

- **Number of electrodes:** a large spread of the Be^+ plasma causes large off-axis plasma motion in both the x and y directions. This was clearly observed in the 5-electrode HD dataset in plot (a). Reducing the number of electrodes to a 3-electrode HD diminished the off-axis motion by 28% in the x direction and by 50% in the y direction. However, there is still a significant displacement caused by the cut.

- **Well-depth:** this parameter was not thoroughly studied, but the deeper side wells show a slight reduction in off-axis motion in the y direction. In the conditions of our Penning-Malmberg trap, deeper electrostatic wells provide better confinement.

- **Cut duration:** longer cut durations minimise the off-axis displacement of the plasma as can be seen in plot (c) of Fig. 4.15. A 300 ms cut shows only a $0.6\,\%$ variation in the x direction and $0.3\,\%$ in the y direction. A slow cut ensures that the plasma responds slowly enough to the potential change, allowing its internal motions to adjust continuously to the changing potential without exciting extra oscillations or heating.

Fig. 4.16 summarises the cut duration time scan for both the $x - y$ position (a) and the Half-Dump image Be^+ number compared to the Final-Dump image Be^+ number (b). Longer cut duration times minimise both the induced off-axis motion and the number variation, the longest studied cut time was 300 ms since the number variation observed with this cut is smaller than long-term SDREVC-like stability. The final HD version was a 3-electrode HD well, -140 V applied to the side wells, 300 ms cut duration; this resulted in less than a $1\,\%$ variation in $x - y$ position and a $2.5\,\%$ variation in ion number. The cut is about 48/52, leaving slightly more particles in the Final-Dump half; however, this ratio is constant shot-to-shot, which allows us to calibrate the HD number and obtain the number of Be^+ ions remaining in the trap for sympathetic cooling.

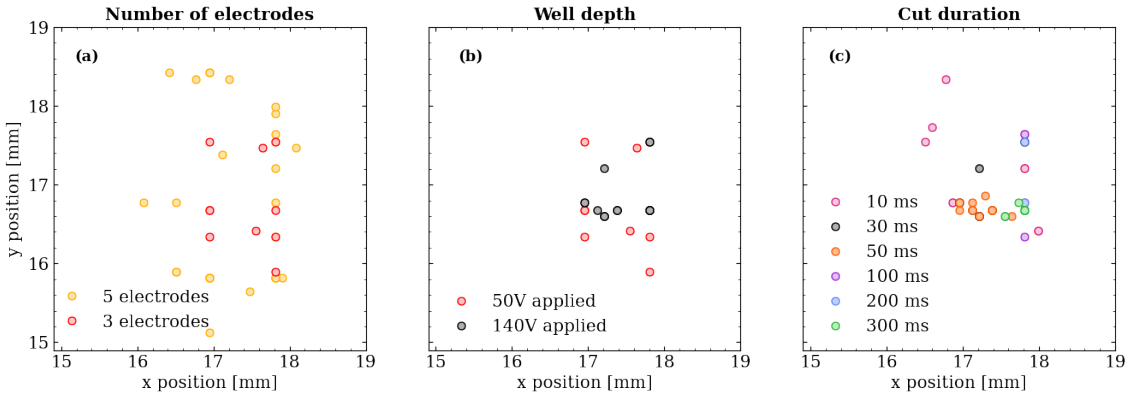

Figure 4.15: Be^+ half dump parameter scan to optimise position stability. Study of $x-y$ position stability by varying the number of electrodes utilised for the half dump (**a**); the well depth of both side wells (**b**); and the rise time of the inner wall, cut duration (**c**). Note that clusters with the same colour across all three plots correspond to the same dataset.

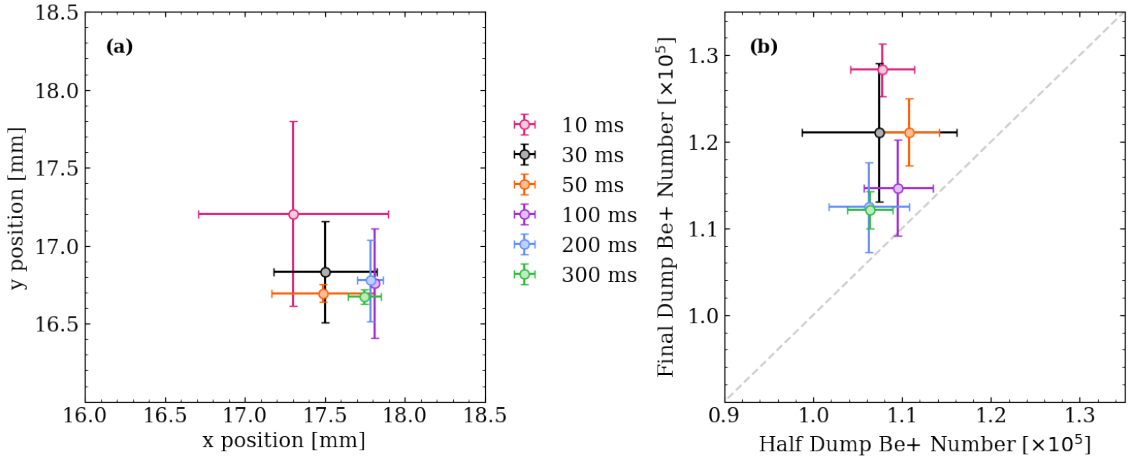

Figure 4.16: Be^+ half dump cut duration scan. (**a**) Average x and y positions for different cut durations. (**b**) Average final and half dump Be^+ numbers for different cut duration times. The dashed grey line demonstrates a perfect 50/50 half-dump process. The error bars correspond to the standard deviation in both plots.

This method was used as a diagnostic during the development of various techniques and during long antihydrogen production periods.

4.4 Be^+ laser cooling implementation and tuning

The main upgrade to the laser cooling setup, during the work presented here, was the implementation of an on-axis cooling beam. There are a few challenges to laser cooling with this beam: the only available fluorescence has a solid angle of 10^{-6} steradians and a limited axial range as it is located in an off-axis laser port; aligning this beam is difficult due to the length of the Penning-Malmberg trap over which it must overlap with the trap axis; and plasma heating complicates temperature diagnostics, as the diagnostic stations must move into place, leaving the ions without cooling for about 15 s.

This section will detail how successful on-axis laser cooling was implemented, also discussing general aspects of laser cooling, including the off-axis beam.

4.4.1 Be^+ Fluorescence Detection

There are no devices inside the vacuum chamber near the trap capable of detecting photons, which severely limits our ability to measure fluorescence from Be^+ ions interacting with the cooling laser. To perform these measurements, we use a *Hamamatsu* C8855-01 counting unit connected to a photomultiplier tube (PMT), mounted outside the vacuum chamber. We refer to this device as the *Photon Counter*. The detector is placed flush to a vacuum window downstream of the ALPHA-2 trap, about 1.6 m from the trap centre (electrode E14). With a 2.4 °angle displacement in the z-axis, the total solid angle of this detector is around 10^{-6} steradians.

Fig. 4.17 shows the range of detection of the Photon Counter in ALPHA-2. Millions of Be^+ ions were trapped and cooled in E14/E15 and then sequentially moved to other trap electrodes. The plasma was laser-cooled at each location using the on-axis cooling beam for 10 s, and the fluorescence signal was recorded. Since the ion preparation happened in the centre of the trap, to scan all the electrodes of the antihydrogen synthesis trap, two samples were used: one sample was shuffled from E14/E15 to E22/E23 (magenta triangles in Fig. 4.17, and another sample was shuffled to E03/E04 (black circles in Fig. 4.17). The data was then background-subtracted and normalised for each sample (the number of ions varied between the two samples, which influences the number of photons emitted during laser cooling). Fluorescence is detected between E09 and E20, almost the entirety of the antihydrogen synthesis trap, but it is more pronounced between E11 and E18. This allows us to study Be^+ laser cooling in the antihydrogen production region, but not under either segmented electrode. This study was performed after the on-axis cooling laser beam alignment to ensure the drop in fluorescence is not due to a drop in cooling power from beam misalignment.

The background detected while using the on-axis cooling beam is over an order of magnitude larger than when using the off-axis cooling beam. In general, there is less scatter from the off-axis beam as this beam does not have to reflect from any mirrors inside the vacuum volume. The higher background from the on-axis beam complicates potential fluorescence-dependent measurements.

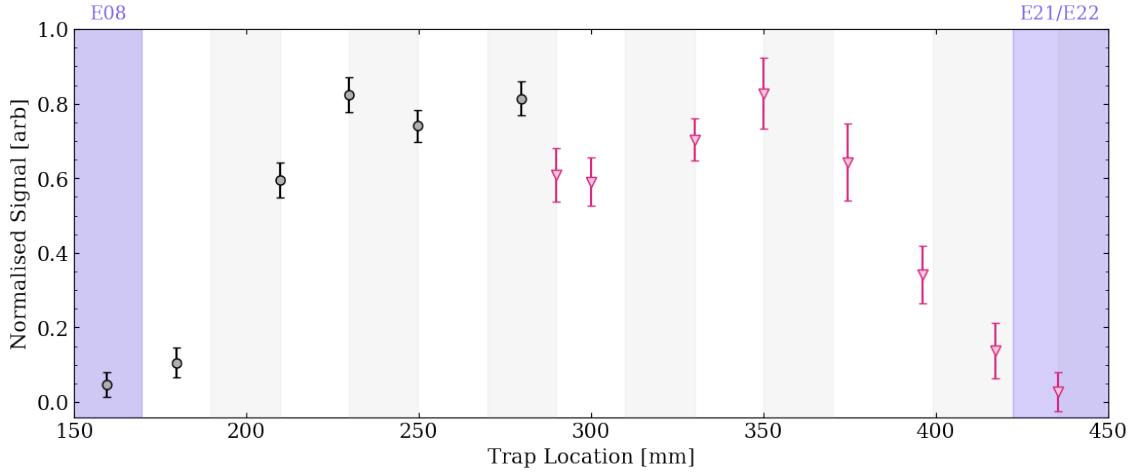

Figure 4.17: Photon counter detection range in ALPHA-2. Millions of Be^+ ions were shuffled through the trap electrodes and laser cooled for 10 s at each location. The black circles and magenta triangles represent two different Be^+ plasma samples. The data points are located at the centre of each plasma location. The data was individually background-subtracted and normalised to the highest count for each sample. In blue are the electrodes where the signal is no longer above the laser background. The photon counter can detect fluorescence between E09 and E20. Shaded in grey and white are the trap electrodes, starting at E08 and ending at E22.

Even with the lower background from the off-axis cooling beam, observing a significant signal above background can only be achieved in the current setup when more than 1 million ions are in the trap. This does not allow for useful diagnostics while utilising Be^+ ions for e^+ sympathetic cooling. However, fluorescence can still be used for qualitative studies or scans which do not require low particle numbers.

4.4.2 Quarter waveplate, ($\lambda/4$ waveplate), angle

The cooling transition of interest requires σ^+-polarised light. To achieve this, we need a quarter-waveplate ($\lambda/4$-waveplate) before the cooling beams enter the vacuum chamber. Since the beams are split using a PBS, two $\lambda/4$-waveplates are required, one for each cooling beam. Upon installation, a scan of the angle of the waveplates is necessary to determine the most beneficial angle for laser cooling.

Accurate laser polarisation is critical for developing further techniques, such as controlling the particle number. At this stage, the fluorescence signal is the most useful diagnostic as it is straightforward to interpret: higher counts indicate more efficient laser cooling. The protocol for this scan was as follows:

- **Step 1:** Ablate and trap Be^+ ions and move them to the centre of the trap (E14/E15);
- **Step 2:** Open the shutter of the cooling laser, ensuring the laser is far detuned from resonance (-4 GHz for this specific scan);
- **Step 3:** Chirp the laser frequency to the frequency where fluorescence is highest (-230 MHz, this value was determined before beginning the scan by chirping the laser past resonance and extrapolating where the fluorescence counts are highest);

During this scan, there was no control of the ion number. To reduce discrepancies in fluorescence counts induced by differing ion numbers, the measurements at each angle were repeated three times and averaged. Fig. 4.18 shows the maximum photon counter signal as a function of the angle of the $\lambda/4$-waveplate for the off-axis cooling beam. The signal plotted in Fig. 4.18 was background-subtracted (the background is taken as the signal in the photon counter when the laser frequency was far detuned). Interestingly, the counts never drop to 0 kcps, indicating some level of laser cooling occurs for all the probed angles. This effect is not entirely understood, it could be due to damage to the vacuum windows through which the cooling beam enters the vacuum chamber, or irregularities on the surface of the waveplate, resulting in impure polarisation. Investigating these effects further would involve scanning different beam paths across the waveplate and window. However, this investigation falls outside the scope of this work. The ideal angle for the off-axis beam was measured to be $137\,°$. The light exiting the laser is vertically polarised, and the magnetic field is antiparallel to the laser propagation direction. In these conditions, to obtain σ^+ polarised light along the propagation axis, we expect a $\lambda/4$- waveplate angle of $-45\,°$. The experimentally measured ideal angle of $137\,°$ is nearly equivalent to this value, confirming the expected orientation.

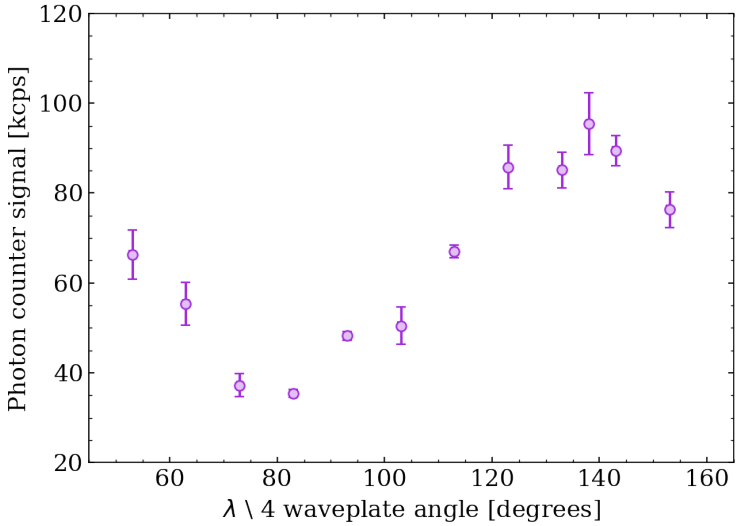

Figure 4.18: Photon counter signal as a function of the angle of the $\lambda/4$- waveplate setting polarisation of the off-axis cooling beam. Each data point corresponds to a new Be^+ sample, the error bars are the standard deviation. Three samples at each angle were taken. The data was background subtracted.

A similar procedure was performed for the on-axis beam. This was, however, complicated by the higher background rate for this cooling beam. Larger ion numbers are necessary to obtain a significant signal-to-noise ratio.

4.4.3 Four plasma steering

One of the biggest challenges of implementing reliable on-axis cooling is minimising the deviation between the beam path and the trap axis. This is extremely difficult due to the geometry of the

system and the long distance the beam must travel with little to no visibility of its path. In addition, many parameters cannot be changed when performing the beam alignment, such as the angle of the mirrors in the diagnostic stations or the size of the cryostat's internal apertures and beam pipe diameters. The radius of the normal trap electrodes is $\sim$ 15 mm. However, at each end of the trap, beam pipes with a 6 mm radius significantly constrain the laser beam's range of movement. The initial on-axis beam alignment consisted of carefully steering the beam until it passed through the centre of both pipes. The downstream pipe is physically attached to the trap mount, ensuring alignment with the trap centre. In contrast, the upstream pipe is not connected to the mount, introducing a possible misalignment with the trap centre. While the system's geometry does not allow for large misalignments, the plasma radii inside the trap are on the order of millimetres, as a result, even a small angular deviation (on the scale of a few tenths of a degree) could cause the beam to miss the plasma within certain regions of the trap.

The best way to check whether or not the laser overlaps with the ions is to try to laser cool them. The initial laser beam alignment described above was sufficient to see fluorescence from ions trapped at the centre of the Penning-Malmberg trap (E14/E15) and set the correct light polarisation. A logical next step is to check the cooling for plasmas trapped in different electrodes. To avoid temperature discrepancies due to variations in ion number, we developed a technique which allows for simultaneous diagnostics at various trap locations.

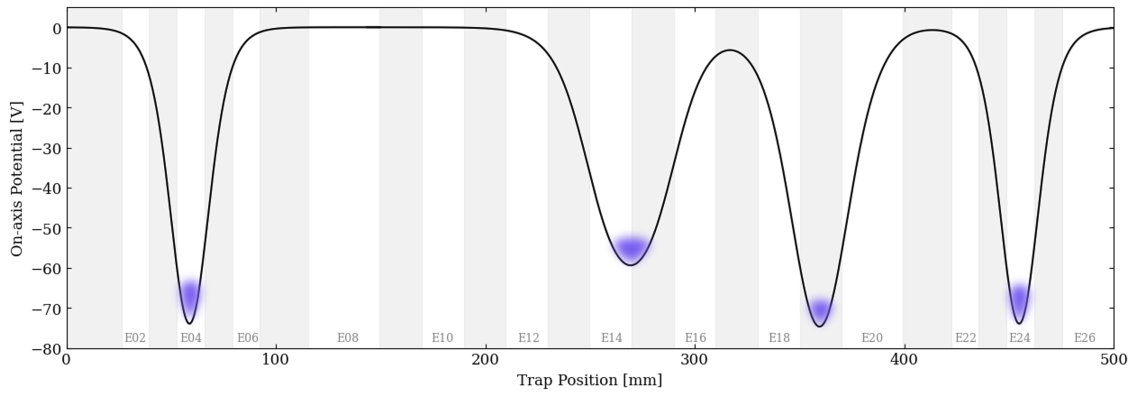

Figure 4.19: On-axis electric potentials for four plasma steering. An initial Be^+ plasma was split into four identical plasmas which were then shuffled to four relevant trap locations: E04 and E24 which are normal electrodes near both rotating wall electrodes in the trap; E14/E15, thin electrodes, this electrode pair is located at the centre of the trap, near the antihydrogen production region; and E19, a thin electrode used to image in a different part of the antihydrogen synthesis trap, for comparison purposes. The purple clouds are illustrations of the Be^+ plasmas.

We loaded a Be^+ plasma and divided it into four identical plasmas, which were moved to various locations across the trap. We then simultaneously laser-cooled the four plasmas with the on-axis cooling beam, -1 GHz for 60 seconds with a beam power of 100 mW. After cooling, either the radial profile or the final temperatures of each plasma were measured. Fig. 4.19 shows the on-axis potential applied during this technique, the four positions were chosen to cover a wide range of the trap but also to investigate the laser cooling efficiency at relevant trap locations: E04 and E24 are normal trap electrodes near the segmented electrodes (E03 and E25), these are two possible positions for Be^+ plasma preparation to occur; E14/E15 (antihydrogen synthesis trap electrodes) is

the centre of the trap near the antihydrogen production region; finally E19 is another antihydrogen synthesis trap electrode where we can almost replicate the well shape from the points in the normal trap. We called this technique *four plasma steering*.

The idea of this technique is to compare the temperatures of the plasma across the trap and use this information to inform beam alignment movements. When the temperatures and radial profiles look identical across the trap, we can conclude that the laser beam overlaps with the ions equally throughout the trap.

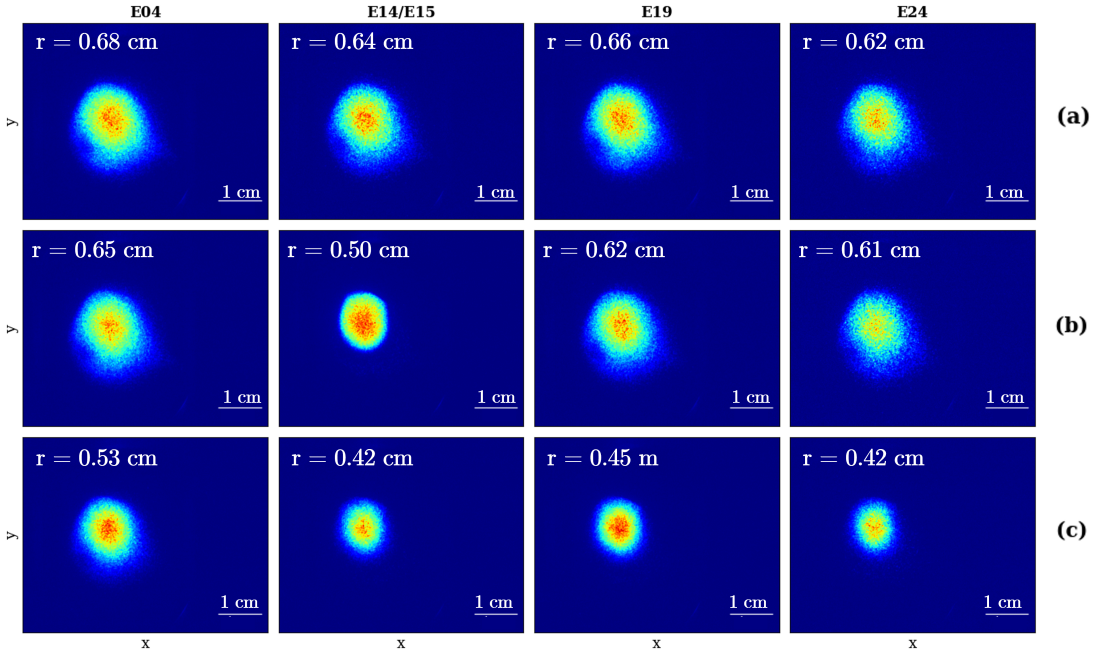

Figure 4.20: Plasma profiles from different trapped electrodes with and without laser cooling. The 4 electrode locations from which the plasmas were imaged are E04 (normal electrode), E14/E15 (thin electrodes), E19 (thin electrode) and E24 (normal electrode). The radii quoted correspond to the plasma sizes at the MCP location. (a) No laser cooling: shows the profiles from each electrode without laser cooling. The profiles are similar across the trap. (b) Off-axis cooling beam: Illustrates the plasma profiles when only the off-axis laser beam is used for laser cooling. Only the plasma in E14/E15 demonstrates signs of interacting with the laser, as expected from the trap geometry and laser beam paths. (c) On-axis cooling beam: If laser cooling is performed with the on-axis laser beam, all plasmas should show a qualitative change in shape. The plasma profile from E04 indicates a possible beam misalignment.

The first diagnostic used during the development of this technique was the radial profile to ensure consistent particle numbers across samples. The first row in Fig. 4.20 shows the radial profile of uncooled plasma samples from the various probing locations. The average radius across the positions is (6.5 ± 0.2) mm, and the particle number varies by about 10 %. The second row on Fig. 4.20 shows the plasma profiles when only the off-axis beam is used for laser cooling. Due to the trajectory of this beam, it overlaps exclusively with the plasma trapped in E14/E15. It is clear from the MCP pictures that the plasma profiles differ between cooled and uncooled samples: the radius decreases by 30 % for the cooled sample, while the number of particles remains the same. Finally, the third row of Fig. 4.20 demonstrates the plasma profiles while cooling with the on-axis beam. In this sample, the overlap with the trapped Be^+ cloud in E04 may be less ideal for cooling

than in the rest of the trap. The radial profiles are a good qualitative way of detecting laser-plasma interactions. However, to better assess alignment and cooling effectiveness, measuring the plasma temperature offers a more quantitative and precise comparison.

To measure the temperatures, the technique described in subsection 3.2.3 was used, the well manipulations were such that the energy dump is identical at the four trap locations. The plasmas were sequentially extracted towards the A2DS diagnostic station, starting with E24 and ending with E04. The time between each temperature measurement was 100 ms, to minimise heating effects. The alignment of the on-axis cooling beam was carried out before the implementation of automated beam steering, meaning that all adjustments were done manually and were difficult to quantify. The procedure was iterative: the beam was shifted, temperatures and radial profiles were measured at the four different locations, and further adjustments were made until the results converged to a roughly consistent set of values. The aim was to obtain similar plasma temperatures at all locations, thereby ensuring that the cooling performance of the on-axis beam was uniform throughout the trap. This measurement was performed without the Neutral Trap magnets, since the magnetic field varies between $1-3$ T across the Penning-Malmberg trap electrodes. The solenoid field from the Penning-Malmberg trap is flat across the range of locations studied.

A complication to this technique was the delay between laser cooling and the temperature diagnostic. Since the A2DS stick has to move to the MCP position to measure temperature, this is not compatible with laser cooling, thus creating a delay between the end of laser cooling and the temperature measurement, during which the particles heat up. Therefore, the temperatures should not be taken as a direct result of laser cooling. After several rounds of alignment, the temperature of the plasmas across the trap was (77.6 ± 10.1) K. This method was successful as the final plasma temperatures were consistent throughout the trap.

It is worth noting that equal temperatures at different trap locations do not confirm that the beam is overlapped with the trap axis, a parallel displacement could still result in consistent final temperatures. In practice, the cooling beam has a waist of 1.90 mm, while the plasmas themselves have radii inside the trap of < 1 mm. This large size difference makes it difficult to miss the plasma altogether, almost ensuring some level of cooling throughout the trap. Nevertheless, this technique proved very effective when originally aligning this beam through the trap.

4.4.4 Laser cooling parameters

The laser beam's physical properties, such as the waist and divergence inside the trap, are difficult to fine-tune due to the path's length and geometry restrictions. Important tunable parameters to optimise laser cooling are the laser detuning from the resonance frequency, the laser power, the laser cooling duration and the beam pointing. This is a large parameter space, as some of these parameters are related. For example, if the beam is misaligned, the ions may be probing a less intense beam region requiring higher laser power or longer cooling duration to achieve the same final temperature.

Optimal parameters vary depending on the experimental goal. For example, if we want to study how the Be^+ plasma is affected by applying a rotating electric field, the final temperature can be a few hundred K. In contrast, if the objective is to study antihydrogen production, we aim for the coldest possible plasma. Thus, thorough parameter searches are needed.

Finally, when performing temperature diagnostics and radial profile measurements, the target diagnostic station must be in a position which aligns the MCP surface with the exit trajectory of the ions. This is incompatible with the laser mirror position necessary to allow the on-axis cooling beam to travel through the trap. Therefore, when trying to measure plasma characteristics, there will always be a delay of about 15 s between the end of laser cooling and the detection. Without an active cooling mechanism, a plasma in an octupole field will heat and expand, thus, it is only possible to extrapolate plasma parameters when using the on-axis cooling beam, not directly measure them. This is not the case with the off-axis beam, since there is no risk of the laser beam path coinciding with the MCP's active surface. It is then preferable to carry out laser cooling-related investigations with the off-axis beam, when possible.

To diagnose Be^+ temperatures we use the method described in Section 3.2. This is not ideal for detecting Be^+ since the MCP efficiency goes down with the particle's mass [80] [100], which can cause information to be lost about the arrival time and rate of the ions. However, if the energy at which the ions are ejected towards the MCP is unchanged, comparisons between different shots can be carried out, even though the absolute temperature cannot be precisely measured. Currently, the small solid angle of the photon detector and high laser background make it unfeasible for the temperature to be determined spectroscopically while using the on-axis beam for cooling. Positrons allow for more reliable temperature and radial profile measurements due to their low mass, thus, the fine parameter search was performed with Be^+/e^+ mixtures.

For Be^+ only plasmas, the main goal is to reduce their temperature from the initial several thousand K to a few hundred K. This is because the technique for setting the plasma ion number and radius is the first objective when preparing Be^+ plasmas and only requires temperatures in that range.

In the absence of a repumping laser beam, we rely on the cooling laser to off-resonantly repump the atoms into the cooling transition. Thus, this initial laser cooling section should be a few GHz detuned from the cooling transition. Fig. 4.21 shows the Be^+ temperature after laser cooling as a function of the laser detuning for different cooling times. Each data point corresponds to the average of five repetitions, and the error bars are the standard deviations. For longer cooling durations (30 s and 60 s), the temperature decreases as the laser detuning approaches the cooling transition resonance. This is the expected behaviour. For 10 s, the cooling duration is too short for smaller detunings to simultaneously off-resonantly repump the transition and cool the plasma.

One of the key necessary improvements is to reduce the preparation time. Since the parameter stabilisation technique only requires temperatures of a few hundred K, we can choose the initial cooling duration to be 10 s and choose a detuning between -8 GHz and -4 GHz. The samples above had ion numbers ranging from 1 to 6 million particles. Even with high particle number variations, the final temperatures are reproducible to about 15 %. The cooling durations and laser cooling power are much larger than usual ion laser cooling procedures in other experiments. As discussed in Section 2.5, the ions trapped in a Penning-Malmberg trap are moving, and the time during which the ions are actually resonant with the cooling transitions is much shorter than the overall cooling time. This results in the need for very high laser powers and long cooling durations.

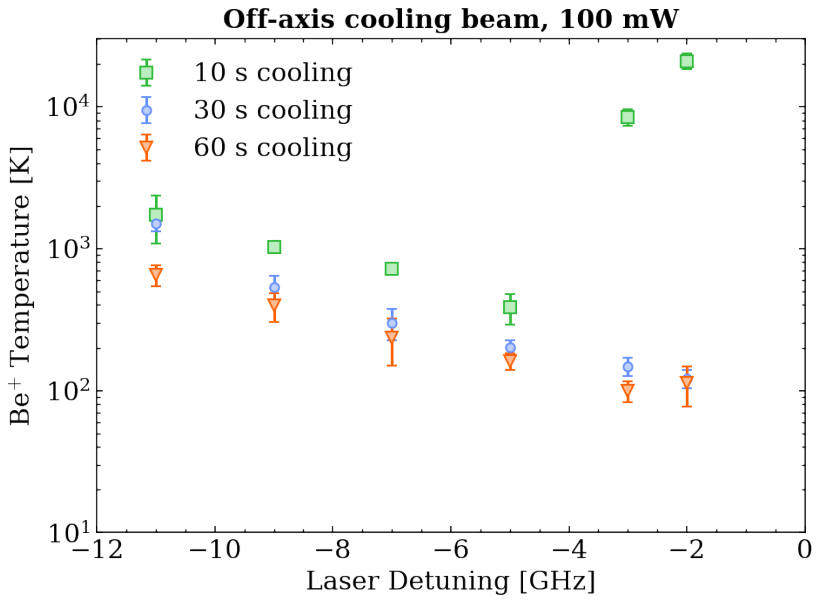

Figure 4.21: Be^+ temperatures as a function of the laser detuning for different cooling times. Millions of Be^+ ions were laser-cooled in E14/E15 with the off-axis cooling beam at 100 mW for different durations: 10 s (green squares), 30 s (blue circles) and 60 s (orange triangles), at different laser detunings for each duration.

4.5 Control of Be^+ plasma parameters

The ablation process used to produce Be^+ plasmas gives large fluctuations in the number of trapped ions up to a factor of 10. Controlling plasma parameters such as number and radius is imperative for producing reproducibly cold Be+ plasmas without changing the cooling protocol for each shot. In 2019, the ALPHA collaboration developed a technique for reproducible control of plasma parameters for non-neutral lepton plasmas, called SDREVC. [18]. The details and caveats of this technique are discussed in subsection 2.2.3. In summary, this technique consists of simultaneously applying a rotating electric field in the strong drive regime to set the rotation frequency of the plasma and evaporatively cooling the plasma. This synchronous approach makes it so that the self-potential and density of the plasma are completely independent of the initial plasma parameters and only depend on the parameters of the rotating electric field and evaporative cooling (EVC) well. The rotating electric field will be referred to as rotating wall RW application. This method is reliant on a cooling method which counteracts the heating of the rotating electric field. Cyclotron cooling is efficient enough to fulfil this criterion for leptons.

It is of great interest to apply this technique to Be^+ plasmas due to the large initial number fluctuations. As for the cooling method, laser cooling is now possible under the segmented electrodes with the on-axis cooling beam.

However, the final plasma parameters do not depend on the RW and EVC parameters as predicted by the model developed in [18]. Hence, why I will not refer to this technique as SDREVC when applied to Be^+ plasmas. Nonetheless, it was still possible to develop an SDREVC-like which allows for reproducibility and fine control of plasma parameters. This approach effectively addresses the challenges from large initial fluctuations, marking a significant step forward in Be^+

plasma preparation.

4.5.1 Technique Development

The Be^+ ions are captured in the left normal trap electrodes. Directly after capture, the temperature of the plasma is $> 10\,000$ K. The first step in plasma preparation must then be laser cooling as described in the previous section. Moreover, we want to minimise the overall duration of the technique. We can define two stages:

- **Stage 1:** initial **laser cooling** only step. The potential is depicted in Fig. 4.22 by the dashed line in (a). While in this deep well, the ions are laser-cooled using the on-axis cooling beam for 10 s, at -4 GHz detuning.
- **Stage 2:** simultaneous **evaporative cooling**, compression through **rotating electric field** application and **laser cooling**. The electric potential is lowered into the full line in (a) in 10 s while a rotating electric field in the strong drive regime is applied to E03 (a segmented electrode) of frequency f_{RW}. The final potential is shown in (b) of Fig. 4.22, the particles exit towards the DS direction (right), where the potential barrier is lower. The final well depth, ϕ_{EVC}, will set the self-potential of the plasma while f_{RW} will set its density. During this stage, laser cooling is necessary to counteract the heating caused by the rotating electric field.

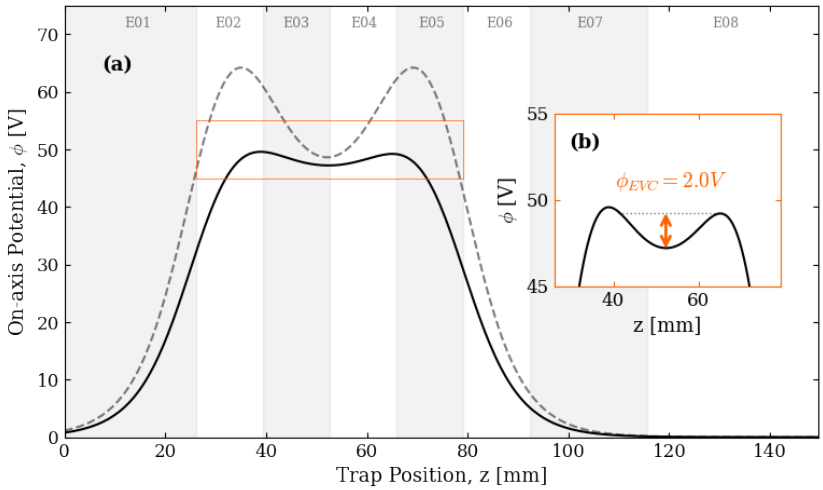

Figure 4.22: Be^+ EVC on-axis electric potentials during SDREVC-like technique. The dashed line in (a) represents the initial electric potential on-axis. Over 10 s, the potential is lowered to the potential shown by the black line. While this manipulation occurs, a rotating electric field of frequency f_{RW} is applied in E03 (a 6-way segmented electrode). (b) zooms into the final EVC well. In this example, the final EVC well depth $\phi_{EVC} = 2.0$ V. The particles exit to the right (DS direction), where the potential barrier is lower.

Fig. 4.23 demonstrates the importance of the simultaneous application of the three techniques during stage 2 evaporative cooling (EVC), the rotating wall field (RW) and laser cooling (LC):

- ***no EVC, no RW, LC* (*orange triangles*):** if only laser cooling is applied, the initial and final numbers are identical, as there is no particle loss mechanism and the final radius increases with the initial number.

- ◇ ***no EVC, RW, LC* (*blue stars*):** the initial and final numbers are comparable, the final radius changes as expected since the rotating electric field couples to the plasma and changes its size. The final radius depends on the initial number of ions.

- ◇ ***EVC, no RW, LC* (*green squares*):** if only EVC and LC are applied, the final ion number is not linear with the initial number; in this case, it stabilises at around 1 million particles, but with some high instabilities. The final radius depends on initial parameters, as there is no mechanism to artificially alter the size of the plasma.

- ◇ ***EVC, RW, LC* (*black diamonds*):** when all three techniques applied, the final number and radius are completely independent of the initial plasma parameters. The average variation in the final number of particles is $2.5\,\%$ and in radius it is $3.2\,\%$.

- ◇ ***EVC, RW, no LC* (*magenta circles*):** no LC during stage 2, EVC and RW are applied. Laser cooling still occurred during stage 1 to bring the plasma temperature down to a few hundred K. For small initial particle numbers, the final number is somewhat independent of the initial number; however, the variations are higher than for the case with laser cooling. For high initial numbers, the final number becomes unstable. The overall ion number variation is $47\,\%$ if we take the full data set into account. The final radius is stable even if laser cooling is not applied during stage 2, with an overall average variation of 2.3 %.

Plots (b) and (d) from Fig. 4.23, zoom into the *EVC, RW, no LC* and *EVC, RW, LC* cases to better observe the variations in each data set with a rescaled vertical axis. For the cases presented in Fig. 4.23, the parameters used were $f_{RW} = 150$ kHz, $\phi_{EVC} = 1.14$ V, laser power 100 mW and laser detuning -4 GHz.

To conclude, the SDREVC-like technique only allows full control of the final Be^+ parameters when evaporative cooling, strong drive regime plasma compression and laser cooling are applied simultaneously. For ions, an extra cooling step must be added before initiating the rotating wall compression and evaporative cooling, to ensure the plasma temperatures are within the necessary range (< 1000 K). Following the procedure described above, the Be^+ number spread is reduced to only a few percent from the initial 400 % variation from laser ablation fluctuations alone.

Evaporative cooling well depth

The final EVC well depth (ϕ_{EVC}) will determine the space charge of the plasma. If the rotation frequency remains unchanged, altering the well depth allows us to predictably change the ion number. Fig. 4.24 plot (a) shows the final Be^+ as a function of the initial Be^+ number for a range of final well depths, $0.8\,\text{V} < \phi_{EVC} < 2.0\,\text{V}$. The final number is completely independent of the initial number of ions for all studied well depths. Deeper wells become more difficult to study, as they require a large initial number of particles. For the technique to be successful, the initial number of particles must be larger than the target number. Higher ablation pulse energies are needed to increase the number of ablated ions, which causes the deposited energy to be above the fluence threshold for Be^{2+}. A second species could affect the technique, and studying dual-species SDREVC was not the goal. Moreover, high ablation energies can deteriorate the Be target and reduce its lifetime.

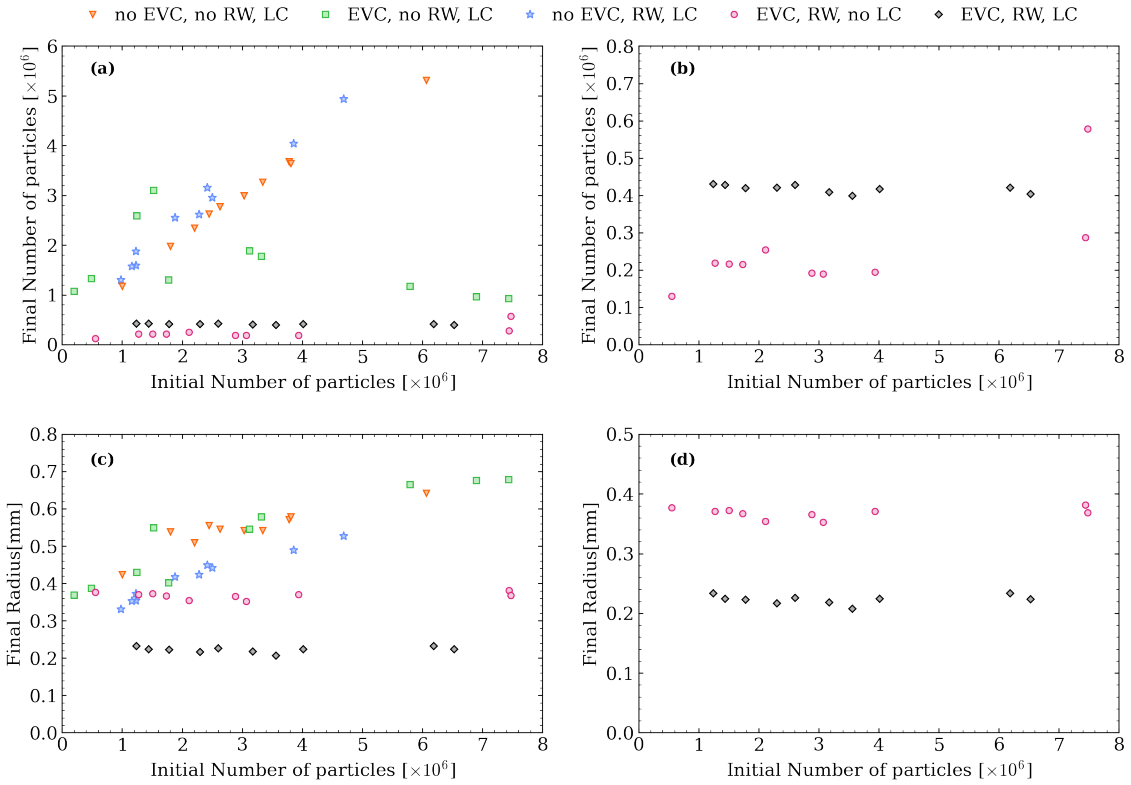

Figure 4.23: Final Be^+ number ((a) and (b)) and radius ((c) and (d)) as a function of the initial Be^+ number for different configurations of the three key parameters, illustrating the effect of evaporative cooling (EVC), the electric field applied by the rotating wall (RW) and laser cooling (LC) by systematically excluding their contribution. The orange triangles show what occurs when only laser cooling is applied at -4 GHz detuning, 100 mW power, *no EVC, no RW, LC*; the green squares illustrate the effect of evaporatively cooling part of the plasma, the final well depth is 1.14 V, *EVC, no RW, LC*; the blue stars highlight the behaviour of the rotating electric field with 150 kHz frequency, *no EVC, RW, LC*; the magenta circles show the instabilities that arise without laser cooling *EVC, RW, no LC*; finally, the black diamonds represent the results if all three techniques are applied simultaneously, SDREVC-like, *EVC, RW, LC*. A detailed explanation of each case can be found in the text.

Plotting the final Be^+ number, N_{final}, against the final EVC well depth, ϕ_{EVC}, Fig. 4.24 plot (b), above 1.0 V well depth, there is a relation between these two parameters, which can be fit with a linear function,

$$N_{final} = 3.27 \times 10^6 \phi_{EVC} - 3.00 \times 10^6. \tag{4.5.1}$$

When tuning the Be^+ number to sympathetically cool positron plasmas, Eq. 4.5.1 can be used to estimate the necessary final well depth.

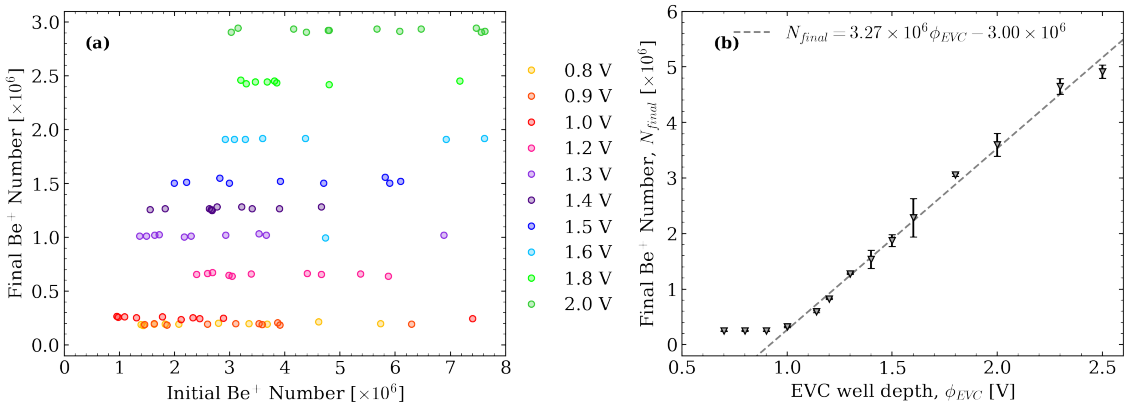

Figure 4.24: Final Be^+ number as a function of the EVC well depth 3-electrode half dump: the dashed line shows the voltage applied to the electrode wall; the solid line is the on-axis potential the ions will experience.

For well depths below 1.0 V, the number of particles stabilises at around 195 thousand Be^+ ions, regardless of the well depth.

Rotating electric field frequency

The frequency of the rotating electric field, if in the strong drive regime, will couple to the plasma and change its rotation frequency. A change in the rotation frequency will affect the density of the plasma. Fig. 4.25 shows the influence of the rotating electric field frequency, f_{RW} on the final Be^+ number (a) and radius (b), for constant final well depth (1.14 V) and laser cooling parameters (-4 GHz detuning, 100 mW power). The plasma behaviour is not as straightforward as for the EVC well depth. There are three distinct regions:

- **< 125 kHz:** the cut-off frequency of the high-pass filters for each rotating wall electrode segment is 100 kHz, such that frequencies below this value are not transmitted to the electrodes. Frequencies near this cut-off are transmitted but attenuated, which reduces the amplitude of the RW field and could be the cause of the instabilities seen for frequencies of 125 kHz and below.
- **125 kHz - 150 kHz:** the final number and radius decrease with the increase of the rotating wall frequency f_{RW}. This is the general expected behaviour as observed for SDREVC with leptons in [18].
- **> 150 kHz:** the final particle number and plasma radius increase as f_{RW} increases. This behaviour is not explained by the current model, and investigations are ongoing to try to explain this relation.

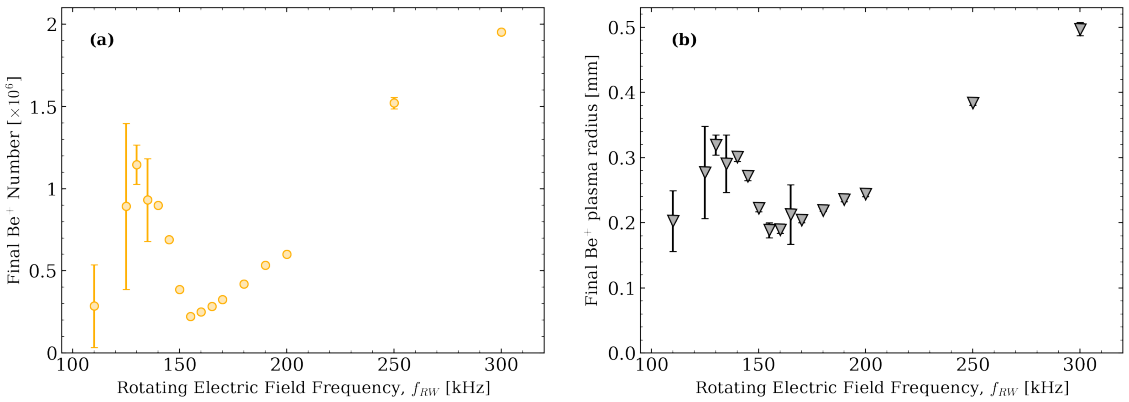

Figure 4.25: Final Be^+ number (a) and radius (b), for constant final well depth (1.14 V) and laser cooling parameters (-4 GHz detuning, 100 mW power) as functions of the rotating electric field frequency, f_{RW}.

Regardless of the unexplained behaviour, final number and radius stability are still achievable for frequencies above 125 kHz, which is the main goal of this technique.

The amplitude of the rotating electric field does not significantly influence the behaviour shown in Fig. 4.25, so long as it is above the threshold where it couples to the plasma. Experimentally, it was concluded that if the amplitude is above 5 V, the RW has enough amplitude to dominate over internal plasma damping processes.

Laser Cooling Power

The plasma temperature is affected by the on-axis cooling beam power. If the beam power is too low, the plasma temperature will not decrease enough to ensure stability when applying the number stabilisation technique, as can be seen in Fig. 4.26. These temperatures were measured after 10 seconds of cooling at -4 GHz detuning using the on-axis cooling beam. The plasma is trapped in E04. The heating from the delay for the diagnostic station movements heats the plasma, so the plasma temperatures for laser powers above 20 mW are within the required range of a few hundred K. The final number of particles stabilises for laser powers above 20 mW, where the temperatures fall within the desired range. Given a beam waist of 1.90 mm, the intensity range studied here is $0 - 1.1$ W.cm^{-2}.

During normal operation, the power in the on-axis cooling beam was kept at around 100 mW.

Disagreement with the near-zero lepton plasma model

The model developed in [18] assumes the plasma is in the zero-temperature limit and its density is constant across the radial profile of the plasma. The effect of a non-zero temperature plasma within the range 30-300 K was calculated to be a 1 % discrepancy from the model in lepton plasmas. The Be^+ temperature concerns were addressed by introducing laser cooling as a cooling source, as discussed above.

The model predicts that the on-axis self-potential, ϕ_c, depends on the particle number N like

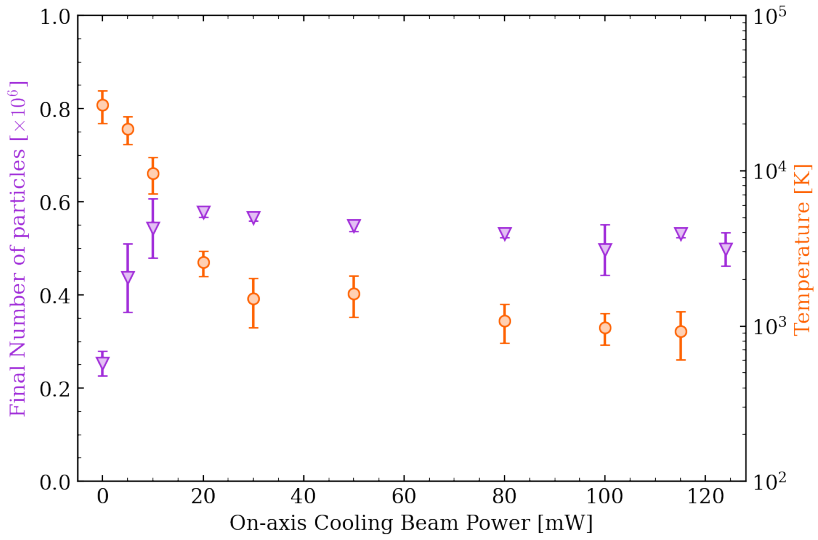

Figure 4.26: Final Be^+ number and temperature as a function of on-axis laser power. The purple triangles show the final Be^+ number as a function of the power of the on-axis cooling beam. Powers over 20 mW yield a stable final particle number. The orange circles show the plasma temperature before the number stabilisation technique is applied.

so,

$$\phi_c = \phi_{c_0} \left(\frac{N}{N_0} \right) \frac{1 + \ln\left(\frac{R_W^2}{r_{p_0}} \frac{N_0}{N} \right)}{1 + \ln\left(\frac{R_W^2}{r_{p_0}} \right)}, \tag{4.5.2}$$

where ϕ_{c_0}, r_{p_0} and N_0 are normalisation points and R_W is the radius of the electrodes. Moreover, the radius of the plasma, r_p is found to depend on the rotation frequency of the plasma, f,

$$r_p = r_{p_0} \sqrt{f_0 / f}, \tag{4.5.3}$$

where r_{p_0} and f_0 are again normalisation points. If the rotation frequency of the plasma is set only by the rotating electric field, then $f = f_{RW}$.

Fig. 4.27 compares the experimental data from the Be^+ SDREVC-like technique and the model developed in [18]. Fig. 4.27 (a) shows the final Be^+ number as a function of the EVC well depth. The experimental data is depicted in black triangles, and the model prediction is the orange line. The absolute Be^+ number predicted by the model does not agree with the measured number of particles. However, the overall behaviour agrees: the deeper the EVC well, the more particles are left after SDREVC. Fig. 4.27 (b) the final Be^+ plasma radius as a function of the rotating electric field frequency. The experimental data is shown in black triangles and the model calculation is the purple line. The model disagrees with the experimental data in both the absolute radius and in overall behaviour.

This disagreement is still under investigation. There are known problems and effects which are candidates for explaining the observed disparities. For instance, the radii quoted in this section have been radii inside the trap, wherein we calibrate the size measured at the MCP location using the fringe factor as shown in Eq. 3.2.2. This relation is valid for low-mass particles which follow

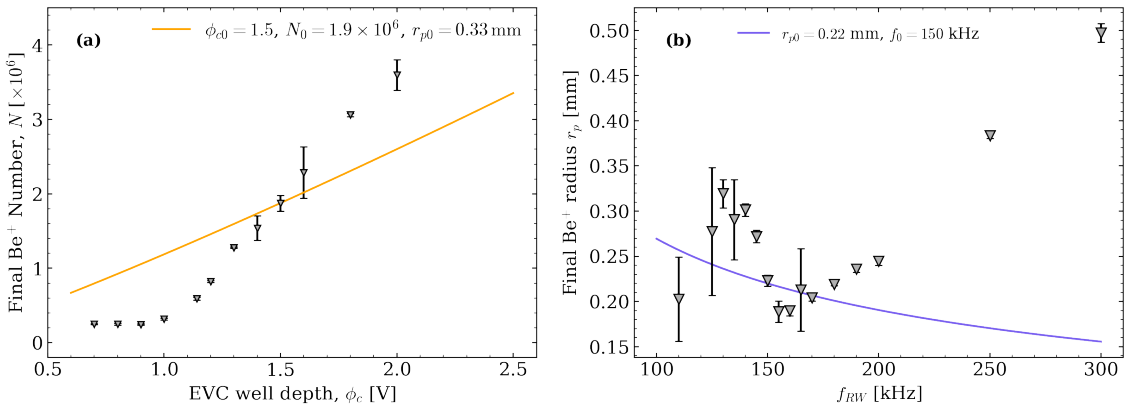

Figure 4.27: Comparisons between the data from Be^+ SDREVC-like technique and the model for zero-temperature lepton plasmas. (a) The final Be^+ number as a function of the EVC well depth. The experimental data is depicted in black triangles, and the model prediction is the orange line. (b) The final Be^+ radius as a function of the rotating electric field frequency. The experimental data is shown in black triangles, and the model calculation is the purple line.

the magnetic field lines almost exactly. Due to its mass, Be^+ does not follow this relation exactly, and knowing the actual size inside the trap is not trivial. Comparisons between different data points are possible using the fringe factor to estimate the size inside the trap, however, the absolute radii values are still unknown. Particle trajectory simulations are currently underway to accurately estimate the absolute size of the Be^+ plasmas inside the trap. Moreover, high plasma temperatures directly influence the plasma's self-potential, effectively reducing it when compared to the zero-temperature limit. If the plasma self-potential does not match the EVC well depth, the number of particles left in the well will not follow the model, possibly causing the disparities in Fig. 4.27 (a).

Finally, there is a hypothesis that the rotating electric field may not be coupling to the plasma rotation frequency, f_{rot}, but rather to the sum of the plasma rotation and axial bounce, f_{bounce}, frequencies,

$$f_{RW} = f_{rot} + f_{bounce}. \tag{4.5.4}$$

Rough estimates of the ranges of each of these frequencies in the potential wells used during the SDREVC-like technique for Be^+ (see Fig. 4.22):

$$\begin{cases} 50 < f_{rot} < 100 \text{ kHz} \\ 100 < f_{bounce} < 300 \text{ kHz} \end{cases} \tag{4.5.5}$$

Since the studied range for f_{RW} was$100 - 300$ kHz, it is possible that the coupling is to a combination of f_{rot} and f_{bounce}. Resonance with the axial bounce frequency has been theoretically described in [101] [102] and experimentally observed in antiproton plasmas at ALPHA in [103]. It could explain the behaviour observed when changing the rotating electric field frequency.

4.5.2 Long-term Be^+ number stability

One of the most important characteristics of the SDREVC-like technique is that it ensures long-term stability of the final plasma parameters. During the antiproton runs Be^+ plasmas are pre-

pared about 100 times a day whenever an experiment needs to be run. This procedure is repeated day after day and monitored using the HD technique described above. Fig. 4.28 demonstrates the average Be^+ number after the SDREVC-like technique during the 2023 and 2024 antiproton runs. The target Be^+ number differs between the two runs due to different experimental needs. During the two weeks depicted from the 2023 run, the target Be^+ number was 130 000 particles, and the average overall variation was 13.6 %, in 2024 the target number was 180 000 particles, and the observed average variation was 13.0 %. The shaded grey lines represent periods during which the ALPHA-2 apparatus was being thermally cycled to improve vacuum conditions. Thermal cycling involves controlled heating and cooling of the apparatus to mitigate outgassing and enhance vacuum quality.

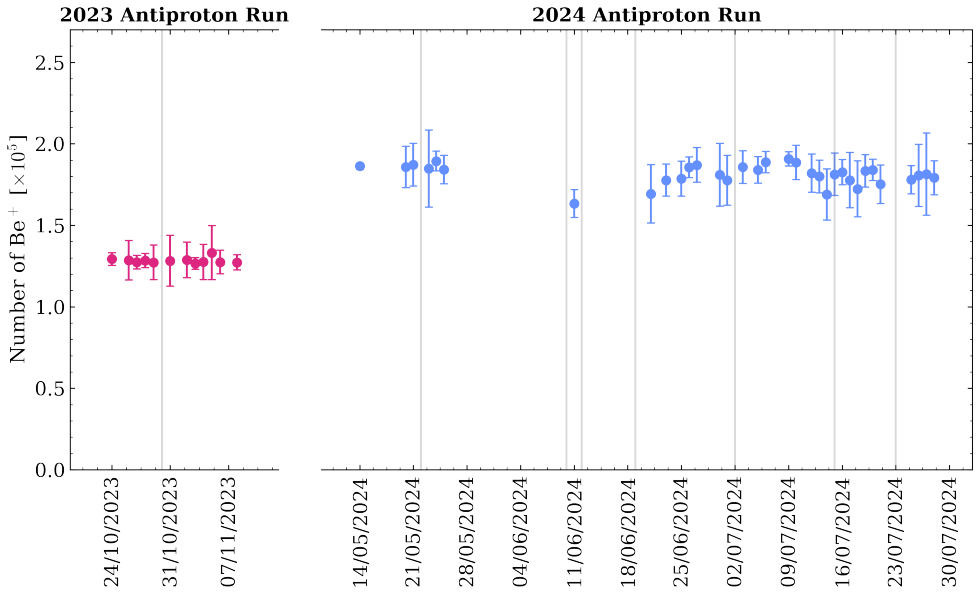

Figure 4.28: Be^+ ion number stability over the 2023 and 2024 antiproton runs. Record of the number of Be+ ions used for sympathetic cooling of positrons over 15 days during which the Be+-assisted antihydrogen accumulation technique was used in 2023 and over the 2.5 months in the 2024 antiproton run. The error bars represent the standard deviation of multiple measurements performed each day. The grey lines represent the dates when the ALPHA-2 apparatus was thermally cycled to improve vacuum conditions.

This technique was shown to be remarkably robust and powerful. Not only are the final plasma parameters independent of the initial conditions, but the data also shows no evidence of dependence on vacuum quality or long-term drifts due to unknown variables.

4.6 Summary of Be^+ preparation

To summarise the overall Be^+ plasma preparation, the process begins by ablating a few million Be^+ ions from a metal Beryllium target located on a diagnostics station upstream of the A2 Penning-Malmberg trap. The ions are magnetically guided towards the trap electrodes and trapped using electric potential barriers. The number of ablated ions can vary by an order of magnitude between successive shots.

Upon trapping, the temperature of the ions is measured to be a few thousand Kelvin. Before any other manipulations are performed, their temperature must be reduced. The on-axis cooling laser path is used for the initial laser cooling. It is far detuned from resonance $(-4\,\mathrm{GHz})$ to allow for off-resonant pumping of the cooling state due to the absence of a repumping beam. The initial cooling phase lasts $10\,\mathrm{s}$, after which the ion plasma temperature is below $1000\,\mathrm{K}$.

After the initial cooling, the SDREVC-like technique is applied to the trapped Be^+ plasma. Simultaneously applying the rotating wall technique and evaporative cooling allows for setting the number and radius of the plasma completely independently of the initial plasma parameters. Since this technique requires an active cooling method, the on-axis cooling beam illuminates the ions throughout the SDREVC-like procedure. The technique duration was chosen to be $10\,\mathrm{s}$. The target Be^+ number depends on the number of positrons needed for antihydrogen synthesis. This will be discussed in detail in the next chapter, but usually, we aim for between $150\,000 - 200\,000$ particles. This technique mitigates the initial variations from the ablation process and allows for a long-term number stability of about $13\,\%$.

The original Be^+ occurred in the right normal trap, however, for the ions to be prepared in this location, millions of ions had to traverse the volume where the anthydrogen atoms are held. This caused antihydrogen losses from the Neutral Trap, and thus, this preparation was moved to the left normal trap. More details about this can be found in Chapter 6. The final version of the preparation described above occurs in the left normal trap, under the segmented electrode (E03). To allow for the electron and antiproton preparation, the ions are moved to the centre of the trap (E14/E15) where they are laser-cooled using the off-axis cooling beam at a detuning of $-800\,\mathrm{MHz}$ while the other particles are prepared.

All of the Neutral Trap magnets are energised in the antihydrogen trapping configuration. The total duration of preparing the Be^+ plasma is about $30\,\mathrm{s}$, including all necessary diagnostic station movements (moving between the uppermost and lowermost devices in the diagnostic station takes about $15\,\mathrm{s}$). This Be^+ preparation is compatible with antihydrogen synthesis and trapping.

5 Sympathetic Cooling of Positron Plasmas in ALPHA-2

In principle, one might aim to separately prepare the Be^+ ions and positrons, merge the species while simultaneously laser-cooling the ions to counteract heating from the merge, and then chirp the laser close to resonance to sympathetically cool the positrons via collisions with laser-cooled Be^+ ions to the coldest possible temperature. Once the desired temperature is reached, the antiprotons would be merged with the positrons to synthesise and trap antihydrogen. While this sequence describes a conceptually straightforward preparation method, implementing it is complicated by a number of practical constraints.

The required movements of the A2 diagnostic stations introduce significant complexity. When new particles need to be loaded into the trap, the diagnostic stations are required to be in the "Pass Through" position. For plasma parameter diagnostics, whether temperature measurements or radial profile imaging, the diagnostic stations must be on the "MCP" position. If electrons are required, the stick must be in the "e-gun" position. Crucially, laser cooling with the on-axis beam requires both diagnostic stations to be in the "Laser Mirror" position, meaning that any of the aforementioned operations preclude laser cooling on-axis, limiting laser cooling to the centre of the trap. Therefore, the movement time of the diagnostic sticks must be factored into the overall timing budget.

If techniques such as the rotating wall or SDREVC are necessary, the particles must be transferred to one of the normal traps, where segmented electrodes are available. However, antihydro-

gen formation occurs in the antihydrogen synthesis trap, as this is where it is confined. Here, the magnetic field is approximately 1 T, whereas in the normal traps, it is about 3 T. Only one laser is used to produce 313 nm light, thus changing the frequency of the laser to enable the switch the location of laser cooling is constrained by the time it takes to chirp the laser frequency.

Additionally, any particle preparation within the antihydrogen trapping volume risks antihydrogen loss due to collisions, an outcome that is clearly undesirable and should be minimised.

Furthermore, the preparation of the Be^+ ions and the Be^+/e^+ mixture must be integrated into a highly intricate sequence, with limited time windows available for each step. Fig. 5.1 presents a simplified diagram of an antihydrogen synthesis cycle without Be^+. The yellow (left normal trap), blue (antihydrogen synthesis trap), and blue (right normal trap) boxes indicate the locations in the ALPHA-2 Penning trap where manipulations take place. The schematics of the devices in each A2 diagnostic station include symbols for each used component: meshed circles for MCPs, empty circles for pass-through positions and rectangles with dots for electron guns. The dashed red line represents a trigger from the AD control system alerting the ALPHA control system that an antiproton bunch will arrive in 35 seconds[1]. The green lines represent ELENA antiproton bunches, with thick green lines indicating which ones are trapped in the Catching Trap.

Be^+ preparation must be completed before electrons are loaded, as both species enter the trap from the same side. Consequently, Be^+ loading and preparation must take no more than 100 seconds. The previous chapter described how the preparation process was designed to last 30 seconds, satisfying this constraint.

There is some flexibility in determining when positrons enter the ALPHA-2 trap. Considering that positron accumulation requires 100 s and system pumping before transfer takes an additional 25 s (not depicted in the scheme shown in Fig. 5.1 since these occur in the positron accumulator), the positron catching and preparation can occur about 35 s before shown in Fig. 5.1. Thus, the Be^+/e^+ preparation can last no more than 35 s. The antiproton preparation sequence has been optimised over many years, and reducing its duration is not straightforward.

To summarise, numerous factors must be considered when integrating the preparation of the Be^+/e^+ mixture into the antihydrogen synthesis cycles. The choices outlined in this chapter are informed by all the constraints discussed above, along with additional challenges encountered throughout the process. The development described here has been equal parts fascinating and frustrating, leaning towards fascinating.

5.1 Positron plasma preparation

As discussed in subsection 3.1.3, the positrons are produced by the beta decay of a ^{22}Na source and accumulated in a three-stage Surko-type accumulator. Accumulation lasts 100 s, yielding around 20 million positrons, which are subsequently transported to the ALPHA-2 trap through a magnetic beamline.

Trapping the positrons is similar to the Be^+ trapping process described in Section 4.3, but the direction that the particles enter the trap is reversed. A positive potential barrier is raised in E16, the incoming positrons reflect off this barrier, preventing them from being lost upstream. To trap

[1] This is a delay set by us and can be changed to accommodate different needs.

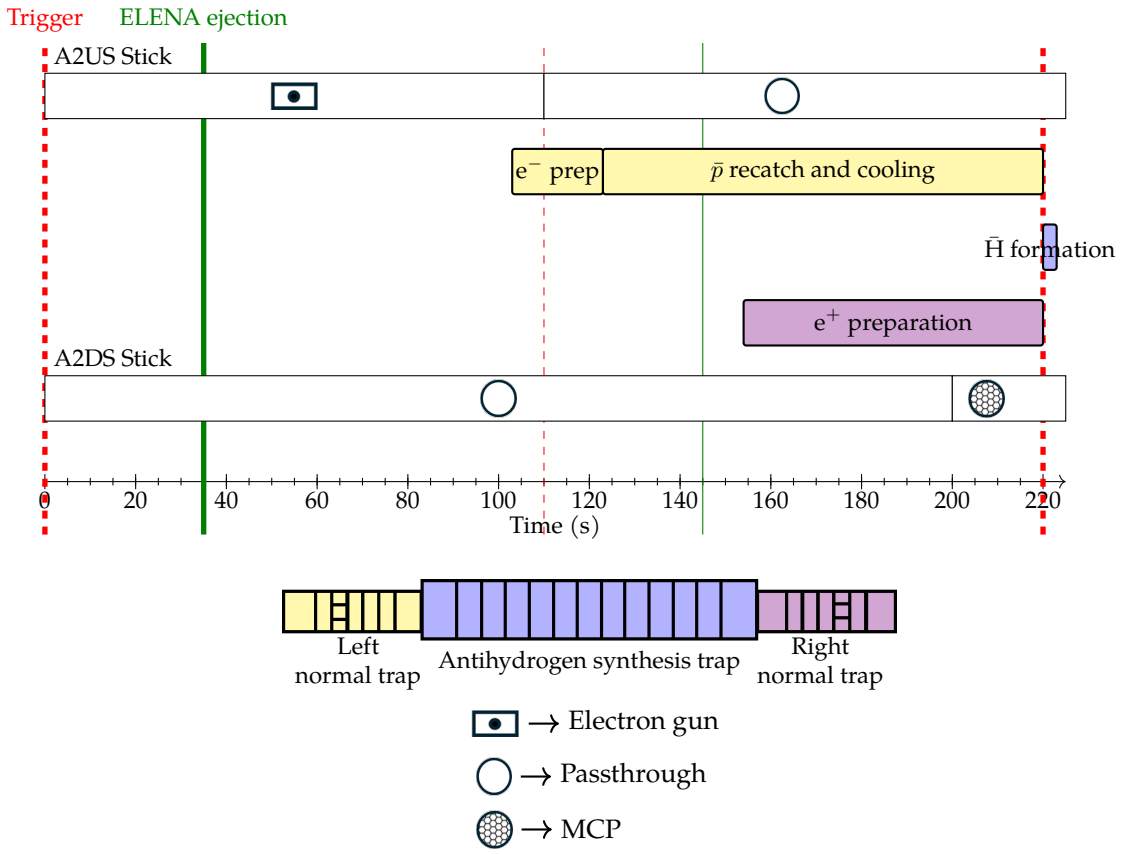

Figure 5.1: Schematic of the antiproton and the positron preparation in ALPHA-2 without Be^+. The yellow (left normal trap), blue (thin trap), and purple (right normal trap) boxes indicate the locations in the ALPHA-2 Penning trap where manipulations take place. The schematics of the devices in each A2 diagnostic station include symbols for each component used: meshed circles for MCPs, empty circles for pass-through positions, and rectangles with dots for electron guns. The dashed red line represents a trigger from the AD control system alerting the ALPHA control system that an antiproton bunch will arrive in 35 seconds. The green lines represent ELENA antiproton bunches, with thick green lines indicating which ones are trapped in the Catching Trap. The thin green line represents an antiproton bunch which cycled through ELENA but was not trapped by ALPHA. The time interval between two ELENA bunches can vary between $110 - 130$ s; here 110 s was chosen to show the shortest possible cycle.

the positrons in the downstream direction, a potential is quickly raised in E27. The time between the beginning of the positron transfer and the raising of the potential barrier in E27 was carefully tuned to maximise capture efficiency. The transfer and trapping efficiency is about $\sim 30\,\%$. The radial profile of the e^+ cloud directly after capture is shown on plot (a) of Fig. 5.2. The cloud is too large to be fully imaged by the MCP. Minimising plasma radii is imperative for stability under the octupole field. Moreover, fully imaging the plasma is essential for determining and monitoring transfer and trapping efficiency. Therefore, an initial compression step is required after positron capture. This compression occurs under E25, the segmented electrode in the right normal trap. The rotating wall technique is applied to the plasma in the strong drive regime, allowing for control of the plasma radius and particle number. The e^+ plasma profile post-compression is shown in plot (b) of Fig. 5.2.

The neon moderator degrades over time, causing a gradual reduction in accumulated positrons

over several weeks. To ensure the number and radial profile of the positron plasma are not affected by this long-term drift or other instabilities, the SDREVC technique is applied to the trapped e^+ plasma. The target e^+ number is set at ~ 3.7 million positrons, a number that was converged on after many years of careful antihydrogen synthesis tuning before the implementation of sympathetic cooling using Be^+ ions. The radial profile of the positron plasma post SDREVC is shown in plot (c) of Fig. 5.2. The duration of the positron accumulation and preparation in ALPHA-2 is nearly 200s.

The radii in Fig. 5.2 are at the MCP, to calculate the radii inside the trap we should take into account the fringe factor as discussed in Section 3.2. In this case, the fringe factor is 18.02 and the radii inside the trap at each stage are $r_{trap(a)} = 0.71$ mm, $r_{trap(b)} = 0.47$ mm and $r_{trap(c)} = 0.22$ mm.

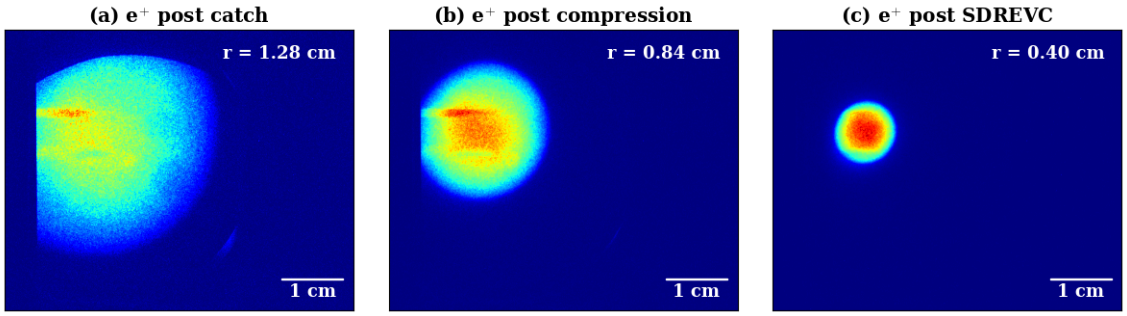

Figure 5.2: Radial profiles of the positron plasma at different preparation stages in ALPHA-2. (a) shows the positrons directly after capture in ALPHA-2, (b) illustrates the positron plasma after the initial compression step, (c) is the radial profile after the SDREVC technique is applied to the plasma. The radii displayed in the top right corner of each plot correspond to the radii of the plasma at the MCP location. Taking into account the fringe factor, the radii inside the trap for each of the plasmas are $r_{trap(a)} = 0.71$ mm, $r_{trap(b)} = 0.47$ mm and $r_{trap(c)} = 0.22$ mm.

The positron preparation takes place entirely in the right normal trap, mainly under electrode E25 (segmented electrode). The field in this region is ~ 3 T, as per Eq. 2.3.1, the characteristic cooling time from cyclotron cooling is less than a second for positron plasmas. Even with the application of the rotating wall technique during compression and SDREVC, cyclotron cooling remains extremely effective.

The positrons would then be moved to the antihydrogen synthesis trap, where the magnetic field is 1 T. The radius of the plasma will increase when compared to the one shown in panel (c) of Fig. 5.2. The average positron plasma radius before antihydrogen formation without Be^+-assisted synthesis was 0.53 ± 0.09 mm, and the average positron plasma temperature was measured to be 14.55 ± 2.17 K.

The positron preparation in ALPHA-2 ensures a well-controlled plasma with a stable number and radius. This preparation protocol provides a reliable and reproducible method for delivering positrons with the necessary properties for antihydrogen synthesis.

5.2 Be^+ and e^+ merge

To sympathetically cool the positrons with the laser-cooled Be^+ ions, the two species must be trapped within the same potential well. The two species are shuffled to adjacent potential wells separated by a middle barrier as shown in plot (a) of Fig. 5.3. The middle barrier is gradually lowered until both particle species are within the same three-electrode well. Finally, the potential configuration is adjusted back to a standard two-electrode holding well to complete the merging process. This process, known as the *Be^+/e^+ merge*, is illustrated in Fig. 5.3, where the purple and orange clouds represent the Be^+ and e^+ plasmas, respectively, while the two-coloured cloud indicates the Be^+/e^+ mixture. The merge is performed near the centre of the trap (E14 to E16), where antihydrogen is synthesised.

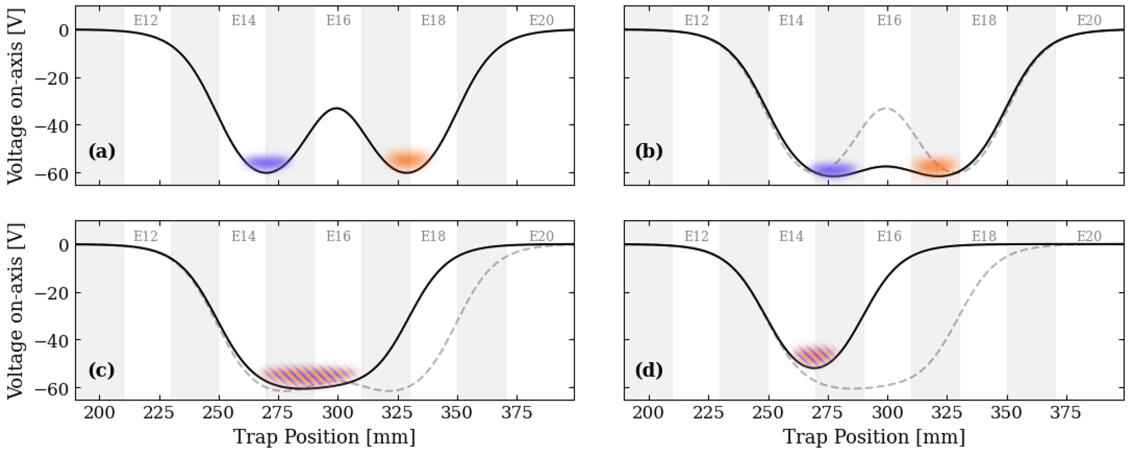

Figure 5.3: On-axis electric potential for the Be^+/e^+ merge in the antihydrogen synthesis trap. (a) shows the initial on-axis potential, (b) to (c) show the merge of the two species, and (d) shows the final confining well. The coloured clouds are illustrations of the plasma within the wells, the purple cloud represents the Be^+ plasma, and the orange cloud represents the e^+. The duration of the merge from the potentials of plot (b) to plot (c) is the most important parameter in this process. The ideal duration for the merge in this trap location (E14-E18) was 450 ms.

Even though the Be^+/e^+ merge is a conceptually simple process, it significantly alters the parameters of both species. Significant heating and expansion were observed directly after the merge of the two plasmas: the positron temperature was measured to be many thousands of K, and the radius increased by a factor of three. The parameters of the Be^+ ions are challenging to measure: the gain of the MCP has to be increased to observe these particles; however, when doing so, the positron signal is also enhanced, leading to saturation of the MCP images and dominating the temperature diagnostic signal. We can speculate about the mechanisms causing the drastic changes to the positron plasma: the plasmas have different densities, thus rotate at different frequencies; when merged, they must stabilise to rotate at equal frequency. To conserve angular momentum, the positron plasma expands, possibly causing the experimentally observed radius increase. Moreover, the shear due to the different rotation frequencies does work on the plasmas, potentially causing their temperature to increase. No experimental tests of this hypothesis were carried out.

Since the positron parameters are the most relevant for studying antihydrogen synthesis, mea-

suring the ion parameters in the mixed Be^+/e^+ plasma was not a priority or necessity for the development of Be^+-assisted antihydrogen synthesis.

The radius of the positrons after the Be^+/e^+ merge is three times larger than the radius of the positrons used for antihydrogen synthesis without the assistance of Be^+ ions. To reduce and stabilise the mixture radius, a recompression step was implemented prior to laser cooling of Be^+ ions and sympathetic cooling of the positrons for antihydrogen production. The mixture is moved to the segmented electrode in the right normal trap, where the rotating wall technique is applied to compress the mixed plasma. When trying to compress the mixture, we observed that its final radius was not locked to the rotating wall frequency (not in the strong drive regime), limiting the final size of the mixture attainable through this method. The mixture radius was reduced from 0.60 mm to 0.50 mm (in the right normal trap), and further reduction was not achievable using the rotating wall technique with the attempted parameters. Increasing the rotating wall amplitude could have allowed the rotating electric field to strongly couple to the plasma, however, this was not attempted . This compression step occurs within a high-field region (3 T), where cyclotron cooling of positrons is highly effective.

Following the rotating wall application, a cyclotron cooling period is introduced to minimise the temperature of the mixture before the laser cooling step: the positrons cool due to efficient cyclotron cooling and, in turn, cool the Be^+ ions via Coulomb collisions, bringing the mixture temperature to approximately 63.2 ± 7.3 K. Lower temperatures are not achievable through cyclotron cooling alone, as the presence of the ions in the positron plasma increases the heating rate, thus raising the minimum achievable temperature without additional cooling mechanisms. Laser cooling of the mixture would be more effective than cyclotron cooling and would yield lower positron temperatures. Since only one laser is available to produce 313 nm light, changing the cooling location between 3 T and 1 T requires chirping the frequency. This transition cannot be done rapidly in the current setup, so it was decided to rely on cyclotron cooling in the 3 T region during the Be^+/e^+ merge. The cooling period lasts 15 s, during which the plasma expands, almost counteracting the compression achieved by the rotating wall technique application. Upon review, it appears that the recompression step may not be required, and a detailed investigation into the necessity of this step would be beneficial in the future.

During antihydrogen synthesis and accumulation studies, it was found that the Be^+/e^+ merge in the centre of the trap causes collisional losses of antihydrogen that was trapped in previous synthesis cycles. The process was then moved to the right normal trap, away from the antiatom volume, thus eliminating the losses during this step. This is discussed in more detail in subsection 6.4.2.

5.3 e^+ Sympathetic Cooling

After the recompression step and cyclotron cooling period in the right normal trap, the final step is to laser cool the Be^+, enabling the sympathetic cooling of the positrons in the mixed plasma. This step is called the *Final Laser Cooling*, or FLC, as it is the last laser cooling step prior to antihydrogen production. The parameter space is complex, with each parameter interdependent rather than isolated. Consequently, a selection of the key parameters was necessary: Be^+ number, laser

detuning, laser beam power. The development process was highly exploratory, comprising several iterations. For instance, the first studied parameter was the laser detuning, the Be^+ number used during this initial search was chosen by picking the most stable point after the SDREVC-like technique which was within estimates from previous studies [30] and simulations [104]. Once an optimal detuning was found (corresponding to the coldest reproducible e^+ plasmas), the Be^+ number was adjusted to achieve even lower temperatures. This iterative approach resembles the fine-tuning of laser beam alignment using two mirrors, adjustments to one parameter influence the optimal value of the other. The following sections present the final studies of each selected parameter.

5.3.1 Be^+ number

The number of Be^+ ions influences the cooling efficiency and the minimum positron temperature. A higher number of ions leads to more Coulomb collisions, thereby increasing the cooling power and enabling lower positron temperatures. However, the ions radially separate from the positrons as the temperature drops, which reduces the cooling efficiency and establishes a minimum positron temperature limit. This temperature is significantly above the Doppler limit for laser-cooled Be^+ with simulations from [104] estimating a lower bound for positron temperature of a few Kelvin, depending on plasma parameters.

The expected theoretical dependence of the minimum positron temperature on the number of Be^+ ions follows a characteristic trend: initially decreasing with increasing Be^+ number until reaching a plateau. Beyond this threshold, additional Be^+ ions are not expected to further reduce the minimum positron temperature. This behaviour was previously observed in [30] for Be^+/e^+ mixtures in the ALPHA-2 trap under conditions where the Neutral Trap magnets were not energised. Fig. 5.4 shows the results from the scan of the Be^+ number scan for two different positron plasmas in 2019. This data was collected without the Neutral trap magnets.

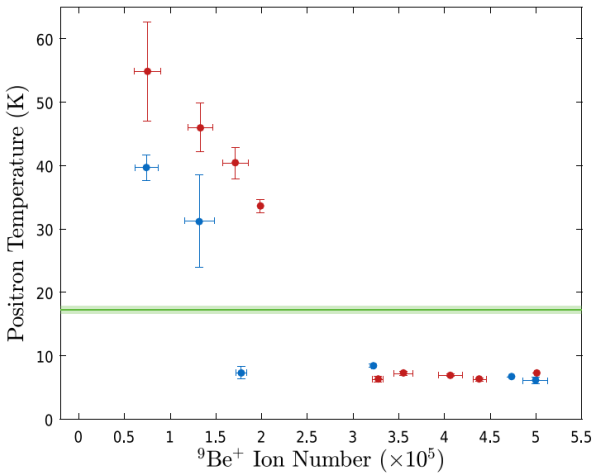

Figure 5.4: Positron temperature as a function of the number of Be^+ ions used for sympathetic cooling (no octupole field). The blue dots correspond to 1.4 million positrons and the red dots to 2.6 million positrons. The green line corresponds to the final temperature of the positrons without sympathetic cooling. Figure taken from page 4 of [30]. The green band and error bars represent the standard deviation.

However, for antihydrogen synthesis compatibility, the Neutral Trap must be energised. The octupole field induces expansion and heating of trapped plasmas, introducing an additional heating source to the Be^+/e^+ mixture, which the sympathetic cooling must overcome. Fig. 5.5 shows the e^+ temperature as a function of Be^+ number in the mixture with the Neutral Trap energised. In this study, the two species were merged, recompressed and subsequently transported to the antihydrogen synthesis location (E13) where the final laser cooling step (FLC) was performed using the off-axis cooling laser. This scan was conducted for 3.7 million positrons, with FLC parameters of -300 MHz detuning, 10 s duration and 130 mW of power. Under these conditions, the observed relationship between minimum positron temperature and Be^+ number deviates from trends seen in previous experimental [30] and simulated [104] studies.

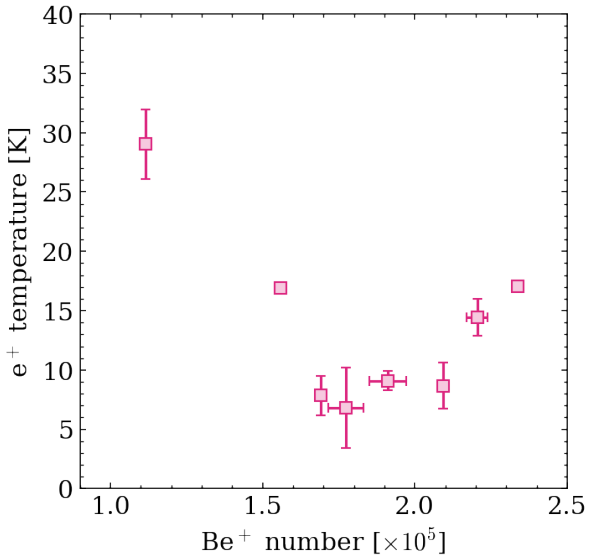

Figure 5.5: e^+ temperature as a function of Be^+ number. The FLC parameters were -300 MHz detuning, 10 s duration at 130 mW power.

As expected, an increasing number of Be^+ ions initially enhances sympathetic cooling, resulting in lower positron temperatures, as seen for Be^+ numbers below 170 000 in Fig. 5.5. Between 170 000 and 210 000 Be^+ ions, the minimum positron temperature remains relatively constant within the resolution of the temperature diagnostic, consistent with prior observations. However, for Be^+ numbers exceeding 210 000, the minimum positron temperature begins to rise with increasing ion population.

Simulations have shown that the minimum positron temperature increases for stronger external positron heating rates. [104] One possible explanation for this discrepancy in the presence of the octupole is that this magnet produces a radially inhomogeneous magnetic field, making the plasma prone to expansion. This expansion increases the energy of the particles, effectively increasing their heating rate. Adding more Be^+ ions increases this heating, since more particles are moving within the mixture. In addition, the radially asymmetric field can cause different rotation frequencies across the plasma, creating shear that can also raise the temperature. With more ions, this shear becomes stronger, further enhancing the heating rate. These speculations could help explain the higher positron temperatures for high Be^+ numbers, however, we don't have a definite

answer as to what mechanism causes this heating when the octupole field is energised. Nevertheless, the minimum positron temperature is dictated by a balance between the heating rate from various mechanisms and the cooling power from sympathetic cooling.

The selected Be^+ number was $191\,000 \pm 4\,000$, positioned near the centre of the plateau region to avoid drifts towards areas where the minimum positron temperature is too high.

5.3.2 Laser cooling parameters

Several laser cooling parameters naturally influence the final Be^+ temperature and, consequently, the final positron parameters. The various relevant parameters are tuned to determine the combination which yields the coldest positrons.

Cooling beam detuning

The cooling beam detuning is defined as the difference between the frequency of the cooling beam and the transition frequency at the magnetic field where cooling occurs. For reference, the natural linewidth of the target cooling transition is $\Gamma = 2\pi \times 19.6$ MHz.

Fig. 5.6 shows the positron temperature and radius after sympathetic cooling via laser-cooled Be^+ions as a function of laser detuning. It is important to note that FLC occurs with a fixed detuning rather than a laser frequency chirp. Performing FLC with a frequency ramp rather than with a fixed value was investigated. However, during the development of this technique, the control system only allowed for requesting linear frequency ramps. The PID loop which controls the frequency change tended to overshoot the target frequency by up to tens of MHz. This overshoot was not reproducible and caused significant positron temperature fluctuations. The fixed detuning was more reproducible, thus, this was the chosen cooling method for developing Be^+-assisted antihydrogen synthesis.

As for the results presented in Fig. 5.6, the blue line and band (standard deviation) represent the positron temperatures (a) and radius (b) without sympathetic cooling. The positrons were prepared using the protocol from before the implementation of Be^+-assisted antihydrogen synthesis. The data points represent the temperature and radius of the positrons in a Be^+/e^+ mixture. The Be^+ number used during these scans was $191\,000 \pm 4\,000$ as found in the Be^+ scan. The off-axis cooling beam had 160 mW of power, and the FLC duration was 10 s. The region between -400 and -300 MHz detuning shows positron temperatures below the minimum cyclotron cooling temperature. It's important to note that the temperature diagnostic's resolution does not allow for differentiation between the temperatures within this frequency range due to the limitations discussed in Section 3.2. Even though Be^+-assisted sympathetic cooling lowers the positron temperature by only a few Kelvin compared to cyclotron radiation emission alone, simulations have demonstrated that even this small temperature decrease can substantially increase antihydrogen production [22].

The positron plasma expands when Be^+ laser cooling is efficient, as shown in plot (b) of Fig. 5.6. When interacting with the ions, the laser can induce a torque, which increases the radius of the Be^+ plasma [60]. The pressure caused by this expansion also increases the radius of the positron plasma. The more the laser interacts with the ions, the more pronounced the expansion. The radius of the positron plasma inside the trap within the detuning range yielding cold positron

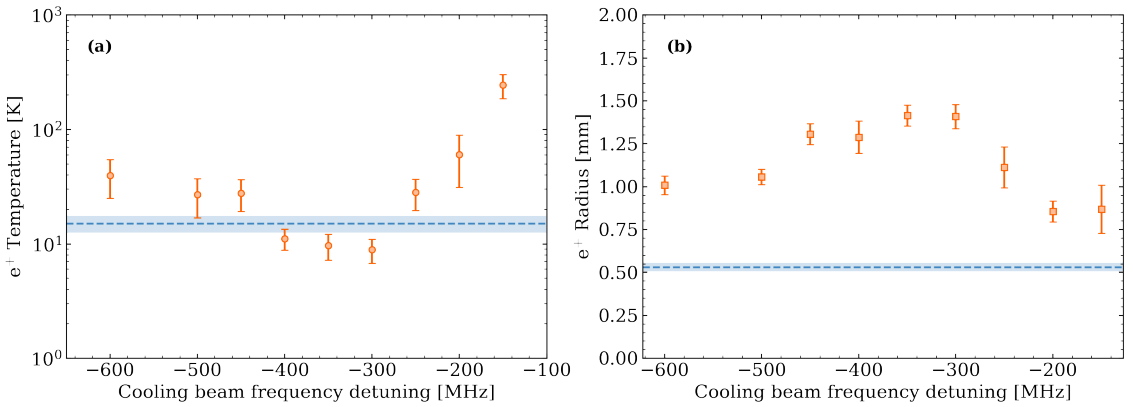

Figure 5.6: e^+ temperature (a) and radius (b) as a function of the off-axis cooling beam detuning. The blue dashed line and band represent the positron temperature (a) and radius (b) without Be^+ sympathetic cooling. The positrons were prepared using the protocol from before the implementation of Be^+-assisted antihydrogen synthesis. The band and error bars are the standard deviation of the data.

plasmas (-400 to -300 MHz) is about three times larger than the radius of the positrons used for antihydrogen production without Be^+ sympathetic cooling. Unfortunately, the large expansion occurs due to efficient laser cooling and thus, efficient sympathetic cooling. Currently, we do not have a reproducible method to control this parameter. The compression obtained from the rotating wall technique during the post-merge recompression step is negated by the expansion occurring during FLC.

The change in radius will alter the density of the positron plasma, potentially reducing it by almost a factor of 10 in the most extreme case. Simulations have shown that lower densities lead to a reduced trappable fraction of antihydrogen [22]. However, since the temperature dependency is thought to have a stronger effect than density, we still expect an increase in the trapped antihydrogen fraction with Be^+-assisted antihydrogen synthesis within the detuning range, yielding cold positron plasmas (-400 to -300 MHz).

Cooling beam power

Higher power broadens the linewidth of the transition and allows for laser cooling of a wider range of velocities. Essentially, it increases the population of the ions that the cooling laser effectively cools. One common disadvantage of using a laser beam with intensities above the saturation intensity of the transition is that the minimum attainable temperature from Doppler cooling alone increases. [58] However, cooling the Be^+ ions to the minimum possible temperature with laser cooling is of no interest for sympathetically cooling positrons. The colder the Be^+ ions, the less the two species overlap [104], eventually not overlapping at all. This is not optimal for the sympathetic cooling technique, as it relies on Coulomb collisions. What we aim for is a balance between cooling the ions to the lowest possible temperature while maintaining enough overlap with the positron cloud to efficiently sympathetically cool them. Therefore, power broadening is not a limitation for achieving the coldest attainable positrons.

A scan of laser power was performed as shown in Fig. 5.7 for three laser detunings, where the FLC duration was 10 s.

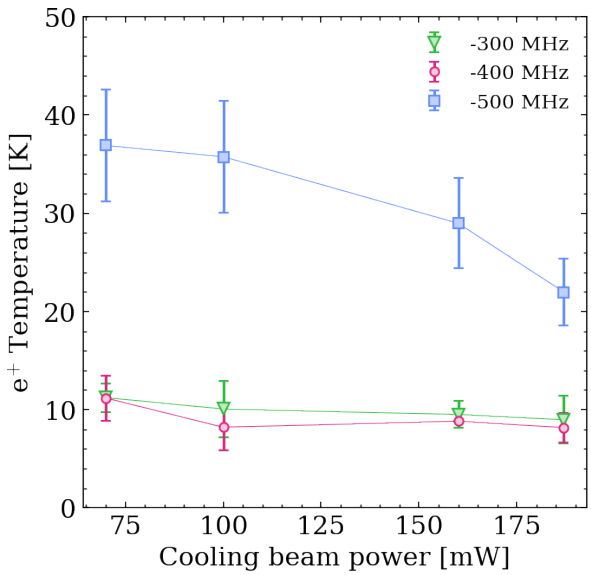

Figure 5.7: Positron plasma temperature as a function of laser power for three laser detunings: -300 MHz (green triangles), -400 MHz (magenta circles) and -500 MHz (blue squares). The data was taken using the off-axis cooling beam with a final laser cooling duration of 10 s.

From Fig. 5.7, it may seem that laser power does not significantly affect the final positron temperature. However, at the low temperatures measured for detunings of -400 MHz and -300 MHz, the resolution limits of the diagnostic procedure make it difficult to distinguish temperatures below about 10 K. The focus is placed on the data at -500 MHz, where the positron diagnostic allows for a more reliable comparison of temperatures. At this frequency, the final positron temperature with 187 mW of cooling beam power is about 1.7 times lower than that with 70 mW. According to the simulated positron temperature dependence [22], this could lead to a trapped antihydrogen fraction twice as large for 187 mW compared to 70 mW. Assuming a similar temperature difference within the detuning range yielding cold positron plasmas (-400 to -300 MHz), the cooling beam power could be a crucial parameter for optimising antihydrogen synthesis.

Laser beam pointing

The trajectory of the cooling beam through the trap influences the overlap between the laser and the Be^+ ions. If the ions probe different regions of the beam, or if the beam does not fully overlap with the ions, the final temperature of the ions changes. This, in turn, affects the sympathetic cooling and, consequently, the final parameters of the positron cloud. With the beam stabilisation system, it is possible to adjust the beam's position and examine how its alignment affects the positron's parameters after FLC.

A comprehensive study of the beam position was not conducted due to the large parameter space involved, which makes such a study time-consuming. However, a partial investigation of the position of the off-axis beam in D1 was carried out to assess the sensitivity of the positron temperature and radius with the angle of the beam. The target position of the beam in D2 was kept fixed during this study. The Be^+/e^+ mixture was prepared as described earlier in this chapter,

and FLC was performed using the off-axis laser, with 130 mW of power at -300 MHz detuning for 10 seconds. Following the FLC step, the positron cloud's temperature and radius were measured using the methods outlined in Section 3.2. After each measurement, the target position of the off-axis cooling beam in D1 was changed, and the measurements were repeated.

The results of this scan are shown in Fig. 5.8. (a) depicts the positron plasma temperature as a function of the x-y position in D1, while (b) shows the positron radius. Control measurements were performed, where the Be^+/e^+ mixture was held in the centre of the trap for 10 s without the laser cooling beam illuminating the ions. The temperature of the positrons without laser cooling the ions was 190 ± 9 K, which is not displayed in plot (a) as it would make the distinction between the relevant temperatures difficult. [2] The radius of the positron plasma without laser cooling of the ions was found to be 0.92 ± 0.10 mm inside the trap, this is marked in red in the colour bar of plot (b) for reference of the expansion resulting from laser cooling.

It is worth noting that the cooling beam has a waist of 1.90 mm, so the positional changes performed during this scan are small compared to the beam size. As a result, the plasma experiences only minor variations in intensity across these moves, which explains why there is a relatively wide range of positions over which effective cooling is observed.

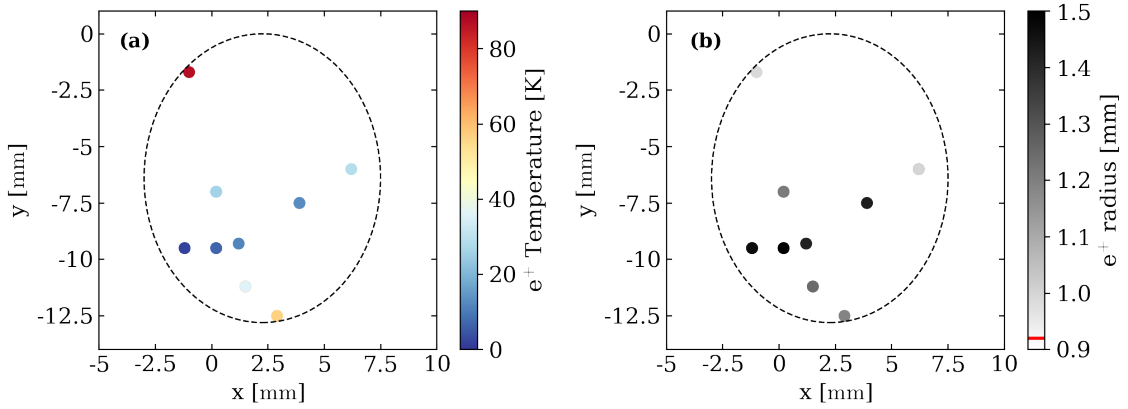

Figure 5.8: Positron plasma temperature (a) and radius (b) as a function of off-axis cooling beam x-y position in D1. The position of the beam in D2 was kept the same during this study. The dashed line represents the aperture for the off-axis beam. The detector active area is between -20 and +20 mm for both x and y. The red line on plot (b) represents the radius of the positron plasma after the 10 s FLC without Be^+ in the mixture.

A change of 1 mm in either direction in D1 will result in a 0.3 mrad change in the beam trajectory and a displacement of about 0.3 mm in the centre of the trap. The dashed lines in Fig. 5.8 represent the aperture for the off-axis beam. The temperature plot (a) shows a region around $x = 0$ mm and $y = -10$ mm where the sympathetic cooling yields the lowest positron temperatures. Any positions with significant cooling also demonstrate significant positron cloud expansion.

[2] Note that this temperature was obtained by going through the Be^+/e^+ preparation but not laser cooling during FLC. Not to the be confused with the $\sim$ 15 K that the positrons reach through cyclotron cooling in the absence of Be^+ ions.

5.3.3 2024 upgrades and final laser cooling adjustments

The Be^+/e^+ preparation method described in this chapter was first developed and implemented for antihydrogen synthesis in 2023. In 2024, hardware and software upgrades were introduced, allowing for further optimisation of Be^+-assisted antihydrogen synthesis.

In 2023, the Half-Dump technique was performed with parameters that induced off-axis motion of the plasma. The study shown in Fig. 4.15 and Fig. 4.16 was conducted after the 2023 antiproton run, improving the Be^+ stability for the upcoming 2024 antihydrogen synthesis season.

The introduction of automatic calibration of the wavelength meter to a reference HeNe laser eliminated long-term drifts of the wavelength meter or drifts due to large temperature fluctuations. In addition, a software upgrade increased the wavemeter's readout rate, considerably improving the frequency stability. This improved the stability and reproducibility of the frequency of the cooling beams. Additionally, a careful realignment of both cooling beams fortuitously resulted in a more favourable trajectory.

These upgrades resulted in a significant change in the FLC parameters. When applying the 2023 FLC parameters (-300 MHz, 10 s), the positron plasma temperature and radius exhibited unexpected instabilities. The red dashed line and band in Fig. 5.9 indicate the 2023 positron plasma temperature and radius with the optimal cooling parameters. As shown in plot (a), an FLC duration of 10 s no longer reliably resulted in cold positron plasmas, and the radius variations fall outside the error band from 2023. Power and detuning scans were performed to address this instability, but neither resolved the issue. However, reducing the FLC duration removed the instability seen in the final positron temperature. Durations of 3 s or less yielded significant cooling compared to the no-FLC case (0 s duration) and fell within the desired temperature range.

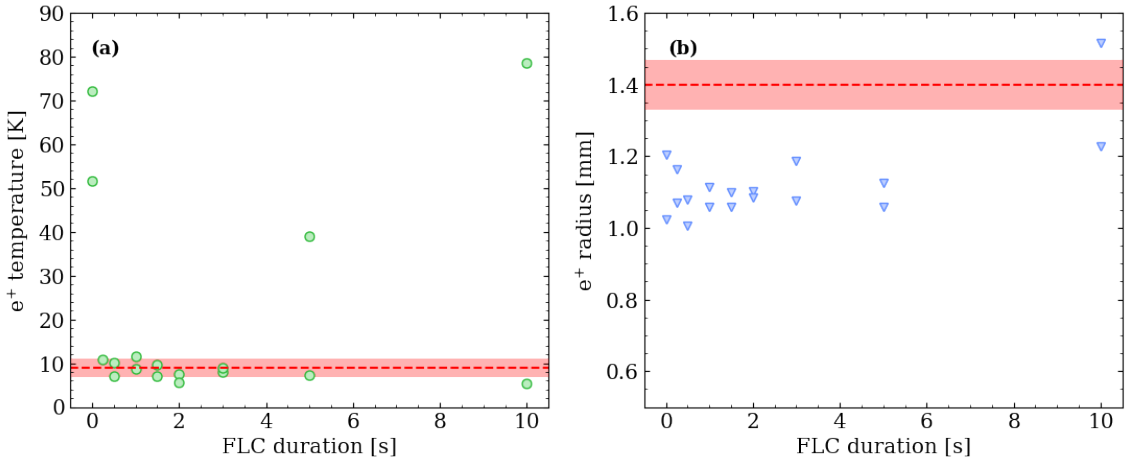

Figure 5.9: Positron plasma temperature (a) and radius (b) as a function of final laser cooling step duration after 2024 upgrades. The red dashed line and band represent the positron plasma temperature (a) and radius (b) in 2023 with the optimal cooling parameters using the off-axis cooling beam. The band and error bars are the standard deviation of the data.

An additional benefit of this adjustment was a reduction in the holding time of the mixture in the inhomogeneous octupole field, minimising the expansion caused by both this field and by the final laser cooling step. The new optimal FLC duration was determined to be 100 ms. Since the

shutters take about 20 ms to open or close, durations too close to this time scale can also introduce instabilities. This scan was repeated using antihydrogen synthesis as a diagnostic, confirming that 100 ms maximised the synthesis yield. A smaller positron radius, increases the density of the plasma which has been simulated to be beneficial to antihydrogen synthesis [22].

Beyond mitigating plasma expansion, this reduced FLC duration shortened the total Be^+/e^+ preparation time to just over 20 s, whereas before, it was close to the 35 s limit imposed by the overall particle preparation routine. This additional margin, enhances the system's robustness against timing fluctuations, improving long-term stability.

5.3.4 Cooling different positron numbers

The initial development focused on the positron number (3.74 million positrons) found to optimise antihydrogen trapping efficiency without Be^+-assisted synthesis. However, demonstrating sympathetic cooling across a wide range of positron numbers is crucial to ensure this is not a limiting factor for future antihydrogen synthesis improvements, as increasing the number of antiprotons trapped and transported to ALPHA-2 is an ongoing effort.

To perform this study, we varied the positron number while maintaining constant plasma dimensions by changing the EVC well depth in the positron SDREVC step. We aimed for positron numbers above and below the optimal value without Be^+-assisted synthesis. The chosen numbers were 2.95 million, 3.23 million, 3.74 million, 4.02 million, and 4.33 million. The goal was to determine the Be^+ number, N_{Be^+}, that yielded the lowest final temperature for each e^+ number, N_{e^+}. For each N_{e^+}, we scanned the EVC final well depth in the Be^+ SDREVC-like step, merged the two species, performed the final laser cooling (without changing the laser cooling parameters) and measured the temperature of the Be^+/e^+ mixture. The different target Be^+ numbers were obtained by setting the EVC well depth according to the relation shown in Eq. 4.5.1. This procedure was repeated five times for each Be^+ number and N_{e^+}, with the Neutral Trap magnets energised (including the octupole field). The final laser cooling parameters were 100 ms duration at -300 MHz detuned from resonance, 130 mW of laser power using the off-axis cooling beam. Fig. 5.10 (a) to (e) show the result of the scans for each positron number in increasing order. The Be^+ number at which the mixture temperature is lowest increases with the number of positrons in the plasma; the location of this minimum is referred to as the *ideal Be^+ number*, $N_{\text{Ideal Be}^+}$. This number is inferred from a range of numbers, as the temperature diagnostic method becomes less sensitive for low temperatures (<10 K). Distinguishing between a e^+ plasma that is 3 K or 5 K is not possible with our current system. However, the temperatures increase steeply if we deviate from the minimum; thus, we chose a Be^+ number at the centre of the range where we observe sub-10 K temperatures.

Moreover, as shown in Fig. 4.24, below 1 V, the EVC well depth ceases to influence the number of Be^+ in the well. This corresponds to about 100 thousand particles. We implemented a second Be^+ plasma cut after applying the SDREVC-like technique to obtain lower numbers.

Fig. 5.10 plot (f) displays the ideal Be^+ number, as a function of the positron number, N_{e^+}. A linear function can be fit to this data set to obtain a guideline function for cooling other positron numbers in the future,

$$N_{\text{Ideal Be}^+} = 0.08 N_{e^+} + 10.76 \times 10^4. \tag{5.3.1}$$

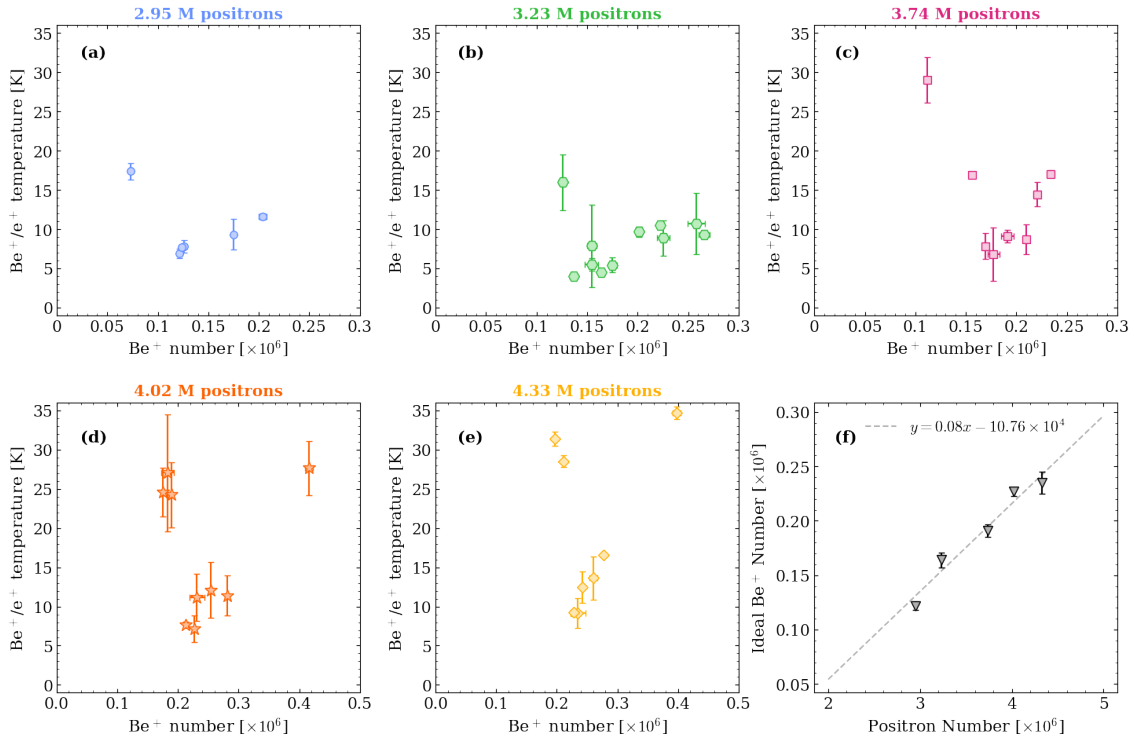

Figure 5.10: (a) to (e): e^+ temperature as a function of Be^+ number for 5 different positron numbers. (f): Ideal Be^+ number as a function of positron number. The studied positron numbers were 2.95 million (a), 3.23 million (b), 3.74 million (c), 4.02 million (d) and 4.33 million (e). The SDREVC technique ensures the positron numbers are stable to about 1 %. The studies of these varying numbers reveal a relationship between the required Be^+ ion number for achieving the coldest positrons and the number of positrons in the plasma, shown in (f).

An interesting and unexpected feature of plots (a) to (e) from Fig. 5.10 is that the final positron temperature is very sensitive to Be^+ numbers larger than $N_{\text{Ideal Be}^+}$. In [30] it was found that above a threshold, the Be^+ number does not influence the final mixture temperature, Fig. 5.4, a figure taken from page 4 of [30], shows the behaviour observed in the past at ALPHA for two different positron numbers. For 1.4 million positrons, the temperature stabilises for Be^+ numbers above 175 thousand, and for 2.6 million positrons, it stabilises above 325 thousand ions. This data was taken without the octupole field (only the solenoidal field of the Penning-Malmberg trap was present).

The data shown in Fig. 5.10 was collected while the octupole magnet was energised, indicating that this field changes the interactions between the two species. The heating rate increases for higher Be^+ numbers, and the cooling power of the laser fails to overcome this heating. This highlights the importance of stable Be^+ numbers post-SDREVC to ensure the reproducibility of sympathetic cooling.

These different positron numbers were used to study how the positron density affects antihydrogen synthesis. We aimed to keep the radius of the Be^+/e^+ mixture constant across the five densities to minimise any changes in trapped antihydrogen yield from the formation of antihydrogen at different radii. Tab. 5.1 summarises the relevant parameters for the five studied positron numbers, the positron temperatures are below 10 K for all five numbers and the radii of the plasmas agree within the standard deviations.

e^+ Number ($\times 10^6$)	Ideal Be^+ number ($\times 10^3$)	e^+ Temperature [K]	e^+ Radius [mm]
2.95 ± 0.02	122 ± 4	6.9 ± 0.6	1.04 ± 0.01
3.23 ± 0.01	164 ± 7	5.5 ± 0.8	1.02 ± 0.03
3.74 ± 0.01	191 ± 6	8.7 ± 1.9	0.99 ± 0.08
4.02 ± 0.01	227 ± 4	7.1 ± 1.7	1.01 ± 0.01
4.32 ± 0.02	235 ± 10	9.2 ± 1.9	0.93 ± 0.07

Table 5.1: Parameter list for the five studied positron numbers. For each e^+ we found the ideal Be^+ number and measured the temperature and radial profile of the Be^+/e^+ mixture.

Higher positron numbers exhibit greater sensitivity to variations in the Be^+ number. Visual inspection suggests that, for Be^+ numbers exceeding $N_{\text{Ideal Be}^+}$, the temperature increase is more pronounced for higher e^+ numbers. The development of more sensitive temperature diagnostics would enable a more precise selection of $N_{\text{Ideal Be}^+}$ and a detailed investigation into the causes and characteristics of the additional heating caused by deviations from this number. As the number of trapped antiprotons in ALPHA-2 increases, correspondingly larger positron numbers may be required. However, without a clear understanding of how to mitigate this additional heating, reproducibly cooling high positron numbers will prove challenging, and maybe limit the efficiency of antihydrogen synthesis and trapping.

5.3.5 Final remarks

All of the above studies were performed using the off-axis beam as the cooling beam for the final laser cooling step. Utilising the on-axis beam does not permit comprehensive studies since the temperature and radius diagnostics cannot be conducted directly after the final laser cooling. However, it is reasonable to assume that the behaviour of the plasma remains largely reproducible between the two cooling beams if the detuning and power are comparable.

These scans serve as a guide for selecting the parameters that produce the coldest positron plasmas. However, the limitations of the temperature diagnostic prevent differentiation between the temperature of the plasmas in the coldest temperature range (between -400 and -300 MHz detuned from resonance). Antihydrogen synthesis, on the other hand, is highly sensitive to variations in positron temperature. Therefore, these parameter studies were repeated by optimising the number of trapped antihydrogen atoms.

Utilising the antihydrogen synthesis as a diagnostic also provides deeper insight into the plasma behaviour when the final laser cooling is performed with the on-axis cooling beam, as the efficiency of the synthesis process is evaluated identically regardless of the beam used for final laser cooling.

5.4 Summary of Be^+/e^+ preparation routine

After the individual preparation of Be^+ and e^+ plasmas, the two are merged. Initially, the merging process was performed at the centre of the trap; however, as discussed in the next chapter, this led to antihydrogen losses. To mitigate these losses, the merge was relocated to the right normal trap,

near the segmented electrode.

The Be^+/e^+ merge causes expansion and heating of both species, likely due to shear forces arising from their different rotation frequencies pre-merge. To counteract this expansion, a re-compression step was introduced using the rotating wall technique in the right normal trap. Laser cooling is not available during recompression, the laser frequency cannot be chirped fast enough to allow for cooling in the centre of the trap (1 T) directly after cooling the ions under the 3 T field. Therefore, cooling must initially rely on positron cyclotron cooling. The positrons will, in turn, sympathetically cool the Be^+ ions. This approach reduces the positron temperature from a thousands of K after the merge to $\sim$ 70 K.

In addition to compressing the mixture, the recompression step plays an important role in stabilising and ensuring the reproducibility of the positron plasma radius after the merge. The recompression and cyclotron cooling steps have a total duration of 25 s.

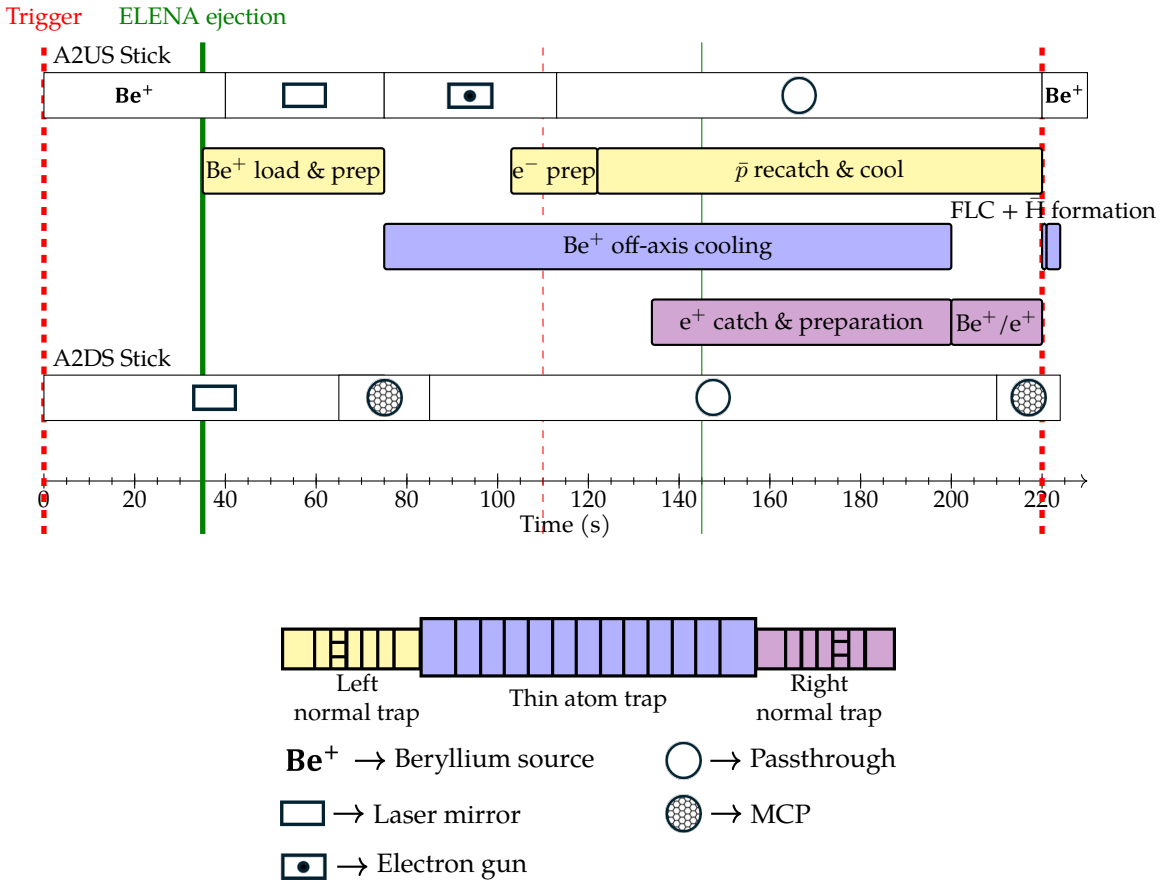

Figure 5.11: Schematic of the antiproton, positron, and Be^+ preparation in ALPHA-2. Yellow, blue, and purple bars indicate processes occurring in the left normal trap, thin atom trap, and right normal trap. Stick schematics include Be^+ source, laser mirror, electron gun, pass-through, and MCP positions. The red dashed line represents a trigger from the AD control system to ALPHA, signalling that an antiproton bunch will arrive in 35 s. The green line indicates the end of an ELENA cycle, the tick line marks an antiproton bunch caught by the ALPHA, and the thin line represents an antiproton bunch not used by the experiment. The time interval between two ELENA bunches can vary between $110 - 130$ s; here 110 s was chosen to show the shortest possible cycle.

Following recompression, the mixture is moved to the centre of the trap where the final laser

cooling step (FLC) occurs. This step is integral to the preparation as it will bring the positron temperature to the sub-10 K regime. The cooling is performed at a fixed frequency throughout the FLC duration, since the laser chirping algorithm often overshoots the target frequency, introducing instabilities in the final temperature. A fixed frequency final laser cooling step avoids this instability. The optimal parameters for the FLC step during the 2023 antiproton run were found to be a detuning of -300 MHz with a 10 s duration for the off-axis cooling beam. Maximising the beam power will be shown to be beneficial to antihydrogen synthesis.

Upgrades to the system resulted in a significant reduction in FLC duration for the 2024 antiproton run. The optimal duration was found to be 100 ms.

Fig. 5.11 is a simplified schematic of the particle preparation with Be^+. The diagnostic station movements are a lot more complex compared to before the implementation of this technique Fig. 5.1, the total Be^+/e^+ preparation in 2023 was approximately 35 s, just within the maximum allotted time. With the improvements in 2024, this was reduced to only 25 s, allowing for greater flexibility in handling timing fluctuations.

It is important to note that the goal is not to produce antihydrogen once, but rather to repeat this process over several hours to accumulate the desired number of antihydrogen atoms. This is known as *antihydrogen accumulation*, and was originally designed so that every other ELENA antiproton bunch was trapped in the Catching Trap. As a result, the completion of an antihydrogen synthesis cycle must not affect the timing of subsequent cycles. This constrains when Be^+ can be loaded into the trap, for example, or when the sticks can move to the initial positions for the next cycle. One of the main goals was to integrate the Be^+ steps into the general protocol without changing the antiproton preparation.

Timing robustness is extremely important, mainly given the sensitivity of the positron plasma temperature and radius to FLC parameters. Variations in FLC duration lead to instability in antihydrogen trapping efficiency.

To conclude, the Be^+/e^+ preparation routine is complex and non-intuitive, but many measures were taken to ensure its stability and reproducibility. While further refinements and studies remain possible, the gains in antihydrogen trapping efficiency resulting from this method were paradigm-shifting for the ALPHA physics programme and for our broader understanding of antihydrogen synthesis, as will be discussed in the following chapter.

6 Antihydrogen Synthesis and Trapping

ALPHA has been trapping antihydrogen since 2010 [11], using various methods over the years [17]. However, the trapping rate had not seen a significant increase since 2017. Antihydrogen is formed via three-body recombination and confined in a magnetic minimum trap subsection 2.4.1. While this process has been theoretically studied and investigated through simulations, experimental studies were challenging for many years. Before the implementation of Be^+-assisted antihydrogen synthesis, the trapping rate was only 16 ± 5 antihydrogen atoms per synthesis cycle[1], making the accumulation of enough antiatoms for experimentation extremely slow, and never having exceeded about $2\,000$ antihydrogen atoms in the trap at once.

As described in previous chapters, sympathetic cooling of positrons via collisions with laser-cooled Be^+ ions reduces the positron temperature to the sub-10 K regime (a range of temperatures not achievable by previous methods). This chapter presents the first antihydrogen formation with positrons at these temperatures. Careful optimisation of particle parameters enabled a near eight-fold increase in the trapping rate, with simultaneous accumulation of almost $15\,000$ antiatoms in the ALPHA-2 trap. This method, referred to as Be^+-assisted antihydrogen synthesis and trapping, not only improved the antihydrogen trapping efficiency and accelerated ALPHA's physics programme, but also facilitated detailed studies of the antihydrogen synthesis process for the first time, by allowing broader control over positron plasma parameters, particularly their temperature.

[1] These numbers correspond to 2023 performance.

6.1 Antiproton Preparation in ALPHA-2

As described in Chapter 3, the antiproton bunch is captured in the catching trap, where it is sympathetically cooled through interactions with a pre-loaded, cold electron plasma. This process results in a mixed antiproton/electron plasma ($\bar{p}/e^-$), in which the antiprotons lose energy through repeated collisions with the colder electrons. Typically, about $500\,000$ antiprotons are cooled in this way, preparing them for transfer into one of the antihydrogen experimentation traps. Before transferring the antiprotons, the electrons are ejected from the $\bar{p}/e^-$ plasma using the lepton removal technique described in Section 2.1. The removal of the electrons occurs in three phases, interspersed with cooling periods to minimise antiproton heating. Once all of the electrons have been ejected from the antiproton plasma, the antiprotons are magnetically guided into either ALPHA-2 or ALPHA-g.

The antiprotons are then re-caught in the ALPHA-2 left normal trap, where another pre-loaded cold electron plasma is in place to re-cool the antiprotons after transfer. A significant number of antiprotons are lost during this transfer: only about $130\,000$ antiprotons per shot were successfully caught and cooled in ALPHA-2 in the 2023 antiproton run.

The antiproton re-cooling procedure is identical to the initial cooling in the catching trap: collisions between the antiprotons and electrons sympathetically cool the antiprotons, after which the electrons are ejected from the plasma in three phases, interspersed with cooling periods to minimise the final antiproton temperature while eliminating all of the electrons from the mixture. Once all of the electrons are ejected, the antiproton cloud is moved to the centre of the trap for antihydrogen production. Fig. 6.1 plot (a) shows the radial profile of an example of antiproton plasma before the antihydrogen production step in ALPHA-2 during the 2023 antiproton run. The radius in the figure refers to the radius at the MCP location, at the antihydrogen synthesis location, the radius is approximately 0.7 mm. The measured temperature of the antiprotons at this point was (140 ± 40) K. Since the antiprotons cool down through collision with the positrons before antihydrogen synthesis, the mixing process is not as sensitive to antiproton temperature as it is to positron temperature. Nonetheless, minimising the antiproton temperature remains good practice, as it helps reduce unwanted positron heating during synthesis. Although colder antiproton clouds, below 10 K, can be achieved through evaporative cooling [47], this comes at the cost of a significantly reduced antiproton number. In practice, the benefits of lower antiproton temperature are generally outweighed by the associated losses in particle number.

In 2024, measurements revealed a significant misalignment between the CT trap and the magnetic field lines, leading to substantial antiproton losses during their transfer to ALPHA-2. Unfortunately, macroscopic adjustments of the magnet relative to the Penning-Malmberg trap were insufficient to correct this misalignment. To address the issue, J. Singh implemented a technique that deliberately displaces the antiprotons away from the electrode centres by offsetting the potential minimum from the electrode centre by biasing of two opposing segments of a segmented electrode. This displacement moves the antiproton cloud off-axis, allowing it to be more effectively guided along magnetic field lines toward the ALPHA-2 trap. This method resulted in a 100% increase in the number of antiprotons successfully transferred to ALPHA-2, with approximately $350\,000$ now available for antihydrogen production. Dr. Jaspal Singh discusses the details of this technique in his thesis [105]. The impact of this improvement will be discussed later in this

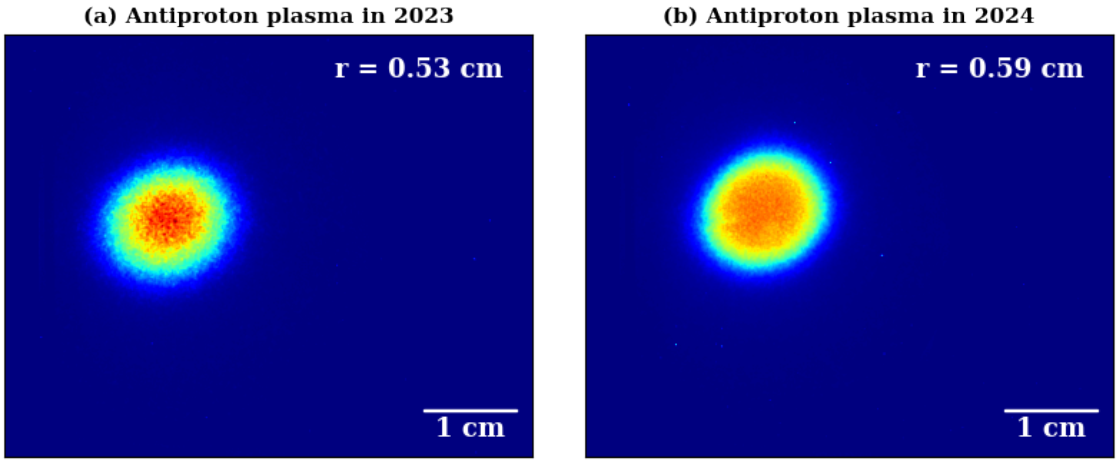

Figure 6.1: Radial profile of antiproton plasmas before antihydrogen production in 2023 (a) and in 2024 (b) in ALPHA-2. In 2023, (a), the number of antiprotons used for antihydrogen production was around 130,000, and in 2024, (b), the number was doubled to roughly 350,000. The increase in number resulted in a slightly higher radius as seen in the upper right corner of each image. The temperature of the antiproton cloud was also higher in 2024, Tab. 6.1 summarises the antiproton parameters during both antiproton runs studied in this thesis.

	Number	Radius [mm]	Temperature [K]
$\bar{p}$ (2023)	$\sim 130,000$	0.72 ± 0.01	140 ± 40
$\bar{p}$ (2024)	$\sim 350,000$	0.80 ± 0.01	247 ± 45
e^+ (no Be^+)	$(3.74 \pm 0.01) \times 10^6$	0.53 ± 0.09	14.55 ± 2.17
e^+ (with Be^+, 2023)	$(3.74 \pm 0.01) \times 10^6$	1.41 ± 0.07	8.92 ± 2.13
e^+ (with Be^+, 2024)	$(3.74 \pm 0.01) \times 10^6$	0.99 ± 0.08	8.70 ± 1.90

Table 6.1: Summary of antiproton and positron parameters before antihydrogen synthesis.

chapter. Fig. 6.1 plot (b) shows a typical antiproton plasma during the 2024 antiproton run, right before the antihydrogen synthesis step after the increase in antiproton number.

The increase in antiproton number in ALPHA-2 resulted in a slight radius and temperature increase in 2024, as shown in Tab. 6.1. This table summarises the particle parameters during the two relevant antiproton runs directly before antihydrogen synthesis. Note that these parameters are also subject to trap conditions and can vary due to degraded vacuum conditions. The values in Tab. 6.1 refer to the particle parameters under ideal conditions, as they were collected after the machine had been thermally cycled [2]. As discussed in Chapter 5, the positron parameters also changed due to hardware and software changes between the antiproton runs. The positron parameters without Be^+ are only relevant in the context of the 2023 antiproton run. After the implementation of Be^+-assisted antihydrogen synthesis, this mode of positron preparation became obsolete.

[2] This procedure is used to improve vacuum conditions in the trap by controllably increasing its temperature (evaporating impurities) and pumping them from the vacuum volume. The trap is then re-cooled to cryogenic temperatures, thus the name: thermally cycle.

6.2 Overview of Antihydrogen synthesis and trapping at ALPHA

Optimising antihydrogen production can enhance the number of trapped anti-atoms. The synthesis efficiency, $f_{\bar{H}}$, quantifies the fraction of antiprotons that successfully form antihydrogen atoms:

$$f_{\bar{H}} = \frac{\text{Number of synthesised antihydrogen atoms}}{\text{Number of antiprotons}}. \tag{6.2.1}$$

Similarly, increasing the number of trappable anti-atoms leads to a greater number of antihydrogen atoms retained in the Neutral Trap. The trapping efficiency, f_{trap}, represents the fraction of synthesised antihydrogen atoms that remain trapped:

$$f_{trap} = \frac{\text{Number of trapped antihydrogen atoms}}{\text{Number of synthesised antihydrogen atoms}}, \tag{6.2.2}$$

also referred to as the trapped antihydrogen fraction.

Understanding the primary mechanism of antihydrogen formation, as well as the influence of various parameters on trapping efficiency, is crucial for optimising f_{trap} through experimental tuning. Several theoretical and simulation efforts have been conducted over many years to better understand antihydrogen synthesis and trapping. The following sections will summarise these efforts and explain the experimental procedure for antihydrogen synthesis.

6.2.1 Three-body Recombination: antihydrogen formation process

When positrons and antiprotons are mixed, a positron (e^+) can become bound to an antiproton ($\bar{p}$), creating an antihydrogen atom ($\bar{H}$). For this binding to occur, a third particle must be involved to carry away the binding energy. The conditions in the ALPHA experiment favour the formation process of three-body recombination (TBR), in which a second positron acts as the carrier,

$$e^+ + e^+ + \bar{p} \rightarrow \bar{H}^{**} + e^+, \tag{6.2.3}$$

where $\bar{H}^{**}$ represent a highly excited antihydrogen atom. This process occurs when two positrons collide near an antiproton, causing one to lose sufficient energy to become bound while the other gains energy. This results in an antihydrogen atom in a highly excited weakly bound state. Such weakly bound states are significantly influenced by the Penning-Malmberg trap environment [106].

If the $\bar{H}^{**}$ is formed within a plasma, further collisions can ionise the anti-atom and separate it into its components, or heat the antihydrogen atom, stopping it from being trapped, or it will undergo a de-excitation collision,

$$e^+ + \bar{H}^{**} \rightarrow \bar{H}^{*} + e^+. \tag{6.2.4}$$

A de-excitation collision will cause the positron and antiproton to become more tightly bound, reducing the probability that a further collision will ionise the antiatom. If the antihydrogen atom exits the plasma, it will reach a location where the electric field is non-zero. The interaction with

this electric field can result in the *field ionisation* of the antiatom and, once again, separate it back to its components. If the antihydrogen remains bound and has low enough kinetic energy, it will stay trapped in the Neutral Trap. Via photon emissions, it will decay to the ground state.

If ionisation occurs, the antiproton can remain trapped and become bound to another positron, repeating the formation process. In fact, simulations show that an antiproton will undergo several antihydrogen formation and ionisation cycles until it forms a stable anti-atom [20] [106] [22].

The radiative cascade cools the antiatoms because each spontaneous decay step reduces the magnetic moment, and therefore the depth and curvature of the magnetic trapping potential, while the atom continues to move within it. A highly excited antihydrogen atom initially experiences strong confinement. As it cascades down to the ground state, the decreasing magnetic moment causes the trapping potential to become progressively shallower. Since this change occurs gradually compared with the antiatom's motion in the trap, the axial bounce action must be conserved. Conservation of this adiabatic invariant requires the energy of the antihydrogen atom to scale with the weakening trap: as the trap becomes shallower, the antiatom's kinetic and potential energies must decrease accordingly. Effectively, the antihydrogen atom ends up colder simply because it finds itself in a shallower potential while preserving its action, so its motional energy must drop during the cascade. This effect was studied in detail in [107], and is akin to the adiabatic cooling technique described in Section 2.3.

In steady-state conditions, the three-body recombination rate is given by [19],

$$\Gamma_{\mathrm{TBR}} = C n_{e^+}^2 v b^5, \tag{6.2.5}$$

where n_{e^+} is the positron density, $v = \sqrt{k_B T / m_{e^+}}$ is the positron thermal velocity, C is a constant and $b = q^2/(4\pi\epsilon_0 k_{\mathrm{B}} T)$ is the distance of closest approach. The value of C has been numerically calculated for different parameters [108], for a 1 T field it was found to be between $C = 0.11$ for $T = 4$ K and $C = 0.19$ for $T = 16$ K. As indicated by 6.2.5, the three-body recombination process is favoured in cold and dense plasmas, with $\Gamma_{TBR} \propto n_{e^+}^2$ and $\Gamma_{TBR} \propto T^{-9/2}$.

A steady-state scenario assumes the antiprotons are immersed within the positron plasma for longer than the three-body recombination time. This is not the case at ALPHA, the antiprotons quickly cross the positron volume and as explained above, there are many iterations of formation and ionisation cycles. This changes the temperature scaling of the three-body recombination rate. F. Robicheaux has estimated that $\Gamma_{TBR} \propto n_{e^+}^2 T^{-3/2}$ in a non-steady-state configuration [21]. This dependence, along with other parameters, has been thoroughly investigated by simulating the three-body recombination process in the conditions of the ALPHA experiment, which will be discussed in more detail in the next section.

Experimentally, the ATHENA experiment measured the antihydrogen synthesis rate, $\Gamma_{\bar{H}}$ as a function of positron temperature [23], $\Gamma_{\bar{H}} \propto T^{-1.1\pm0.5}$, a result inconsistent with the non-steady-state prediction. The antihydrogen synthesis protocol in ATHENA differed from the current protocol at ALPHA: ATHENA used a nested potential well configuration [23] [109], where the antiprotons are injected into the positron plasma with energy higher than the space charge of the plasma. The current technique used at ALPHA involves slowly merging antiprotons and positrons, allowing the antiprotons to enter the positron plasma and for positrons to traverse the antiproton cloud simultaneously [17] without increasing the energy of the particles. Before the work presented in

this thesis, the temperature dependence of three-body recombination had not been extensively studied using the potential merge technique. However, since three-body recombination remains the primary formation mechanism in both approaches, significant deviations from the ATHENA results are not expected.

6.2.2 Simulations of Antihydrogen Formation Mechanisms

Over time, numerous simulations have been carried out to study antihydrogen synthesis and trapping. Of particular relevance to this discussion are the simulations by S. Jonsell et al. [106] [110] [22], which have been progressively refined to better reflect the experimental conditions at ALPHA. This section outlines the most recent published simulations [22], along with additional refinements introduced by S. Jonsell since.

Classical trajectories of antiprotons and positrons were calculated using the full equations of motion in a combination of magnetic (axial 1 Tesla) and electric (self-charge of the positron plasma) fields by integrating Newton's equations of motion for particles subject to the Lorentz force. The positron plasma was modelled as an infinitely long cylinder with a 1 mm radius. Antiprotons were initialised from a thermal distribution matching the positron plasma temperature. At each time step, the probability of a positron entering a predefined region around an antiproton was calculated. The trajectory of a positron inside this region was explicitly solved, and an antihydrogen atom was defined as a region containing a single positron. Throughout the simulation, the positron plasma temperature and density remained constant.

The radiative cascade was not included in the simulations, requiring additional selection criteria to determine which stable antihydrogen atoms could be trapped. An atom can be trapped if its potential energy increases with magnetic field strength. This condition can be met by imposing a negative canonical angular momentum. Moreover, the atom must have kinetic energy less than 0.54 K. Since the trapping efficiency is usually rather small (10^{-3} to 10^{-4}) many trajectories are necessary to obtain statistically relevant results. To compromise between computational time and statistical relevance, about 20,000 antiproton trajectories were conducted per studied parameter in [22]. To achieve this, the simulated trap depth was increased from 0.54 K to 2 K, and the number of trapped antihydrogen atoms was subsequently scaled to account for this adjustment. For the studied temperature range (10 K to 30 K), about $13\,\%$ of the antihydrogen atoms with kinetic energy below 2 K also satisfied the more restrictive 0.54 K trapping condition.

Finally, the simulation assumes the antiprotons and positrons are at the same temperature before antihydrogen formation begins. This has not been experimentally shown to be true, however, there is strong evidence that the antiprotons significantly cool during the slow merge technique and that the antihydrogen distribution depends on the initial positron temperature [111].

It is important to note that the simulations do not capture certain experimental parameter, such as details of field configurations and the change of positron plasma parameters during the synthesis process. Regardless, the results are valuable guides when optimising antihydrogen synthesis and trapping.

Positron Temperature

The positron temperature is the most interesting parameter in the context of this thesis. The number of positrons is about 25 times higher than the number of antiprotons. Simulations assume the antiprotons thermalise with the positrons before synthesising antihydrogen [22], for simplicity. Thus, the positron temperature during the antihydrogen synthesis process will significantly influence the kinetic energy of the resulting atoms and play a crucial role in determining the trapping efficiency. This is then a relevant parameter to study in the simulations.

The data presented in Fig. 6.2 is based on the simulations developed in [22]. Some improvements have been made since its development that have not yet been published. The number of antiproton trajectories was increased, between 162,500 and 650,000 antiproton trajectories were simulated for each e+ temperature, eliminating the need for the rescaling factor introduced in [22] to account for the 0.54 K Neutral Trap depth. The simulation does not include the subsequent evolution of the antiatom, meaning the radiative cascade to the ground state is not modelled. Instead, anti-atoms are selected based on conditions favourable for trapping: the canonical angular momentum must be negative (indicating a low-field-seeking state), and the kinetic energy must be below 0.54 K. To estimate the fraction of trappable antiatoms, the total number was first halved, assuming that only half form in a low-field-seeking spin state. This value was then adjusted by a factor of 1.4 to account for spin-orbit interactions, as discussed in [21].

The data shown in Fig. 6.2 was performed for a range of positron densities matching the experimental parameters of the positron plasmas at the different temperatures, the antiprotons were injected on axis, and the electric field gradient was kept at 0 V/cm. The simulation set shows a strong temperature dependency: $f_{trap} \propto T_{e^+}^{-1.25}$. As expected, the simulations support the hypothesis that colder positron plasmas are greatly beneficial for maximising the trapped antihydrogen fraction.

Positron Density

The effect of positron plasma density was thoroughly studied in [22]. Fig. 6.3 is a reproduction of Figure 1 of the cited paper. Three different temperatures were studied for a wide range of densities: 10 K (orange circles), 15 K (blue triangles) and 30 K (green squares). As expected, the temperature significantly impacts the trapped antihydrogen fraction. The 30 K data set does not show a significant dependency on positron plasma density, n_{e^+}. However, for colder temperatures, this parameter becomes relevant. The trapped antihydrogen fraction was simulated to increase with the positron density: for the 10 K data set: $f_{trap} \propto n_{e^+}^{0.47}$; and for the 15 K data set: $f_{trap} \propto n_{e^+}^{0.38}$.

The binding energy that can be attained by an antihydrogen atom before leaving the positron volume depends on the number of collisions with positrons it undergoes. Higher positron densities will increase the probability of a de-excitation collision, thus increasing the number of antiatoms which can evolve into a trappable state. These simulations suggest that increasing the positron density could be beneficial for increasing f_{trap}. The positron radius was kept at 1 mm for the data sets in Fig. 6.3. The effect of changing the positron plasma radius has not been investigated.

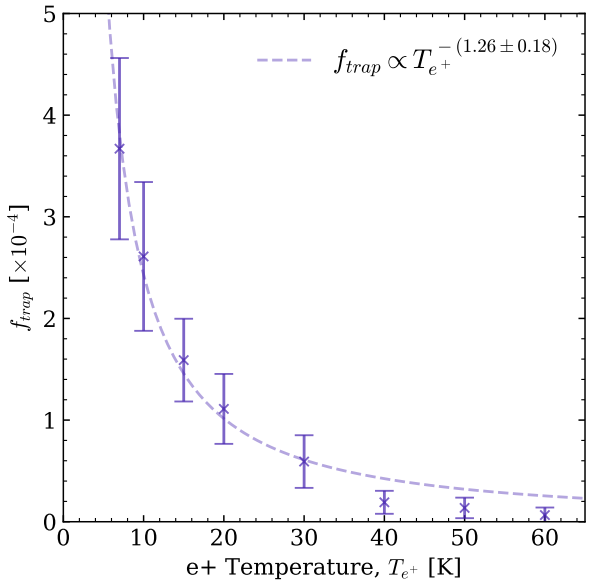

Figure 6.2: Trapped antihydrogen fraction, f_{trap}, as a function of positron temperature, T_{e+}. The positron density for this set matches the experimentally observed densities of positron plasmas in the corresponding temperature ranges. The antiprotons were injected on axis, and the electric field gradient was set to zero. The dashed purple line is a power law fit $f_{trap} \propto T_{e+}^{-1.26}$.

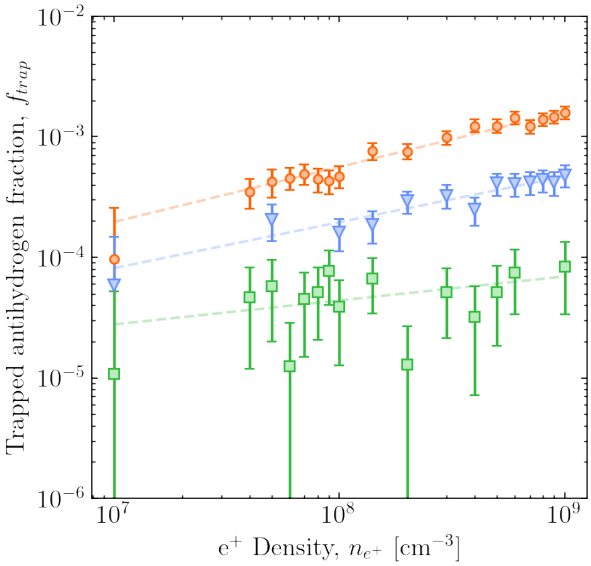

Figure 6.3: Trapped antihydrogen fraction as a function of positron density pre-slow merge for three temperatures: 10 K (orange circles), 15 K (blue triangles) and 30 K (green squares). The antiproton trajectories were initialised on the axis of the trap. The error bars represent uncertainties proportional to $\sqrt{N}$, where N is the total number of trapped antihydrogen atoms. The dashed lines are power law fits to the different temperatures. Orange dashed line, 10 K: $f_{trap} \propto n_{e^+}^{0.47}$. Blue dashed line, 15 K: $f_{trap} \propto n_{e^+}^{0.38}$. Green dashed line, 30 K: $f_{trap} \propto n_{e^+}^{0.20}$.

Antiproton Injection Radius

In the real experimental protocol, the antiproton plasma has a non-zero radius. Therefore, some antiprotons will interact with the positron plasma away from the trap electrode axis. This effect was investigated by changing the antiproton injection radius, ρ_{start}, for different positron plasma densities. The positron plasma radius remained at 1 mm. Fig. 6.4 shows the results from this set of simulations. For low positron plasma densities $< 2 \times 10^8$ cm^{-3}, f_{trap} is largely independent of ρ_{start}, however, for higher densities, the trapped antihydrogen falls as the injection radius increases.

Therefore, if we aim to increase the antihydrogen trapped fraction by increasing the positron plasma density, it should be beneficial to minimise the antiproton injection radius.

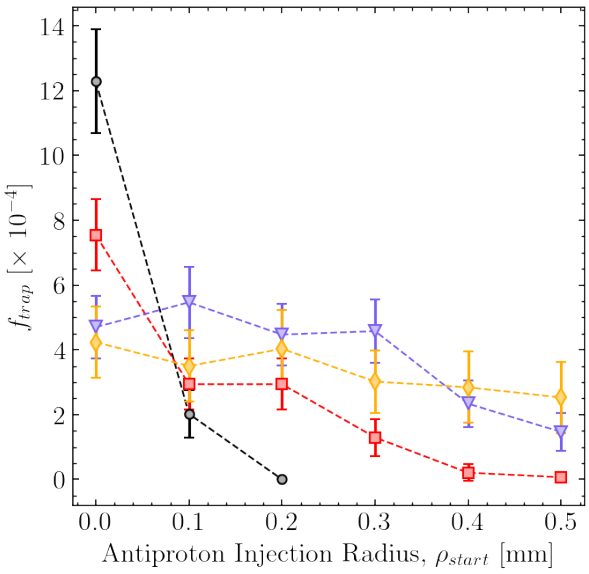

Figure 6.4: Trapped antihydrogen fraction, f_{trap}, as a function of the antiproton injection radius, ρ_{start} for $T_{e+} = 10$ K for different positron densities: $n_{e+} = 5 \times 10^7$ cm^{-3} (yellow diamonds), $n_{e+} = 1 \times 10^8$ cm^{-3} (blue triangles), $n_{e+} = 2 \times 10^8$ cm^{-3} (red squares) and $n_{e+} = 5 \times 10^8$ cm^{-3} (black circles). The positron temperature was 10 K for all simulations. the dashed lines are to guide the eye.

6.2.3 Antihydrogen synthesis at ALPHA: the potential slow merge technique

At ALPHA, antihydrogen is synthesised by slowly merging the antiproton and positron plasmas. Approximately 10^5 antiprotons at $\sim$ 100 K are trapped in a well adjacent to about 3.7 million positrons at $\sim$ 15 K. At this stage, the potential wells are as shallow as possible without allowing contact between the two species, plot (a) of Fig. 6.5.

The potential well depth for both species is then reduced in 1-3 s, merging the two species. An intermediate step is shown in plot (b) of Fig. 6.5, where the two species begin to overlap. At their interface, three-body recombination occurs, leading to the formation of antihydrogen. During this phase, antiprotons can enter the positron plasma, while positrons are free to escape to the left and traverse the antiproton cloud. Although allowing positrons to escape may seem counter-intuitive, this mechanism facilitates evaporative cooling, thereby lowering the positron plasma

temperature, a crucial factor for improving antihydrogen trapping efficiency, as discussed in the previous section.

The final potentials are shown in plot (c) of Fig. 6.5, the positron well depth is not brought to zero, as the remainder of positrons can serve as a diagnostic tool, and we see little formed antihydrogen towards the end of the potential merge. This synthesis technique minimises the potential difference between the two species, ensuring the antiprotons are not accelerated into the positron plasma. This process was first demonstrated in [17] and is known as the *potential slow merge*.

Importantly, the positron temperature after antihydrogen synthesis is lower than before due to the evaporative cooling that occurs during the potential slow merge technique. This is an upside of this technique over previous antihydrogen synthesis protocols, and resulted in a sharp increase in the trapping rate [17], once again emphasising the importance of controlling and minimising this parameter.

Most of the antihydrogen formed will not remain trapped; it will either be too hot, in the wrong state or ionised during the cascade to the ground state. These antiatoms will be detected by the ALPHA-2 SVD.

To quantify antihydrogen synthesis and trapping, two complementary metrics are defined and used throughout this chapter.

- ◇ **Synthesis SVD triggers:** the number of detector triggers during antihydrogen synthesis. These are effectively synonymous with the number of antihydrogen atoms formed, since in a few seconds over 10^5 triggers are detected, while at most $\sim 10^2$ antihydrogen atoms are trapped. The potential configuration shown in Fig. 6.5 prevents antiprotons from escaping the Penning-Malmberg trap during this phase, ensuring all triggers must originate from antiatom annihilations. No event selection cuts are applied, as the signal is many orders of magnitude above background.

- ◇ **Trapped antihydrogen:** after antihydrogen synthesis, the Neutral Trap magnets can be deenergised to zero current, gradually reducing the trap depth and releasing the trapped antihydrogen. These events also trigger the SVD, but unlike the synthesis stage, they undergo a series of event selection cuts to suppress the background signal. For details on the selection cuts applied to the SVD signal, see [77, 112]. [3] The raw SVD signal represents *detected antihydrogen*. During this thesis, the term *trapped antihydrogen* refers to the efficiency-corrected number, obtained using the event selection detection efficiency of (78.6 ± 0.2) % [77].

The antiproton and positron plasma parameters vary between antiproton runs. The AD and ELENA teams typically increase the number of antiprotons available to each experiment every year, sometimes even during the antiproton run. This increase, along with other optimisations by the ALPHA team, can change the positron plasma conditions required for optimal antihydrogen synthesis and trapping. When referring to antihydrogen synthesis without the Be^+-assisted technique, the antiproton and positron plasma parameters correspond to the 2023 antiproton run numbers, as this was the last period during which this method was thoroughly tuned and routinely used.

[3] For example, only events with a reconstructed annihilation vertex radius r_{vertex} within the trap wall radius R_{wall} are counted as antihydrogen atoms.

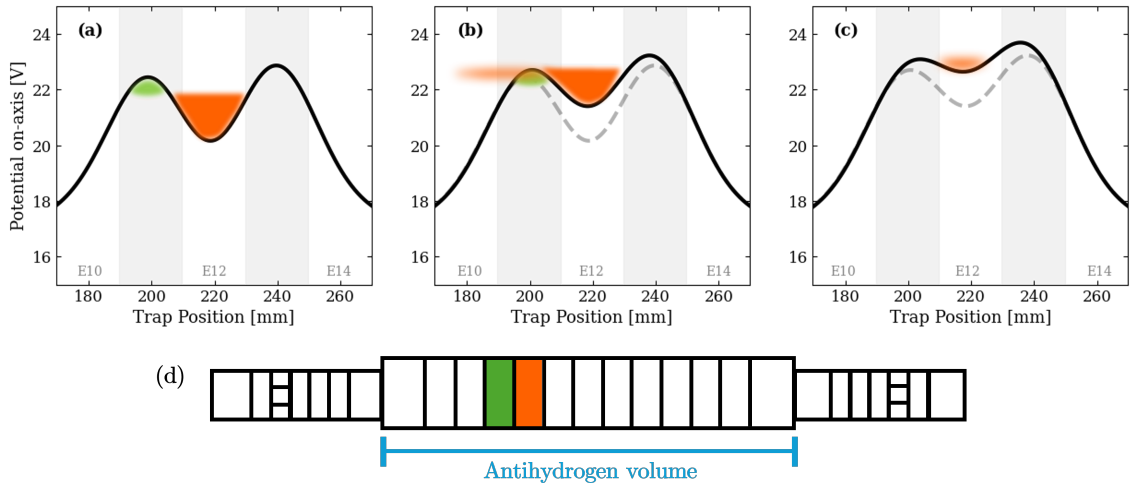

Figure 6.5: Antihydrogen synthesis on-axis potentials using the potential slow merge technique. Panels (a) to (c) show the evolution of the on-axis potential: (a) the initial on-axis potentials, the two species are not in contact; (b) intermediate potentials, the interface where the two species meet allows for antihydrogen production, positron exit to the left, evaporatively cooling the confined plasma; and (c) the final potential wells, with some positrons left for diagnostic purposes. The manipulation from (a) to (c) lasts 1-3 s, a duration that can be tuned to optimise the trapped antihydrogen fraction. Panel (d) shows a schematic of the ALPHA-2 Penning-Malmberg trap electrodes, highlighting the regions where the antiprotons (green) and positrons (orange) are confined during antihydrogen synthesis, as well as the volume where the antihydrogen atoms are trapped (blue). The antihydrogen volume extends from -14 and $+14$ cm, with 0 cm corresponding to the centre of the trap.

While, in general, a greater number of antiprotons leads to an increase in trapped antihydrogen, this relationship is not strictly proportional. For instance, in [17], increasing the number of antiprotons by 60 % resulted in only a 20 % increase in the number of trapped and detected antihydrogen atoms.

Be^+-assisted antihydrogen synthesis was introduced by adapting the Be^+ preparation and parameters to the previously optimised positron plasma conditions. The antihydrogen synthesis procedure itself remained largely unchanged, with the *potential slow merge* technique still employed. However, adjustments to the initial potential well depths were required to account for changes in Be^+/e^+ density and self-potential.

6.2.4 Antihydrogen Trapping and Accumulation

The depth of the Neutral Trap at ALPHA allows for trapping of antihydrogen atoms with a temperature of 0.54 K or lower. Immediately before synthesis, antiprotons typically have temperatures around 100 K and positrons around 15 K. Consequently, only a small fraction of the formed antihydrogen atoms are sufficiently cold to be trapped. Before the implementation of Be^+-assisted synthesis, approximately $130\,000$ antiprotons and 3.7×10^6 positrons resulted in $70\,044\pm11904$ antihydrogen formed, 16.3 ± 2.3 trapped antihydrogen per synthesis cycle and $f_{trap} = (2.07\pm0.36)\times10^{-4}$.

To obtain reliable experimental results, minimise systematic errors, and reduce the impact of shot-to-shot fluctuations, many hundreds or even thousands of antiatoms are required. This is achieved by repeating antihydrogen synthesis cycles without de-energising the Neutral Trap mag-

nets, allowing previously formed antihydrogen to remain trapped and adding to it with each cycle. This process is called *antihydrogen accumulation* and was first demonstrated in [17]. The lifetime of magnetically trapped antihydrogen has been determined to be approximately 66 hours [113]. A typical synthesis cycle lasts about four minutes, allowing nearly 1000 cycles to be performed over the lifetime of the antiatoms.

The antihydrogen synthesis process inherently involves the presence of charged particles within the volume occupied by the antiatoms. As a result, collisional interactions lead to losses through ionisation and other mechanisms. Eventually, the number of antihydrogen atoms lost per cycle equals or exceeds the number being synthesised, causing the accumulation of antihydrogen to saturate. Typically, antihydrogen accumulation lasts 6-12 hours followed by experimentation. Fig. 6.6 illustrates how the number of trapped antihydrogen atoms increases with the number of synthesis cycles before the implementation of Be^+-assisted antihydrogen synthesis. In this data set, insufficient cycles were performed to observe accumulation saturation; however, this effect will become apparent during the optimisation processes described in future sections of this chapter.

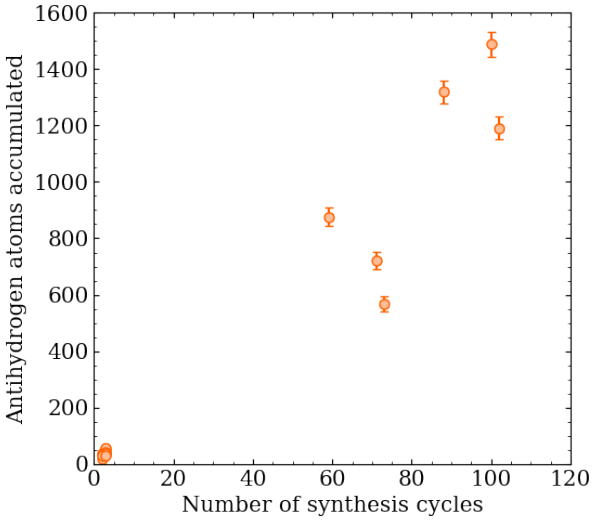

Figure 6.6: Antihydrogen atoms accumulated in the ALPHA-2 trap without Be^+-assisted synthesis as a function of the number of synthesis cycles. This data set was taken during the 2023 antiproton run for specific experiments rather than for studying antihydrogen accumulation, which explains the limited variety in the number of stacks analysed. Moreover, the data was collected over several weeks, meaning there were changes in the trap conditions, which may have contributed to the large fluctuations observed here. The error bars represent the total uncertainty in the measured counts, which includes contributions from the background rate and the uncertainty in the detector efficiency.

6.2.5 Antihydrogen Production Nomenclature at ALPHA

It is important to introduce a few key concepts that are integral to understanding the rest of this chapter:

- **Synthesis cycle:** A synthesis cycle consists of a complete round of simultaneous positron and antiproton preparation, followed by antihydrogen production. Colloquially, a synthesis cycle is referred to as a stack at ALPHA.

- ◇ **Antihydrogen accumulation:** This refers to repeating multiple synthesis cycles consecutively without de-energising the neutral trap magnets, thereby increasing the number of trapped antihydrogen atoms. Accumulations typically span several hours.

- ◇ **Antihydrogen volume:** During this chapter I will often refer to the "antihydrogen volume", this corresponds to the region of the trap where the antihydrogen is being held, also referred to as the thin atom trap. This region is between $-14 < z < 14$ cm, with $z = 0$ cm being the centre of the Penning-Malmberg trap electrodes.

- ◇ **Run:** The SVD only records data during an active run. Starting a run initiates the saving of SVD triggers. Whenever antihydrogen synthesis or related experimentation is taking place, a run is started. Each run is identified by a unique sequential number (e.g., run 1000 is denoted as R1000). Once a run is stopped, data recording also stops. Not to be confused with the antiproton run which is the period of the year when CERN provides antiprotons to the AD for experimentation.

6.3 Be^+-Assisted Antihydrogen Synthesis

We now have reproducible Be^+ plasma preparation and reliable Be^+/e^+ merging, with positron plasmas consistently cooled below 10 K. This plasma preparation is compatible with antihydrogen production, both in terms of spatial requirements and duration. The only step left is to synthesise antihydrogen with this technique.

The goal was to make the Be^+ effectively "invisible", allowing it to fit within a standard synthesis cycle without modifying other plasma preparations, and to continue using the potential slow merge technique for antihydrogen synthesis. Since the Be^+ sits at high radius due to centrifugal separation during sympathetic cooling, antiproton annihilations with Be^+ ions were not expected to be a significant issue.

When we first attempted Be^+-assisted antihydrogen synthesis and trapping, it succeeded, yielding 36 trapped antihydrogen atoms on the first try, which instantly became my new favourite number. This figure reflects raw detector counts, correcting for detector efficiency and subtracting the cosmic background, it corresponds to 46.7 trapped antiatoms. The antihydrogen formed as a function of time, and the z distribution of the detected trapped antihydrogen atoms for this first attempt are shown in Fig. 6.7. A total of 83 837 antiatoms were formed, corresponding to a trapped fraction of $f_{trap} = 5.58 \times 10^{-4}$. This represents an almost threefold improvement in both the number of trapped atoms and the trapping fraction compared to pre-Be^+-assisted synthesis. [4] However, this was only the first attempt; fine-tuning of many parameters eventually raised the average to about 166 ± 18 trapped antihydrogen atoms per synthesis cycle by the end of the 2024 antiproton run. Two distinct operational regimes can be identified. In the *tuning phase*, studies are carried out on small numbers of synthesis cycles to avoid saturation effects observed at higher cycle counts. In the *experiment phase*, the optimised parameters are kept fixed over many synthesis cycles (typically > 100) before performing a physics measurement, such as $1S - 2S$ spectroscopy.

[4] The pre-Be^+-assisted synthesis numbers were quoted in subsection 6.2.4, but as a reminder: $70\,044 \pm 11904$ antihydrogen formed, 16.3 ± 2.3 trapped antihydrogen per synthesis cycle and $f_{trap} = (2.07 \pm 0.36) \times 10^{-4}$.

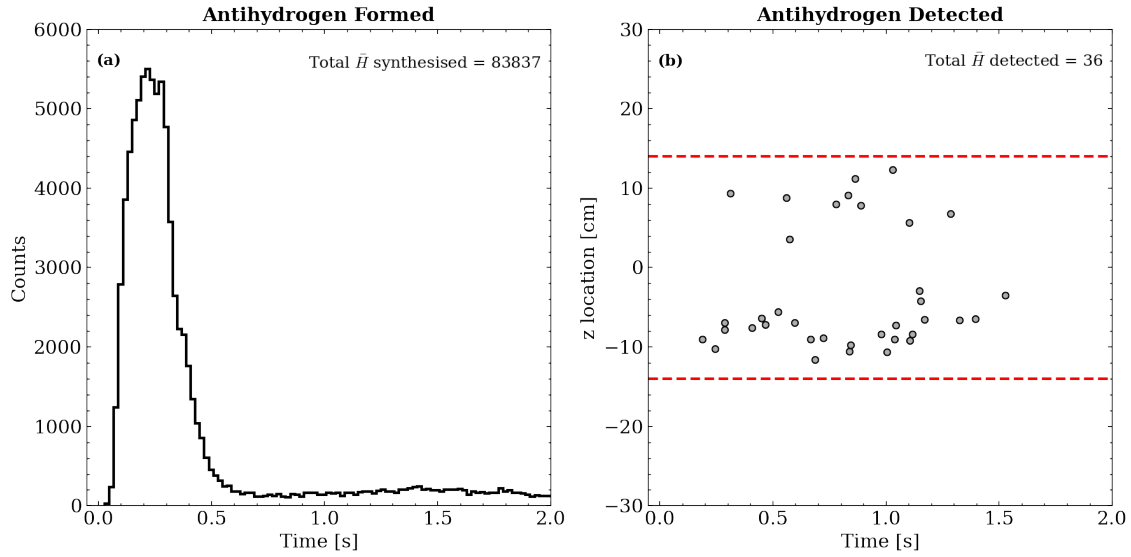

Figure 6.7: Antihydrogen formed as a function of time (a) and z distribution of antihydrogen detected (b) for the first attempt of Be^+-assisted antihydrogen synthesis and trapping. The dashed red lines represent the z region of the Neutral Trap (where the antihydrogen is trapped).

The studies presented in this chapter were not performed in quick succession but span two years and two different antiproton runs. Between each antiproton run, experimental conditions changed, for example, hardware upgrades were made, improving the laser and sympathetic cooling performance (see Chapter 5), and the number of antiprotons was increased in 2024. Even within a single antiproton run, iterative optimisation of parameters and shifts in vacuum quality or other unknown drifts in the experimental conditions out of our control affected synthesis performance. Many scans were therefore repeated multiple times under varying conditions. For this reason, the examples shown in this chapter should be regarded as representative studies of how changing a parameter influences antihydrogen synthesis and trapping, not as an exhaustive record of every scan performed. Since the parameters are interdependent, their optimal values and the absolute numbers of antihydrogen formed and trapped will differ from case to case, making comparisons between subsections in this chapter not meaningful. As a rule of thumb, datasets with more than 100 trapped antihydrogen atoms correspond to the 2024 antiproton run. Unless otherwise specified, the final laser cooling step (FLC) step was performed using the off-axis cooling beam in both years, since this configuration enables positron parameter diagnostics. In contrast, the main 2023 experimental campaigns used the on-axis cooling beam.

Overall, what is presented in this section belongs to the tuning phase: controlled parameter scans designed to probe the dynamics of antihydrogen synthesis, rather than the long stable runs used for physics experiments. A broader discussion of the overall synthesis is given in the following section on antihydrogen accumulation.

6.3.1 Effect of positron temperature on antihydrogen synthesis and trapping

Studying the effect of positron temperature on antihydrogen synthesis and trapping is at the core of this thesis, the whole point was to make positron colder and see how that affects the antihydro-

gen formation process.

Cooling beam detuning

The simplest way to vary the positron plasma temperature is to change the laser detuning during the FLC step, which varies the Be^+ ion temperature and thereby the positron temperature.

Fig. 6.8 shows the number of antihydrogen atoms formed (a) and trapped (b) as a function of the cooling beam frequency detuning. Black data points correspond to Be^+-assisted antihydrogen synthesis, while the blue dashed line and band show the results before implementing this technique. This study was performed in 2023 using the off-axis cooling beam at 160 mW during the FLC step.

The detuning range -400 to -300 MHz is optimal for antihydrogen synthesis. Here, the number of antihydrogen atoms formed plateaus at about $130\,000$ atoms, which is likely limited by the number of antiprotons available in ALPHA-2. Within this region, the positron plasma temperature falls below 10 K (see Chapter 5), consistent with the hypothesis that cold positron plasmas strongly enhance the antihydrogen trapping efficiency. The trapped fraction peaks at -300 MHz, suggesting slightly colder plasmas at this detuning, but the variations relative to -350 and -400 MHz remain within one standard deviation. Since the antihydrogen trapping efficiency is sensitive to positron temperature, this indicates that the plasmas in this range are at similar temperatures, thus supporting the existence of a real temperature plateau, rather than a limitation of the temperature diagnostic.

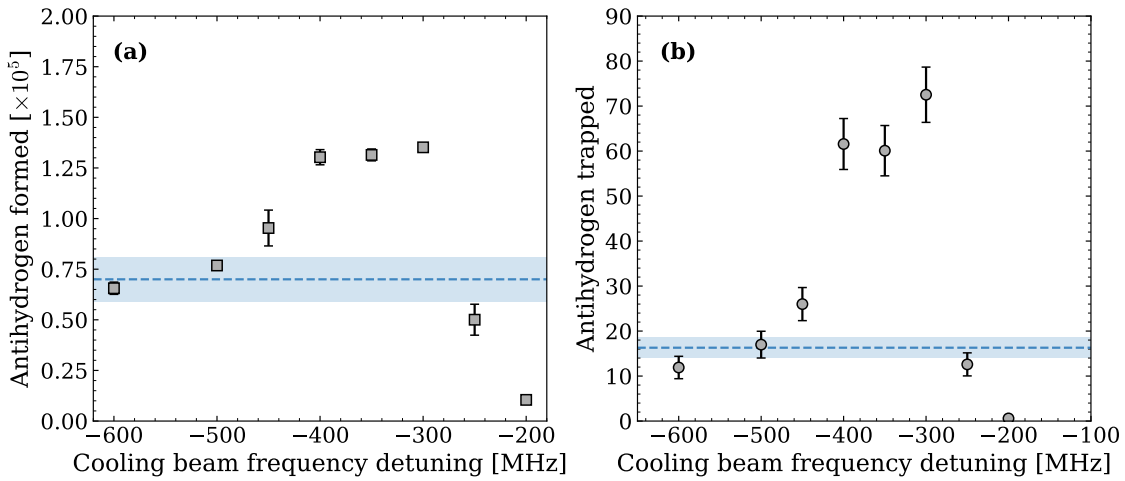

Figure 6.8: Antihydrogen formed (a) and trapped (b) as a function of cooling beam frequency detuning. The black data points represent the data taken with Be^+-assisted antihydrogen synthesis and trapping, the blue dashed line and band show the results before this technique was applied (e^+ cyclotron cooling only). The error bars include the standard deviation and the error from detector efficiency added in quadrature.

The radius of the positron plasma also varies across all of the detunings studied, modifying the positron density, which has also been simulated to impact the trapping efficiency. The positron plasma parameters in this study, along with the antihydrogen results are summarised in Tab. 6.2. In general, lower positron temperatures strongly enhance the antihydrogen trapping efficiency.

Laser Detuning [MHz]	e^+ Temperature [K]	e^+ Density [$\times 10^7 cm^{-3}$]	$\bar{H}$ formed [$\times 10^5$]	$\bar{H}$ trapped	f_{trap} [$\times 10^{-4}$]
-200	54.90 ± 3.92	9.24 ± 0.35	0.10 ± 0.01	0.6 ± 0.5	0.56 ± 0.46
-250	25.01 ± 0.90	5.69 ± 0.79	0.50 ± 0.07	12.6 ± 2.6	2.52 ± 0.64
-300	8.70 ± 1.07	2.73 ± 0.71	1.35 ± 0.02	72.5 ± 6.1	5.57 ± 0.46
-350	9.43 ± 1.71	2.34 ± 0.15	1.31 ± 0.03	60.1 ± 5.6	4.57 ± 0.44
-400	8.64 ± 0.31	3.21 ± 0.85	1.30 ± 0.04	61.6 ± 5.7	4.73 ± 0.46
-450	24.47 ± 5.60	4.56 ± 0.95	0.95 ± 0.09	26.0 ± 3.7	2.72 ± 0.46
-500	34.50 ± 4.87	5.65 ± 0.22	0.77 ± 0.02	17.0 ± 5.0	2.21 ± 0.32
-600	41.00 ± 6.54	5.90 ± 0.74	1.30 ± 0.02	11.90 ± 2.5	1.81 ± 0.39

Table 6.2: Summary of the study of the effect of positron temperature on antihydrogen synthesis and trapping. This study was performed during the 2023 antiproton run, using 160 mW on the off-axis cooling beam for the FLC step.

Comparisons with simulations

Simulations in [22] predicted a strong dependence of trapping efficiency on temperature,

$$f_{trap} \propto T_{e^+}^{-(1.26 \pm 0.18)}. \tag{6.3.1}$$

To compare, we fitted the same form to the experimental data from the detuning scan,

$$f_{trap} \propto T_{e^+}^{-(0.67 \pm 0.08)}. \tag{6.3.2}$$

The trapping efficiency as a function of positron temperature is displayed in Fig. 6.9: the purple crosses represent the simulated data and the magenta squares the raw experimental data.

The experimentally measured temperature dependence is weaker than predicted, although both simulation and experiment show the same overall trend and lie within the same order of magnitude. Differences are not surprising, given that the simulation assumes some simplifications and lacks some features:

(i) the detailed electric potential manipulations during antihydrogen synthesis are not reflected in the simulation;

(ii) cooling from the radiative cascade of antihydrogen is not included in the simulation; this process reduces the antiatoms' kinetic energy and increases the trapping efficiency, leading the simulations to likely underestimate f_{trap};

(iii) in the experiment, the positron plasma parameters change as antihydrogen synthesis evolves, whereas in the simulation, they remain constant.

The implementation of these in the simulations would allow for a more direct comparison between them and experiments.

Note that, as evidenced in Tab. 6.2, the positron plasma density is not constant across the temperature range studied. The simulations were performed with positron densities matching the

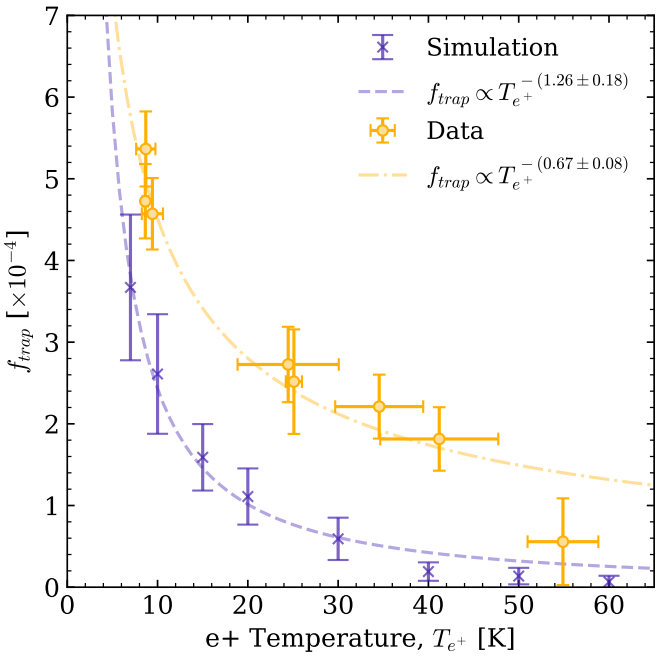

Figure 6.9: Trapping efficiency, f_{trap}, as a function of positron temperature, T_{e+}, for simulated points (purple crosses), and data (yellow circles). The error bars for the experimental data are the propagation of the errors from the number of trapped antihydrogen and formed datasets. The fits to each dataset are also shown along with the fitted parameters and uncertainties.

experimental data in order to untangle the density effect from the temperature effect and allow for a more direct comparison between the two.

The overall conclusion is clear: **lower positron temperatures consistently lead to higher trapping efficiencies.** Whether viewed in terms of absolute numbers or trapping fractions, cooling the positrons below ~ 10 K significantly improves antihydrogen trapping.

Cooling beam power

The cooling beam power influences the positron plasma temperature. As shown in Chapter 5, cooling beam powers above 100 mW yield positron plasmas below 10 K for detunings of -300 and -400 MHz, with the temperature then stabilising at higher powers, consistent with a temperature plateau for laser powers above 100 mW observed in Chapter 5. A similar behaviour is observed in the number of formed and trapped antihydrogen atoms, shown in Fig. 6.10. The -500 MHz dataset shows a steady increase in antihydrogen production and trapping with beam power. The -300 MHz data displays a dip at a laser power of 187 mW, however, since higher powers were not available at the time, it was not possible to determine if this decrease would continue.

In practice, we aim to maximise the power of the cooling beam through the trap, as the usual negative effects of operating above the saturation threshold are not relevant here: the desired Be^+ temperatures are well above the Doppler cooling limit temperature.

The high laser power needed comes from the fact that the ions are trapped in a Penning-Malmberg trap, their motion while confined results in only being resonant with the cooling tran-

sition for short periods of time during an overall motion cycle, as discussed in Section 2.5.

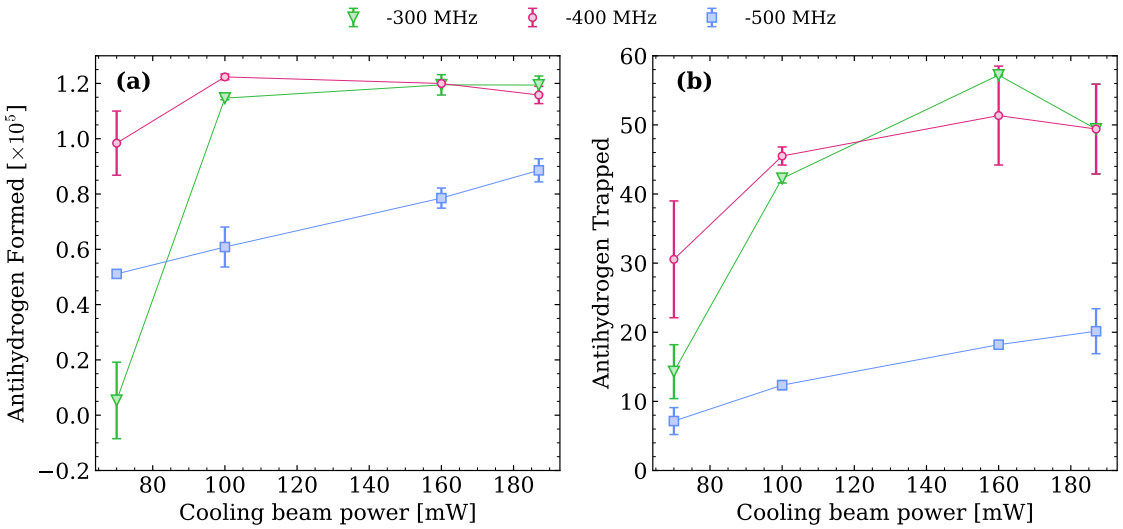

Figure 6.10: Antihydrogen formed (a) and trapped (b) as a function of cooling beam power. Three laser detunings were studied for each laser power: -300 MHz (green triangles), -400 MHz (magenta squares) and -500 MHz (blue circles). The error bars include the standard deviation and the error from detector efficiency added in quadrature.

6.3.2 Effect of positron plasma density on antihydrogen synthesis and trapping

As discussed in subsection 6.2.2, simulations predict that positron plasma density should influence the antihydrogen trapping efficiency, but this had never been experimentally tested. In 2024 we carried out the first direct study of this effect by preparing five different positron plasmas with varying numbers of particles, all sympathetically cooled to below 10 K. The experimental protocol was designed to maintain nearly constant radii across the five numbers, thus changing the plasma densities (details in Chapter 5). This avoids the confounding effect of changing the positron radius, which simulations suggest can alter the trapping efficiency through the radial distribution of antihydrogen formation. The densities corresponding to each number are summarised in Tab. 6.3.

The main challenge of this study was that the sympathetic cooling efficiency depends strongly on the Be^+ population. For each positron number, there is a range of Be^+ ion numbers where the positrons can be stably cooled below 10 K. The width of this range becomes narrower as the positron number increases: for 2.95×10^6 positrons, the stable range width was $\sim 56\,000$ ions, but at the highest studied number, 4.32×10^6 positrons, it was only $\sim 10\,000$ ions. At the intermediate numbers, the range widths were $\sim 88\,000$, $\sim 30\,000$ and $\sim 15\,000$, respectively. Such narrow windows make the experiments increasingly more sensitive at higher densities.

This study was performed with suboptimal vacuum conditions, which increased the variations in Be^+ number. During antihydrogen synthesis, drifts in this parameter can push the system outside its ideal range, resulting in hotter positrons and suppressed antihydrogen formation. For the three lowest densities, fewer than three every ten synthesis cycles fail due to instabilities in Be^+

number, even under non-ideal vacuum conditions. In contrast, for a density of 4.37×10^7 cm^{-3}, the failure rate increased to 55 % and for the highest density, the observed failure rate was 70 %. In these cases, Be^+ number fluctuations were more than twice the ideal range for reliable positron sympathetic cooling. The data used to study the effect of density was filtered to eliminate failed attempts clearly due to Be^+ number only. In this context, a failed attempt is defined as a synthesis cycle with less than 100 000 antihydrogen are formed and the Be^+ number measured in the half-dump is outside the ideal sympathetic cooling range.

The results of this study are shown in Fig. 6.11, the error bars correspond to the standard deviation, taking into account the uncertainty in the detector efficiency. The data shows large statistical fluctuations, nevertheless, a positive trend can be identified: both antihydrogen formation and trapping increase with positron density. This confirms the general simulated prediction that denser positron plasmas result in higher trapping efficiencies.

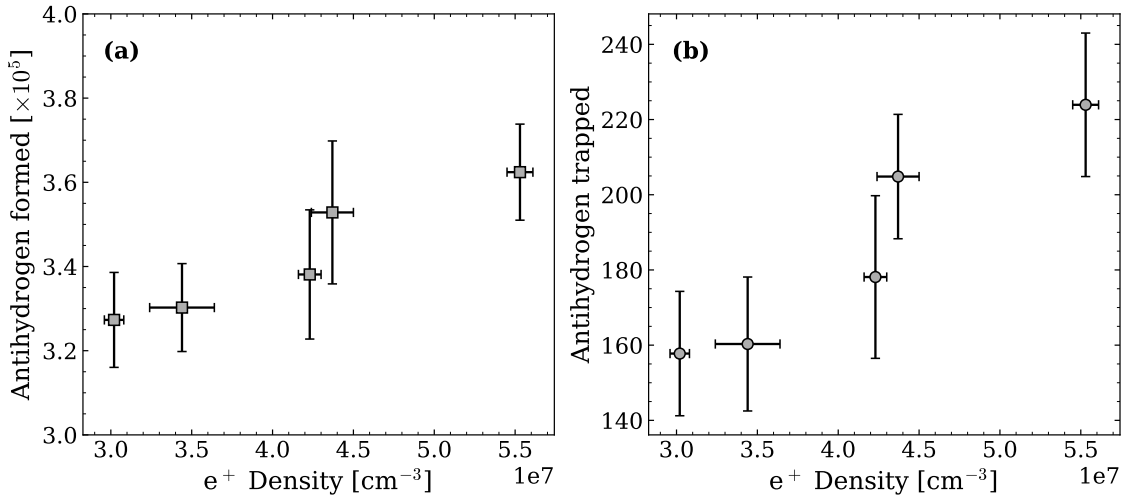

Figure 6.11: Antihydrogen formed (a) and trapped (b) as a function of the positron plasma density. The error bars include the standard deviation and the error from detector efficiency added in quadrature. The data was filtered to eliminate clear failures from Be^+ fluctuations.

Moreover, the density dependence seems to become less prominent at lower densities, as shown in both plots of Fig. 6.11, indicating a possible plateau. Repeating this study under better trap conditions would help minimise the Be^+ instabilities and hopefully reduce the statistical spread of the data. The summary of the positron plasma parameters during this study and the antihydrogen results are shown in Tab. 6.3.

Time structure of antihydrogen formation

The antihydrogen formation over time can inform on the conditions of the particles during synthesis. The time structure of antihydrogen formation for the five studied densities is shown in Fig. 6.12. The data was shifted to start the rise at $t = 0$ for easier shape comparison.

The potential merge rate is fixed across all positron densities during this study. At higher positron densities, the flux of positrons exiting the well is greater, so more positrons interact with antiprotons per unit time. This can explain the sharper, higher peak in the number of formed anti-

e^+ Number $[\times 10^6]$	e^+ Density $[\times 10^7 \mathrm{cm}^{-3}]$	e^+ Temperature [K]	$\bar{H}$ formed $[\times 10^7]$	$\bar{H}$ trapped	f_{trap} $(\times 10^{-4})$
2.95 ± 0.02	3.02 ± 0.06	6.9 ± 0.6	3.27 ± 0.11	157.8 ± 16.5	4.82 ± 0.53
3.23 ± 0.01	3.44 ± 0.20	5.5 ± 0.8	3.30 ± 0.10	160.3 ± 17.8	4.85 ± 0.56
3.74 ± 0.01	4.23 ± 0.07	8.7 ± 1.9	3.38 ± 0.15	189.6 ± 21.6	5.27 ± 0.68
4.02 ± 0.01	4.37 ± 0.13	7.1 ± 1.7	3.53 ± 0.17	204.8 ± 16.5	5.81 ± 0.55
4.32 ± 0.02	5.53 ± 0.08	9.2 ± 1.9	3.63 ± 0.11	223.9 ± 19.0	6.18 ± 0.56

Table 6.3: Summary of the study of the effect of positron density on antihydrogen synthesis and trapping. This study was performed during the 2024 antiproton run under similar vacuum conditions for each studied density.

hydrogen atoms in the initial stages of synthesis for higher densities (yellow and orange data). Furthermore, theory suggests that before antihydrogen synthesis begins, the antiprotons are cooled through collisions with the positrons, and higher positron numbers should accelerate this process, allowing synthesis to start at a higher rate. However, the antiproton population is depleted more rapidly, shortening the overall synthesis period. Since the initial production rate is higher, more antiprotons will interact with the cold denser positrons, both of which are favourable conditions, thus increasing both the synthesis and trapping numbers for higher positron densities.

Interestingly, the two lowest positron densities show little difference in either the time structure of the number of formed antihydrogen atoms. This suggests a lower density plateau where this parameter stops significantly influencing the antihydrogen yield, such behaviour is not predicted by simulations.

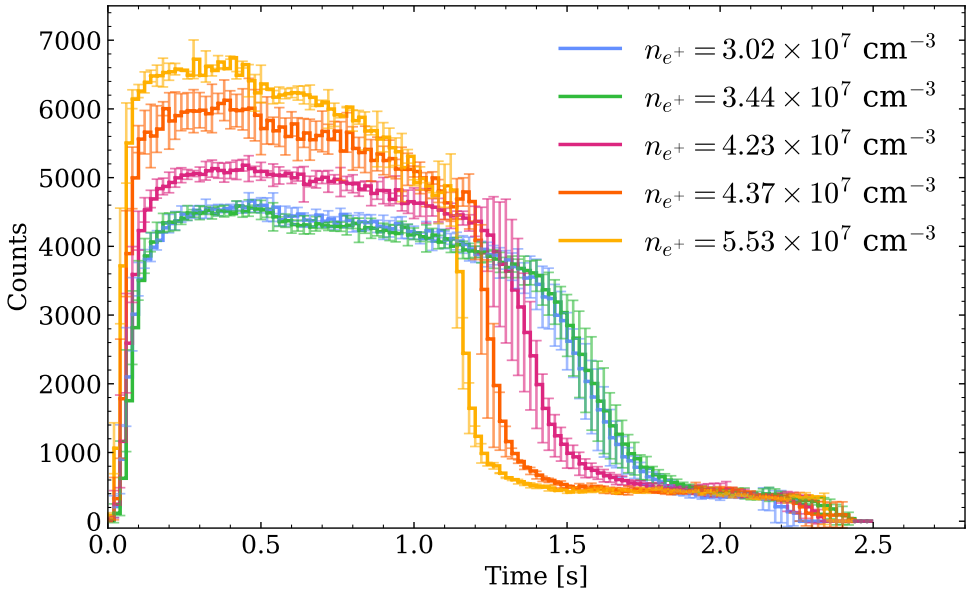

Figure 6.12: Antihydrogen formed as a function of time for five positron densities. The curves are shifted so that the signal rise starts at $t = 0$, binned in 20 ms intervals, allowing a direct comparison of the time structure of the antihydrogen formation.

Comparisons with simulations

Let us revisit the simulations from [22] regarding the effect of positron density, n_{e^+}, on the antihydrogen trapping efficiency, f_{trap}. The predicted relation follows a power law,

$$f_{trap} = A n_{e^+}^{\alpha}, \tag{6.3.3}$$

where A and α are constants.

The density effect was simulated for three different positron temperatures (10 K, 15 K, and 30 K); here, we focus on the 10 K case, as all the positron temperatures were measured to be $\lesssim 10$ K. The simulated points and the corresponding fit using Eq. 6.3.3 are shown in orange in Fig. 6.13, yielding

$$f_{trap} = (9.44 \pm 0.69) \times 10^{-8} n_{e^+}^{0.47 \pm 0.04}, \tag{6.3.4}$$

where the uncertainties arise from the fit error.

The experimental data is also shown in black in Fig. 6.13 for the five studied densities, and the corresponding fit gives

$$f_{trap} = (1.73 \pm 0.64) \times 10^{-7} n_{e^+}^{0.46 \pm 0.21}. \tag{6.3.5}$$

This result closely matches the simulated data, aside from a vertical offset, which may reflect the fact that the simulation assumes $T_{e^+} = 10$ K, whereas the experimental positron temperature is likely lower. Despite the simulation limitations discussed in the previous section, the agreement is

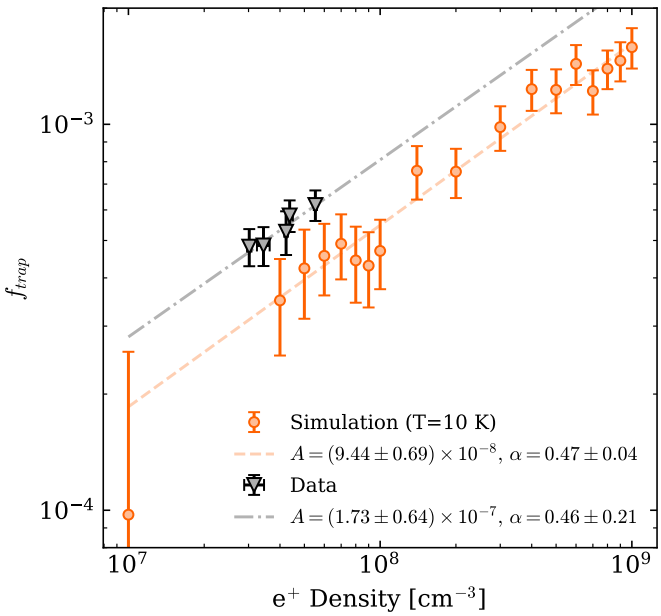

Figure 6.13: Antihydrogen trapping efficiency as a function of positron density for simulated (orange circles) and experimental data (black squares). Both datasets were fit with a power law defined in Eq. 6.3.3, the fit parameters are shown in the legend of the image.

encouraging and supports the use of simulations as a tool to guide future experiments. A broader range of positron densities should be studied to fully understand the density dependence of an-

tihydrogen synthesis and trapping. For instance, the uncertainty in the α parameter is very large (Eq. 6.3.5), could be reduced with higher-density data to constrain this parameter. Additionally, the antihydrogen formation time structure shown in Fig. 6.12 indicates a plateau between the two lowest densities, which is not captured by the simulations. Studying even lower positron densities would clarify the extent of this effect.

This represents the first direct experimental study of the effect of positron plasma density on antihydrogen synthesis and trapping. The high trapped antihydrogen numbers and promising agreement with simulations suggest that more thorough investigations could both improve the antihydrogen yield per synthesis cycle and provide a deeper understanding of the dynamics of antihydrogen formation via three-body recombination.

6.3.3 Effect of cooling beam pointing during antihydrogen synthesis and trapping

During the physics programme, one of the detectors used for beam stabilisation (off-axis D2 in Fig. 4.8) was accidentally moved. Although the beam position was stabilised to the same location on the detector, the detector itself had shifted relative to the trap, altering the beam's angle through the trap. This misalignment resulted in a significant drop in antihydrogen trapping rate, prompting an investigation into how beam pointing affects antihydrogen synthesis.

The experimental procedure for this study was as follows: the target x-y position of the off-axis cooling beam on D2 (downstream of the trap) was adjusted, and three consecutive antihydrogen synthesis cycles were performed at this new position. The Neutral Trap magnets were then de-energised, releasing the trapped antihydrogen atoms, which were then detected and counted by the SVD. This gave a measurement of the number of trapped antihydrogen atoms per beam position. This procedure was repeated for a set of x-y positions. Results are shown in Fig. 6.14, where the number of trapped antihydrogen atoms per synthesis cycle is plotted against the x-y positions of the off-axis beam on D2. Due to time constraints, the full 2D parameter space could not be thoroughly explored. Instead, an initial scan identified an optimal x-position, followed by a scan of the y-position around this ideal x-position target. The x-y position which maximises the number of trapped antihydrogen atoms was found to be (-0.5, 1.0) mm.

A more detailed study is necessary to have a deeper understanding of the effect of the cooling beam alignment through the trap. Future scans should include measurements of the positron radial profile and temperature at each beam position to provide a more complete characterisation. A finer map of the 2D space should be performed, as the maximum of the x position at y = 0 mm may not match the maximum in x at the new ideal y = 1.0 mm position. Since changes at D2 alter the beam's angle through the trap, studying pure beam translations would also be of interest. This would be more complex as it would require simultaneous D1 and D2 target position changes.

Despite the limitations of the scan in Fig. 6.14, several conclusions can still be drawn. Notably, there appears to be a relatively wide range of x positions, between –2 mm and –0.75 mm, over which the trapping rate remains largely insensitive to the x-position, with negligible variations in the number of trapped antihydrogen atoms. This is most likely due to the beam waist (1.90 mm), which, compared to the usual plasma radii of < 1 mm, is big enough to allow for a broad range of motion where the cooling efficiency is mostly unchanged. In contrast, the trapping rate appears

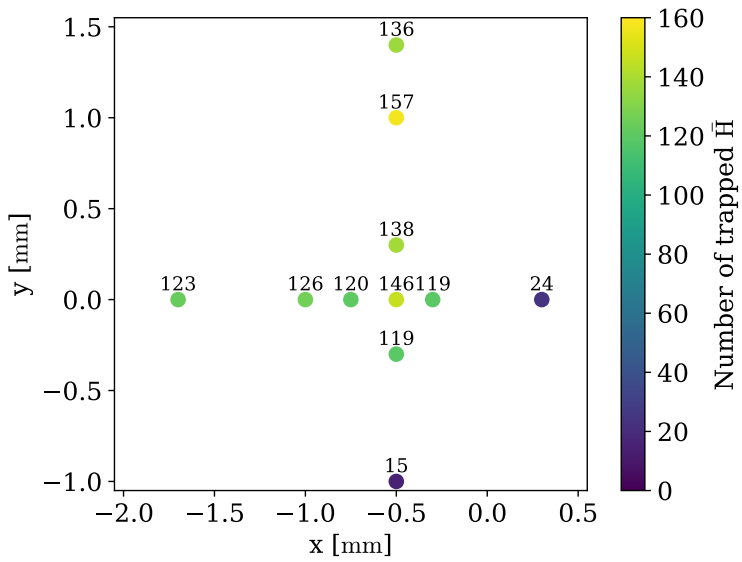

Figure 6.14: Number of trapped antihydrogen atoms per synthesis cycle as a function of the x-y position of the off-axis cooling beam in D2. The values are shown near each data point to facilitate the interpretation of the plot. The x-y position which maximises the number of trapped antihydrogen atoms is (-0.5, 1.0) mm.

more sensitive to changes in the y-position: within a 2 mm range, variations of about 15% are observed in the number of trapped antihydrogen atoms. This is consistent with the scan presented in Fig. 5.8, where the final positron temperature was found to be more sensitive to changes in the y position of the cooling beam in D1. However, for both x and y directions, there appears to be a sharp cut-off beyond which the trapping rate drops to negligible values. This suggests that while the system is relatively robust to small misalignments, precise alignment remains critical for efficient antihydrogen synthesis.

6.3.4 Effect of slow potential merge rate on antihydrogen synthesis and trapping

The effect of the potential well merge rate on antihydrogen synthesis was studied by varying the duration of the synthesis window while maintaining the initial and final wells unchanged. Let's define the rate at which the potential well depths change during the antihydrogen synthesis process as the merge rate, R. The summary of these results for the 2023 and 2024 synthesis protocols are shown in Fig. 6.15.

For the 2023 dataset (yellow circles in Fig. 6.15), the number of formed and trapped antihydrogen atoms was largely insensitive to the merge rate for $R \gtrsim 1$ V/s, both the formed and trapped antihydrogen numbers stabilised in this region. Slower merge rates, however, led to fewer trapped antihydrogen atoms, even though not by a significant amount.

The 2024 dataset (black squares in Fig. 6.15), displays a different behaviour. If the potentials change too quickly ($R = 1.33$ V/s, for example), almost no antihydrogen is formed, and consequently, negligible amounts are trapped. There is a trapped fraction plateau for intermediate merge rates ($0.25 \lesssim R \lesssim 1.00$ V/s), while very slow merges again reduce both the number of

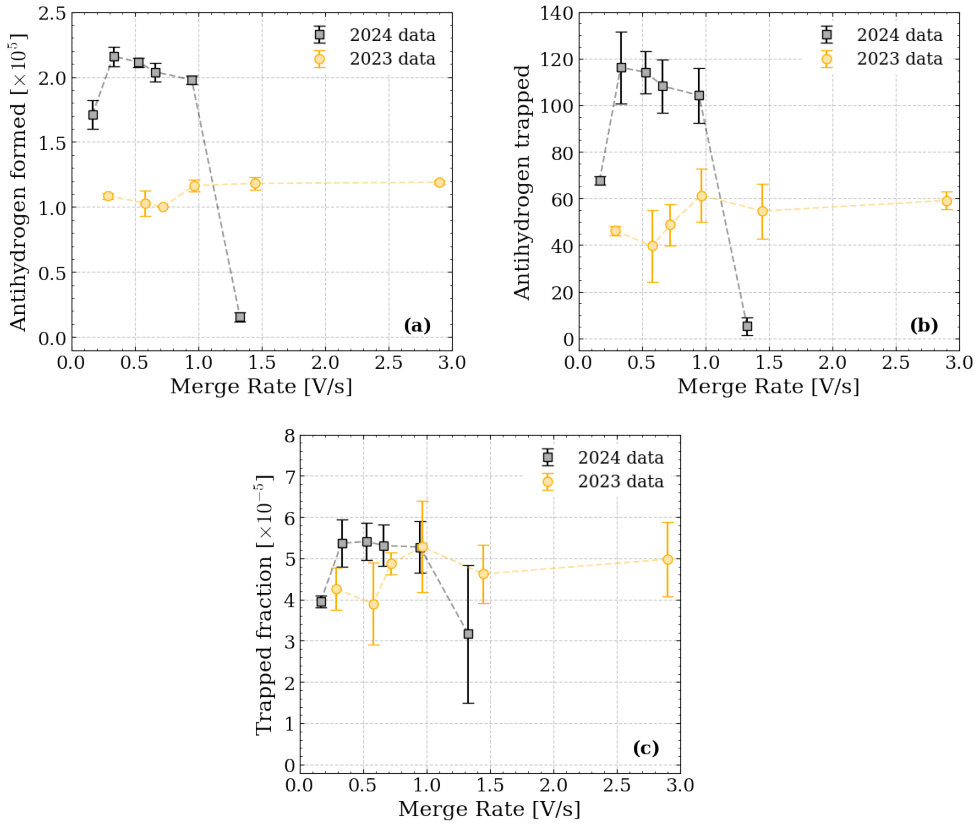

Figure 6.15: Antihydrogen formed (a), antihydrogen trapped (b) and trapped fraction (c) as a function of the merge rate of the potentials in the slow merge technique for 2023 (yellow circles) and 2024 (black squares) data. The error bars include the standard deviation and the error from detectors efficiency added in quadrature.

formed and trapped antiatoms.

The different behaviour between the 2023 and 2024 datasets could be related to the larger number of antiprotons in 2024: the antiproton density was higher, and thus, to obtain similar antiproton ejection rates, the potentials had to be merged more slowly (lower merge rates). The positron number remained constant between the two antiproton runs, but their density may have differed slightly, since the 2023 dataset used the on-axis cooling beam for FLC, which would also affect the ideal merge rate for antihydrogen synthesis.

Other factors, such as positron heating, become increasingly important for longer synthesis windows (some of the data here corresponds to $8 - 10$ s windows). Overall, these observations suggest that the merge rate has an effect on the antihydrogen formation, but there exists a broad range of rates yielding statistically similar results. This optimal range depends on both the antiproton and positron conditions, and if either of these changes significantly, a new scan of this parameter is recommended to ensure ideal antihydrogen synthesis performance.

On the other hand, the timescale of the potential slow merge is in the order of seconds, which is very long compared to any plasma motions. Intuitively, the antihydrogen synthesis should be lower if the potential merge rate is too small, not allowing for time for the antiprotons to cool and for many formation cycles to occur. However, slow potential merges should not greatly affect the

total antihydrogen trapping efficiency, unless they are so long that heating and expansion in the octupole field yield positron and antiproton plasmas unfavourable for antihydrogen synthesis. There should be a broad range of merge rates where the antihydrogen formation flattens.

6.3.5 Positron evolution during antihydrogen synthesis

To study the evolution of the positron plasma parameters during antihydrogen synthesis, we interrupted the slow potential merge at different points and measured the positron temperature and radial profile. The potential wells of the five different stages examined are shown in Fig. 6.16:

- (a) $t = 0$ s: immediately before the merge begins, well depth 3.30 V;
- (b) $t = 0.5$ s: well depth 2.65 V;
- (c) $t = 1.0$ s: well depth 2.06 V;
- (d) $t = 1.5$ s: well depth 1.44 V;
- (e) $t = 3.0$ s: end of the synthesis window, well depth 0 V.

Unlike changing the overall synthesis duration (which alters the slow potential merge rate, keeping the same final potential well depth), here, the ramp rate is fixed and the merge is interrupted at set times, with the final well depth adjusted for each stage.

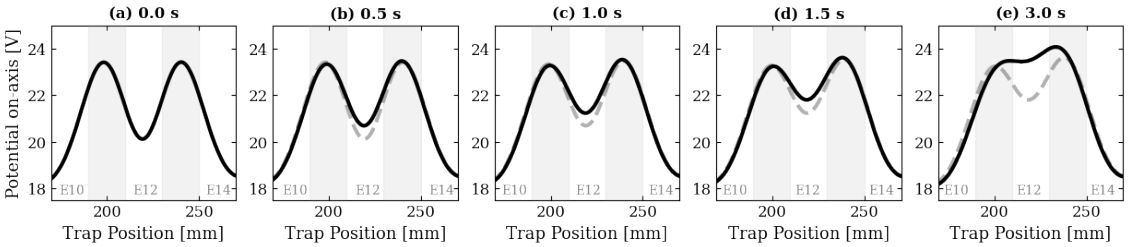

Figure 6.16: Potential well on-axis as the antihydrogen synthesis process evolves: 0 s (a), 0.5 s (b), 1 s (c), 1.5 s (d) and 3 s (e). The depth of the well in which the particles are confined decreases over time, with the positrons and antiprotons beginning to interact as their spatial distributions overlap. The on-axis potential well depths at each stage are: 3.30 V at 0 s (a), 2.65 V at 0.5 s (b), 2.06 V at 1.0 s (c), 1.44 V at 1.5 s (d), and 0.00 V at 3.0 s (e).

Radial profile evolution

After each step, the remaining positrons were released towards the US-facing A2DS MCP. The resulting images are shown in Fig. 6.17 along with fitted radii obtained from 2-D Gaussian fits, (Section 3.2). No profile was taken at $t = 3.0$ s since all of the positrons had been released from the well at that point. As expected, the positron number decreases and the plasma radius increases as antihydrogen synthesis progresses, as summarised in Tab. 6.4.

The plasma radius increases by $\sim 38\,\%$ during the first 1.5 s of antihydrogen synthesis, while the positron number decreases by $\sim 66\,\%$. A summary of the positron parameters as antihydrogen synthesis evolves is shown in Tab. 6.4. The radial expansion is not linear; in fact, most of the

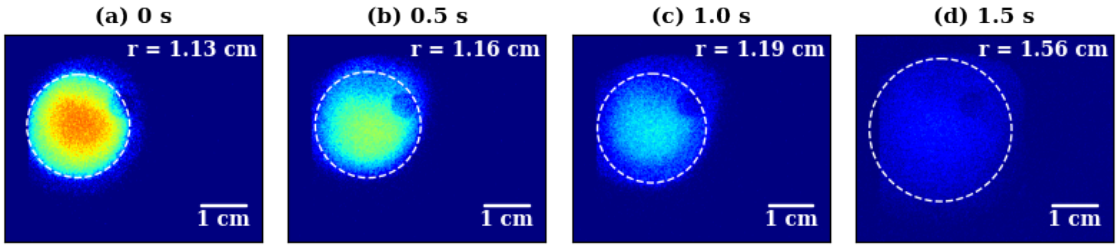

Figure 6.17: Radial profile of the positron plasma at different stages of the mixing process: 0 s (a), 0.5 s (b), 1.0 s (c) and 1.5 s (d). As the slow potential merge evolves (according to the potentials in Fig. 6.16), the remaining positron cloud in the well expands. The dashed line represents the fit using Eq. 3.2.1, as described in Section 3.2. The radii quoted here correspond to the radii at the MCP location, the plasma was imaged in the US-facing A2DS MCP. As the plasma expands, it begins to clip on an aperture during extraction, which increasingly complicates accurate fitting. The colour scale across all four images is based on the pixel intensity of the image at $t = 0$ s (a), allowing for a qualitative comparison of the number of particles remaining in the well at each stage. A damaged region on the MCP causes the anomalies observed in the images and does not correspond to actual structures in the positron cloud.

expansion occurs between 1.0 s and 1.5 s. On the other hand, the positron number decreases in a relatively linear manner with the potential well reduction. This suggests that the positron density does not evolve uniformly throughout the process. While the plasma length does decrease slightly during synthesis, its effect on the density is small compared to the contributions from the radial expansion and the significant reduction in positron number.

Since lower positron density is expected to reduce the antihydrogen trapping fraction, this effect likely contributes to the decline in trapping efficiency as synthesis progresses. However, the dominant factor in the reduction of the antihydrogen synthesis rate is the steady depletion of antiprotons as they combine with positrons to form antihydrogen, a constraint that ultimately limits the synthesis yield.

Duration [s]	e^+ number	e^+ radius [mm]	e^+ temperature [K]
0	$(3.70 \pm 0.19) \times 10^6$	1.08 ± 0.02	9.12 ± 0.85
0.5	$(2.62 \pm 0.13) \times 10^6$	1.11 ± 0.02	6.73 ± 0.99
1.0	$(2.07 \pm 0.10) \times 10^6$	1.13 ± 0.3	9.17 ± 1.96
1.5	$(1.27 \pm 0.07) \times 10^6$	1.49 ± 0.04	7.64 ± 0.23

Table 6.4: Summary of the parameters of the positron (e^+) plasma at different stages of antihydrogen synthesis. The uncertainty in the e^+ number combines the sample standard deviation with the uncertainty from the MCP number calibration, added in quadrature. Similarly, the e^+ radius and temperature include uncertainties from both the statistical spread of the samples and the fitting errors, also combined in quadrature. Three MCP radial profiles and five temperature measurements were obtained for each duration. The radii quoted in this table correspond to the radii of the plasma inside the trap.

The expected scaling $N_0/N =< r^2 > / < r_0^2 >$ (see Section 3.2) is not satisfied by the data. Computing the relative deviation from the theoretical expectation, for the first point the agreement is exact by definition, but as the synthesis evolves, the radii are systematically smaller than expected, with deviations of $25-39\,\%$. This indicates that the simple scaling does not fully capture the behaviour of the plasma in these measurements, although the trend is qualitatively consistent.

Positron temperature evolution

The positron temperature remains below 10 K throughout the whole synthesis time window, as shown in Tab. 6.4. No significant variations or trends were observed. However, the current temperature diagnostics limit our ability to distinguish small variations at these low temperatures.

Antihydrogen formation evolution

The datasets were collected over a five-hour period, mitigating fluctuations in antiproton number due to the ELENA performance of vacuum quality. Fig. 6.18 plots (b) and (c) show the number of formed and trapped antihydrogen atoms as a function of the time since the start of the antihydrogen synthesis, respectively. The green squares indicate the normal synthesis procedure: laser cooling of Be+ ions continues during the antihydrogen formation. Almost 90 % of antihydrogen is produced within the first second of synthesis, and consequently, the number of trapped antiatoms plateaus after the 1.0 s mark. It is important to emphasise that the times referred to here are for this specific data set. If, for example, the potential merge rate were shorter, all of the key times quoted throughout this section would also be shorter.

Role of laser cooling during antihydrogen synthesis

We also investigated the effect of switching off the laser cooling during synthesis. In this case, the final laser cooling step is still applied, but the shutter is closed once the slow potential merge begins. The magenta circles in Fig. 6.18 show the dataset without laser cooling during antihydrogen synthesis. Without laser cooling, the positron temperature rises sharply to $\sim$ 100 K within 0.5 s and remains constant thereafter (Fig. 6.18 plot (a)). As a result, antihydrogen synthesis and trapping drop nearly to zero, as seen in Fig. 6.18 plots (b) and (c). This highlights once again the critical role of low positron temperature in enabling efficient antihydrogen synthesis and trapping.

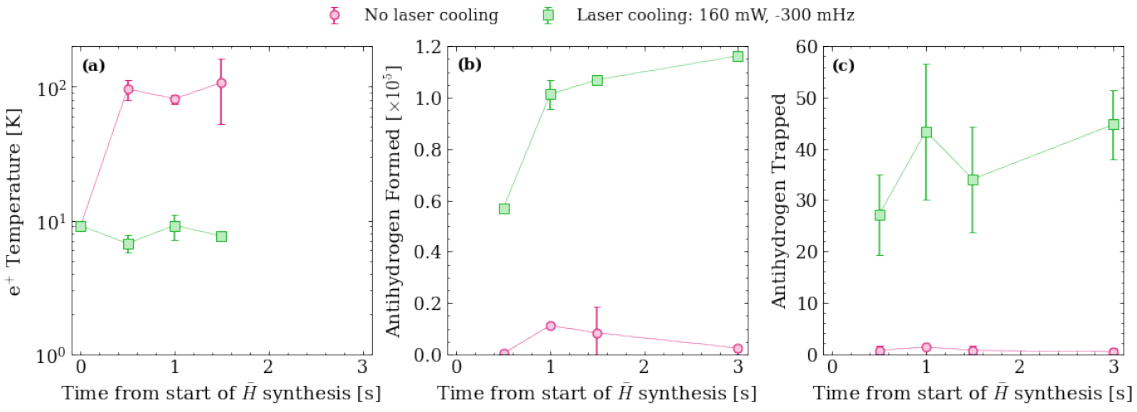

Figure 6.18: Positron temperature (a), antihydrogen formed (b) and antihydrogen trapped (c) at different stages of antihydrogen synthesis. The green squares show data with laser cooling active during the antihydrogen synthesis, and the magenta circles represent data taken without laser cooling during synthesis.

6.3.6 On-axis vs Off-axis cooling beams for Final Laser Cooling (FLC) step

The initial implementation of Be^+-assisted antihydrogen synthesis and trapping in 2023 employed the Final Laser Cooling (FLC) step using the on-axis cooling beam. This configuration did not permit post-synthesis diagnostics. Due to time constraints, the on-axis cooling beam was used for the FLC step for the remainder of the 2023 antiproton run. The off-axis cooling beam, by contrast, was exclusively used in 2023 for studies of antihydrogen synthesis, as it enabled diagnostics immediately after synthesis. Demonstrating robust and reproducible FLC with the on-axis cooling beam was also a crucial proof of principle for implementing the Be^+ system in ALPHA-g [5]. Nevertheless, the use of the off-axis cooling beam for FLC remained of particular interest for ALPHA-2.

At the beginning of the 2024 antiproton run, one of the first developments was a comparison of antihydrogen synthesis performance between the two cooling beams, followed by the implementation of the off-axis beam as the primary FLC beam during antihydrogen accumulation for subsequent experiments.

The technique was re-established with the on-axis beam, and the parameters were re-optimised for this configuration. The procedure was then adapted to enable the use of the off-axis cooling beam for the FLC step, and its parameters were subsequently optimised. Slightly different settings were required for the two beams to maximise the number of trapped antihydrogen atoms: the optimal laser detuning for the on-axis cooling beam was found to be -500 MHz, whereas for the off-axis cooling beam, it was -300 MHz. The different Doppler shifts experienced by the ions due to the beam orientations can shift the ideal detuning for laser cooling. The on-axis beam has less of a radial component than the off-axis beam thus will interact with the ions differently. In a Penning-Malmberg trap, the plasma rotates, and the ions have an azimuthal velocity in addition to their thermal motion. The on-axis beam is aligned with the trap axis, so the Doppler shift from the plasma rotation is minimal. On the other hand, the off-axis beam is tilted by 2.4° with respect to the trap axis. Thus, the velocity distribution sampled by the off-axis beam is shifted relative to that seen by the on-axis beam, leading to a different effective Doppler shift, and consequently, a different optimal detuning for laser cooling.

To compare the performance of each cooling beam under comparable conditions, five synthesis cycles were performed with the optimal on-axis parameters, followed by five synthesis cycles with the optimal off-axis parameters. This ensured identical vacuum conditions and minimised variations in the injected antiproton number from ELENA. The summary of this study is shown in Tab. 6.5. FLC with the off-axis cooling beam yielded a marginally higher number of antihydrogen formed and trapped. The trapped fraction, f_{trap}, is the same between the two beams. Combined with the increased performance, the availability of post-synthesis diagnostics led to the implementation of the off-axis beam for FLC for the remainder of ALPHA-2 operation.

6.3.7 Summary

The conditions of the positron plasma have a strong influence on antihydrogen synthesis and trapping. Lower positron temperatures are clearly beneficial, improving the trapping efficiency. It was shown that laser powers of above 100 mW are desired to avoid a decrease in trapping efficiency.

[5] The details of the plans for this implementation and its associated challendes are discussed in Chapter 8.

FLC beam	$\bar{H}$ formed	$\bar{H}$ trapped	f_{trap}
On-axis	$149\,590 \pm 4\,486$	68.7 ± 12.7	$(4.59 \pm 0.81) \times 10^{-4}$
Off-axis	$155\,551 \pm 3\,450$	86.5 ± 14.0	$(5.56 \pm 0.66) \times 10^{-4}$

Table 6.5: Comparison of antihydrogen synthesis and trapping performance depending on the cooling beam used for the FLC step. The table lists the mean number of antihydrogen atoms formed ($\bar{H}$ formed), the number trapped ($\bar{H}$ trapped), and the trapping fraction (f_{trap}), for each beam configuration.

Precise beam pointing is also critical: there is a broad range over which antihydrogen synthesis is relatively insensitive, but once a threshold is crossed, the trapping rate drops sharply, highlighting the importance of active beam stabilisation.

The first systematic experimental study of the effect of positron plasma density on antihydrogen synthesis and trapping was carried out. Higher positron densities improve the trapping efficiency, but they are also more prone to instabilities due to fluctuations in positron cooling. Comparisons with simulations show good agreement for the positron density dependence, while the observed temperature dependence is consistent with the simulation in order of magnitude. Overall, these studies provide quantitative insight into the key parameters that optimise antihydrogen synthesis and trapping.

6.4 Be^+-Assisted Antihydrogen Accumulation

Antihydrogen accumulation is the process of repeating synthesis cycles without de-energising the Neutral Trap magnets. In a typical ALPHA-2 spectroscopy experiment, about 200 synthesis cycles are repeated overnight for experimentation during the day, but this number can be adjusted to achieve different target amounts of antihydrogen atoms and tailored to various experiments. During long accumulations, some synthesis cycles inevitably fail due to the complexity of the experimental protocol; timing variations or fluctuations in particle numbers can impact the antihydrogen trapping efficiency. A synthesis cycle is classified as 'good' or 'bad' based on a threshold of 50 % of the average number of antihydrogen atoms formed per cycle. Under normal operational conditions, only about 5 % of the synthesis cycles fail. The data in this chapter was filtered to only include synthesis cycles above this threshold. To quantify the accumulation performance, the following expression can be used,

$$N(x) = \frac{\Gamma}{\eta}\left(1 - e^{-\eta x}\right), \tag{6.4.1}$$

where N is the number of accumulated antihydrogen atoms, x is the number of synthesis cycles, Γ is the number of antiatoms added per synthesis cycle, and η is the fractional loss per synthesis cycle. This function reflects the balance between antihydrogen accumulation and loss: for low synthesis cycle numbers, the number of accumulated antiatoms grows approximately linearly with the number of cycles, while for large x, it asymptotically approaches the limit Γ/η.

Antihydrogen losses can arise through different mechanisms. The lifetime of trapped antihydrogen in ALPHA-2 has been estimated to be about 66 hours [113], although this depends strongly on the trap vacuum conditions. Annihilations with background gas molecules constitute a con-

stant source of loss, which can only be mitigated by improving the vacuum conditions in the trap. By contrast, losses arising from interaction with charged particles traversing the antihydrogen volume during their preparation can, in principle, be reduced or eliminated through modifications to the experimental procedure.

Be^+-assisted antihydrogen synthesis and trapping not only increased the number of trapped antihydrogen atoms per synthesis cycle but also made it easier to identify and address antihydrogen losses during the accumulation process. The increased amount of trapped antihydrogen atoms made such losses much easier to detect over the background signal. The evolution of the performance of Be^+-assisted antihydrogen stacking is shown in Fig. 6.19. To simplify this discussion, the four experimental conditions shown in this figure are labelled as follows:

- **Dataset A:** pre-Be^+-assisted synthesis accumulation (black circles)
- **Dataset B:** initial 2023 Be^+-assisted accumulation procedure (magenta crosses)
- **Dataset C:** post-loss reduction 2023 Be^+-assisted accumulation procedure (blue squares)
- **Dataset D:** post-antiproton number increase 2024 Be^+-assisted accumulation procedure (purple diamonds)

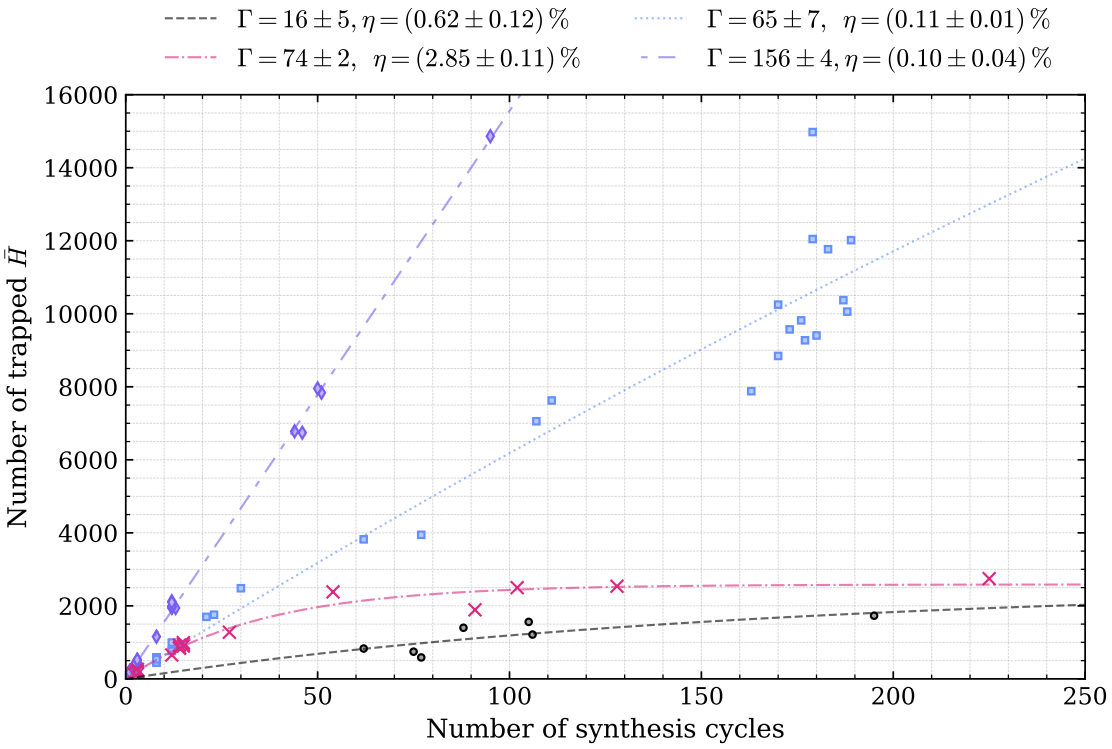

Figure 6.19: Number of trapped antihydrogen atoms as a function of the number of synthesis cycles during accumulation for four different experimental conditions (Datasets A-D, see text). The datasets were fit with the function defined in Eq. 6.4.1, and the optimal fitting parameters for each case are shown at the top of the figure. The number of antihydrogen trapped increased from 16 (magenta dashed line) to 156 after all of the improvements the synthesis and accumulation processes.

Dataset A yields $\Gamma = 16 \pm 5$ antihydrogen per stack; additional points at higher stack numbers would be required to observe significant saturation effects. Dataset B shows an increase in the number of trapped antihydrogen atoms per synthesis cycle of 4.6. However, the accumulation exhibited strong saturation, as reflected by the fractional loss per synthesis cycle of $\eta = 2.85\,\%$. Subsequent improvements reduced these losses, leading to the performance observed in Dataset C: $\Gamma = 65 \pm 7$ antihydrogen per synthesis cycle, and a fractional loss of $\eta = (0.11 \pm 0.01)\,\%$. The antihydrogen loss study and elimination will be discussed in detail in subsection 6.4.2. In conclusion, the application of Be^+-assisted antihydrogen synthesis and trapping resulted in an almost 5-fold increase in the accumulation performance in ALPHA.

Finally, Dataset D represents the improvement in accumulation performance during the 2024 antiproton run. The stark increase from $\Gamma = 65 \pm 7$ trapped antihydrogen per synthesis cycle to $\Gamma = 156 \pm 4$ was a result of an increase in the antiproton number trapped in ALPHA-2 and available for antihydrogen production.

Overall, the increase in the number of trapped antihydrogen atoms per synthesis cycle during accumulation increased by a factor of 9.75 between the pre Be^+- assisted antihydrogen accumulation and the last iteration of this new technique.

6.4.1 Effect of antiproton number increase on antihydrogen trapping rate

The number of antiprotons available for antihydrogen production in ALPHA-2 can be measured by releasing them towards a very well-defined annihilation point near which sits a scintillator which detects the annihilations from the antiproton impact. The detected counts are proportional to the released antiproton number. In 2024, J. Singh developed a technique to increase the number of antiprotons transferred from the CT into ALPHA-2. Combined with an increase in the number of antiprotons delivered to ALPHA by ELENA, the number of antiprotons available for antihydrogen synthesis in ALPHA-2 increased $(164 \pm 9)\,\%$.

To compare this increase with the corresponding change in the number of trapped antihydrogen atoms per synthesis cycle, we can restrict the analysis to the initial portion of the accumulation curves, where the behaviour is approximately linear,

$$N_{\mathrm{lin}}(x) \approx \Gamma_{\mathrm{lin}} x. \tag{6.4.2}$$

Tab. 6.6 shows the fit parameters for the final 2023 iteration (Dataset C) and final 2024 iteration (Dataset D) of the Be^+-assisted accumulation truncated at $x < 20$. The increase in trapped antihydrogen atoms was of $(148 \pm 10)\,\%$, which is compatible with the increase in antiproton number. In the past, changing the antiproton number had been attempted as a way to improve the number of trapped antiatoms. However, the increase was not proportional: a $(63 \pm 6)\,\%$ increase in antiproton number resulted in only a $(20 \pm 11)\,\%$ increase in trapped antihydrogen.

Be^+-assisted antihydrogen synthesis enables a regime where the antiprotons are more efficiently used, and thus a change in antiproton number produces a directly proportional change in trapped antihydrogen. This is evidenced by the shape of the antihydrogen formation curves shown in Fig. 6.20: the black curve corresponds to a synthesis cycle from Dataset A, while the blue curve corresponds to Dataset C. In the absence of sympathetic cooling (Dataset A), the antihy-

	Γ_{lin}	Fit error in Γ_{lin}
Dataset C for $x < 20$	67	3
Dataset D for $x < 20$	164	2
Relative increase [%]	148	10

Table 6.6: Number of accumulated antihydrogen atoms per synthesis cycle for Dataset C and D for accumulations with less than 20 synthesis cycles, using the linear behaviour defined in Eq. 6.4.2. The error in Γ_{lin} was obtained from the fitting algorithm. The relative increase was calculated to be $(148 \pm 10)\,\%$ from Dataset C to D.

drogen formation rate decreases rapidly, whereas in the Be^+-assisted case (Dataset C), it steeply increases and stays relatively constant for about 0.6 s. Since the positron and antiproton densities evolve similarly in both datasets, the key difference must be the positron temperature stability over time. With sympathetic cooling, the positrons remain colder throughout the synthesis cycle, extending the period during which the antihydrogen can be successfully synthesised. By contrast, in Dataset A, the positrons are subject to rapid octupole-induced heating during antihydrogen synthesis with a less efficient cooling mechanism (cyclotron cooling only), rapidly reducing the antihydrogen formation efficiency.

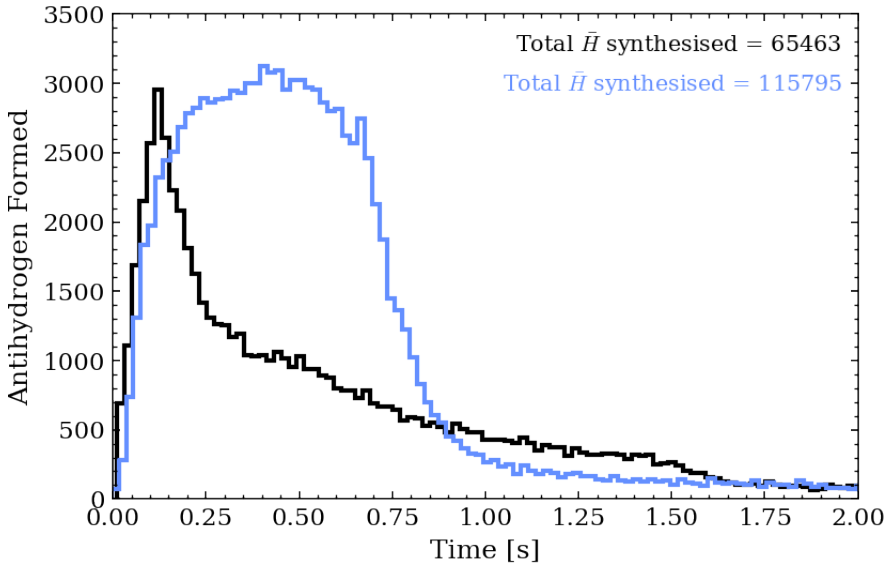

Figure 6.20: Antihydrogen formed as a function of time for an example synthesis cycle of Dataset A (black histogram) and Dataset D (blue histogram). The SVD counts have been binned in 20 ms bins for both datasets.

This emphasises that the proportional scaling observed in 2024 was not solely the result of a greater antiproton supply, but critically depended on the Be^+-assisted technique, which ensured that the additional antiprotons could efficiently be converted into trapped antihydrogen.

6.4.2 Antihydrogen losses during accumulation

As mentioned in the previous section, the increase in trapping rate allows for the investigation of antihydrogen losses during accumulation, since we now have enough losses to distinguish from the background rate. This allowed for a thorough investigation into the accumulation performance and to eliminate the most evident antihydrogen loss sources.

The different events that happen during a synthesis cycle can be identified by the timestamps in the log of the run operations. At ALPHA, each operation, such as Be^+ loading into the trap, is labelled with a start and stop time, along with all of the SVD information to make analysis easier. Each of these blocks is called a *spill*. To search for antihydrogen losses, we can go through all of the recorded spills and check the SVD annihilation counts to find time windows where annihilations are abnormally high.

Upon this investigation, three main loss sources were identified, these time windows are shown in Fig. 6.21. The plots are the vertices detected in the SVD during antihydrogen synthesis cycles. Each panel corresponds to a different spill. The red dashed lines mark the axial barriers of the antihydrogen volume (antihydrogen is only accumulated between -14 to 14 cm). Any signal outside of this axial range is either a background signal or antiprotons being released from the trap by annihilations with background gas, not antihydrogen losses. Moreover, if the losses within a certain time window are independent of the number of antihydrogen atoms in the trap (equal for every synthesis cycle), this can be attributed to background signal, as losses of trapped antihydrogen atoms will increase with the number of confined antiatoms.

(a) Losses due to electron SDREVC

Tens of millions of electrons are loaded and trapped into ALPHA-2 to sympathetically cool the antiprotons upon their recapture. To avoid fluctuations from the electron gun and to control the electron plasma parameters, the SDREVC technique (see subsection 2.2.3) is employed. During this process, millions of electrons are evaporatively cooled out of the well and exit the trap. This preparation occurs in the left normal trap, and the electrons can either exit the well towards the antihydrogen volume, as shown in panel (a) of Fig. 6.22, or away from it, as illustrated in (b) of Fig. 6.22. In case (a), the electrons traverse the trap volume where the antihydrogen atoms are confined, leading to annihilations. If an electron annihilates with a positron in an antihydrogen atom, gamma rays are produced, which cannot be detected by ALPHA. However, the remaining antiproton eventually annihilates with the trap walls, producing pions that leave tracks in the SVD. These annihilations are shown in panel (a) of Fig. 6.21.

The signal in panel (a) of Fig. 6.21 corresponds to the losses from a single experiment with 225 synthesis cycles (run R68965). During the run, $2\,224$ antihydrogen atoms were lost during the electron SDREVC window, while $2\,835$ remained at the end of accumulation, corresponding to $\sim 44\,\%$ losses relative to the final sample size. Fortunately, eliminating these losses was very straightforward: the electron ejection direction was reversed so that they no longer crossed the antihydrogen volume. After this modification, the losses during electron SDREVC fell to negligible levels.

Fig. 6.23 compares the two cases. In plot (a), the data were binned in intervals of three synthesis cycles; within each bin, the mean annihilations per cycle were calculated, and the standard

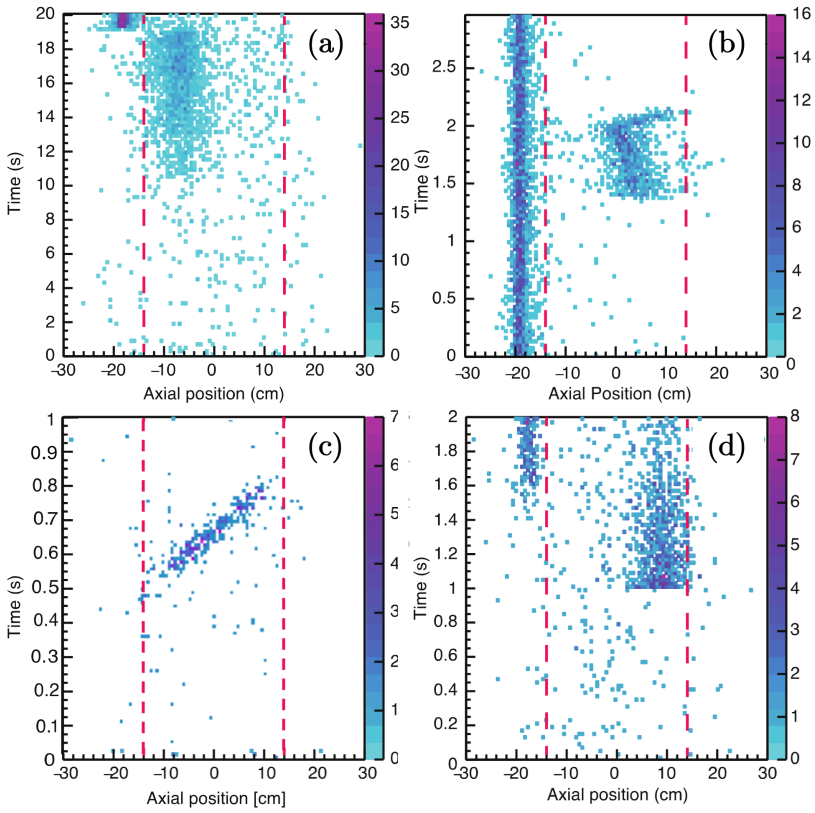

Figure 6.21: Antiproton annihilations observed in the SVD during various steps of an antihydrogen synthesis cycle. Each plot corresponds to the cumulative annihilations in a specific time window over many synthesis cycles. Annihilations between two dashed red lines correspond to antihydrogen losses. The significant annihilation line centred around $z = -20$ cm is due to the antiproton annihilation with residual gas during their preparation in the left normal trap. Panels (a) to (d) correspond to electron SDREVC, Be^+ shuffle through the antihydrogen volume, Be^+/e^+ merge in E14/E15, and positron capture in ALPHA-2, respectively.

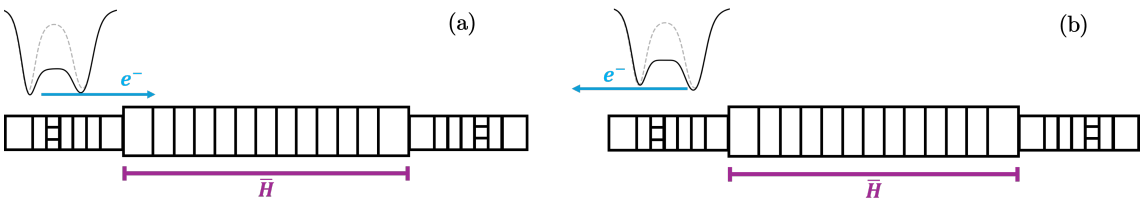

Figure 6.22: Sketch of electron release towards (a) and away (b) from the antihydrogen volume during electron SDREVC. The dashed lines represent the initial on-axis potentials and the full lines the final potentials. The blue arrow shows the direction from which the electrons exit the confining wells.

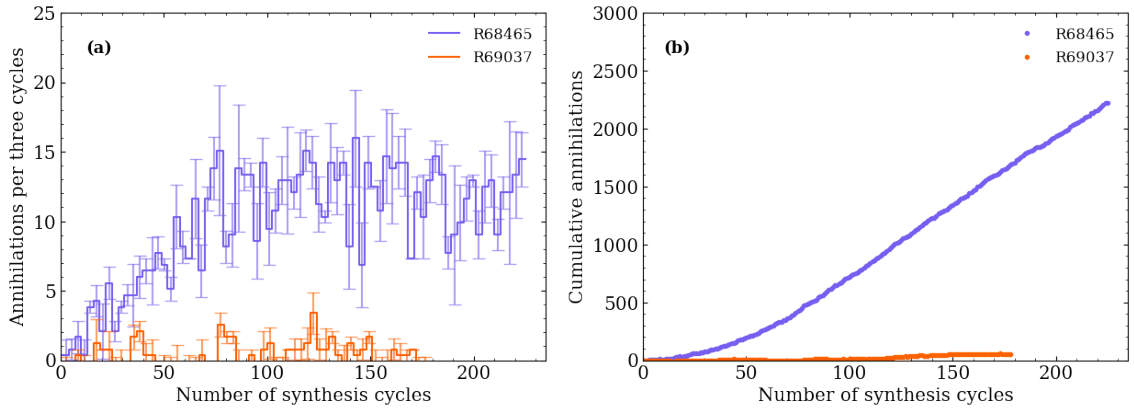

Figure 6.23: Antihydrogen losses due to annihilations with electrons during electron SDREVC with the electrons being expelled towards the antihydrogen volume (R68465) and away from the antihydrogen volume (R69037). Data were binned over intervals of three synthesis cycles, and the mean number of antihydrogen losses per cycle calculated for each bin. The resulting values are shown as a histogram, with the error bars representing the standard deviation of the mean within each bin (panel (a)). Panel (b) shows the cumulative losses as accumulation evolves.

deviation of the mean quantifies the statistical spread. Plot (b) shows the cumulative losses as accumulation progresses. The purple data corresponds to the high-loss configuration (R68465): after about 70 synthesis cycles, the number of losses per three cycles stabilises, and the loss rate stays at around 15 antihydrogen losses per cycle. At this stage, the population in the trap remains approximately constant, as newly formed antihydrogen atoms are lost at the same rate they are produced. [6] The orange data represents R69037, after the direction of electron ejection was changed. In this configuration, the number of losses no longer scales with the number of trapped antihydrogen atoms, and the loss rate remains low as accumulation progresses.

(b) Losses due to Be^+/e^+ merge near the centre of the trap

As described in Chapter 5, the Be^+ and e^+ plasmas must be merged into the same potential well to create a mixed plasma, enabling interactions between the ions and leptons. The first implementation of this process took place near the centre of the trap (between electrodes E14 and E18), as shown in panel (a) of Fig. 6.24. This location coincides with part of the antihydrogen volume. About 3.7 million positrons were transported to the trap centre for merging with the ions. The raw SVD annihilation signal during this process are shown in panel (b) of Fig. 6.21.

The time structure of the annihilations is particularly interesting. The Be^+ were held at $z = 0$ cm for the first two seconds of the window, but significant number annihilations only began at around $t = 1.5$ s. This corresponds to shuffling of positrons from the right normal trap ($z > 14$ cm), where they were prepared. Indeed, the axial position of the annihilations closely follows the motion of the positrons through the electrodes. The actual Be^+/e^+ merge occurred at $t = 2$ s, after which the mixture was transported to the right normal trap for recompression. The axial distribution of the annihilations again clearly reflects this plasma motion in the trap. From these observations, we can infer that the main source of antihydrogen losses in this window was the

[6] Note that the total number of losses per synthesis cycle will be higher than the ones shown in this subsection, as it only addresses losses occurring during the electron SDREVC time window.

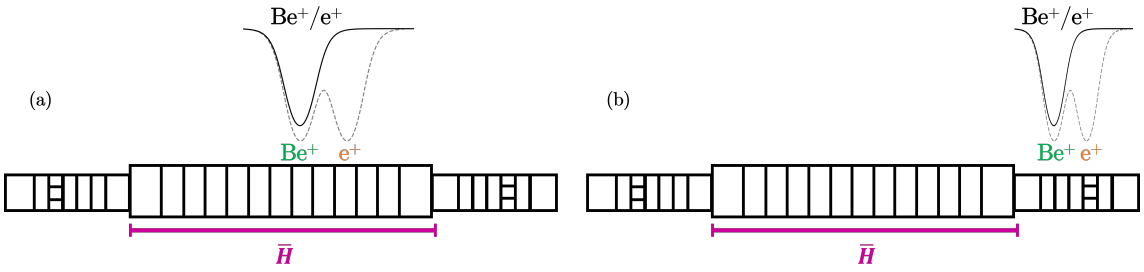

Figure 6.24: Sketch of Be^+/e^+ merge near the centre of the trap (a) and in the right normal trap (b). The dashed lines represent the initial on-axis potentials and the full lines the final potentials.

positron plasma: inelastic collisions between positrons and antihydrogen atoms will cause the antiatoms to be lost from the trap.

The effect of the losses can be seen in the data from run R69126, shown in blue in Fig. 6.25. When the merge is performed near the trap centre, the average loss per synthesis cycle (panel (a)) increased with the number of trapped antihydrogen atoms, and the cumulative loss rate (panel (b)) grew as accumulation progressed. In this example run, after 159 synthesis cycles, a total of 939 antiatoms were lost from the trap in this time window alone. The final trapped population was 9 274, without the merge related losses, this number could have been up to $\sim 10\,\%$ larger.

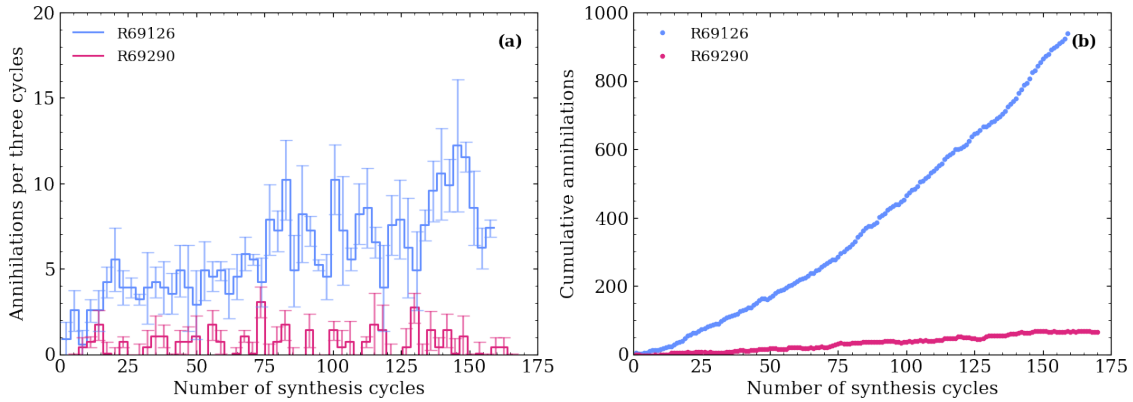

Figure 6.25: Antihydrogen losses due to annihilations with Be^+ ions or ionisations through collisions with positrons due to the Be^+/e^+ merge occurring in the centre of the trap (E14 to E18) (R69126) and in the right normal trap, away from the antihydrogen volume (R69290). Data were binned over intervals of three synthesis cycles, and the mean number of antihydrogen losses per cycle calculated for each bin. The resulting values are shown as a histogram, with the error bars representing the standard deviation of the mean within each bin (panel (a)). Panel (b) shows the cumulative losses as accumulation evolves.

Fortunately, the solution was once again rather straightforward: move the Be^+/e^+ merge to a region of the trap outside the antihydrogen volume. The chosen location was the right normal trap, near the segmented electrode (panel (b) of Fig. 6.24). This not only removed the overlap with the antihydrogen volume but also simplified the subsequent recompression step, since the mixed plasma is now already in the correct trap location and does not need to be shuffled around the trap. This change eliminated the losses associated with the Be^+/e^+ merge, as is evidenced by the magenta data in Fig. 6.25, from run R69290. In this configuration, the average losses per synthesis cycle are independent of the number of synthesis cycles, and thus independent of the number of

antihydrogen in the trap. The cumulative losses after moving this step of the particle preparation are now negligible, amounting to $< 1\,\%$ of the total number of atoms after 175 synthesis cycles in R69290.

(c) Losses due to Be^+ shuffle through the antihydrogen volume

The initial iteration of the Be^+ plasma preparation was as follows: first, a few million Be^+ ions were caught in the left normal trap; next, the ions were shuffled too the right normal trap where and SDREVC-like technique was used to reduce the Be^+ ion number to $\sim$ 200 000 ions; finally the ion cloud was transported to the centre of the trap to be laser cooled while other particles are prepared elsewhere. This protocol, however, required moving millions of ions through the antihydrogen volume, which resulted in antihydrogen losses due to inelastic collisions with Be^+ ions. These losses are shown in panel (c) of Fig. 6.21. Once again, the structure of the annihilations reflects the motion of the particles through the trap.

The vertices shown in Fig. 6.21 (c) correspond to two experimental runs, totalling 199 synthesis cycles and yielding a final antihydrogen population of 9 715 antiatoms. The losses during this window amounted to 197 antihydrogen atoms, corresponding to about $2\,\%$ of the final population. While already close to negligible, these losses were eliminated entirely by preparing the Be^+ ions directly in the left normal trap, avoiding any need to shuffle them through the thin atom trap.

After Be^+ preparation, the plasma is still transferred to E13 and held there with off-axis cooling while other particles are being prepared. The $\bar{H}$-Be^+ collision rate depends on the density of the ion cloud, n, and has been theoretically predicted to be, $\lambda = 2 \times 10^{-9}\, n\,\mathrm{cm}^{-3}\,\mathrm{s}^{-1}$ [104], for energies less than 1 eV. With this protocol, only $\sim$ 200 000 ions are held near the trap centre, as opposed to a few million, reducing the collision rate by an order of magnitude, thus bringing any possible losses during this time window to negligible levels.

(d) Losses due to e^+ capture in ALPHA-2

The positron bunch length when it approaches the ALPHA-2 Penning-Malmberg trap is around 1.4 m, almost three times the length of the trap itself. To maximise the number of trapped positrons, the capture region must therefore be as long as possible, while still minimising the overlap between the positron cloud with the antihydrogen volume. The best compromise is shown in Fig. 6.26, where potentials walls are raised between E16 and E27. Even so, there is still a small region where the antihydrogen atoms can interact with the positrons, leading to the losses shown in Fig. 6.21, panel (d). The vertices represent the sum of eight different experimental runs, with a total of 1443 synthesis cycles and a final population of 92,779 antihydrogen atoms. The total losses in this window were only 506 antiatoms, less than $0.6\,\%$ of the final population.

Avoiding these losses would require shortening the capture region, which in turn reduces the number of positrons trapped. Since such a reduction could introduce instabilities in long-term operation due to fluctuations in the positron number from the accumulator, and the losses themselves are very small, the experimental procedure was unchanged, accepting this minor loss source.

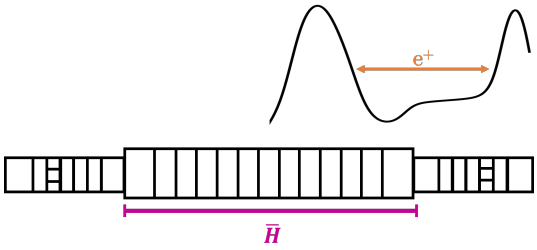

Figure 6.26: Sketch of electron release towards (a) and away (b) from the antihydrogen volume during electron SDREVC. The dashed lines represent the initial on-axis potentials and the full lines the final potentials. The blue arrow shows the direction from which the electrons exit the confining wells.

Conclusion and Summary

The large trapped antihydrogen numbers enabled a detailed study of antiatom loss during accumulation. Several distinct loss sources were identified and eliminated, bringing accumulation into a regime where all identifiable loss mechanisms are comparable to the intrinsic antihydrogen loss rate due to annihilations with background gas. A lifetime of 66 hours [113], corresponds to a loss rate of $0.10\,\%$, which is comparable to the loss rates calculated in the accumulation curves for the final 2023 and final 2024 antihydrogen production protocols shown in Fig. 6.19.

7 Further Beryllium Endeavours

Besides their role in Be^+-assisted antihydrogen synthesis and trapping, Be^+ ions enable several other interesting research paths at ALPHA. During my PhD, I contributed significantly to the development of magnetic field measurements using trapped Be^+ plasmas. The latest published results on this project are presented in J. Peszka's PhD thesis [29]. In parallel, the implementation of a fluorescence-based temperature diagnostic for Be^+ plasmas is in progress, as well as investigations into alternative antihydrogen synthesis schemes. This chapter provides an overview of these projects.

7.1 Be^+ microwave spectroscopy for magnetic field measurements

Besides improving the antihydrogen trapping fraction, Be^+ ions can also be used as a complementary measurement of the magnetic field inside the trap. The electronic structure of these ions is well understood, and the separation between their energy levels depends directly on the magnetic field. This allows magnetic field measurements by Be^+ ion spectroscopy to benchmark current methods. Because Be^+ spectroscopy is a non-destructive method, it could be performed continuously, even during magnetic field ramps, without the need for reloading into the trap.

The microwaves sent into ALPHA-2 create a standing-wave pattern inside the apparatus, pro-

ducing spatial modes with regions of high and low microwave amplitude. The pattern depends on the microwave wavelength, 28 GHz corresponds to a wavelength of $\sim$ 1 cm, making the microwaves highly sensitive to all the structural variations of the trap (electrode diameters, for example, are a few cm), making the microwave pattern difficult to model. Thus, its structure remains largely unknown. Uncertainty in the microwave field amplitude can be a significant limitation for certain excited-state antihydrogen spectroscopy measurements, as the microwave power can strongly influence some transition lineshapes and limit the precision when extracting a centre frequency. For example, the 2s-2p transition in antihydrogen is driven by the magnetic component of the microwave field, and the uncertainty in the microwave amplitude will greatly influence the precision of the measurement of this transition.

Microwave spectroscopy has been performed on Be^+ ions for various studies, specifically targeting the following transition,

$$^2S_{1/2}\,(m_J = +1/2, m_I = +3/2) \rightarrow {}^2S_{1/2}\,(m_J = -1/2, m_I = +3/2)\,. \tag{7.1.1}$$

where the spin of the valence electron is flipped such that it goes to a dark state, and fluorescence levels go down. The energy level structure with this transition highlighted can be seen in Fig. 7.1. The experimental protocol developed for this measurement at ALPHA was inspired by the works of T. Nakamura et al. [114] and N. Shiga et al. [63].

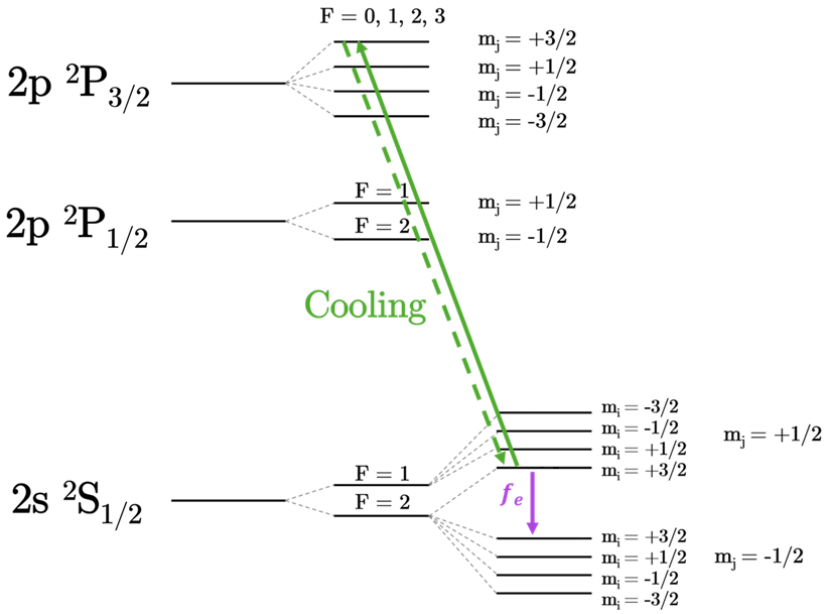

Figure 7.1: $^9Be^+$ energy level structure with highlighted spin-flip transition (purple). The cooling transition is highlighted in green and the electron spin-flip transition in purple.

Two experimental protocols were used at ALPHA to determine the magnetic field using Be^+ microwave spectroscopy:

- **"Laser On" Method:** the cooling laser remains on during the microwave pulse. Fig. 7.2 panel (a) shows the timing sequence for this method (upper diagram) and an example lineshape

(lower diagram). When the microwave pulse flips an ion into a dark state (a state not addressed by the laser), the ion stops scattering photons, causing a drop in fluorescence during the microwave pulse. After the pulse ends, the cooling laser off-resonantly pumps the ions back into the cooling cycle, and fluorescence returns to its pre-pulse level. This method allows for direct observation of spin flips during the microwave pulse, but causes broadening of the line as well as a shift in the central frequency. Both of these are known broadening and frequency shift effects from the laser radiation.

- **"Laser Off" Method:** the cooling laser beam is blocked during the microwave pulse. Fig. 7.2 panel (b) shows the corresponding timing sequence (upper diagram) and an example lineshape (lower diagram). The fluorescence level drops to zero during the microwave pulse since there is no light in the trap. After the pulse, the laser beam is unblocked and the fluorescence level recorded: if the microwave pulse did not interact with the ions, the fluorescence returns fully; if the microwave pulse flipped the ions, the level is reduced until the laser pumps the ions back into the cooling cycle. Therefore, the relative fluorescence drop after the pulse serves as a measure of the microwave-driven transition probability. This method avoids the broadening and frequency shift caused by laser illumination. As shown in Fig. 7.2, the standard deviation is reduced by over a factor of four compared to the "Laser On" method.

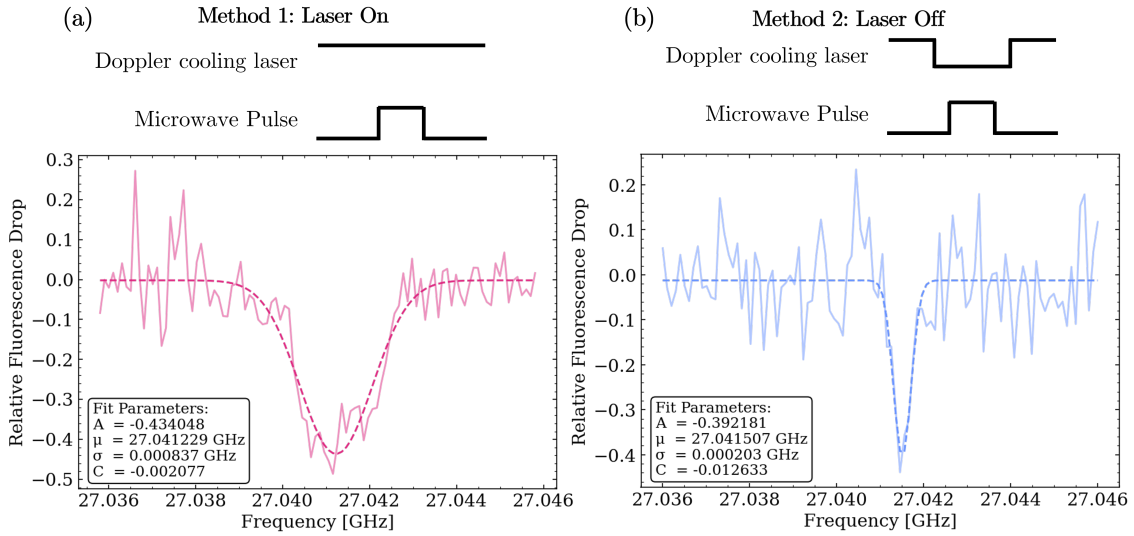

Figure 7.2: Two experimental methods used for electron spin-flip measurements. Method 1 (left) maintains the laser cooling beam in the trap while the microwave pulse is applied. Method 2 (right), on the other hand, blocks the laser cooling beam during the microwave spectroscopy pulse. The microwave pulse parameters were identical for both lineshapes presented here: 100 ms duration, 15 dBm of power out of the microwave synthesiser.

The relative fluorescence drop F_{drop} can be defined as,

$$F_{drop} = \frac{F_{post} - F_{pre}}{F_{pre}}, \tag{7.1.2}$$

where F_{pre} and F_{post} are the average fluorescence levels before and after the microwave pulse, respectively. Each value is obtained by averaging over a defined time window. The duration of

these windows depends on the data acquisition rate of the photon detector and on the background fluctuations. It is chosen during analysis to optimise the signal-to-noise ratio. In practice, a few representative datasets are used to identify the averaging windows that maximise the sensitivity to fluorescence changes. Once established, these window lengths are fixed and consistently applied to subsequent analyses. It is important to note that the pulse duration is rather long $(100\ \text{ms})$, causing decoherence during the microwave pulse and reducing the population that interacts with it. If the pulse duration matched a π-pulse, the excitation probability would be $100\,\%$ and the relative fluorescence would equal -1.

The relative fluorescence drop for both methods is shown in Fig. 7.2 and was fitted as a function of microwave frequency, f_{MW}, with a Gaussian function of the form,

$$F_{drop}(f_{MW}) = Ae^{-\frac{(f_{MW}-\mu)^2}{2\sigma^2}} + C, \tag{7.1.3}$$

where A is the amplitude of the signal, μ is the centre frequency, σ is the Gaussian standard deviation, and C is a constant representing an offset in the vertical axis.

This method was used for magnetic field measurements and compared to the ECR technique described in subsection 2.4.1. The magnetic field measurements agree between ECR and the Be^+ microwave spectroscopy; the details of this measurement can be found in [29], as this was the focus of Dr. J. Peszka's PhD thesis.

7.1.1 Determining the microwave field amplitude

The Rabi frequency, Ω, for a magnetic dipole transition can be defined as

$$\Omega = \frac{g_J \mu_B B_1}{\hbar}, \tag{7.1.4}$$

where B_1 is the amplitude of the magnetic component of the microwave field at the Be^+ ion location, $g_J = 2.00226239(31)$, $\mu_B = 9.2740100783(28) \times 10^{-24}$ J/T, $\hbar = h/2\pi$ and $h = 6.62607015 \times 10^{-34}$ J.s [62]. Determining B_1 therefore, requires an experimental measurement of the Rabi frequency.

The probability, $\mathcal{P}$, of exciting an atom after a microwave pulse of duration t is given by

$$\mathcal{P} = \frac{\Omega^2}{\Omega^2 + \delta^2} \sin^2\left(\frac{t}{2}\sqrt{\Omega^2 + \delta^2}\right), \tag{7.1.5}$$

where δ is the detuning of the microwave pulse from resonance. The corresponding depletion of the bright-state population, P_{dep} (i.e. the relative fluorescence drop), is

$$P_{dep} = 1 - \frac{\Omega^2}{\Omega^2 + \delta^2} \sin^2\left(\frac{t}{2}\sqrt{\Omega^2 + \delta^2}\right). \tag{7.1.6}$$

For a pulse duration of $t_\pi = \pi/\Omega$, the excitation probability $\mathcal{P} = 1$, leading to maximum fluorescence suppression, without taking decoherence into account.

In practice, decoherence during the microwave pulse can dampen the Rabi oscillations. Mag-

netic or microwave field inhomogeneities throughout the Be^+ plasma can be the source of this decoherence. This can be described by introducing a decoherence time, τ, to the probability expression,

$$\mathcal{P} = \frac{\Omega^2}{\Omega^2 + \delta^2} \sin^2\left(\frac{t}{2}\sqrt{\Omega^2 + \delta^2}\right) e^{-t/\tau}. \tag{7.1.7}$$

The exponential factor dampens the oscillations but leaves the frequency unchanged. Most importantly, the Rabi frequency, and thus B_1 can still be reliably extracted from the early oscillations before decoherence dominates. As is the case in the example shown in Fig. 7.2 with a pulse duration of 100 ms.

A possible experimental protocol would be first to use microwave frequency scans to locate the resonance frequency, employing the "Laser Off" method described above. For this purpose, relatively long pulse durations can be used: for example, the curves presented in Fig. 7.2 were performed with a pulse duration of $t = 100$ ms. Once the resonance frequency is determined, the microwave detuning, δ, can be fixed at $\delta = 0$ MHz, and the pulse duration varied. Fitting the resulting fluorescence depletion with the decoherence probability function defined in Eq. 7.1.7 would then allow the π-pulse to be extracted, from which the Rabi frequency and hence the amplitude of the magnetic component of the microwave field could be calculated.

Directly measuring the Rabi side peaks from a frequency scan is not a reliable approach with our current fluorescence detection method. As seen in Fig. 7.2, the background fluorescence signal varies by $10 - 20\,\%$ of the total signal, which is comparable to the expected magnitude of the Rabi side peaks.

If successfully implemented, the same protocol could be repeated at different trap axial locations to map the spatial distribution of the microwave field modes inside the trap for various microwave frequencies. Independently of the antihydrogen measurement, the magnetic field can be adjusted such that the Be^+ spin-flip frequency matches that of the 2s-2p transition in antihydrogen, providing a direct measurement of the microwave amplitude at the relevant frequency. This would greatly reduce one of the main sources of uncertainty in measurements using microwaves at ALPHA.

7.2 Be^+ spectroscopy for temperature measurements

As mentioned throughout this thesis, the temperature diagnostic method described in Section 3.2 has some limitations. The positron temperatures achieved through sympathetic cooling with Be^+ ions approach the temperature diagnostic limit defined in Eq. 3.2.9, making it challenging to distinguish between temperatures below this threshold. Developing a new temperature diagnostic is therefore crucial to reliably differentiate these lower temperatures, which is essential for improved control over plasma parameters and a deeper understanding of the antihydrogen synthesis process.

Moreover, the existing method does not perform adequately for Be^+ ions themselves. Introducing fluorescence-based diagnostic techniques would enable direct measurements of Be^+ temperatures and establish a lower bound for the positron temperatures when using Be^+ fluorescence-based diagnostics in mixed Be^+/e^+ plasmas.

As the laser frequency approaches the resonance frequency, the probability that an ion will absorb a photon increases, resulting in a higher scattering rate and, consequently, increased fluorescence. The Be^+ plasma has a temperature, and the thermal motion of the ions causes Doppler broadening of the transition linewidth. The width of this line is known as the Doppler width and depends on the ions' temperature.

It is therefore possible to measure the temperature of the plasma by probing the cooling transition lineshape. After initial laser cooling, the cooling beam can be briefly switched to a different frequency to measure the fluorescence at that point. This is followed by another cooling period, after which the probing frequency is changed again, repeating this process to incrementally build up a measurement of the lineshape of this transition. The switching between the probe and cooling frequencies must be done as rapidly as possible to minimise the temperature-changing effects of the probe. To achieve this quick switching, an Acousto-Optic Modulator (AOM) was installed in the beam path. The model used was 3200-1210 by Gooch & Housego (G&H), with a tuning range of 280 MHz.

In 2019, this method was applied to measure the temperature of a pure Be^+ plasma trapped in ALPHA-2 [30]. The results are shown in Fig. 7.3, the sample in this example was determined to be at about 150 mK. The temperature is extracted by fitting a Voigt function, $V(\nu)$,

$$V(\nu) = \int_{-\infty}^{\infty} du \frac{e^{-u^2}}{\left[\frac{\nu-\nu_0}{\Delta\nu_D} - u\right]^2 + \frac{1}{4}\left[\frac{\gamma}{2\pi\Delta\nu_D}\right]^2}, \tag{7.2.1}$$

a convolution of a Gaussian and a Lorentzian. ν is the frequency of the probe laser, ν_0 is the centre frequency of the probe transition, γ is the Lorentzian width, and $\Delta\nu_D$ is the Gaussian width. The Lorentzian nature of the transition is due to its natural linewidth and will dominate the lineshape at temperatures near the Doppler limit. The Gaussian contribution comes from the Doppler broadening and is dominant at higher temperatures. [115]. In this scheme, the probe and cooling transition are the same, defined in Eq. 2.5.9. The natural linewidth of the transition is $\Gamma = 2\pi \times 19.6$ MHz [59]. The following line profile can then be fitted to the data,

$$f(\nu) = e^{aV(\nu)}, \tag{7.2.2}$$

where a is the amplitude of the signal. The Lorentzian width is fixed to the natural linewidth, and the Gaussian width can be extracted from the fit. From $\Delta\nu_D$ we can then calculate the temperature of the ions, T,

$$\Delta\nu_D = \frac{\nu_0}{c}\sqrt{\frac{2k_BT}{m}}, \tag{7.2.3}$$

where c is the speed of light, k_B is Boltzmann's constant and m is the mass of a Be^+ ion.

Applying this fitting method to the red data shown in Fig. 7.3, the ions were estimated to be at about 150 mK. Note the asymmetric profile of the data points; this sharp decay in fluorescence is attributed to heating of the ions when the probe frequency sits on the blue-detuned side of the transition. Therefore, the Voigt profile was only fit to the data on the red-detuned part of the transition (left from 0 MHz detuning).

The frequency range and performance of AOMs available for ultraviolet laser frequencies limit

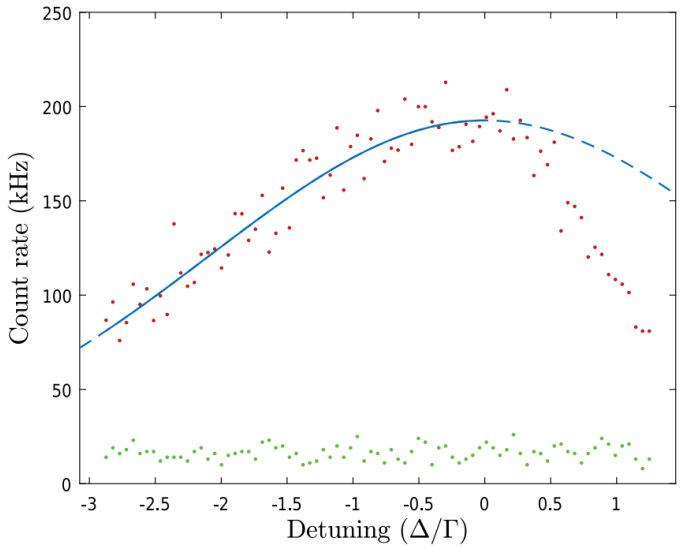

Figure 7.3: Fluorescence signal of a pure Be^+ as the frequency of the cooling laser is scanned across the laser cooling transition. Figure taken from [30]. The green dots represent the laser background fluorescence, the red dots the fluorescence signal during spectroscopy and the blue line is a Voigt function corresponding to about 150 mK.

this method. The widest-range AOM we could find working at 313 nm allowed for a 280 MHz shift in a single-pass configuration. To extend the range and avoid beam displacement during frequency sweeps, the AOM was set up in a double-pass configuration, enabling a total frequency shift of 560 MHz. This 560 MHz range restricts the accessible plasma temperature range to approximately 6 K. [1]

The double-pass configuration incurs significant power losses. Fig. 7.4 shows the double-pass efficiency as a function of frequency shift for three different AOM input laser powers. This efficiency strongly depends on the frequency shift. In principle, this could be compensated by adjusting the AOM's RF drive power to maintain constant optical power throughout the frequency sweep. Doing so would result in double-pass efficiency of only around 5 % during spectroscopy. Even with the full beam power, which is safe within the AOM damage thresholds (about 200 mW) only 30 mW would be output. This limited optical power, combined with the relatively narrow temperature range accessible, constrains the viability of this method for accurate temperature measurements. An alternative approach is required to probe the plasma temperature effectively.

Instead of probing the temperature using the cooling transition, a different one can be used for this purpose,

$$^2S_{1/2}\,(m_J = +1/2, m_I = +3/2) \rightarrow {}^2P_{3/2}\,(m_J = -1/2, m_I = +3/2)\,. \tag{7.2.4}$$

As shown in Fig. 7.5, if the probe beam is resonant with the probe transition, the ions will decay into a dark state and will no longer interact with the cooling beam. The protocol for this temperature probe method is similar to the one described above. The ions are cooled using the cooling beam, the cooling beam is blocked, and a probe beam is sent towards the ions. After probe exposure,

[1] A $FWHM$ of about 216 MHz corresponds to 1 K, it scales with temperature as $FWHM \propto \sqrt{T}$.

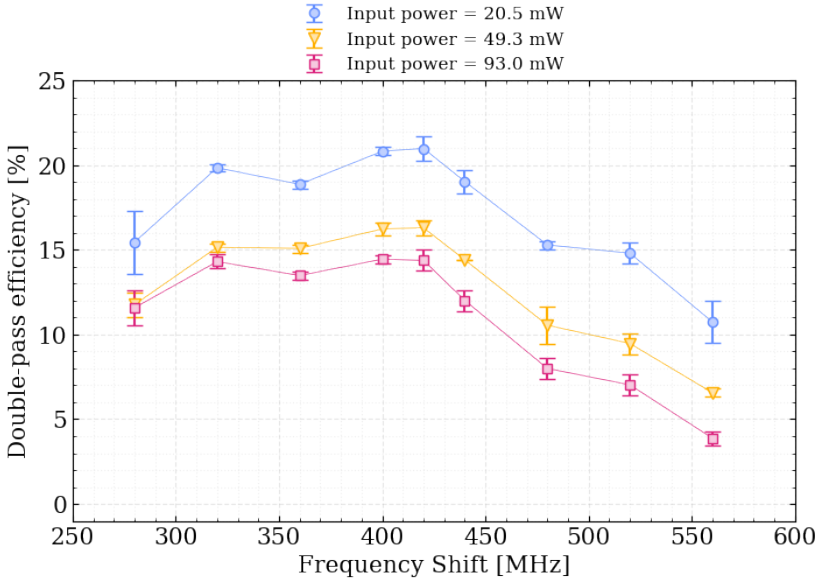

Figure 7.4: Efficiency of AOM transmission in the double-pass configuration as a function of the frequency shift applied. The double-pass efficiency was studied for three different AOM input powers: 20.5 mW (blue circles), 49.3 mW (yellow triangles), and 93.0 mW (magenta squares). The measurements were performed in three consecutive days to test for the set-up stability. The lines connecting the experimental data points are simply guides to the eye.

the cooling beam is unblocked, and the fluorescence level is recorded. This process is repeated for different probe frequencies, and the lineshape of the probe transition is extracted. Here, two different lasers can be used for the probe and cooling beams, allowing for large frequency differences between the two and quick switching without being limited by the AOM frequency range. Moreover, the probe beam will not influence the ions' temperature when blue-detuned, and a full line profile should be easy to obtain. However, it requires repumping of the cooling transition, which can slow down the process.

The fitting routine is slightly different with this method. A Voigt function, as defined in Eq. 7.2.1, is still used, but since here, the lineshape is extracted using fluorescence reduction, the following line profile to fit the signal should be used,

$$f(\nu) = e^{-aV(\nu)}. \tag{7.2.5}$$

The Lorentzian width can be fixed to the theoretical value for the transition, and once again, $\Delta\nu_D$ can be extracted from the fit and the temperature calculated using Eq. 7.2.3. This method was used at NIST to measure the heating rate of Be^+ crystals in a Penning trap [115].

The implementation of this fluorescence-based temperature diagnostic technique is currently underway. This advancement is expected to significantly enhance our ability to characterise plasma conditions.

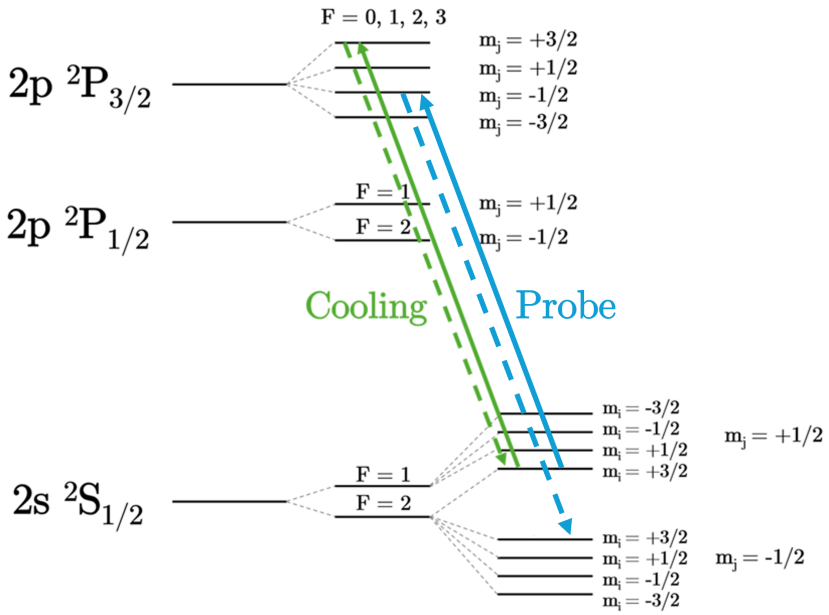

Figure 7.5: $^9Be^+$ energy level structure with highlighted temperature probe transition (blue). The cooling transition is highlighted in green and the temperature probe transition in blue.

7.3 Autoresonant (AR) antiproton injection for antihydrogen synthesis

ALPHA has historically used other ways beside the slow potential merge for antihydrogen production. Another technique used in the early days of ALPHA was the autoresonant injection of antiprotons into the positron plasma.

An RF field is applied to the electrode where the antiprotons are being held, the frequency of this field is tuned to be resonant with the bounce frequency of the antiprotons in the well. The frequency is then swept, and the antiprotons follow this sweep and are eventually ejected from the well into the positron plasma, where three-body recombination can occur. This method, however, was shown to significantly increase the positron temperature, [17] quotes an increase in positron temperature from 27 ± 3 K before antihydrogen synthesis to 54 ± 1 K after. High positron temperature will, of course, negatively impact the trapping fraction and decrease the total number of trapped antihydrogen atoms.

As opposed to the slow potential merge, autoresonant injection does not involve electric potential manipulations, maintaining the number of positrons trapped in the well and limiting their expansion to the expansion rate of a positron plasma in the octupole field. [2]

This method was shown to be significantly worse at producing trappable antihydrogen when compared to the slow potential merge technique. Therefore ALPHA moved away from it [17]. However, it may be worth revisiting this method, since high positron temperatures can be mitigated by sympathetically cooling with the Be^+ ions.

[2] The expansion from the octupole field is inevitable since this field is needed for trapping antihydrogen.

7.3.1 Effect of density evolution during antihydrogen synthesis on trapping efficiency

Let's look into the evolution of the positron density over the duration of antihydrogen synthesis with the current production technique. Fig. 6.17 shows the positron plasma radial profile at different stages in the mixing process, as discussed in Chapter 6, the positron density decreases as the potential well depth is reduced: the radius increases as the potentials are merged, coupled with a decrease in positron number, the density of the plasma decreases significantly. We can try to estimate how this positron density decrease affects the antihydrogen trapping fraction, f_{trap}. Assuming a positron temperature of $T_{e^+} = 10$ K, simulations predict

$$f_{trap} = 1.2 \times 10^{-7} n_{e^+}^{0.45}, \tag{7.3.1}$$

where n_{e^+} is the positron density. The simulations from which this relation was extracted were discussed in Chapter 6. Let's also assume the positron temperature remains constant over the duration of the antihydrogen synthesis and the positron density decreases by an order of magnitude over the synthesis. In agreement with the experimental protocol, we take the total synthesis time to be 1.5 s. Therefore, the density depends on time, and thus so will the trapped fraction : $f_{trap}(n_{e^+}(t))$.

The way the density decreases is not clear from the data shown in Fig. 6.17, so we can study two possibilities: a linear decrease in positron density,

$$n_{e^+}(t) = n_{e+}(t_{in}) + \frac{n_{e+}(t_{final}) - n_{e+}(t_{in})}{t_{final}} t, \tag{7.3.2}$$

and an exponential decrease in density,

$$n_{e+}(t) = n_{e+}(t_{in}) e^{-kt}, \tag{7.3.3}$$

where $t_{in} = 0$ s and $t_{final} = 1.5$ s are the initial and final times, and the constant k meets the following condition,

$$k = \ln \frac{n_{e+}(t_{final})}{n_{e+}(t_{in})} / t_{final}. \tag{7.3.4}$$

The trapping fraction depends on the positron density and changes as the synthesis evolves. The total efficiency across the full synthesis process can be taken as the integral of the efficiency function over the total time of 1.5 s. If the positron density stays constant during antihydrogen synthesis, the efficiency remains constant throughout the whole process. Taking the initial density to be 3.6×10^8 cm^{-3}, as per the experimental parameters, we then have a total of three cases:

- ◇ **Case 1, constant density:** f_{trap} remains constant over the duration of the synthesis cycle, as shown by the blue line in Fig. 7.6. The total trapped fraction is $f_{trap} = 8.5 \times 10^{-4}$, according to Eq. 7.3.1.
- ◇ **Case 2, linear density decrease:** f_{trap} decreases over time as shown by the yellow line in Fig. 7.6. The total trapped fraction is the integral of that function over the duration of the

synthesis cycle, 1.5 s : $f_{trap} = 6.2 \times 10^{-4}$.

◇ **Case 3, exponential density decrease:** f_{trap} decreases over time as shown by the magenta line in Fig. 7.6. The total trapped fraction is the integral of that function over the duration of the synthesis cycle, 1.5 s : $f_{trap} = 5.5 \times 10^{-4}$.

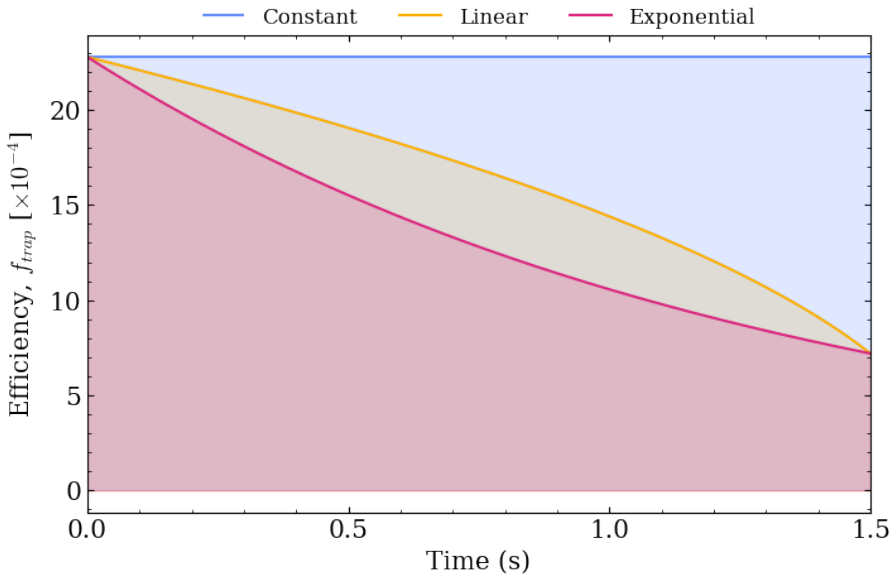

Figure 7.6: Antihydrogen trapping efficiency f_{trap} as function of time for different positron density evolutions: constant density (blue), linear density decrease (yellow) and exponential density decrease (magenta). For the constant positron density: $n_{e^+}(t) = n_{e^+}(0)$, the linear density decrease follows the behaviour defined in Eq. 7.3.2. The exponential density decrease is defined in Eq. 7.3.3.

The most efficient method for producing antihydrogen is one where the density remains constant during the synthesis process. Linear decay will yield about 28% less antihydrogen than case 1, and exponential decay will result in 36% less antiatoms trapped. An interesting observation we can make from this calculation is that the total trapped fraction for case 3 (exponential decay) is the one that most closely matches the experimental data for Be^+-assisted antihydrogen synthesis and trapping. However, more in-depth studies are needed to draw further conclusions.

7.3.2 Motivation for antihydrogen synthesis by autoresonant antiproton injection

As mentioned earlier, autoresonant antiproton injection does not involve electric potential manipulations maintaining the positron number. Moreover, the positron plasma expansion can be made to be negligible by minimising the initial positron radius [3]. Additionally, with sympathetic cooling, the positron temperature can be maintained below 10 K for many seconds. These conditions are such that the positron density and temperature can remain constant during antihydrogen synthesis, which would correspond to Case 1 discussed above.

[3] The smaller the plasma radius, the less susceptible it is to the expansion caused by the octupole field.

Attempting to re-establish autoresonant antiproton injection for antihydrogen synthesis with the addition of the sympathetic cooling of positrons using laser-cooled Be^+ is a promising avenue for increasing the trapped antihydrogen fraction. This method would keep the density and temperature of the positrons constant during the synthesis process, which, based on the rough estimate shown in Fig. 7.6, could increase f_{trap} by a factor of up to 1.5, bringing the number of trapped antihydrogen atoms from 160 antiatoms per cycle to 240.

8 Conclusions and Future Work

The work presented in this thesis culminated in a major advancement in antihydrogen synthesis and trapping, with far-reaching implications for ALPHA's operation.

Be^+-assisted antihydrogen synthesis has proven to be a remarkably successful technique. It has enabled an almost eight-fold increase in the antihydrogen trapping rate in ALPHA-2 and has required the development of novel methods for handling and stabilising ion plasmas as well as a complex control system. This technique is now used daily at ALPHA, and its implementation has accelerated the collaboration's physics programme by many years.

This increase in trapping efficiency has not only made existing measurements significantly faster, but it has also unlocked new experimental possibilities. One clear example is *adiabatic cooling of antihydrogen*. This technique was first demonstrated in [49], allowing for colder antihydrogen temperatures than laser cooling: a 21 mT deep adiabatic well corresponds to about 14 mK antiatoms. However, this technique is limited by the number of antihydrogen atoms in the trap; all of the trials in [49] consisted of less than 150 antihydrogen atoms. Thanks to Be^+-assisted synthesis, a sample of many hundreds or even 1,000 antiatoms is possible post-adiabatic expansion, providing a significant sample for spectroscopy with adiabatically cooled antiatoms.

To provide some perspective, the 2018 characterisation of the 1S-2S transition in antihydrogen required about 16,000 trapped antiatoms collected over ten weeks and over 1,000 synthesis cycles [12]. Along with the introduction of antihydrogen accumulation [13], Be^+-assisted anti-

	2023 pre-Be^+	2023 post-Be^+	2024 post-Be^+
Total number of days	33	77	112
Operational days	8	52	78
Efficiency	24%	67%	69%

Table 8.1: Comparison of the number of operational days in ALPHA-2 between pre and post Be^+-assisted antihydrogen synthesis. An operational day is defined as a day when antihydrogen was accumulated and an experiment was performed with those antiatoms. Some operational days have multiple trials for experiments requiring higher repetition rates.

hydrogen synthesis and trapping now allow for the same measurement with equivalent statistics to be performed in less than a day. During the 2023 antiproton run alone, ALPHA trapped more antihydrogen atoms than in all previous years of operation combined. Across the 2023 and 2024 antiproton runs, over 2 million antiatoms were trapped and utilised for experimentation, facilitating a range of measurements, some of which represent improvements on previous results, and others which constitute entirely new findings.

The data from these experiments is being analysed and will be presented in forthcoming publications. The progress achieved during the 2023 and 2024 antiproton runs marks only the beginning of what is possible with this new synthesis technique. As more exploration of its capabilities occurs, further increases in the number of trapped antihydrogen atoms are not only expected, but likely.

The impact of this shift is clearly visible in ALPHA's recent performance. Tab. 8.1 shows the number of operational days (defined as days when antihydrogen was trapped and used in an experiment) before and after the implementation of Be^+-assisted antihydrogen synthesis and trapping. The operational efficiency jumped from 24% pre-Be^+ to nearly 70% in 2024, reflecting the stability and reproducibility of this technique.

In addition to increasing the antihydrogen trapping fraction, this technique also opens the door to detailed investigations of the antihydrogen formation process. Previously, controlling particle parameters before antihydrogen synthesis was heavily limited by environmental factors such as vacuum conditions, making systematic studies challenging. For example, exploring how different positron temperatures influence three-body recombination was extremely convoluted, as it would require fine-tuning of the positron preparation for each different desired temperature. Now, such adjustments can be achieved simply by changing the laser detuning used for the final cooling step. Moreover, positron sympathetic cooling allows for the decoupling of the positron temperature and radial size and density, which was not possible when the only cooling mechanism was cyclotron cooling[1].

The comprehensive studies of positron temperature and studies of positron density on the three-body recombination process presented in this work are the first of their kind for antimatter and serve as an initial experimental test of theoretical simulations of this fundamental process. This deepens our understanding of antihydrogen formation and paves the way for discovering new methods to further improve the antihydrogen trapping efficiency.

[1] Studying higher positron densities without sympathetic cooling via laser-cooled Be^+ was complicated by higher heating and expansion rates for high positron densities.

8.1 Future Work

There are still many possible avenues for improving the trapping rate using Be^+-assisted antihydrogen synthesis and trapping. For example, there is strong evidence that increasing the positron density and increasing the antiproton number leads to an increase in the trapped fraction, f_{trap} [22]. Moreover, exploring other techniques beyond the slow potential merge is also promising for increasing f_{trap}, such as AR antiproton injection as discussed in Chapter 7.

Besides antihydrogen trapping rate optimisation, Be^+ has other exciting potential uses for the ALPHA collaboration.

8.1.1 Further antihydrogen synthesis and trapping enhancement

Higher positron density

Simulations suggest that increasing the positron density can lead to a higher antihydrogen trapping fraction. According to the relation found in [22] and shown in Fig. 6.3, the trapping efficiency scales as $f_{trap} \propto n_{e^+}^{0.45}$ for 10 K positron clouds, where n_{e^+} is the positron density. Consequently, a factor of two increase in n_{e^+} could result in a 36% increase in the trapping rate.

An initial investigation into this effect was conducted, indicating general agreement with the simulations. During this study, the positron density was increased by changing the number of positrons in the plasma, while keeping the radius fixed at 1 mm (in the antihydrogen synthesis location). This was done to decouple the effect of changing the density from other variables, such as variations in the positron plasma radius, which can influence the axial location of antihydrogen formation.

However, increasing the number of positrons in ALPHA-2 is challenging due to low positron transfer efficiency. Moreover, higher positron numbers require smaller variations in the Be^+ ion number to maintain consistently cooling below 10 K, as evidenced by the scans shown in Fig. 5.10. This presents a challenge, as the SDREVC-like technique achieved at best a $\sim 5\%$ variation in the Be^+. Further reducing this is not realistic in the long term due to gradual drifts in trap conditions, such as vacuum deterioration or accumulation of patch potentials.

An alternative method for increasing the positron density is reducing the plasma radius. Approximating the shape of the plasma to a cylinder, its density, n_{plasma} is given by

$$n_{plasma} = \frac{N}{\pi r^2 L}, \tag{8.1.1}$$

where N is the number of particles, r is the radius, and L is the plasma length. This expression highlights how a small decrease in radius can result in a substantial increase in density.

By fine-tuning the recompression step before antihydrogen synthesis, it may be possible to achieve smaller-radius, stable plasmas, potentially increasing the number of trapped antihydrogen atoms per synthesis cycle. This approach avoids relying on high positron numbers, which are limited by low transfer efficiencies and are particularly challenging to cool due to Be^+ number instabilities.

Decreasing the antiproton radius

As evidenced by the simulations shown in Fig. 6.4, the antiproton injection radius strongly impacts the trapping efficiency for high positron plasma density ($n_{e^+} \geq 5 \times 10^8$ cm^3). If the positron density is increased to maximise the number of trapped antiatoms per synthesis cycle, simulations suggest it would be beneficial to also reduce the antiproton cloud radius. This would minimise high antiproton injection radii, and increase f_{trap}.

Currently, the antiproton cloud radius prior to antihydrogen synthesis is about 0.8 mm inside the trap. Decreasing the radius increases the number of antiprotons injected into the positron plasma during the early stages of the slow potential merge technique, when the injection occurs on-axis. As the potential barrier is gradually lowered, antiprotons at progressively higher radii begin to exit the well, since the barrier diminishes first near the trap axis and later at higher radii.

Increasing antiproton number

Experimentally, it has been measured that, in a successful antihydrogen synthesis cycle, all of the antiprotons recombine with positrons to create antihydrogen. Most of these will not remain trapped due to their high temperature, field ionisations or being synthesised in the non-trappable state. Naively, one can then assume that increasing the antiproton number should proportionally increase the number of produced antihydrogen atoms.

This effect was investigated in [17], where the antiproton number was increased from 5.5×10^4 to 9.0×10^4, a $60\,\%$ increase in the total antiproton number, however, the trapped antihydrogen atoms per synthesis cycle only demonstrated a $20\,\%$ increase. Therefore, even though an increase in antiproton number shows a positive effect on the antihydrogen trapped fraction, it is not necessarily a one-to-one increase.

This can be explained, perhaps due to the fact that essentially, antiprotons behave as ion impurities in the cold positron plasma, which are known to significantly increase the plasma heating rate. A higher heating rate results in higher positron temperatures as the synthesis process progresses, and thus a gradual decrease in the trapping efficiency as the potential wells are lowered.

However, as shown in Chapter 6, with the Be^+ technique, doubling the number of antiprotons resulted in roughly a factor of two increase in the number of trapped antihydrogen atoms per synthesis cycle. The hypothesis is that the cooling power from the sympathetic cooling technique is enough to overcome the additional heating induced by the higher antiproton number. To understand this effect in greater depth, a more effective temperature diagnostic technique needs to be developed. If measuring the positron temperature at different stages of the synthesis process is possible with a method that is sensitive to temperatures below 10 K, a great deal more understanding is possible.

Regardless, it is now more interesting than ever to increase the antiproton number, since we are now in a regime where the increase in the number of trapped antiatoms is directly proportional to the increase in trapped antiprotons.

Autoresonant (AR) antiproton injection for antihydrogen synthesis

As discussed in Chapter 7, this other technique for antihydrogen synthesis could increase the number of trapped antihydrogen atoms per cycle since it maintains the positron density relatively constant throughout the synthesis process. This technique was a predecessor to the slow potential merge technique and had a much smaller trapped antihydrogen yield due to high positron temperatures. Sympathetic cooling of positrons using laser-cooled Be^+ ions may reduce the heating caused by AR injection and potentially make it a viable antihydrogen synthesis procedure.

8.1.2 Be^+-assisted antihydrogen synthesis and trapping in ALPHA-g

In 2023, the ALPHA collaboration published the first observation of the effect of gravity on the motion of antihydrogen [16]. This landmark result was the culmination of five weeks of data taking during which a total of 4541 antihydrogen atoms were trapped over 4350 synthesis cycles, thus exhibiting an average trapping rate of 1.04 antiatoms per cycle. The antihydrogen used in this study was synthesised without the Be^+-assisted technique.

However, a trapping rate of one antiatom per synthesis cycle imposes limitations on experimental protocols. For example, powerful techniques such as adiabatic cooling of antihydrogen are not realistic with such small numbers of atoms, as there would be no significant signal after reducing the trap depth. At this rate, trapping 100 atoms in ALPHA-g takes more than six hours. To achieve statistical significance in our measurement of the effect of gravity on the motion of antihydrogen, multiple trials were required, over several days [16]. This introduces additional challenges such as increased susceptibility to systematic drifts or fluctuations in the trap environment between runs.

Therefore, improving the trapping rate in ALPHA-g has become one of the collaboration's highest priorities to expand the physics programme in this trap.

The primary reason for the extremely low trapping rate in ALPHA-g is believed to be high positron temperature before and during antihydrogen synthesis. Tab. 8.2 shows a comparison between the positron temperatures achieved in ALPHA-2 during the 2023 antiproton run (before Be^+-assisted antihydrogen synthesis was implemented) and the positron temperatures in ALPHA-g during the 2022 gravity measurement campaign [2]. The data reveals that positrons in ALPHA-g are three times hotter than in ALPHA-2. As discussed throughout this thesis, higher positron temperatures strongly suppress the antihydrogen trapping rate. This discrepancy indicates a higher heating rate in the ALPHA-g trap, possibly caused by factors such as increased electrical noise or poorer vacuum conditions.

Sympathetic cooling via laser-cooled Be^+ ions has proven to be extremely effective at reducing positron temperatures in ALPHA-2, even in high heating rate conditions. Given this success, extending the Be^+-assisted antihydrogen synthesis and trapping technique to ALPHA-g represents the most promising and direct path to achieving a substantial increase in antihydrogen trapping rate.

As a conservative estimate, let us assume that even with Be^+ sympathetic cooling, the heating rate in ALPHA-g limits the positron temperature to no lower than three times the average tem-

[2] All of the positron temperatures in ALPHA-g are the result of positron cyclotron cooling.

	e^+ temperature [K]	Standard Deviation [K]
ALPHA-2	14.6	2.2
ALPHA-g	43.7	3.2

Table 8.2: Positron temperatures before antihydrogen synthesis in ALPHA-2 and ALPHA-g. The positron temperatures for ALPHA-2 correspond to the average temperatures during the 2023 antiproton run without Be^+-assisted sympathetic cooling. The positron temperatures from ALPHA-g correspond to the average positron temperatures during the data-taking campaign of the 2022 antiproton run.

perature in ALPHA-2[3]. This would correspond to a minimum positron temperature of 26.1 K in ALPHA-g. As discussed in Chapter 6, experimental data shows the trapping rate scales according to $f_{trap} \propto T^{-0.70}$. If this relation remains the same in ALPHA-g, the trapping rate would decrease by a factor of about 2.3 compared to ALPHA-2. Corresponding to about 50 antihydrogen atoms trapped in ALPHA-g if 300,000 antiprotons are caught in this trap.

While this is a rough estimate, it illustrates the great potential improvement in performance. Even with a trapping rate of just a few tens of antiatoms per synthesis cycle, data collection in ALPHA-g would become significantly more efficient: instead of requiring weeks and thousands of synthesis cycles, comparable statistics to the 2022 result could be achieved in roughly 100 synthesis cycles, reducing the data-taking time to just a few days.

Implementation Challenges

While extending Be^+-assisted antihydrogen synthesis in ALPHA-g would yield substantial gains in antihydrogen trapping fraction, it does not come without its challenges, both technical and procedural:

- **Long beam path:** the laser path needed for Be^+ cooling in ALPHA-g is substantially longer than in ALPHA-2, increasing the complexity of the optical alignment and raising concerns about beam stability and pointing over time. It could also mean additional focusing and collimating are necessary further down the optical path[4] which complicates the active beam stabilisation protocol.

- **Diagnostic stations upgrade:** the lower diagnostic station (LDS) and upper diagnostic station (UDS) are located upstream and downstream of the ALPHA-g apparatus, respectively. These diagnostic stations were not initially designed to include a Beryllium source or laser mirrors for the on-axis cooling beam. Including these elements is not trivial, as it involves the redesign of these diagnostic stations and interventions which involve opening the experimental apparatus to air.

- **On-axis cooling only:** ALPHA-g does not have dedicated off-axis laser ports, thus, it is only feasible to implement an on-axis laser path. One direct consequence of this hardware limitation is that no direct post-cooling diagnostics are possible. After laser cooling, the diagnostic

[3] In ALPHA-2, the minimum positron temperature was estimated to be about 8.7 K during the 2024 antiproton run. Given the limitations of the temperature diagnostic technique, this corresponds to higher threshold of the positron temperature directly before antihydrogen synthesis.

[4] Currently, all focusing and collimating optics for the ALPHA-2 cooling path are located in the laser laboratory. This simplifies the active beam stabilisation protocol and ensures the optical elements are in the cleanest environment possible.

station must physically move away from the "Laser Mirror" (which reflects the beam in and out of the trap) into the "MCP" position for radial profile and temperature diagnostics. This mechanical translation takes about 30 s, making it impossible to directly measure particle characteristics immediately after cooling.

- **Lack of fluorescence diagnostics:** the absence of laser ports in ALPHA-g also means there is no practical location to install a photon detector for fluorescence diagnostics. This complicates the development process, for example, it means determining the correct beam polarisation is solely dependent on temperature diagnostics, which, as mentioned above, is also not a reliable diagnostic method with this experimental set-up. New experimental protocols will need to be developed during the implementation of the technique.

- **Long development time:** the lack of real-time diagnostics means that mostly all parameters (laser detuning, Be^+ number, cooling duration...) would have to be optimised indirectly by observing the effects on antihydrogen synthesis alone. This iterative process takes significantly longer than measuring particle parameters directly, and depends on the smooth operation of many other systems before Be^+-assisted synthesis is relevant.

Despite these challenges, none of these limitations are fundamental showstoppers. The Beryllium team is actively working towards implementing Be^+-assisted antihydrogen synthesis and trapping in ALPHA-g, and solutions to the technical hurdles have been designed. Hardware upgrades are underway, and the experimental protocols have been developed. The next major result from ALPHA-g will utilise this technique for antihydrogen trapping. A more detailed account of the hardware implementation and experimental development of Be^+-assisted antihydrogen synthesis and trapping in ALPHA-g will be the subject of a dedicated future PhD thesis and is beyond the scope of the present work.

8.1.3 Spectroscopy with Be^+

As discussed in Chapter 7, Be^+ ions provide a versatile and non-destructive tool for probing the conditions inside the ALPHA-2 trap. They can be used to measure magnetic fields, providing a direct comparison to existing techniques, and alternative Be^+-based magnetometry methods (though not described in detail in this thesis) could allow measurements across a wider range of magnetic fields, including lower fields currently inaccessible in ALPHA [5] Moreover, Be^+ ion spectroscopy can also be used to characterise the microwave amplitude and modes inside the trap, which is currently a major source of uncertainty in some ALPHA measurements.

Be^+ spectroscopy also provides an independent method to determine ion plasma temperature, which can be used to benchmark the current SiPM temperature diagnostic and give a lower bound on the positron temperature when performed with Be^+/e^+ mixtures.

Together, these capabilities highlight the potential of Be^+ ions to enhance precision and control in antihydrogen experiments.

[5] Microwave injection into the ALPHA-2 trap limits the ECR technique to $0.9 - 1.1$ T.

8.2 Final Remarks

To finalise this work, let's revisit Fig. 1.1, now plotted with the antihydrogen trapped per hour in the 2023 and 2024 antiproton runs with Be^+-assisted antihydrogen synthesis and trapping in Fig. 8.1. The dramatic increase between the 300 trapped antiatoms per hour in 2022 and the 2500 trapped antiatoms per hour in 2024 illustrates the impact of this technique. Be^+-assisted antihydrogen synthesis and trapping have not only greatly accelerated data collection at ALPHA but also fundamentally changed the scope of what is experimentally achievable, setting the stage for a new era of precision measurements and deepening our ability to probe fundamental symmetries.

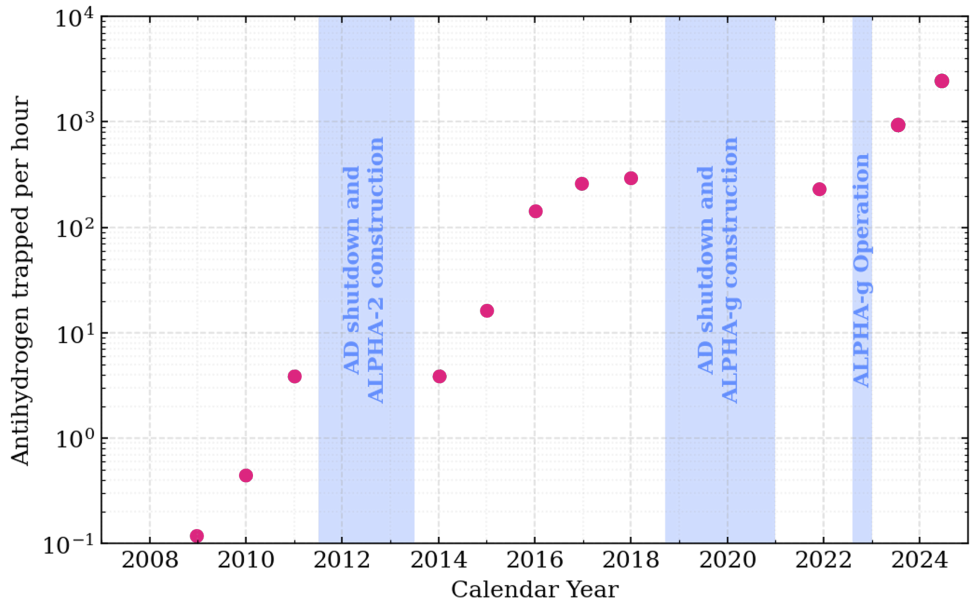

Figure 8.1: Updated antihydrogen trapped per hour over the years of operation of ALPHA-2. The trapping rate saw a dramatic increase between the 2022 antiproton run (300 antiatoms per hour) and the 2023 antiproton run (1000 antiatoms per hour) due to the implementation of Be^+-assisted antihydrogen synthesis and trapping. And again between the 2023 and 2024 antiprotons runs (2500 antiatoms per hour in 2024) due to more developments of the aforementioned technique and an increase in antiproton number.

A Supplementary Lists

List of Figures

List of Tables

List of Acronyms

AD Antiproton Decelerator

ALPHA Antihydrogen laser PHysics Apparatus

AOM Acousto-Optic Modulator

AR Autoresonant

BASE Baryon-Antibaryon Symmetry Experiment

CERN European Organization for Nuclear Research

CT Catching Trap

DS Downstream

ECR Electron Cyclotron Resonance

ELENA Extra Low ENergy Antiproton ring

EVC EVaporative Cooling

FFF Feed-Forward Factor

FHG Fourth Harmonic Generation

FLC Final Laser Cooling

FWHM Full Width Half Maximum

HD Half-Dump

MCP MicroChannel Plate

NNI Norm Net Intensity

PBS Polarisation Beam Splitter

PID Proportional-Integral-Derivative

PLA Pulsed Laser Ablation

PMT Photomultiplier Tube

PS Proton Synchrotron

RW Rotating Wall

SDREVC Strong Drive Regime Evaporative Cooling

SiPM Silicon PhotoMultiplier

SVD Silicon Vertex Detector

TBR Three-body Recombination

US Upstream

Bibliography

[1] Paul A. M. Dirac. The quantum theory of the electron. *Proc. Roy. Soc. Lond. A*, 117:610–624, 1928. doi:10.1098/rspa.1928.0023.

[2] Carl D. Anderson. The positive electron. *Phys. Rev.*, 43:491–494, Mar 1933. URL: https://link.aps.org/doi/10.1103/PhysRev.43.491, doi:10.1103/PhysRev.43.491.

[3] Owen Chamberlain, Emilio Segrè, Clyde Wiegand, and Thomas Ypsilantis. Observation of antiprotons. *Phys. Rev.*, 100:947–950, Nov 1955. URL: https://link.aps.org/doi/10.1103/PhysRev.100.947, doi:10.1103/PhysRev.100.947.

[4] Richard L. Garwin, Leon M. Lederman, and Marcel Weinrich. Observations of the failure of conservation of parity and charge conjugation in meson decays: the magnetic moment of the free muon. *Phys. Rev.*, 105:1415–1417, Feb 1957. URL: https://link.aps.org/doi/10.1103/PhysRev.105.1415, doi:10.1103/PhysRev.105.1415.

[5] L. Landau. On the conservation laws for weak interactions. *Nuclear Physics*, 3(1):127–131, 1957. URL: https://www.sciencedirect.com/science/article/pii/0029558257900615, doi:10.1016/0029-5582(57)90061-5.

[6] Matthias Borchert, Jack Devlin, S. Erlewein, Markus Fleck, James Harrington, T. Higuchi, Barbara Latacz, Frederik Völksen, E. Wursten, Fatma Abbass, Matthew Bohman, A. Mooser, D. Popper, M. Wiesinger, C. Will, K. Blaum, Y. Matsuda, C. Ospelkaus, Werner Quint, and Stefan Ulmer. A 16-parts-per-trillion measurement of the antiproton-to-proton charge–mass ratio. *Nature*, 601:53–57, 01 2022. doi:10.1038/s41586-021-04203-w.

[7] B. M. Latacz, B. P. Arndt, B. B. Bauer, J. A. Devlin, S. R. Erlewein, M. Fleck, J. I. Jäger, M. Schiffelholz, G. Umbrazunas, E. J. Wursten, and et al. Base—high-precision comparisons of the

fundamental properties of protons and antiprotons. *The European Physical Journal D*, 77(6), Jun 2023. doi:10.1140/epjd/s10053-023-00672-y.

[8] Ralf Lehnert. CPT symmetry and its violation. *Symmetry*, 8(11):114, Oct 2016. doi:10.3390/sym8110114.

[9] M. Amoretti, C. Amsler, G. Bonomi, A. Bouchta, P. Bowe, C. Carraro, C. L. Cesar, M. Charlton, M. J. Collier, M. Doser, and et al. Production and detection of cold antihydrogen atoms. *Nature*, 419(6906):456–459, Sep 2002. doi:10.1038/nature01096.

[10] G. Gabrielse, N. S. Bowden, P. Oxley, A. Speck, C. H. Storry, J. N. Tan, M. Wessels, D. Grzonka, W. Oelert, G. Schepers, T. Sefzick, J. Walz, H. Pittner, T. W. Hänsch, and E. A. Hessels. Driven production of cold antihydrogen and the first measured distribution of antihydrogen states. *Phys. Rev. Lett.*, 89:233401, Nov 2002. URL: https://link.aps.org/doi/10.1103/PhysRevLett.89.233401, doi:10.1103/PhysRevLett.89.233401.

[11] G. B. Andresen, M. D. Ashkezari, M. Baquero-Ruiz, W. Bertsche, P. D. Bowe, E. Butler, C. L. Cesar, S. Chapman, M. Charlton, A. Deller, and et al. Trapped antihydrogen. *Nature*, 468(7324):673–676, Nov 2010. doi:10.1038/nature09610.

[12] M. Ahmadi, B. X. R. Alves, C. J. Baker, and et al. Characterization of the 1s–2s transition in antihydrogen. *Nature*, 557:71–75, 2018. doi:10.1038/s41586-018-0017-2.

[13] C. J. Baker, W. Bertsche, A. Capra, C. Carruth, C. L. Cesar, M. Charlton, A. Christensen, R. Collister, A. Cridland Mathad, S. Eriksson, and et al. Precision spectroscopy of the hyperfine components of the 1s–2s transition in antihydrogen. *Nature Physics*, 21(2):201–207, Jan 2025. doi:10.1038/s41567-024-02712-9.

[14] C. J. Baker, W. Bertsche, and A. Capra et al. Laser cooling of antihydrogen atoms. *Nature*, 592:35–42, 2021. doi:10.1038/s41586-021-03289-6.

[15] M. Ahmadi, B. X. Alves, C. J. Baker, W. Bertsche, E. Butler, A. Capra, C. Carruth, C. L. Cesar, M. Charlton, S. Cohen, and et al. Observation of the hyperfine spectrum of antihydrogen. *Nature*, 548(7665):66–69, Aug 2017. doi:10.1038/nature23446.

[16] E. K. Anderson, C. J. Baker, and et al. Bertsche, W. Observation of the effect of gravity on the motion of antimatter. *Nature*, 621(7980):716–722, Sep 2023. doi:10.1038/s41586-023-06527-1.

[17] M. Ahmadi, B. X. Alves, C. J. Baker, W. Bertsche, E. Butler, A. Capra, C. Carruth, C. L. Cesar, M. Charlton, S. Cohen, and et al. Antihydrogen accumulation for fundamental symmetry tests. *Nature Communications*, 8(1), 2017. doi:10.1038/s41467-017-00760-9.

[18] M. Ahmadi, B. X. R. Alves, C. J. Baker, W. Bertsche, A. Capra, C. Carruth, C. L. Cesar, M. Charlton, S. Cohen, and et al. Enhanced control and reproducibility of non-neutral plasmas. *Phys. Rev. Lett.*, 120:025001, Jan 2018. URL: https://link.aps.org/doi/10.1103/PhysRevLett.120.025001, doi:10.1103/PhysRevLett.120.025001.

[19] Michael E. Glinsky and Thomas M. O'Neil. Guiding center atoms: Three-body recombination in a strongly magnetized plasma. *Physics of Fluids B: Plasma Physics*, 3(5):1279–1293, May 1991. doi:10.1063/1.859820.

[20] F. Robicheaux. Simulations of antihydrogen formation. *Phys. Rev. A*, 70:022510, Aug 2004. URL: https://link.aps.org/doi/10.1103/PhysRevA.70.022510, doi:10.1103/PhysRevA.70.022510.

[21] F Robicheaux. Atomic processes in antihydrogen experiments: a theoretical and computational perspective. *Journal of Physics B: Atomic, Molecular and Optical Physics*, 41(19):192001, sep 2008. URL: https://dx.doi.org/10.1088/0953-4075/41/19/192001, doi:10.1088/0953-4075/41/19/192001.

[22] S. Jonsell and M. Charlton. On the formation of trappable antihydrogen. *New J. Phys.*, 20(4):043049, 2018. doi:10.1088/1367-2630/aabc71.

[23] M. C. Fujiwara, M. Amoretti, C. Amsler, G. Bonomi, A. Bouchta, P. D. Bowe, C. Canali, C. Carraro, C. L. Cesar, M. Charlton, M. Doser, A. Fontana, R. Funakoshi, P. Genova, J. S. Hangst, R. S. Hayano, L. V. Jørgensen, A. Kellerbauer, V. Lagomarsino, R. Landua, E. Lodi-Rizzini, M. Macri, N. Madsen, G. Manuzio, D. Mitchard, P. Montagna, H. Pruys, C. Regenfus, A. Rotondi, G. Testera, A. Variola, L. Venturelli, D. P. van der Werf, Y. Yamazaki, and N. Zurlo. Temporally controlled modulation of antihydrogen production and the temperature scaling of antiproton-positron recombination. *Phys. Rev. Lett.*, 101:053401, Jul 2008. URL: https://link.aps.org/doi/10.1103/PhysRevLett.101.053401, doi:10.1103/PhysRevLett.101.053401.

[24] D. J. Wineland, R. E. Drullinger, and F. L. Walls. Radiation-pressure cooling of bound resonant absorbers. *Phys. Rev. Lett.*, 40:1639–1642, Jun 1978. URL: https://link.aps.org/doi/10.1103/PhysRevLett.40.1639, doi:10.1103/PhysRevLett.40.1639.

[25] D. J. Larson, J. C. Bergquist, J. J. Bollinger, Wayne M. Itano, and D. J. Wineland. Sympathetic cooling of trapped ions: A laser-cooled two-species nonneutral ion plasma. *Phys. Rev. Lett.*, 57:70–73, Jul 1986. URL: https://link.aps.org/doi/10.1103/PhysRevLett.57.70, doi:10.1103/PhysRevLett.57.70.

[26] B. M. Jelenković, A. S. Newbury, J. J. Bollinger, W. M. Itano, and T. B. Mitchell. Sympathetically cooled and compressed positron plasma. *Phys. Rev. A*, 67:063406, Jun 2003. URL: https://link.aps.org/doi/10.1103/PhysRevA.67.063406, doi:10.1103/PhysRevA.67.063406.

[27] Muhammed Sameed. *Laser-ablated beryllium ions for cold antihydrogen in ALPHA*. PhD thesis, Swansea University, 2017. URL: https://cronfa.swan.ac.uk/Record/cronfa53255.

[28] Jack McCauley Jones. *Sympathetically Laser-Cooled Positron Plasmas for Antihydrogen Formation*. PhD thesis, Swansea University, 2021. doi:10.23889/SUthesis.59731.

[29] Joanna Peszka. *Laser-cooled Be+ for improved antihydrogen trapping and magnetometry*. PhD thesis, Swansea University, 2023. doi:10.23889/SUthesis.65173.

[30] C.J. Baker, W. Bertsche, A. Capra, and et. al. Sympathetic cooling of positrons to cryogenic temperatures for antihydrogen production. . *Nat Comm*, 12:6139, 2021. doi:10.1038/s41467-021-26086-1.

[31] R. Akbari, L.O. de Araujo Azevedo, C.J. Bake, and et al. Be+ assisted, simultaneous confinement of more than 15000 antihydrogen atoms. *Nat Commun*, 16, 10106, (2025). doi:10.1038/s41467-025-65085-4.

[32] H.G. Dehmelt. Radiofrequency spectroscopy of stored ions i: Storage. In D.R. Bates and Immanuel Estermann, editors, *Advances in Atomic and Molecular Physics*, volume 3 of *Advances in Atomic and Molecular Physics*, pages 53–72. Academic Press, 1968. URL: https://www.sciencedirect.com/science/article/pii/S0065219908601700, doi:10.1016/S0065-2199(08)60170-0.

[33] J. H. Malmberg and J. S. deGrassie. Properties of nonneutral plasma. *Phys. Rev. Lett.*, 35:577–580, Sep 1975. URL: https://link.aps.org/doi/10.1103/PhysRevLett.35.577, doi:10.1103/PhysRevLett.35.577.

[34] Madsen N. Knoop M. and Thompson R. C. *Trapped Charged Particles: A Graduate Textbook with Problems and Solutions*. World Scientific, 2016.

[35] Daniel H. E. Dubin. First-order anharmonic correction to the free energy of a coulomb crystal in periodic boundary conditions. *Phys. Rev. A*, 42:4972–4982, Oct 1990. URL: https://link.aps.org/doi/10.1103/PhysRevA.42.4972, doi:10.1103/PhysRevA.42.4972.

[36] Guy S. Stringfellow, Hugh E. DeWitt, and W. L. Slattery. Equation of state of the one-component plasma derived from precision monte carlo calculations. *Phys. Rev. A*, 41:1105–1111, Jan 1990. URL: https://link.aps.org/doi/10.1103/PhysRevA.41.1105, doi:10.1103/PhysRevA.41.1105.

[37] Michael E. Glinsky, Thomas M. O'Neil, Marshall N. Rosenbluth, Kenji Tsuruta, and Setsuo Ichimaru. Collisional equipartition rate for a magnetized pure electron plasma. *Physics of Fluids B: Plasma Physics*, 4(5):1156–1166, 05 1992. URL: https://nnp.ucsd.edu/pdf_files/PFB_1156_92.PDF, doi:10.1063/1.860124.

[38] T. M. O'Neil. Centrifugal separation of a multispecies pure ion plasma. *The Physics of Fluids*, 24(8):1447–1451, 08 1981. arXiv:https://pubs.aip.org/aip/pfl/article-pdf/24/8/1447/12680932/1447_1_online.pdf, doi:10.1063/1.863565.

[39] G. B. Andresen, M. D. Ashkezari, M. Baquero-Ruiz, W. Bertsche, P. D. Bowe, E. Butler, C. L. Cesar, S. Chapman, M. Charlton, A. Deller, S. Eriksson, J. Fajans, T. Friesen, M. C. Fujiwara, D. R. Gill, A. Gutierrez, J. S. Hangst, W. N. Hardy, M. E. Hayden, A. J. Humphries, R. Hydomako, S. Jonsell, N. Madsen, S. Menary, P. Nolan, A. Olin, A. Povilus, P. Pusa, F. Robicheaux, E. Sarid, D. M. Silveira, C. So, J. W. Storey, R. I. Thompson, D. P. van der Werf, J. S. Wurtele, and Y. Yamazaki. Centrifugal separation and equilibration dynamics in an electron-antiproton plasma. *Phys. Rev. Lett.*, 106:145001, Apr 2011. URL: https://link.aps.org/doi/10.1103/PhysRevLett.106.145001, doi:10.1103/PhysRevLett.106.145001.

[40] X.-P. Huang, F. Anderegg, E. M. Hollmann, C. F. Driscoll, and T. M. O'Neil. Steady-state confinement of non-neutral plasmas by rotating electric fields. *Phys. Rev. Lett.*, 78:875–878, Feb 1997. URL: https://link.aps.org/doi/10.1103/PhysRevLett.78.875, doi:10.1103/PhysRevLett.78.875.

[41] Daniel H. E. Dubin and T. M. O'Neil. Trapped nonneutral plasmas, liquids, and crystals (the thermal equilibrium states). *Rev. Mod. Phys.*, 71:87–172, Jan 1999. URL: https://link.aps.org/doi/10.1103/RevModPhys.71.87, doi:10.1103/RevModPhys.71.87.

[42] J. R. Danielson and C. M. Surko. Torque-balanced high-density steady states of single-component plasmas. *Phys. Rev. Lett.*, 94:035001, Jan 2005. URL: https://link.aps.org/doi/10.1103/PhysRevLett.94.035001, doi:10.1103/PhysRevLett.94.035001.

[43] E. M. Hollmann, F. Anderegg, and C. F. Driscoll. Confinement and manipulation of non-neutral plasmas using rotating wall electric fields. *Physics of Plasmas*, 7(7):2776–2789, 07 2000. arXiv:https://pubs.aip.org/aip/pop/article-pdf/7/7/2776/19154186/2776_1_online.pdf, doi:10.1063/1.874128.

[44] S. A. Prasad and T. M. O'Neil. Finite length thermal equilibria of a pure electron plasma column. *The Physics of Fluids*, 22(2):278–281, 02 1979. doi:10.1063/1.862578.

[45] B. R. Beck, J. Fajans, and J. H. Malmberg. Temperature and anisotropic-temperature relaxation measurements in cold, pure-electron plasmas. *Physics of Plasmas*, 3(4):1250–1258, 04 1996. arXiv:https://pubs.aip.org/aip/pop/article-pdf/3/4/1250/19084692/1250_1_online.pdf, doi:10.1063/1.871749.

[46] G. Gabrielse, X. Fei, L. A. Orozco, R. L. Tjoelker, J. Haas, H. Kalinowsky, T. A. Trainor, and W. Kells. Cooling and slowing of trapped antiprotons below 100 mev. *Phys. Rev. Lett.*, 63:1360–1363, Sep 1989. URL: https://link.aps.org/doi/10.1103/PhysRevLett.63.1360, doi:10.1103/PhysRevLett.63.1360.

[47] G. B. Andresen, M. D. Ashkezari, M. Baquero-Ruiz, W. Bertsche, P. D. Bowe, E. Butler, C. L. Cesar, S. Chapman, M. Charlton, J. Fajans, T. Friesen, M. C. Fujiwara, D. R. Gill, J. S. Hangst, W. N. Hardy, R. S. Hayano, M. E. Hayden, A. Humphries, R. Hydomako, S. Jonsell, L. Kurchaninov, R. Lambo, N. Madsen, S. Menary, P. Nolan, K. Olchanski, A. Olin, A. Povilus, P. Pusa, F. Robicheaux, E. Sarid, D. M. Silveira, C. So, J. W. Storey, R. I. Thompson, D. P. van der Werf, D. Wilding, J. S. Wurtele, and Y. Yamazaki. Evaporative cooling of antiprotons to cryogenic temperatures. *Phys. Rev. Lett.*, 105:013003, Jul 2010. URL: https://link.aps.org/doi/10.1103/PhysRevLett.105.013003, doi:10.1103/PhysRevLett.105.013003.

[48] G. Gabrielse, W. S. Kolthammer, R. McConnell, P. Richerme, R. Kalra, E. Novitski, D. Grzonka, W. Oelert, T. Sefzick, M. Zielinski, D. Fitzakerley, M. C. George, E. A. Hessels, C. H. Storry, M. Weel, A. Müllers, and J. Walz. Adiabatic cooling of antiprotons. *Phys. Rev. Lett.*, 106:073002, Feb 2011. URL: https://link.aps.org/doi/10.1103/PhysRevLett.106.073002, doi:10.1103/PhysRevLett.106.073002.

[49] M. Ahmadi, B. X. R. Alves, C. J. Baker, W. Bertsche, A. Capra, S. Cohen, C. Torkzaban, C. L. Cesar, M. Charlton, R. Collister, S. Eriksson, A. Evans, N. Evetts, J. Fajans, T. Friesen, M. C.

Fujiwara, P. Granum, J. S. Hangst, M. E. Hayden, D. Hodgkinson, C. A. Isaac, M. A. Johnson, S. A. Jones, S. Jonsell, N. Kalem, N. Madsen, D. Maxwell, J. T. K. McKenna, S. Menary, T. Momose, J. Munich, K. Olchanski, A. Olin, P. Pusa, C. Ø. Rasmussen, F. Robicheaux, R. L. Sacramento, M. Sameed, E. Sarid, D. M. Silveira, C. So, G. Stutter, T. D. Tharp, R. I. Thompson, D. P. van der Werf, and J. S. Wurtele. Adiabatic expansion cooling of antihydrogen. *Phys. Rev. Res.*, 6:L032065, Sep 2024. URL: https://link.aps.org/doi/10.1103/PhysRevResearch.6.L032065, doi:10.1103/PhysRevResearch.6.L032065.

[50] R. Akbari, B.X.R. Alves, C.J. Baker, M. Baquero-Ruiz, W. Bertsche, E. Butler, C. Burrows, A. Capra, C.L. Cesar, M. Charlton, R. Collister, A. Cridland, S. Eriksson, A. Evans, L.T. Evans, N. Evetts, J. Fajans, T. Friesen, M.C. Fujiwara, D.R. Gill, P. Grandemange, P. Granum, A. Gutierrez, J.S. Hangst, M.E. Hayden, D. Hodgkinson, C.A. Isaac, A. Ishida, M.A. Johnson, J.M. Jones, S.A. Jones, S. Jonsell, A. Khramov, L. Kurchaninov, A. Little, N. Madsen, D. Maxwell, J.T.K. McKenna, S. Menary, J.M. Michan, T. Momose, P.S. Mullan, K. Olchanski, A. Olin, J. Peszka, A. Povilus, A. Powell, P. Pusa, C.Ø. Rasmussen, R.L. Sacramento, M. Sameed, E. Sarid, D.M. Silveira, C. So, S. Stracka, G. Stutter, T.D. Tharp, R.I. Thompson, C. Torkzaban, D.P. van der Werf, and J.S. Wurtele. The ALPHA-2 apparatus - facilitating experimentation with trapped antihydrogen. *Nuclear Instruments and Methods in Physics Research Section A: Accelerators, Spectrometers, Detectors and Associated Equipment*, 1072:170194, 2025. URL: https://www.sciencedirect.com/science/article/pii/S0168900224011203, doi:10.1016/j.nima.2024.170194.

[51] J Fajans and A Schmidt. Malmberg–penning and minimum-b trap compatibility: the advantages of higher-order multipole traps. *Nuclear Instruments and Methods in Physics Research Section A: Accelerators, Spectrometers, Detectors and Associated Equipment*, 521(2):318–325, 2004. URL: https://www.sciencedirect.com/science/article/pii/S0168900203031127, doi:10.1016/j.nima.2003.11.194.

[52] J. Fajans, W. Bertsche, K. Burke, S. F. Chapman, and D. P. van der Werf. Effects of extreme magnetic quadrupole fields on penning traps and the consequences for antihydrogen trapping. *Phys. Rev. Lett.*, 95:155001, Oct 2005. URL: https://link.aps.org/doi/10.1103/PhysRevLett.95.155001, doi:10.1103/PhysRevLett.95.155001.

[53] G. Andresen, W. Bertsche, A. Boston, P. D. Bowe, C. L. Cesar, S. Chapman, M. Charlton, M. Chartier, A. Deutsch, J. Fajans, M. C. Fujiwara, R. Funakoshi, D. R. Gill, K. Gomberoff, J. S. Hangst, R. S. Hayano, R. Hydomako, M. J. Jenkins, L. V. Jørgensen, L. Kurchaninov, N. Madsen, P. Nolan, K. Olchanski, A. Olin, A. Povilus, F. Robicheaux, E. Sarid, D. M. Silveira, J. W. Storey, H. H. Telle, R. I. Thompson, D. P. van der Werf, J. S. Wurtele, and Y. Yamazaki. Antimatter plasmas in a multipole trap for antihydrogen. *Phys. Rev. Lett.*, 98:023402, Jan 2007. URL: https://link.aps.org/doi/10.1103/PhysRevLett.98.023402, doi:10.1103/PhysRevLett.98.023402.

[54] Steven Chapman. *The Effect of Multipole-Enhanced Diffusion on the Joule Heating of a Cold Non-Neutral Plasma*. PhD thesis, UC, Berkeley, 2011. URL: https://alpha.web.cern.ch/sites/default/files/2020-05/SChapmanThesis.pdf.

[55] E. D. Hunter, A. Christensen, J. Fajans, T. Friesen, E. Kur, and J. S. Wurtele. Electron cyclotron resonance (ecr) magnetometry with a plasma reservoir. *Physics of Plasmas*, 27(3):032106, 03 2020. arXiv:https://pubs.aip.org/aip/pop/article-pdf/doi/10.1063/1.5141999/13806318/032106_1_online.pdf, doi:10.1063/1.5141999.

[56] A. M. W. Powell. *Magnetic field characterisation for gravitational free fall measurements of antihydrogen in the ALPHA-g experiment*. PhD thesis, University of Calgary, 2024. URL: https://prism.ucalgary.ca.

[57] Andrew Jordan Christensen. *Exploiting Electron Magnetron Motion in a Penning-Malmberg Trap to Measure Patch Potentials, Misalignment, and Magnetic Fields*. PhD thesis, UC Berkeley, 2024.

[58] C. J. Foot. *Atomic physics*. Oxford University Press, USA, Oxford, 2005. URL: http://scholar.google.com/scholar.bib?q=info:RG8FFqhmF0kJ:scholar.google.com/&output=citation&hl=en&ct=citation&cd=0.

[59] T. Andersen, K. A. Jessen, and G. Sørensen. Mean-life measurements of excited electronic states in neutral and ionic species of beryllium and boron. *Phys. Rev.*, 188:76–81, Dec 1969. URL: https://link.aps.org/doi/10.1103/PhysRev.188.76, doi:10.1103/PhysRev.188.76.

[60] J. J. Bollinger, D. J. Wineland, and Daniel H. E. Dubin. Non-neutral ion plasmas and crystals, laser cooling, and atomic clocks. *Physics of Plasmas*, 1(5):1403–1414, 05 1994. arXiv:https://pubs.aip.org/aip/pop/article-pdf/1/5/1403/19168123/1403_1_online.pdf, doi:10.1063/1.870690.

[61] J. J. Bollinger, J. S. Wells, D. J. Wineland, and Wayne M. Itano. Hyperfine structure of the $2p^2P_{\frac{1}{2}}$ state in $^9Be^+$. *Phys. Rev. A*, 31:2711–2714, Apr 1985. URL: https://link.aps.org/doi/10.1103/PhysRevA.31.2711, doi:10.1103/PhysRevA.31.2711.

[62] Peter J. Mohr, Barry N. Taylor, and David B. Newell. Codata recommended values of the fundamental physical constants: 2006. *Rev. Mod. Phys.*, 80:633–730, Jun 2008. URL: https://link.aps.org/doi/10.1103/RevModPhys.80.633, doi:10.1103/RevModPhys.80.633.

[63] N. Shiga, W. M. Itano, and J. J. Bollinger. Diamagnetic correction to the $^9Be^+$ ground-state hyperfine constant. *Phys. Rev. A*, 84:012510, Jul 2011. URL: https://link.aps.org/doi/10.1103/PhysRevA.84.012510, doi:10.1103/PhysRevA.84.012510.

[64] Claudio Torregrosa Martin, Antonio Perillo-Marcone, Marco Calviani, and José-Luis Muñoz Cobo. Cern antiproton target: Hydrocode analysis of its core material dynamic response under proton beam impact. *Phys. Rev. Accel. Beams*, 19:073402, Jul 2016. URL: https://link.aps.org/doi/10.1103/PhysRevAccelBeams.19.073402, doi:10.1103/PhysRevAccelBeams.19.073402.

[65] D. Möhl. Production of low-energy antiprotons. *Hyperfine Interactions*, 109(1/4):33–41, 1997. doi:10.1023/a:1012680728257.

[66] J.Y. Hémery and S. Maury. The antiproton decelerator: Overview. *Nuclear Physics A*, 655(1–2):c345–c352, Aug 1999. doi:10.1016/s0375-9474(99)00223-7.

[67] Laurette Ponce, Lajos Bojtár, Christian Carli, Bruno Dupuy, Yann Dutheil, Pierre Freyermuth, Davide Gamba, Lars Jørgensen, Bertrand Lefort, and Sergio Pasinelli. ELENA - From Commissioning to Operation. *JACoW*, IPAC2022:2391–2394, 2022. doi:10.18429/JACoW-IPAC2022-THOXGD1.

[68] Vinod Chohan, C Alanzeau, M E Angoletta, J Baillie, D Barna, W Bartmann, P Belochitskii, J Borburgh, H Breuker, F Butin, M Buzio, O Capatina, C Carli, E Carlier, M Cattin, T Dobers, P Chiggiato, L Ducimetiere, T Eriksson, S Fedemann, T Fowler, R Froeschl, R Gebel, N Gilbert, S Hancock, J Harasimowicz, M Hori, L V Jorgensen, R Kersevan, D Kuchler, J M Lacroix, G LeGodec, P Lelong, L Lopez-Hernandez, S Maury, J Molendijk, B Morand, A Newborough, D Nisbet, A Nosych, W Oelert, M Paoluzzi, S Pasinelli, F Pedersen, D Perini, B Puccio, J Sanchez-Quesada, D Schoerling, L Sermeus, L Soby, M Timmins, D Tommasini, G Tranquille, G Vanbavinckhove, A Vorozhtsov, C Welsch, and T Zickler. *Extra Low ENergy Antiproton (ELENA) ring and its Transfer Lines: Design Report*. CERN Yellow Reports: Monographs. CERN, Geneva, 2014. URL: https://cds.cern.ch/record/1694484, doi:10.5170/CERN-2014-002.

[69] Mark Johnson. *Design and commissioning of beamlines for the ALPHA antihydrogen experiment*. PhD thesis, University of Manchester, 2019.

[70] Siara Fabbri. *Optimization of antiproton capture and delivery for the ALPHA antihydrogen experiment*. PhD thesis, Manchester University, 2021. URL: https://www.librarysearch.manchester.ac.uk/permalink/44MAN_INST/1r887gn/alma992983764170101631.

[71] M K Ramaswamy. A reinvestigation of the decay of na-22. *Indian Journal of Physics (India) Beginning in 1977 alternate issues designated as [Part] A or [Part] B Includes Proc. Indian Assoc. Cultiv. Sci.*, Vol: 33, 07 1959. URL: https://www.osti.gov/biblio/4193336.

[72] D.P van der Werf, L.V Jørgensen, T.L Watson, M Charlton, M.J.T Collier, M Doser, and R Funakoshi. The athena positron accumulator. *Applied Surface Science*, 194(1):312–316, 2002. 9th International Workshop on Slow Positron Beam Techniques for Solids and Surfaces. URL: https://www.sciencedirect.com/science/article/pii/S0169433202001411, doi:10.1016/S0169-4332(02)00141-1.

[73] T. J. Murphy and C. M. Surko. Positron trapping in an electrostatic well by inelastic collisions with nitrogen molecules. *Phys. Rev. A*, 46:5696–5705, Nov 1992. URL: https://link.aps.org/doi/10.1103/PhysRevA.46.5696, doi:10.1103/PhysRevA.46.5696.

[74] R. G. Greaves, M. D. Tinkle, and C. M. Surko. Creation and uses of positron plasmas*. *Physics of Plasmas*, 1(5):1439–1446, 05 1994. arXiv:https://pubs.aip.org/aip/pop/article-pdf/1/5/1439/19167988/1439_1_online.pdf, doi:10.1063/1.870693.

[75] M Amoretti, C Amsler, G Bazzano, G Bonomi, A Bouchta, P Bowe, C Carraro, C.L Cesar, M Charlton, M Doser, V Filippini, A Fontana, M.C Fujiwara, R Funakoshi, P Genova,

J.S Hangst, R.S Hayano, L.V Jørgensen, V Lagomarsino, R Landua, D Lindelöf, E Lodi Rizzini, M Macri, N Madsen, G Manuzio, M Marchesotti, P Montagna, H Pruys, C Regenfus, P Riedler, A Rotondi, G Rouleau, G Testera, A Variola, and D.P van der Werf. High rate production of antihydrogen. *Physics Letters B*, 578(1):23–32, 2004. URL: https://www.sciencedirect.com/science/article/pii/S0370269303016319, doi:10.1016/j.physletb.2003.10.062.

[76] G B Andresen, M D Ashkezari, M Baquero-Ruiz, W Bertsche, P D Bowe, E Butler, C L Cesar, S Chapman, M Charlton, A Deller, S Eriksson, J Fajans, T Friesen, M C Fujiwara, D R Gill, A Gutierrez, J S Hangst, W N Hardy, M E Hayden, A J Humphries, R Hydomako, M J Jenkins, S Jonsell, L V JØrgensen, L Kurchaninov, N Madsen, J T K McKenna, S Menary, P Nolan, K Olchanski, A Olin, A Povilus, P Pusa, F Robicheaux, J Sampson, E Sarid, D Seddon, S Seif el Nasr, D M Silveira, C So, J W Storey, R I Thompson, J Thornhill, D Wells, D P van der Werf, J S Wurtele, and Y Yamazaki. The ALPHA – detector: Module production and assembly. *Journal of Instrumentation*, 7(01):C01051, jan 2012. URL: https://dx.doi.org/10.1088/1748-0221/7/01/C01051, doi:10.1088/1748-0221/7/01/C01051.

[77] Andrea Capra. *Testing CPT and antigravity with trapped antihydrogen at ALPHA*. PhD thesis, York University, 2015.

[78] W A Bertsche, E Butler, M Charlton, and N Madsen. Physics with antihydrogen. *Journal of Physics B: Atomic, Molecular and Optical Physics*, 48(23):232001, oct 2015. URL: https://dx.doi.org/10.1088/0953-4075/48/23/232001, doi:10.1088/0953-4075/48/23/232001.

[79] G. B. Andresen, W. Bertsche, P. D. Bowe, C. C. Bray, E. Butler, C. L. Cesar, S. Chapman, M. Charlton, S. Seif El Nasr, J. Fajans, M. C. Fujiwara, D. R. Gill, J. S. Hangst, W. N. Hardy, R. S. Hayano, M. E. Hayden, A. J. Humphries, R. Hydomako, L. V. Jørgensen, S. J. Kerrigan, L. Kurchaninov, R. Lambo, N. Madsen, P. Nolan, K. Olchanski, A. Olin, A. P. Povilus, P. Pusa, E. Sarid, D. M. Silveira, J. W. Storey, R. I. Thompson, D. P. van der Werf, Y. Yamazaki, and ALPHA Collaboration. Antiproton, positron, and electron imaging with a microchannel plate/phosphor detector. *Review of Scientific Instruments*, 80(12):123701, 12 2009. doi:10.1063/1.3266967.

[80] M. Krems, J. Zirbel, M. Thomason, and R. D. DuBois. Channel electron multiplier and channelplate efficiencies for detecting positive ions. *Review of Scientific Instruments*, 76(9):093305, 09 2005. arXiv:https://pubs.aip.org/aip/rsi/article-pdf/doi/10.1063/1.2052052/15828074/093305_1_online.pdf, doi:10.1063/1.2052052.

[81] So Chuckman. *Antiproton and positron dynamics in antihydrogen production*. PhD thesis, University of California, Berkeley, 2014. URL: https://alpha.web.cern.ch/sites/default/files/2020-05/thesis_chukman_dec23_dist.pdf.

[82] Eric Hunter. *Cavity and Microwave Experiments on Electron Plasma*. PhD thesis, UC, Berkeley (main), 2019.

[83] Len Takahashi Evans. *Phenomenology of creation of antihydrogen and measurement of antihydrogen properties*. PhD thesis, UC, Berkeley (main), 2016.

[84] E. D. Hunter, J. Fajans, N. A. Lewis, A. P. Povilus, C. Sierra, C. So, and D. Zimmer. Plasma temperature measurement with a silicon photomultiplier (SiPM). *Review of Scientific Instruments*, 91(10):103502, 10 2020. doi:10.1063/5.0006672.

[85] Yves Colombe, Daniel H. Slichter, Andrew C. Wilson, Dietrich Leibfried, and David J. Wineland. Single-mode optical fiber for high-power, low-loss uv transmission. *Opt. Express*, 22(16):19783–19793, Aug 2014. URL: https://opg.optica.org/oe/abstract.cfm?URI=oe-22-16-19783, doi:10.1364/OE.22.019783.

[86] Sarah Price. Performance characterisation of an optical fibre for ALPHA. Technical Report CERN-STUDENTS-Note-2023-127, CERN, September 2023. URL: https://repository.cern/records/yfbh0-9pd22.

[87] D. Bäuerle. *Laser Processing and Chemistry*. Springer, 2011. URL: https://link.springer.com/book/10.1007/978-3-642-17613-5.

[88] Sebastian Wolf, Dominik Studer, Klaus Wendt, and Ferdinand Schmidt-Kaler. Efficient and robust photo-ionization loading of beryllium ions. *Applied Physics B*, 124, 01 2018. doi:10.1007/s00340-018-6903-3.

[89] G. Baraldi, A. Perea, and C. N. Afonso. Dynamics of ions produced by laser ablation of several metals at 193 nm. *Journal of Applied Physics*, 109(4):043302–043302–6, 02 2011. arXiv:https://pubs.aip.org/aip/jap/article-pdf/109/4/043302/14885797/043302_1_online.pdf, doi:10.1063/1.3549159.

[90] S Amoruso, V Berardi, R Bruzzese, N Spinelli, and X Wang. Kinetic energy distribution of ions in the laser ablation of copper targets. *Applied Surface Science*, 127-129:953–958, 1998. URL: https://www.sciencedirect.com/science/article/pii/S0169433297007721, doi:10.1016/S0169-4332(97)00772-1.

[91] J.I. Apiñaniz, Borja Sierra, Roberto Martínez, Asier Longarte, Carolina Redondo, and Fernando Castaño. Ion kinetic energy distributions and mechanisms of pulsed laser ablation on al+. *The Journal of Physical Chemistry C*, 112:16556–16560, 10 2008. doi:10.1021/jp805610h.

[92] B. Toftmann, J. Schou, and S. Canulescu. Energy distribution of ions produced by laser ablation of silver in vacuum. *Applied Surface Science*, 278:273–277, 2013. Laser materials processing for micro and nano applications, E-MRS 2012 Symposium V. URL: https://www.sciencedirect.com/science/article/pii/S0169433213002894, doi:10.1016/j.apsusc.2013.01.214.

[93] Lorenzo Torrisi, Santo Gammino, L Andò, Vincenzo Nassisi, Domenico Doria, and A Pedone. Comparison of nanosecond laser ablation at 1064 and 308 nm wavelength. *Applied Surface Science - APPL SURF SCI*, 210:262–273, 04 2003. doi:10.1016/S0169-4332(02)01467-8.

[94] R. D. Knight. Storage of ions from laser-produced plasmas. *Applied Physics Letters*, 38(4):221–223, 02 1981. arXiv:https://pubs.aip.org/aip/apl/article-pdf/38/4/221/18443073/221_1_online.pdf, doi:10.1063/1.92315.

[95] Toshihiko Ooie, Tetsuo Yano, Masafumi Yoneda, and Munehide Katsumura. An ion source using laser ablation. *Journal of Laser Applications*, 12(4):171–174, 08 2000. arXiv:https://pubs.aip.org/lia/jla/article-pdf/12/4/171/11966565/171_1_online.pdf, doi:10.2351/1.521929.

[96] Fabio Belloni, Domenico Doria, Antonella Lorusso, Vincenzo Nassisi, and Lorenzo Torrisi. Development of an Ion Source via Laser Ablation Plasma. *Proceedings of EPAC 2006*, 2006. URL: https://cds.cern.ch/record/1079188.

[97] Kevin Sheridan, W. Lange, and Matthias Keller. All-optical ion generation for ion trap loading. *Applied Physics B*, 104:755–761, 09 2011. doi:10.1007/s00340-011-4563-7.

[98] K. Zimmermann, M. V. Okhapkin, O. A. Herrera-Sancho, and E. Peik. Laser ablation loading of a radiofrequency ion trap. *Applied Physics B*, 107(4):883–889, February 2012. URL: http://dx.doi.org/10.1007/s00340-012-4884-1, doi:10.1007/s00340-012-4884-1.

[99] Kevin Thomas Sheridan. *Experimental techniques for cold chemistry and molecular spectroscopy in an ion trap*. PhD thesis, University of Sussex, 2013.

[100] K. Fehre, D. Trojanowskaja, J. Gatzke, M. Kunitski, F. Trinter, S. Zeller, L. Ph. H. Schmidt, J. Stohner, R. Berger, A. Czasch, O. Jagutzki, T. Jahnke, R. Dörner, and M. S. Schöffler. Absolute ion detection efficiencies of microchannel plates and funnel microchannel plates for multi-coincidence detection. *Review of Scientific Instruments*, 89(4):045112, 04 2018. arXiv:https://pubs.aip.org/aip/rsi/article-pdf/doi/10.1063/1.5022564/15768657/045112_1_online.pdf, doi:10.1063/1.5022564.

[101] Steven Crooks. *Rotational Pumping Transport in Magnetized, Non-Neutral Plasmas*. PhD thesis, University of California San Diego (UCSD), 1995.

[102] Thomas M. O'Neil. Rotational pumping revisited. *Physics of Plasmas*, 28(10):102103, 10 2021. arXiv:https://pubs.aip.org/aip/pop/article-pdf/doi/10.1063/5.0064401/15877654/102103_1_online.pdf, doi:10.1063/5.0064401.

[103] Andrea Gutierrez. *Cold antihydrogen experiments and radial compression of antiproton clouds in the ALPHA apparatus at CERN*. PhD thesis, University of British Columbia, 2016. URL: https://open.library.ubc.ca/collections/ubctheses/24/items/1.0223173, doi:http://dx.doi.org/10.14288/1.0223173.

[104] Niels Madsen, Francis Robicheaux, and Svante Jonsell. Antihydrogen trapping assisted by sympathetically cooled positrons. *New Journal of Physics*, 16:063046, 06 2014. doi:10.1088/1367-2630/16/6/063046.

[105] Jaspal Singh. *Magnetometry advancements for precision antihydrogen gravity measurements*. PhD thesis, Manchester University, 2025. URL: https://www.librarysearch.manchester.ac.uk/permalink/44MAN_INST/bofker/alma9929921911975016 31.

[106] S Jonsell, D P van der Werf, M Charlton, and F Robicheaux. Simulation of the formation of antihydrogen in a nested penning trap: effect of positron density. *Journal of Physics B:*

Atomic, Molecular and Optical Physics, 42(21):215002, oct 2009. URL: https://dx.doi.org/10.1088/0953-4075/42/21/215002, doi:10.1088/0953-4075/42/21/215002.

[107] C L Taylor, Jingjing Zhang, and F Robicheaux. Cooling of rydberg during radiative cascade. *Journal of Physics B: Atomic, Molecular and Optical Physics*, 39(23):4945, nov 2006. doi:10.1088/0953-4075/39/23/012.

[108] F. Robicheaux. Three-body recombination for electrons in a strong magnetic field: Magnetic moment. *Physical Review A*, 73(3), Mar 2006. doi:10.1103/physreva.73.033401.

[109] G. Gabrielse, S. L. Rolston, L. Haarsma, and W. Kells. Possible antihydrogen production using trapped plasmas. *Hyperfine Interactions*, 44(1–4):287–293, Mar 1989. doi:10.1007/bf02398677.

[110] S Jonsell, M Charlton, and D P van der Werf. The role of antihydrogen formation in the radial transport of antiprotons in positron plasmas. *Journal of Physics B: Atomic, Molecular and Optical Physics*, 49(13):134004, jun 2016. URL: https://dx.doi.org/10.1088/0953-4075/49/13/134004, doi:10.1088/0953-4075/49/13/134004.

[111] D Hodgkinson. *On the Dynamics of Adiabatically Cooled Antihydrogen in an Octupole-Based Ioffe-Pritchard Magnetic Trap*. PhD thesis, Manchester University, 2022.

[112] Lukas Golino. *Machine learning methods for Antihydrogen Detection*. PhD thesis, Swansea University, 2024. doi:10.23889/SUThesis.69339.

[113] A. Capra and ALPHA collaboration. Lifetime of magnetically trapped antihydrogen in ALPHA. *Hyperfine Interactions*, 240(9), 2019. doi:10.1007/s10751-018-1526-y.

[114] Takashi Nakamura, Michiharu Wada, Kunihiro Okada, Ichiro Katayama, Shunsuke Ohtani, and H.A. Schuessler. Precision spectroscopy of the zeeman splittings of the $^9Be^+ 2^2S_{1/2}$ hyperfine structure for nuclear structure studies. *Optics Communications*, 205(4):329–336, 2002. URL: https://www.sciencedirect.com/science/article/pii/S0030401802012592, doi:10.1016/S0030-4018(02)01259-2.

[115] Marie J. Jensen, Taro Hasegawa, and John J. Bollinger. Temperature and heating rate of ion crystals in penning traps. *Phys. Rev. A*, 70:033401, Sep 2004. URL: https://link.aps.org/doi/10.1103/PhysRevA.70.033401, doi:10.1103/PhysRevA.70.033401.